Performance Improvement of Embedded Electric Actuators by means of a Thermal Management Optimisation

Francesco de Giorgi

Université Fédérale
Toulouse Midi-Pyrénées

THÈSE

En vue de l'obtention du

DOCTORAT DE L'UNIVERSITÉ DE TOULOUSE

Délivré par :

Institut National des Sciences Appliquées de Toulouse (INSA Toulouse)

Présentée et soutenue par

Francesco DE GIORGI
le: 28/06/2021

Performance Improvement of Embedded Electric Actuators by means of a Thermal Management Optimisation

---

École doctorale : MEGEP - Génie Mécanique, Energétique, Génie civil, Procédés

Discipline ou spécialité : Génie mécanique, mécanique des matériaux

Unité de recherche : Institut Clément Ader (UMR CNRS 5312)

Directeur de Thèse:
Marc BUDINGER, Maître de Conférences (HDR), INSA Toulouse, ICA

Co-Directeur(s) de Thèse:
Ion HAZYUK, Maître de Conférences, INSA Toulouse, ICA
Jean-Charles MARÈ, Professeur, INSA Toulouse, ICA

Jury:
Craig LAWSON, Senior Lecturer, Cranfield University, Rapporteur
Susan LISCOUET-HANKE, Associate Professor, Concordia University, Rapporteur
Christian GHIAUS, Professeur, INSA Lyon, Examinateur (Présidente)
Bruno SARENI, Professeur, INP ENSEEIHT Toulouse, Examinateur
Jérôme PAILHES, Professeur, ENSAM Bordeaux, Examinateur
Lionel YAPI, Ingénieur simulations thermiques et systèmes, COLLINS, Invité
Jérôme SOCHELEAU, Responsable commandes de vol primaires, COLLINS, Invité

To Mirella

Abstract

Thermal management issue is one of the remaining barriers to the use of electrical actuators for primary flight control applications, as their performance and especially their reliability are highly dependent on the operating temperature. Until now, hydraulic technologies have allowed excess heat to be evacuated through the hydraulic network. The problem was relocated and heat exchangers were used to cool the hydraulic fluid. The increasing electrification of aircraft pushes toward the suppression of the hydraulic network and, as a result, the hydraulic fluid will not be available to transport and dissipate the heat generated by the actuators. New thermal management solutions for dealing with the component heat load at a local level are needed. Several studies have looked specifically to this purpose, which provided efficient potential solutions for the thermal management of electrical flight actuators. This thesis mainly focuses on a topic that has not yet been fully explored in the literature, which concerns the optimal design and coupling of such solutions with the actuator. In fact, if these solutions are optimally integrated during the preliminary design phase of the actuator, they can provide not only an improvement in the performances of the actuation system, but also the development of a lighter and more compact system, leading to considerable advantages at aircraft level. The objective of this thesis is to provide effective methods and tools suited for the preliminary design of electrical actuators, with a particular attention to the thermal management. The first part of the thesis concerns the identification of potential thermal management solutions. Thermal management devices such as plate fin heat exchanger, heat pipes, thermal straps and phase change materials are investigated. The second part of the thesis regards the implementation of a procedure to optimally preliminary design the system composed by the actuator and its associated thermal management device. Firstly, estimation models are generated in order to estimate the dimensions and performance of cooling devices and actuator components. To this purpose, a new methodology for obtaining simpler and lighter surrogate models is proposed. Subsequently the preliminary design procedure is defined via a Multidisciplinary Design Optimization with a view focused on the mass minimization and thermal constraints satisfaction. Two different approaches for sizing the system are proposed. The first approach consists of performing the preliminary design on the basis of static specifications extrapolated from the mission profile. This approach allows a rapid estimation of the system dimensions and performance, but does not guarantee

optimal thermal dynamics over the entire flight duration. The second approach, more expensive from a computational point of view, consists in integrating the mission profile in the preliminary design, thus allowing the realisation of a system which ensures an optimal thermal dynamic along the mission. Based on the case study of an Airbus A320 and referring to an electro-mechanical actuator, the proposed approaches are applied here to conduct the preliminary design for the whole set of primary flight control surfaces: Aileron, Rudder and Elevator. A quantitative comparison of the most suitable thermal management concepts is made for each of these applications.

Résumé

La problématique de la gestion thermique est l'un des derniers verrous à l'utilisation des actionneurs électriques pour les applications de commandes de vol primaires, car leurs performances et surtout leur fiabilité dépendent fortement de la température de fonctionnement. Jusqu'à présent, les technologies hydrauliques permettaient d'évacuer l'excès de chaleur par le réseau hydraulique. Le problème était délocalisé et des échangeurs de chaleur étaient utilisés pour refroidir le fluide hydraulique. L'électrification croissante des avions pousse à la suppression du réseau hydraulique et, par conséquent, le fluide hydraulique ne sera plus disponible pour transporter et dissiper la chaleur générée par les actionneurs. De nouvelles solutions de gestion thermique permettant de traiter la charge thermique des composants au niveau local sont nécessaires. Plusieurs études se sont penchées spécifiquement sur ce sujet et ont fourni des solutions potentielles efficaces pour la gestion thermique des actionneurs de vol électriques. Cette thèse se concentre principalement sur un sujet qui n'a pas encore été complètement exploré dans la littérature, qui concerne la conception optimale et le couplage de telles solutions avec l'actionneur. En effet, si ces solutions sont intégrées de manière optimale lors de la phase de conception préliminaire de l'actionneur, elles peuvent apporter non seulement une amélioration des performances du système d'actionnement, mais aussi le développement d'un système plus léger et plus compact, conduisant à des avantages considérables au niveau de l'avion. L'objectif de cette thèse est de fournir des méthodes et des outils efficaces adaptés à la conception préliminaire d'actionneurs électriques, avec une attention particulière à la gestion thermique. La première partie de la thèse concerne l'identification des solutions potentielles de gestion thermique. Les dispositifs de gestion thermique tels que les radiateurs à ailettes, les caloducs, les bandes thermiques et les matériaux à changement de phase sont étudiés. La deuxième partie de la thèse concerne la mise en œuvre d'une procédure pour la conception préliminaire optimale du système composé de l'actionneur et de son dispositif de gestion thermique associé. Tout d'abord, des modèles d'estimation sont générés afin d'estimer les dimensions et les performances des dispositifs de refroidissement et des composants de l'actionneur. Dans ce but, une nouvelle méthodologie pour obtenir des modèles de substitution plus simples et plus légers est proposée. Ensuite, la procédure de conception préliminaire est définie par le biais d'une optimisation multidisciplinaire dans le but de minimiser la masse et de satisfaire les contraintes thermiques. Deux approches différentes

pour le dimensionnement du système sont proposées. La première approche consiste à effectuer la conception préliminaire sur la base de spécifications statiques extrapolées à partir du profil de la mission. Cette approche permet une estimation rapide des dimensions et des performances du système, mais ne garantit pas une dynamique thermique optimale sur toute la durée du vol. La seconde approche, plus coûteuse d'un point de vue computationnel, consiste à intégrer le profil de mission dans la procédure de conception préliminaire, permettant ainsi la réalisation d'un système qui assure une dynamique thermique optimale tout au long de la mission. En se basant sur le cas d'un Airbus A320 et en se référant à un actionneur électromécanique, les approches proposées sont appliquées ici pour réaliser le dimensionnement préliminaire de l'ensemble des commandes de vol primaires : aileron, rudder et elevator. Une comparaison quantitative des concepts de gestion thermique les plus appropriés est effectuée pour chacune de ces applications.

Acknowledgements

First, I would like to thank all the members of the jury for accepting to examine my work. I particularly would like to thank Prof. Liscouet-Hanke and Prof. Craig Lawson for accepting to review the work presented in this thesis. The quality of their reviews and their suggestions have significantly helped me to improve the quality of the dissertation. I am also very thankful to Prof. Christian Ghiaus, Prof. Bruno Sareni and Prof. Jérôme Pailhes for their significant remarks and the interesting discussions we had during the defense.

The accomplishment of this thesis would not have been possible without the support of my supervisors, with whom I spent 3 wonderful years:

- My thesis director, Marc Budinger. Thank you Marc for your implication, interest and willingness to coordinate the thesis project. Your great experience and knowledge in different fields of engineering allowed me to grow very professionally and to conduct a thesis that I am fully satisfied with. Thank you for always stimulating me to give my best, to do new and interesting things and for always encouraging me and suggesting new alternatives in the most difficult moments of my thesis. I hope that we will continue to collaborate on different topics in the near future.

- My co-director, Ion Hazyuk. Thank you Ion for your implication and all your advices during these last 3 years. Thank you for your professionalism, but most of all thank you for your great interest shown in achieving this thesis path. To you, I professionally owe my growth in the domain of thermal engineering, but above all your great willingness to receive and help me in any moment of difficulty, including vacations, encountered during the thesis. I hope, like Marc, that we will collaborate again through future projects.

- My co-director, Jean-Charles Maré. Although I did not have the pleasure of working side by side with you, you have been a source of incredible advice and knowledge that has allowed me to achieve the results of this thesis. I thank you for all that you brought to me during these years through the different meetings between Toulouse and Paris.

I also wish to thank my industrial supervisors, Lionel Yapi and Jérôme Socheleau.

- Lionel, thank you for always being available at key moments of my work. Your advice and help have helped guide this work to meet both scientific and industrial issues. Thank you also for having shared a part of your great expertise and your experiences in implementing thermal simulations at different moments of the thesis.
- Jérôme, thank you for contributing so that this thesis runs smoothly. Thank you for the meetings you attended, for your advice, and for contributing to the success of this project.

I have enjoyed working with you and I hope we can continue to collaborate in the future. I couldn't have asked for better supervisors and mentors, thank you again.

I would also like to thank all the members, former members, colleagues and especially friends of the Institut Clément Ader for the friendly atmosphere that I have experienced over the past few years: Florian, Scott, Aurelien, Aitor, Varun, Adama, Louis, Landry, Laure, Montassar, Thome, Marcos and so many others.
It is now time to thank my colleagues at Collins Aerospace. Thanks to Sylvain, Sulivan, Damian, Karl, Fernando, Arnauld, Federico for the good times spent together at work, although the complicated period due to COVID did not allow us to spend much time together.
The success of a thesis is undoubtedly conditioned by a good balance between work and personal life. So I will now thank my family and friends who have given me unparalleled support and countless opportunities to get my head out of this thesis. Thanks to my friends in Toulouse, especially Silvio, Guilherme, Dominique, Daniel, Nico, Jeremi and David for the wonderful evenings and adventures we spent together. To you, I owe the risk of not achieving my thesis. Thanks also to my Parisian friends, especially Sebastian, Roman, Dario, Dani and Adi. Without you, the move to Paris would not have been easy. Thank you for always being there in times of difficulty and for the crazy evenings we spent together.
Last, but certainly in first place for order of importance, the biggest thanks goes to my family. Thanks to my grandmother Eleonora, my uncle Umberto and aunt Adele for their great affective support reserved for me not only in these last 3 years of thesis. Thanks to

my parents, who through their enormous economic sacrifices and more, have allowed me to realize my dreams. To you, I dedicate this success of mine, hoping to make you more and more proud of me every day, so that one day I can reciprocate the enormous love and great efforts made by you to ensure me an exceptional future.

Contents

Nomenclature **xxvii**

1 Context **1**

1.1 Industrial context 1

1.1.1 Toward a More Aircraft Electrification 1

1.1.2 Electrical flight control actuators: EMA and EHA 3

1.1.3 Thermal management of electric actuators: challenges, solutions and design approaches 6

1.1.4 Objectives 9

1.2 Scientific context 10

1.2.1 Preliminary design and optimization of electrical actuators: the need of Multidisciplinary Design Optimization 10

1.2.2 Models needed for preliminary design: Surrogate models 11

1.2.3 Previous theses conducted at Institut Clément Ader 12

1.2.4 Objectives 13

1.3 Dissertation overview 14

2 Challenges and Solutions for Thermal Management of Electric Actuators 17

2.1 Introduction 17

2.2 Analysis of thermal challenges of electric actuators 18

2.2.1 The sources of heat 18

2.2.2 Operating temperature requirements 20

2.2.3 Thermal environment and design scenarios 22

2.2.4 Mission profile analysis and design approaches 23

2.3 State of the art of thermal management solutions 25

2.3.1 Improve the losses management 26

2.3.2 Improve the heat transfer 31

2.3.3 Improve the transient generation and storage . . . 37
2.4 Selected solutions for thermal management . . . 40
2.5 Conclusion . . . 44

3 Methodologies and Models for the Preliminary Design 47
3.1 Introduction . . . 48
3.2 State of the Art of Surrogate Modelling . . . 49
3.2.1 Surrogate Modelling Approaches for Multi-Disciplinary Design Optimization . . . 49
3.2.2 Surrogate Modelling Techniques . . . 51
3.3 VPLM Methodology . . . 54
3.4 Generalization of model reduction procedure via a sensitivity analysis based on optimization . . . 58
3.5 Generation of surrogate models of a PM brushless motor . . . 61
3.5.1 Dimensional Analysis . . . 62
3.5.2 Sensitivity analysis for the selection of meaningful π numbers . . . 65
3.5.3 Model generation . . . 67
3.6 Conclusion . . . 70

4 Primary Flight Control Actuation System Design Based on Static Approach 73
4.1 Introduction . . . 74
4.2 Overview of the design problem and description of the sizing procedure . . . 74
4.3 Definition of specifications for the established EMA architecture . . . 76
4.3.1 Definition of architectures . . . 76
4.3.2 Design Drivers . . . 79
4.3.3 Sizing scenarios . . . 81
4.3.4 Mission profile analysis and extrapolation of design specifications . . . 82
4.4 Generation of component and system models . . . 87
4.4.1 Sizing scenario models . . . 88
4.4.2 Component models . . . 91
4.5 Definition of the sizing procedure . . . 106
4.6 Design and optimization . . . 108
4.6.1 Computation, capitalization and model construction times . . . 113

4.7 Conclusion 114

5 Model Generation of Unconventional Thermal Management Systems: Solutions for Steady State 115

5.1 Introduction 116
5.2 Characterization of aircraft heat sink 117
5.2.1 Proposed installation method of the heat transfer devices 117
5.2.2 Computation of the heat transfer coefficient 119
5.3 Heat Pipe 121
5.3.1 Heat transfer and temperature difference 124
5.3.2 Estimation model of heat pipe 126
5.3.3 Heat pipe design 129
5.4 Thermal Strap 130
5.4.1 Estimation model of thermal straps 132
5.4.2 Thermal strap design 134
5.5 Thermal spreader 135
5.5.1 Estimation model of a Thermal Spreader 136
5.5.2 Thermal spreader design 138
5.6 Thermal interface material 138
5.6.1 Estimation model of TIM 139
5.6.2 TIM design 145
5.7 Conclusion 146

6 Model Generation of Unconventional Thermal Management Systems: Solutions for Transient Regime 149

6.1 Introduction 149
6.2 Characterisation and classification of mission profiles 150
6.2.1 Analysis of PST and PSE indicators for the considered mission profiles 153
6.3 Sensible heat storage 155
6.3.1 Design techniques to improve sensible heat storage 157
6.4 Phase Change Materials 158
6.4.1 Mathematical representation of the phase transition of a PCM Slab 160
6.4.2 Application of the mathematical formulations 163
6.4.3 Model of the PCM integrated in a finned plate 166

6.4.4 PCM-Fin module design 170
6.5 Conclusion 172

7 A Dynamic Approach for the Preliminary Design of Primary Flight Control Actuators 173
7.1 Introduction 174
7.2 Actuator dynamic model for thermal behaviour 176
7.2.1 Electro-mechanical transmission chain model 177
7.2.2 Motor Losses Model 178
7.2.3 Motor Thermal Model 179
7.2.4 Atmospheric model 181
7.2.5 Thermal management system models 183
7.2.6 Validation of the electro-mechanical actuators designed with the static approach 187
7.3 Preliminary design and evaluation of the discussed TMS concepts 189
7.3.1 Model integration in the preliminary design framework 189
7.3.2 Case study 1: Finned thermal housing 190
7.3.3 Case study 2: Heat pipe 196
7.3.4 Case study 3: Thermal Strap 200
7.3.5 Case study 4: PCM 203
7.3.6 Trade-off analysis 205
7.3.7 Computational times and design compromises 209
7.4 Conclusion 210

8 Conclusions and Perspectives 213
8.1 Summary 213
8.2 Limitations and propositions for future works 219

Bibliography 237

A Finite Element Model of the PM Brushless Motor 239

B Mission Profiles used for the Preliminary Designs 243

C Static Preliminary Design Case Studies 249

D Dynamic Preliminary Design Case Studies 265

List of Figures

1.1 The two axis of More Electrical Aircraft [7]. 2
1.2 Example of AIRBUS A330: power efficiency for the different energy types [10]. 3
1.3 The different technologies of on-board actuators [12] 4
1.4 Some examples of primary flight control EHAs [8]. 4
1.5 Some examples of primary flight control EMAs [8]. 5
1.6 A family of flexible heat pipes used in aircraft [26]. 7
1.7 Evolution of the actuator temperature along the mission profiles for three different design cases. 8
1.8 Sequential approach for preliminary design of EA. 11
1.9 Multidisciplinary approach for preliminary design of EA. 11

2.1 Example of synchronous motor losses distribution [40]. 19
2.2 Classes of winding insulation material [43] 21
2.3 Aircraft flight phases [12]. 22
2.4 Examples of mission profiles for each primary flight control surface. 24
2.5 Strategies for improving the thermal management of EAs. 26
2.6 Strategies for improving the losses management. 26
2.7 Examples of different types of winding. 27
2.8 Determination of a machine with concentrated windings and an irregular distribution of slots from an initial machine with 12 slots and 4 poles [46]. 28
2.9 Example of Halbach magnet arrangement [52]. 28
2.10 Example of partly slots opening [54]. 29
2.11 Conceptual integration process in switch mode converters from (left) discrete component design to (right) more integrated design [58]. 30
2.12 Strategies for improving the losses management. 31
2.13 Example of motor housing with fin arrays [61]. 31
2.14 Underwing scoops for actuator cooling (EHA of the Airbus A350 aileron) [8]. 32

2.15 Example of flexible thermal straps [65]. 33
2.16 Geometry and structure of flexible heat pipes [26]. 33
2.17 Example of the waviness and roughness of two contacting surfaces and how thermal interface material improve the contact area between the surfaces [67]. 34
2.18 Geometry and structure of thermosyphon [13]. 35
2.19 Liquid Cooling system circuit [13]. 36
2.20 Strategies for improving the transient generation and storage. 37
2.21 Examples of design techniques to embed PCM into aluminium heat sinks. . 38
2.22 Mind map of all presented thermal management solutions for EAs. 39
2.23 Selected solutions for thermal management of EAs. 40
2.24 Motor thermal housing with fins arrays. 42
2.25 Examples of thermal straps (a) and heat pipes (b) configurations. 42
2.26 Examples of PCM configuration and integration. 43
2.27 Coupling between finned thermal housing and PCM module. 44

3.1 Surrogating approaches employed in MDO: a) MBDO and b) SBAO. . . . 51
3.2 VPLM methodology flowchart 55
3.3 Example of results of sensitivity analysis after ranking the terms (in absolute value) according to their importance for the case of two dimensionless numbers [77]. 57
3.4 Example of evolution of maximum and mean relative errors as a function of the number of terms adopted for the definition of the model. 57
3.5 a) Comparison of VPLM model with finite element simulations for a selected model with 5 terms a b) error distribution. 58
3.6 Flowchart of the proposed model reduction process. 60
3.7 a) Parvex NX 310 servomotor [89] and b) its representative finite elements model. 61
3.8 Stator and Rotor geometrical variables. 62
3.9 Results of sensitivity analysis. 66
3.10 Model reduction process applied on the PM brushless motor model. 67
3.11 (a) Evolution of the error for the model of torque and b) comparison of VPLM model with FEMM model for the selected model with 5 terms. . . . 68
3.12 (a) Evolution of the error for the model of Joule losses and b) comparison of VPLM model with FEMM model for the selected model with 3 terms. . 69

3.13 (a) Evolution of the error for the model of iron losses and b) comparison of VPLM model with FEMM model for the selected model with 5 terms. . . . 69
3.14 Variables representation space. 70

4.1 Methodologies and methods adopted for the preliminary design. 76
4.2 Actuator components considered for the case study. 76
4.3 Considered EMA architectures for the case study. 77
4.4 Electric Motor and gearbox types considered for this study. 77
4.5 Screw nut and thrust bearing considered for this study. 78
4.6 Thermal housing with fins. 78
4.7 Component design drivers. 80
4.8 Mission profiles of an aileron surface of an Airbus A320 (NORMALISED DATA). 83
4.9 Extracted mission profiles (NORMALISED DATA). 84
4.10 Fatigue distribution. 86
4.11 System layer and component layer modelling (adapted from [95]. 88
4.12 Aileron EMA integration. 90
4.13 Screw nut model reference:"SRC 25x5" [93] 92
4.14 Thrust bearing model reference: "SKF QJ" [93] 95
4.15 Gearbox geometry. 100
4.16 Application factors for weight estimation [98]. 101
4.17 Thermal housing geometry. 102
4.18 Fin modal analysis. 104
4.19 Problem graphical representation and orientation [95]. 106
4.20 Extended design structure matrix of the EMA preliminary design. 110
4.21 Mass distribution of EMA components for the different types of primary flight control application. 111
4.22 Resulting geometry of Aileron EMA for gear drive configuration. 112
4.23 Resulting geometry of Aileron EMA for direct drive configuration. 112

5.1 Representation of thermal aspects related to heat pipes/thermal straps. . . 116
5.2 HP mounted on the inner side of aircraft wing skin. 117
5.3 HP mounted on a thermal spreader on the exterior side of aircraft wing skin. 118
5.4 Heated surfaces with unheated starting length. 120
5.5 The main composition of heat pipe [108]. 121

5.6 Merit Number vs Temperature for different working fluids [26]. 123
5.7 Heat Pipe Thermal Resistance Network. 125
5.8 Simplified Heat Pipe Thermal Resistance Network. 126
5.9 Heat pipe reference model [109]. 127
5.10 Heat transfer capability of heat pipes at given diameter and fluid temperature [109]. 128
5.11 Representation of the operating environment of heat pipes. 129
5.12 Thermal strap structure [113]. 130
5.13 Example of different types of thermal straps [113]. 131
5.14 Thermal strap reference model. 132
5.15 Thermal conductivity of pyrolitic graphite [119]. 133
5.16 Representation of the operating environment of thermal straps. 134
5.17 Connection of the spreader with the heat pipe. 135
5.18 Spreader geometry of the considered case study. 135
5.19 Example of surface deformation due to bolted joints [67]. 138
5.20 Contact zone of bare interface (left) and interface with polymeric TIM (right)[126]. 139
5.21 Representation of interfacing surfaces. 140
5.22 Geometry of the analysed model. 141
5.23 Example of contact surfaces shape (red zone). 144
5.24 Representation of the interfacing problem for the heat pipe case study. . . 145

6.1 Two examples of theoretical missions and the associated PST 151
6.2 Two examples of theoretical missions differentiated by their PST and E_u. . 152
6.3 Aerodynamic torque profile of the considered applications. 153
6.4 Geometry of the adopted electric motor model. 157
6.5 Temperature Variation in a TMS with PCM [133]. 159
6.6 Geometry and temperature coordinates representing the melting process of a PCM slab. 161
6.7 Dymola model of the PCM slab *Dymola*. 164
6.8 Example of thermal behavior of the Dymola model. 165
6.9 Thermal Behavior of PCM with a heat flux duty-cycle. 166
6.10 PCM embedded in a plate-fin container. 166
6.11 2-D representation of the problem. 166

6.12 Evolution of the liquid frontier (red area representing the liquid phase) of PCM during the melting process. 167
6.13 Decomposition of the PCM-Fin problem. 168
6.14 PCM-fin model implemented in Dymola. 169
6.15 Comparison of the results obtained with Dymola and Ansys models of the PCM. 170
6.16 PCM module integrated in the finned thermal housing. 171

7.1 V design cycle. 174
7.2 Examples of thermal profile of an optimally-sized system. 175
7.3 Actuator dynamic model architecture and interfaces. 177
7.4 Electro-mechanical transmission chain model. 178
7.5 Motor losses model. 179
7.6 Example of 2-body thermal motor model. 180
7.7 Motor Thermal Model. 180
7.8 Atmospheric Model. 182
7.9 Thermal Housing Model. 183
7.10 2-D visualisation of the results obtained with finite volume method simulation for the case study of confined space. 185
7.11 2-D visualisation of the results obtained with finite volume method simulation for the case study of open space. 185
7.12 Heat Pipe Model. 186
7.13 Thermal Strap Model. 187
7.14 Dynamic thermal profile of EMAs designed with the static approach. . . . 188
7.15 Extended design structure matrix of the EMA preliminary design of case study 1. 192
7.16 Thermal profile of EMAs designed with the finned thermal housing. 194
7.17 Effect of a reduced fins size ($L_a = 11.38\,mm$) on the thermal profile of the sized EMA Elevator. 195
7.18 Extended design structure matrix of the EMA preliminary design of case study 2. 197
7.19 Thermal profile of EMAs designed with the heat pipes. 198
7.20 Extended design structure matrix of the EMA preliminary design of case study 3. 201

7.21 Thermal profile of EMAs designed with the thermal straps. 202
7.22 Thermal profile of EMA Aileron designed with PCM module. 203
7.23 Summary of the results obtained from the performed preliminary designs. . 205
7.24 Evolution of the component masses for the designed Aileron EMAs. 210

A.1 a) Parvex NX 310 servomotor and b) its representative finite elements model.239
A.2 Stator and Rotor geometrical variables. 240
A.3 Geometric description of the copper volume per slot pair. 241
A.4 Magnetic flux density on yoke and teeth. 242

B.1 Mission profiles of an aileron surface of an Airbus A320 (NORMALISED DATA). 244
B.2 Mission profiles of an elevator surface of an Airbus A320 (NORMALISED DATA). 245
B.3 Mission profiles of an Rudder surface of an Airbus A320 (NORMALISED DATA). 246

C.1 XDSM of the EMA preliminary design case studies. 251

D.1 XDSM of the preliminary designs of case study 1. 266
D.2 Thermal profiles (Aileron - Case study 1). 269
D.3 Heat transfer coefficients of finned thermal housing (Aileron - Case study 1). 269
D.4 Motor Losses (Aileron - Case study 1). 269
D.5 Thermal profiles (Elevator - Case study 1). 272
D.6 Heat transfer coefficients of finned thermal housing (Elevator - Case study 1).272
D.7 Motor Losses (Elevator - Case study 1). 272
D.8 Thermal profiles (Rudder - Case study 1). 275
D.9 Heat transfer coefficients of finned thermal housing (Rudder - Case study 1). 275
D.10 Motor Losses (Rudder - Case study 1). 275
D.11 XDSM of the preliminary designs of case study 2. 277
D.12 Thermal profiles (Aileron - Case study 2). 280
D.13 Motor Losses (Aileron - Case study 2). 280
D.14 Aircraft speed profile (TAS) (a), convective heat transfer coefficient on wing (b) and spreader resistance (per TMS unit) (c) (Aileron - Case study 2). . 281
D.15 Thermal profiles (Elevator - Case study 2). 284

D.16 Motor Losses (Elevator - Case study 2). 284
D.17 Aircraft speed profile (TAS) (a), convective heat transfer coefficient on wing (b) and spreader resistance (per TMS unit) (c) (Elevator - Case study 2). . 285
D.18 XDSM of the preliminary designs of case study 3. 287
D.19 Thermal profiles (Aileron - Case study 3). 290
D.20 Motor Losses (Aileron - Case study 3). 290
D.21 Aircraft speed profile (TAS) (a), convective heat transfer coefficient on wing (b) and spreader resistance (per TMS unit) (c) (Aileron - Case study 3). . 291
D.22 Braid resistance (Aileron - Case study 3). 291
D.23 Thermal profiles (Elevator - Case study 3). 294
D.24 Motor Losses (Elevator - Case study 3). 294
D.25 Aircraft speed profile (TAS) (a), convective heat transfer coefficient on wing (b) and spreader resistance (per TMS unit) (c) (Elevator - Case study 3). . 295
D.26 Braid resistance (Elevator - Case study 3). 295
D.27 XDSM of the preliminary design of case study 4. 297
D.28 Thermal profiles (Aileron - Case study 4). 300
D.29 Heat transfer coefficients of finned thermal housing (Aileron - Case study 4). 300
D.30 Motor Losses (Aileron - Case study 4). 300

List of Tables

1.1 Industrial and scientific objectives established for this thesis project. 14

3.1 Synthesis of mathematical forms of pure mathematical approaches [79]. . . 53
3.2 Synthesis of mathematical forms of dimensional analysis based approaches [79]. 54
3.3 Dimensional variables 63
3.4 Dimensionless variables 64
3.5 Variables Π_1 and Π_4 selected for the surrogate model inputs and the value of the remaining dimensionless numbers that conserve geometrical similarity 67

4.1 Verification matrix. 82
4.2 Analysis of mission profile specifications of Aileron (normalised data). . . . 86
4.3 Analysis of mission profile specifications of Elevator (data normalised to Aileron specifications). 86
4.4 Analysis of mission profile specifications of Rudder (data normalised to Aileron specifications). 87
4.5 Component reference for screw-nut (SRC 25x5) [93]. 92
4.6 Component reference for bearing (SKF QJ) [93]. 95
4.7 Dimensionless variables of surrogate models of electric motor 97
4.8 Results of optimizations 109

5.1 Constants for use with Eq. 5.3 [107] 120
5.2 Example of Heat pipe working fluids usable in this context. 122
5.3 Material - Working fluid compatibility [26]. 124
5.4 Possible Material - Fluid combinations in the temperature range -30°C - 100°C. 124
5.5 Characteristics of the reference heat pipes. 128
5.6 Characteristics of the reference thermal strap [113] 132

5.7 "CHO-THERM 1671" TIM properties. 141
5.8 Dimensional variables of the system under study. 142
5.9 Dimensionless variables of the system under study. 143

6.1 PST and PSE values for the considered mission profiles. 154
6.2 Illustrative example of materials used for actuator. 156
6.3 Thermophysical properties of PCMs investigated for different applications [135]. 160
6.4 Functionalized Bio-PCM *0500- Q100 BioPCM.* 164

7.1 Results of optimizations for case study 1 193
7.2 Results of optimizations for case study 2 198
7.3 Results of optimizations for case study 3 202
7.4 Results of optimizations for case study 4 204
7.5 Summary of Case studies TMS concepts. 208

8.1 Industrial and scientific objectives. 213

B.1 Mission profile specifications of Aileron (normalised data). 247
B.2 Mission profile specifications of Elevator (data normalised to aileron specifications). 247
B.3 Mission profile specifications of Rudder (data normalised to aileron specifications). 247

C.1 Inputs parameters values 250
C.2 Design variables, constraints and objective (Aileron gear drive). 252
C.3 System output values (Aileron gear drive). 253
C.4 Design variables, constraints and objective (Aileron direct drive). 254
C.5 System output values (Aileron direct drive). 255
C.6 Design variables, constraints and objective (Elevator gear drive). 256
C.7 System output values (Elevator gear drive). 257
C.8 Design variables, constraints and objective (Elevator direct drive). 258
C.9 System output values (Elevator direct drive). 259
C.10 Design variables, constraints and objective (Rudder gear drive). 260
C.11 System output values (Rudder gear drive). 261
C.12 Design variables, constraints and objective (Rudder direct drive). 262

C.13 System output values (Rudder direct drive). 263

D.1 Inputs parameters values (Case study 1). 266
D.2 Design variables, constraints and objective (Aileron - Case study 1). 267
D.3 System output values (Aileron - Case study 1). 268
D.4 Design variables, constraints and objective (Elevator - Case study 2). . . . 270
D.5 System output values (Elevator - Case study 1). 271
D.6 Design variables, constraints and objective (Rudder - Case study 1). 273
D.7 System output values (Elevator - Case study 1). 274
D.8 Inputs parameters values (Case study 2). 277
D.9 Design variables, constraints and objective (Aileron - Case study 2). 278
D.10 System output values (Aileron - Case study 2). 279
D.11 Design variables, constraints and objective (Elevator - Case study 2). . . . 282
D.12 System output values (Elevator - Case study 2). 283
D.13 Inputs parameters values (Case study 3). 287
D.14 Design variables, constraints and objective (Aileron - Case study 3). 288
D.15 System output values (Aileron - Case study 3) 289
D.16 Design variables, constraints and objective (Elevator - Case study 3). . . . 292
D.17 System output values (Elevator - Case study 3). 293
D.18 Inputs parameters values (Case study 4). 297
D.19 Design variables, constraints and objective (Aileron - Case study 4). 298
D.20 System output values (Aileron - Case study 4). 299

Nomenclature

Acronyms / Abbreviations

DoE	*Design of Experiment*
EA	*Electric Actuator*
ECU	*Electronic Control Unit*
EMA	*Electro-Mechanical Actuator*
EMI	*Electro-Magnetic Interference*
EHA	*Electro-Hydraulic Actuator*
FEM	*Finite Element Method*
FEMM	*Finite Element Method Magnetics*
FMI	*Functional Mock-up Interface*
FMU	*Functional Mock-up Unit*
HP	*Heat Pipe*
LHS	*Latin Hypercube Sampling*
MBDO	*Meta-model-Based Design Optimization*
MDO	*Multidisciplinary Design Optimisation*
MEA	*More Electrical Aircraft*
NACA	*National Advisory Committee for Aeronautics*
PCM	*Phase Change Material*
PGF	*Prolytic Graphite Foils*
PM	*Permanent Magnet*

PST	*Thermal Storage Potential*
PSE	*Energy Storage Potential*
RBS	*Radial Basis Function*
RMS	*Response Surface Methodology*
SBAO	*Surrogate-Based Analysis and Optimization*
SHA	*Servo-Hydraulic Actuator*
SiC	*Silicon Carbide*
TIM	*Thermal Interface Materials*
TMS	*Thermal Management System*
TS	*Thermal Strap*
VPLM	*Variable Power Law Meta-model*
XDSM	*eXtended Design Structure Matrix*

Chapter 1

Context

Contents

1.1 Industrial context **1**

1.1.1 Toward a More Aircraft Electrification 1

1.1.2 Electrical flight control actuators: EMA and EHA 3

1.1.3 Thermal management of electric actuators: challenges, solutions and design approaches 6

1.1.4 Objectives 9

1.2 Scientific context **10**

1.2.1 Preliminary design and optimization of electrical actuators: the need of Multidisciplinary Design Optimization 10

1.2.2 Models needed for preliminary design: Surrogate models 11

1.2.3 Previous theses conducted at Institut Clément Ader 12

1.2.4 Objectives 13

1.3 Dissertation overview **14**

1.1 Industrial context

1.1.1 Toward a More Aircraft Electrification

The increasing electrification of aircraft is becoming in these days and age a fundamental and formative objective on which the aeronautical industry is strongly focused, as evidenced

by the More Electrical Aircraft (MEA) program [1]. The MEA has involved numerous research programs over the past twenty years, both in the academic [2] [3] [4] and industrial worlds [5] [6], in order to overcome many technological and scientific barriers. The major electrifications of aircraft consist of incrementing the electrical power sources for both propulsion and non-propulsion on-board power transmission systems. This can be done according to two strategies, as illustrated in Fig. 1.1: the replacement of pneumatic networks ("bleedless") and/or the replacement of hydraulic networks ("hydraulicless"). The first strategy has a strong impact on air conditioning, de-icing and engine starting systems, particularly with the use of high-power electrical machines, associated converters and new electrical network architectures. The second strategy mainly impacts flight control and landing gear systems.

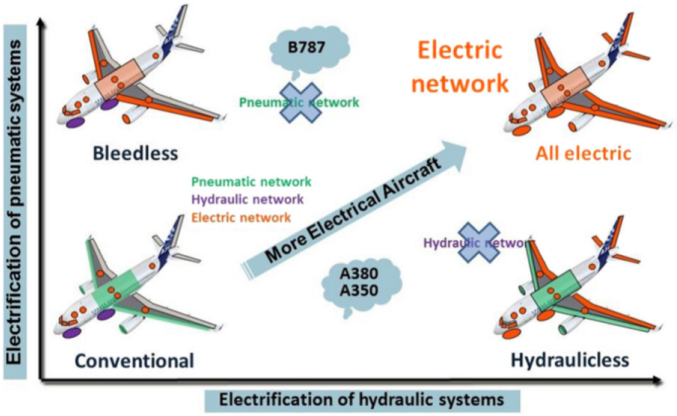

Figure 1.1: The two axis of More Electrical Aircraft [7].

The interests of aircraft electrification are multiple, both in terms of safety and the environment. An overall aircraft weight and fuel burn reduction is expected through the unification of the hydraulic and pneumatic systems, which tend to be heavy and bulky, into a single and lightweight electric system. On larger aircraft, almost 75% of the mass of the hydraulic system comes from the power distribution and only 25% comes from the equipment (pumps and actuators) [8]. The only presence of the electrical power would help to simplify the aircraft design by involving a quicker and simpler assembly and maintenance compared to hydraulic and pneumatic systems which are traditionally labor-intensive [9]. Electric systems have the advantage they exactly provide the necessary amount of power required ("power-on-demand") and can be easily switched off when they are not in use, compared to centralized hydraulic and pneumatic systems, which continuously draw large amounts of power from the engines, regardless of end-user demand. In addition, as it can be observed

when analysing the overall energy flows of aircraft [10], illustrated in Fig. 1.2, electrical power systems are characterised by higher efficiency than hydraulic and pneumatic ones.

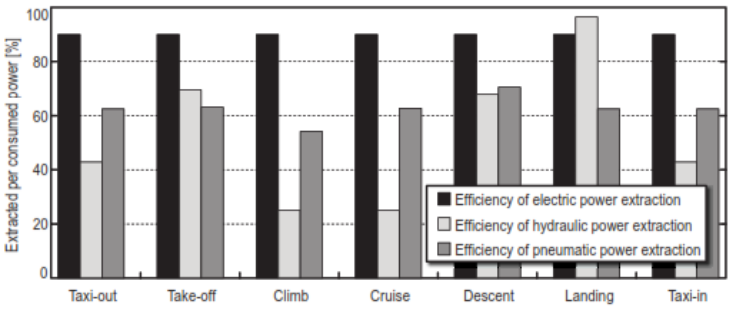

Figure 1.2: Example of AIRBUS A330: power efficiency for the different energy types [10].

Other numerous advantages are expected due to their fault-tolerant capability and suppression of pipes and fluids: increased safety and reliability due to the absence of harmful and toxic hydraulic fluids, reduced costs due to the lack of hydraulic leaks and better dynamic characteristics. All of these aspects lead to lower aircraft acquisition and operating costs for aircraft customers, as well as a reduction in the development time and cost for manufacturers [11].
This transition into MEA introduces a new technological concept which has evolved and is still evolving: the electrical flight control actuators. The conventional hydraulic flight control actuators will be gradually replaced by the electric actuators (EA), commonly called power-by-wire actuators, which are the focus of the next section.

1.1.2 Electrical flight control actuators: EMA and EHA

Figure 1.3 illustrates three families of flight control actuator technologies: the electromechanical (EMA) and electro-hydraulic (EHA) actuators which represent the consequence of the electrification of flight control servo-hydraulic actuators (SHA).
Although the conventional servo-hydraulic actuator has many decades of service experience on aircraft and it reached a high level of technological maturity, the suppression of the hydraulic network will limits their utilization. With the development of MEA, power-by-wire actuators are widely taking their place. Beyond the previously mentioned advantages of aircraft electrification, electric actuators aim to improve the maintainability, reliability,

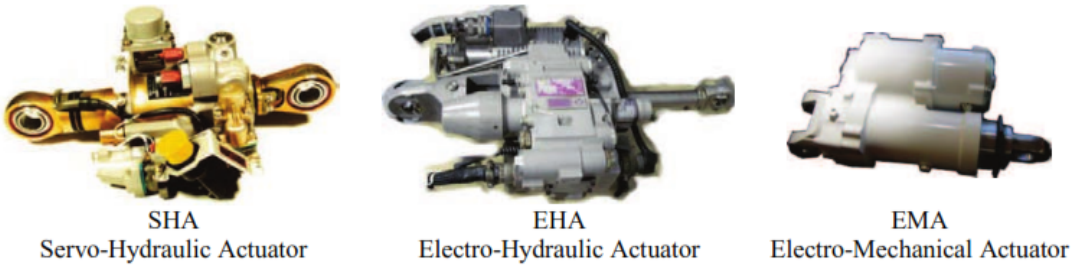

Figure 1.3: The different technologies of on-board actuators [12]

and controllability of future aircraft as well as operating costs and efficiency.
The first evolution towards electrical actuators is represented by the EHAs (depicted in Fig. 1.4). In contrast with a fully hydraulic system, the power control in a EHA is done by a bi-directional variable speed displacement motor- pump. By transferring back and forth the fluid from one cylinder chamber to the other, the electric motor and pump assemblies control the position of the piston connected to the load. In this way, maintainability and weight advantages can be achieved by removing the central hydraulic system and replacing it with a small localized hydraulic circuit at each actuator [13] [8].

Figure 1.4: Some examples of primary flight control EHAs [8].

Although this self-contained hydraulic arrangement enables the principle of power on demand, the effective efficiency of EHA is affected by energy losses associated with the many power transformations [8]. The EHAs can be seen as an intermediate solution toward

the more electrical aircraft, while waiting to obtain more mature solutions for electromechanical actuators. Numerous research programs have been committed first with aileron actuation of single-aisle aircraft (i.e. EGIDE and ELAC [14]) and then were extended to larger aircraft (i.e. ELISA [15] and POA [16]). The EHAs entered in service (for backup mainly) in double-deck Airbus A380, starting their use for the primary flight control of latest aircraft (Airbus A400M and A350) [17]. EHAs were also investigated for application in landing gear extension/retraction in the frame of the POA research program and more recently in the frame of the THERMAE II project [18] [17]. While EHA can offers several improvements compared to the servo-hydraulic actuator, it is typically heavier and it still presents many of the disadvantages associated with the use of hydraulic fluid such as the possibility of leakage and significant maintenance. Higher benefits can be potentially achieved with electro-mechanical actuators (depicted in Fig. 1.5).
The EMA consists of replacing the hydraulic motion circuit with an electric drive and a mechanical transmission chain. In this way a lighter and more compact actuator is obtained. Moreover, since there is no more hydraulic transmission, EMAs tend to be stiffer and more efficient than EHAs.

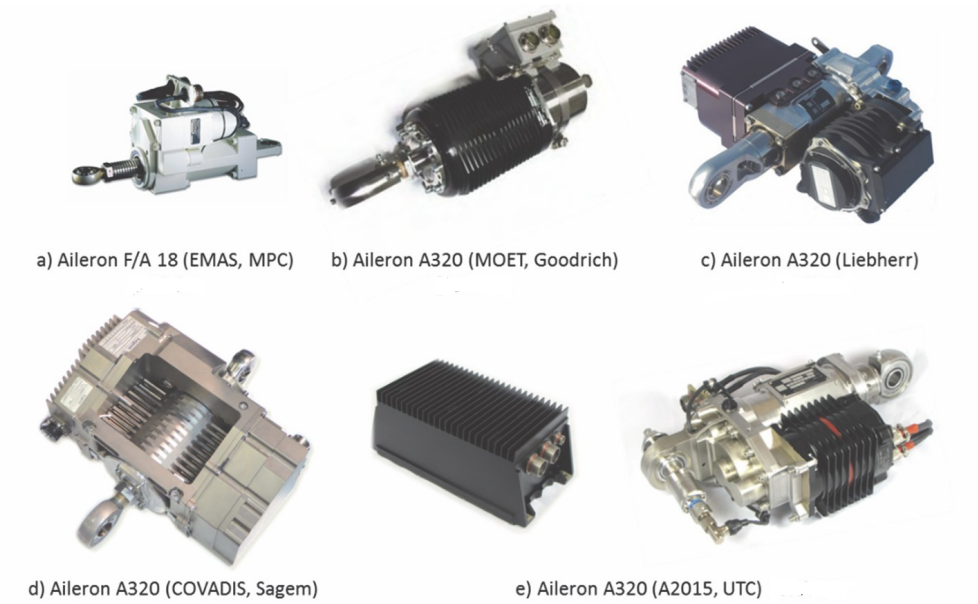

Figure 1.5: Some examples of primary flight control EMAs [8].

The fundamental components of an EMA are: an electric motor, the electronic control unit and a mechanical transmission which typically includes a screw-nut (ball screw or roller screw) in the case of linear actuators, flanged housing in the case of rotary hinge-line

actuators and a gearbox for gear drive architectures. Although the above advantages, the application of EMAs is still limited to low-power aircraft trim, landing gear braking and secondary flight control functions [19]. Numerous research and development programs have been investigated the utilization of EMAs for primary flight control of airplanes, such as MOET [20], COVADIS [21] , and ACTUATION 2015 [22] projects. For the time being, EMAs have not entered into service for primary flight control applications, mainly because of their risk failures due to jamming and in particular the issue of thermal management.

1.1.3 Thermal management of electric actuators: challenges, solutions and design approaches

Thermal management issue is one of the remaining barriers to the use of EAs for primary flight control, as their performance and especially their reliability are highly dependent on the operating temperature. In fact, the reliability of the actuation systems is critical to the ability of the aircraft to be flown. Until now, hydraulic technologies have allowed excess heat to be evacuated through the hydraulic network to the hydraulic reservoir. The problem was relocated and heat exchangers were used to cool the hydraulic fluid. With the suppression of the hydraulic network the hydraulic fluid will not be available to transport and dissipate the heat generated by the actuators. The lack of a convenient heat transfer pathway from the actuator involves highly concentrated heat surrounding the actuation device. The actuators themselves are generally located in confined spaces distributed around the extremities of the air-frame (wing, empennage, etc.), which makes a centralised thermal management system difficult to implement. So, a new approach of dealing with the component heat load at a local level is needed. In addition, technological and aerodynamic constraints deprive the utilisation both of highly efficient active cooling solutions and forced convection by means of ram-air. All of these constraints involve the search for alternative solutions for the thermal management of the electrical actuators. Several studies have looked specifically to this purpose. Solutions have been proposed to transport or store the heat from the actuator motor and power electronics by means of heat pipes (Fig. 1.6) and phase change materials [23] [24] [25] specified for individual application cases. These and other interesting solutions, such as air-cooled plates and thermosiphons, were proposed by Lawson and Pointon ([13], [25]) with a more extensive approach. Starting from the specification of a hypothetical all-electric transport jet, very

similar in configuration to the Airbus A320, they provided a design estimation of the proposed thermal management systems for the different primary control surfaces (Aileron, Elevator and Rudder) and Spoiler.

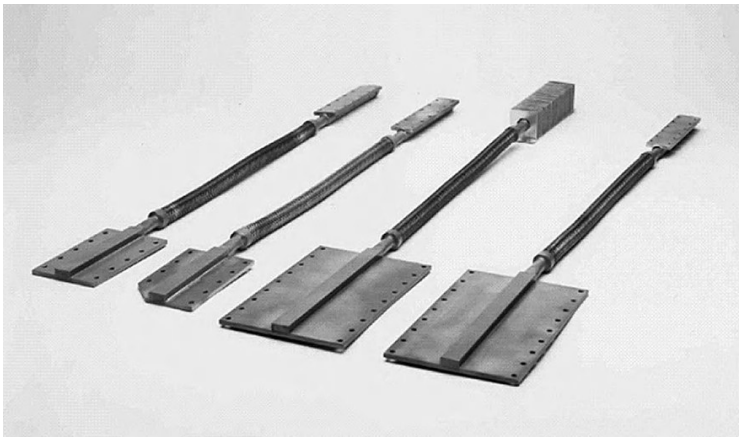

Figure 1.6: A family of flexible heat pipes used in aircraft [26].

Although all the mentioned studies provided efficient potential solutions for electrical flight actuation systems, a particular topic has not yet been fully explored in the literature. This concerns the optimal design and coupling of such solutions with the actuator. In fact, if these solutions were optimally integrated during the preliminary design phase of the actuator, they could provide not only an improvement in the performance of the actuator, but also the development of a lighter and more compact system, leading to considerable advantages at aircraft level. As a matter of fact, a classical approach widely used in the industrial world, is to design the cooling system once the actuator has been specified. In terms of design, the thermal constraint is a design driver for electrical actuators. For example, for a given electromagnetic torque, a larger motor generates less energy losses and lighten the cooling system as consequence. In contrast, a small sized motor involves more energy losses and therefore a larger cooling device is needed. Taking into account the thermal management into the preliminary design phase involves an optimal design compromise between the actuator mass and the mass of its associated cooling device. Another fundamental aspect from the thermal and design point of view is the analysis of the mission profile, which should be part of the specifications of the actuator. A classical approach widely used in the industrial world consists of performing the preliminary design on the basis of steady-state specifications extrapolated from the mission profile. This approach allows a rapid estimation of the actuator dimensions and performance, but does not guarantee optimal thermal dynamics over the entire flight duration, as show in the

example in Fig.1.7a. If the temperature limits are exceeded on the time duration of the mission profile, the system designer will adopt the necessary measures, either by acting on the already designed system, or by proceeding again the preliminary design.

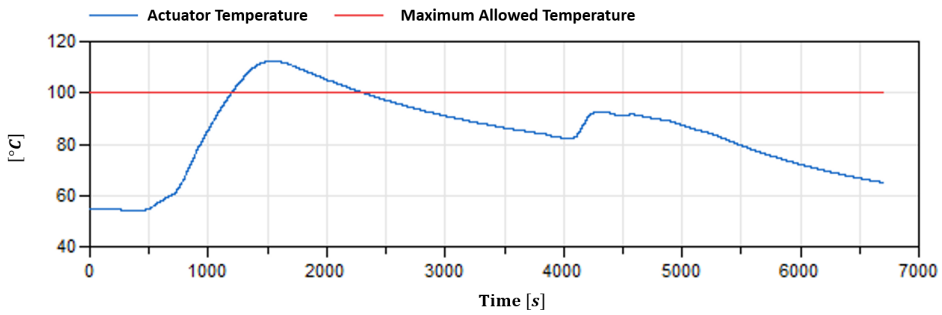

(a) Example of undersized system

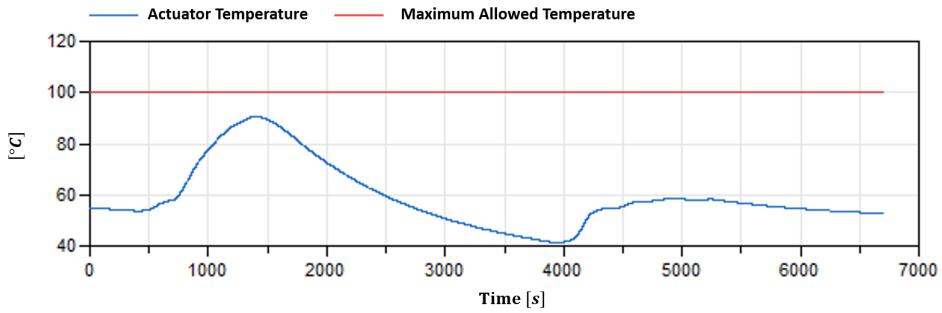

(b) Example of oversized system

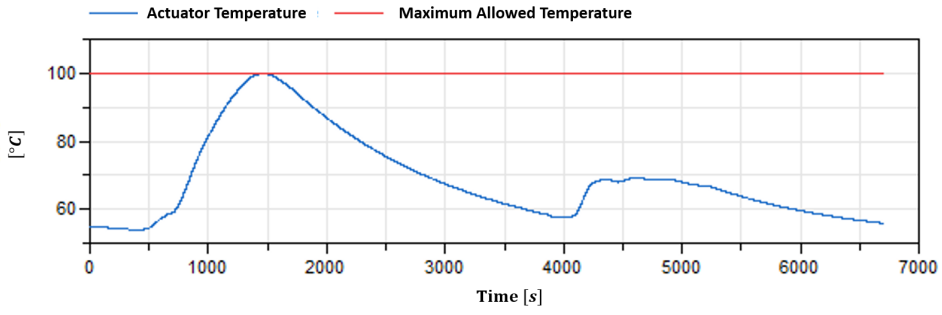

(c) Example of optimally sized system

Figure 1.7: Evolution of the actuator temperature along the mission profiles for three different design cases.

A common practice of using "design margins" during the preliminary design may ensure that the temperature is kept far below the expected limits (Fig.1.7b), to the expense

of an oversized and more heavy system. The most interesting approach would consist in integrating the mission profile in the preliminary design phase, thus allowing the realisation of a system which ensures an optimal thermal dynamics along the flight phase. This means evaluating the thermal dynamics during the sizing process in order to optimally design the device to conveniently match its thermal operational limits (Fig.1.7c). In this way, a system with minimal mass is obtained and the preliminary dynamic validation phase is already achieved. On the basis of these considerations, the industrial objectives described in the following section are defined.

1.1.4 Objectives

The industrial objective of this thesis is to improve the performance of primary flight control electric actuators by means of an optimisation of the thermal constraint. This is achieved through two phases. Phase 1 consists of identifying potential thermal management solutions suitable for electrical actuators. In this regard, three strategies are investigated, which consist of:

- Improve the losses management by designing the actuator so that it generates as less heat as possible.
- Improve the heat transfer from the actuator to the exterior environment through the use of components such as plate fin heat exchangers, heat pipes and thermal straps.
- Use transient heat storage solutions such as phase change materials.

Phase 2, which represents the main innovative contribution of this thesis, aims to consider the solutions investigated in Phase 1 in the actuator preliminary design phase. In this respect, two approaches will be investigated:

- A static approach which consists of conducting the preliminary design on the basis of steady-state specifications extrapolated from the mission profile.
- A dynamic approach that involves the integration of the mission profile in the preliminary design phase.

Based on the case study of an Airbus A320 and referring to an EMA, the proposed approaches will be applied here to conduct the preliminary design for the whole set of primary flight control surfaces: Aileron, Rudder and Elevator. A quantitative comparison of the most suitable thermal management concepts will be provided for each of these applications. The study of Spoilers, in some cases considered as primary control surface (since sometimes they can be used to increase roll control) is not considered in this thesis. This choice is motivated by the fact that, since they operate in an open space environment (when deployed), the thermal management should not represent a particular operational constraint, at least compared to other primary flight control applications. Moreover, as it will be demonstrated in Chapter 6, given the form of the mission profile of the Spoiler, the use of particular cooling systems is not required for this type of application.

1.2 Scientific context

1.2.1 Preliminary design and optimization of electrical actuators: the need of Multidisciplinary Design Optimization

The technological transition towards the electric actuators introduces new challenges for the preliminary design. In this phase multiple physics are involved which demand the mastering of different engineering disciplines. This phase consists of modelling the dimensions, performance and particularly the interactions between the components. A widely general approach used in the industry to preliminary design multi-physic systems is represented by the sequential intervention of the several engineering domains involved in the system (electronic, mechanical, thermal etc.) without dynamic cross-links between the sizing criteria for each discipline. So, if we take the example of an electro-mechanical flight control actuator design (Fig. 1.8), the mechanical discipline is designed firstly (screw-nut, bearing ...), which provides the design input (torque, speed, dimensions ...) of the electrical discipline (motor, converter ...). The process is completed with the intervention of the thermal domain, where the dedicate cooling and/or heat storage devices (motor housing, fins plate, PCM ...) are sized in order to dissipate the system energy losses.
This approach leads to an optimal sizing of each component rather than an optimization of the whole system. With the advent of the multidisciplinary design optimisation (MDO) approaches, this trend is gradually falling in disuse. The performance of a multidisciplinary system is led not only by the individual disciplines performance, they depend also

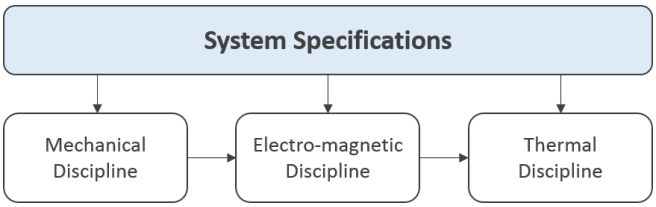

Figure 1.8: Sequential approach for preliminary design of EA.

on the interactions between the disciplines that can be more or less strong. Indeed, when the interdisciplinary interactions are weak or in-existent, a sequential analysis is sufficient. However, when the interactions are strong, the sequential analysis is no longer appropriated [27]. Taking the example of the EMA design (Fig. 1.9), the MDO approach leads to manage the mechanical-electromagnetic-thermal couplings between the several components in order to optimize the whole system according to specific criteria (e.g. minimize the mass of the system in order to decrease the fuel consumption) and satisfy constraints (envelope, vibration, reliability, temperature...). The MDO approach provides effective computational tools to optimally preliminary design multi-disciplinary systems, enforcing rational trade-offs rather than ad-hoc or historically-mandated priority cycles [28].

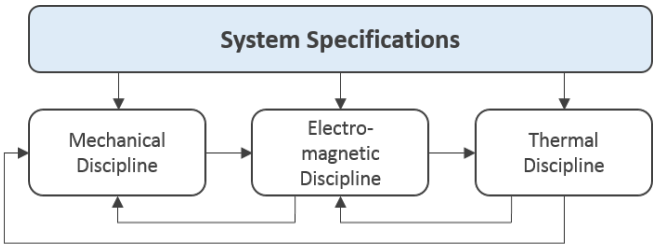

Figure 1.9: Multidisciplinary approach for preliminary design of EA.

1.2.2 Models needed for preliminary design: Surrogate models

Albeit MDO methods have now become valuable tools for preliminary design, increasingly used in the aircraft industry [29], [30], they could be very hard to implement. This is why, they require a certain number of iterations and discipline analyses tools which can involve enormous computational times, especially if 2-D or 3-D finite element method (FEM) models are involved to simulate the behavior of the different technological domains of components. The calculation time can be even inhibitory if a large number of disci-

plines compose the system. As a consequence, during this phase mathematical models are adopted to represent the quantities of interest by means of system of equations that could be linear, non-linear, differential or partial derivative in certain cases. However it can be really difficult to find the exact solution for real technical systems or the solution could be implicit. Often, for conventional subsystems, conceptual phase designers [31] might have access to a vast historical database which can be represented by regression techniques, but unfortunately it is not always the case for new technologies. Otherwise the design of a system or a component shall require experimental tests or resolution of FEM models to evaluate the variables of interest. These activities could be time consuming. To overcome this problem, surrogate models are employed. Their purpose is to approximate by analytical formulations the behavior of highly detailed simulation models, avoiding in this way the use of simulation tools that are finally replaced by surrogate models. As a result, the system designer is faced to simpler and handier models that allow at the same time adequate efficiency in terms of obtained results and reduce drastically the computation burden of the optimization. Scientific literature offers several surrogate modelling techniques aiming to build simpler and handier models [32], [33], [34]. Even if they allow good levels of precision in terms of obtained results and computation time, they do not take into account the capitalization criteria, meant as the capability of the model to be reused for different system requirements with the least redevelopment or tuning effort. Reuse is key in capitalization as it implies time saving. Especially in this context, where during the preliminary design phase different architectures, configurations and specifications of the system are evaluated in order to conduct trade-off analyses and comparisons. A new approach to generate surrogate models which can be capitalized and reused in preliminary design phases of electrical actuators must be investigated.

1.2.3 Previous theses conducted at Institut Clément Ader

Several research projects, around the design and optimization of embedded aeronautical system, took place in the Actuation System team of Institut Clément Ader and greatly contributed to the work done in this thesis. Liscouet-Hanke investigated aircraft power architectures and propose design methodology which enable aircraft level trade-offs [10] [35]. Liscouet and Hospital focused on developing sizing models based on inverse simulations and scaling laws [36]. Giraud developed a methodology for the sizing of aircraft

electrical networks [37]. Reysset developed preliminary design tools such as specification generation based on mission profile analysis [38]. A great reference for the development of this thesis was made to the theses of Sanchez [12] and Delbecq [29]. Sanchez proposed a methodology, named VPLM, to generate lightweight surrogate models from finite element simulations by focusing on the thermal aspect of the actuators and their components. Although this methodology is very efficient in generating compact and reusable models, the representation of components with complex geometries can involve a large number of input variables. The use of the model can therefore lead to inhibitory computation times when used to conduct sizing problems based on optimization processes. This methodology is thus improved with the integration of a new method of sensitivity analysis developed in this thesis which aims to highlight optimal geometric ratios and to further reduce the inputs variables of the component model under consideration (as explained in detail in Chapter 3). In this way, a more compact and reusable model can be obtained. Delbecq proposed a sizing method, based on an MDO approach, to design electro-mechanic actuators, for flight control applications, on the basis of static specifications extracted from the mission profile. This sizing method is then adapted in this thesis in order to perform the preliminary design of the actuator along the mission profile, i.e. the dynamic sizing approach previously introduced and explained in detail in Chapter 7.

1.2.4 Objectives

The scientific objective of this thesis is to provide effective methods and tools necessary to carry out the defined industrial objectives. These can be summarized as follows:

- The development of a methodology to generate surrogate models that can be easily reusable inside different preliminary design problems.
- The development of sizing models of the selected thermal management systems. Estimation models such as scaling laws, regression on data-sheet catalogues, analytical relationships and surrogate models are used to this purpose.
- The development of a preliminary design procedure and an associated software tool. This tool shall handle optimization of coupled systems in reasonable computation time. Moreover, it must allow a certain degree of interchangeability of models uti-

lization to analyze and compare several actuator architectures (gear or direct drive), or different technological solutions (motors type, cooling devices, etc.).

- The development of a virtual prototype in order to analyse the thermal dynamics of the actuator over the entire duration of the mission profile.

The industrial and scientific objectives here defined are summarised in the Table below.

Table 1.1: Industrial and scientific objectives established for this thesis project.

Industrial Objectives		Scientific Objectives	
I1	Identification of potential thermal management solutions	S1	Generation of a surrogate modelling methodology
I2	Perform the preliminary design of primary flight control EMAs with a static approach	S2.	Model development of selected thermal management solutions
I3	Perform the preliminary design of primary flight control EMAs with a dynamic approach	S3.	Implementation of a preliminary design procedure and an associated sizing tool
		S4.	Development of a virtual prototype

1.3 Dissertation overview

Chapter 1 introduced the context of this thesis by outlining the needs which led to the creation of this collaboration between Collins Aerospace and Institut Clément Ader. The industrial objectives and the supporting scientific objectives were defined.
Chapter 2 examines and discusses challenges and solutions for thermal management of electrical actuators. The thermal challenges are outlined and a state of the art of the candidate thermal management solutions is presented. Subsequently, the best potential solutions are selected.
Chapter 3 presents a state of the art of the surrogate modelling and proposes a new methodology for obtaining reusable surrogate models suitable for the preliminary design of aircraft application systems. An example of an application is provided, which depicts the generation procedure for obtaining surrogate models of a permanent magnet brushless motor.
Chapter 4 shows how the surrogate models are used to perform the preliminary design. To this purpose, the complete sizing procedure of EMAs for primary flight control applications is implemented. A tool has been developed in Python programming language to perform

the design via an optimisation procedure with a view focused on the mass minimisation and thermal constraints satisfaction. The preliminary design here is based on the static approach, whereby static specifications are extracted from the mission profile. A case study of a mission profile of an Airbus A320 flight with a duration of 112 minutes is examined.
In Chapter 5 and Chapter 6, the models of the thermal management systems selected in Chapter 2 are generated. In addition, a particular attention is given to the analysis of the mission profiles of the different primary flight control surfaces. This analysis allows to highlight the convenience of using heat storage systems.
A new preliminary design methodology based on a dynamic approach is presented in Chapter 7. The proposed approach is applied here to the preliminary design for the whole set of primary flight control EMAs: Aileron, Rudder and Elevator. A quantitative comparison of the most suitable thermal management concepts is made for each application.
Results are summarized in Chapter 8. Conclusions are made and perspectives are outlined.

Chapter 2

Challenges and Solutions for Thermal Management of Electric Actuators

Contents

2.1 Introduction **17**

2.2 Analysis of thermal challenges of electric actuators **18**

2.2.1 The sources of heat 18

2.2.2 Operating temperature requirements 20

2.2.3 Thermal environment and design scenarios 22

2.2.4 Mission profile analysis and design approaches 23

2.3 State of the art of thermal management solutions **25**

2.3.1 Improve the losses management 26

2.3.2 Improve the heat transfer 31

2.3.3 Improve the transient generation and storage 37

2.4 Selected solutions for thermal management **40**

2.5 Conclusion **44**

2.1 Introduction

In this chapter, two topics relating to the thermal management of electric actuators are discussed. The first topic involves design constraints on both the actuator and the cooling device, as they are strongly coupled. A careful analysis of the mission profiles becomes essential to ensure optimal sizing of the two interacting components. A new sizing approach

is introduced, in order to integrate the mission profile during the preliminary design phase and achieve optimal compromises between the actuator and thermal management system dimensions, while satisfying the required performance and operational thermal constraints. The second topic concerns the research of solutions to improve the thermal management of actuators. Three different strategies are introduced and a state of the art of potential solutions is presented. At the end of the chapter, the most favourable solutions are selected, taking into account the major industrial requirements and the resources available to conduct this thesis project. The modelling, design and integration of the chosen solutions is discussed later in this thesis.

2.2 Analysis of thermal challenges of electric actuators

The analysis of thermal issue is fundamental in order to identify and design the most efficient solutions for the thermal management of electric flight control actuators. This analysis is conducted in four main steps:

- The localization of the sources of heat within the actuator.
- The identification of operating temperature requirements.
- The analysis of thermal environment and scenarios of the actuator.
- The analysis of the mission profile, useful for the definition of the design specifications.

The four aspects mentioned above are discussed in detail in the following sections.

2.2.1 The sources of heat

The heat source of electric actuators is essentially produced by the energy losses generated by the electrical and electronic components forming part of the system. These are the electric motor and the electronic control unit (ECU). An electric motor with high power

density, high reliability and acceptable heat dissipation is required for primary flight control applications. Permanent magnet (PM) synchronous motors are commonly used, since compared to other motor types, they are characterised by a higher power density and small losses in the rotor [39], which is advantageous for thermal management. On the other hand, their efficiency is affected by the temperature, since the residual induction of the magnetic materials decreases as the operating temperature increases (for example, the induction of a samarium-cobalt magnet decreases by 4% when its temperature increases by 100°C). The total losses in the motor (which percentage distribution is depicted in Fig. 2.1) derive from Joule (or copper) losses, iron losses, stray losses, friction and windage losses.

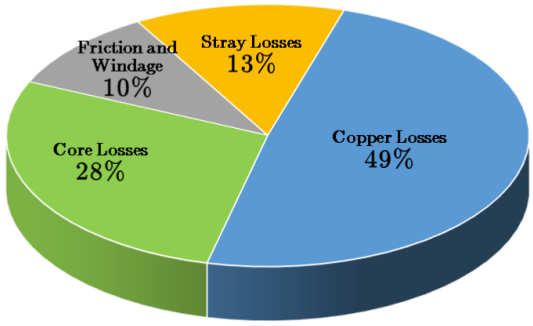

Figure 2.1: Example of synchronous motor losses distribution [40].

The effects of friction, windage and stray losses are generally negligible compared to the Joule and iron losses. Copper losses are generally the largest source of power loss or inefficiency in the motor. They are due to the resistance to current flow in the windings which results in heat generation that is proportional to the resistance of the material and the square of the current. The resistivity of the copper motor windings increases by 42% in correspondence of a 100 °C of temperature augmentation. Therefore the losses in the windings increase and the motor efficiency is reduced. In addition, a thermal runaway effect may occur which could cause the failure of the device. Moreover, high temperatures of the motor windings could affect the reliability and lifetime (according to the Arrhenius law [41]) of the insulation material and they can involve its degradation in worst case. Furthermore, these losses are highly localized at the motor slots, which makes the heat dissipation even more difficult. After copper losses, iron losses are generally the second largest source of losses of electric motors. They arise from the variation of magnetic flux-density throughout the core, which is strictly dependent on the electro-magnetic frequency. As a consequence,

for low-speed applications, as generally the case of primary flight control actuators, these types of losses are not very relevant. Moreover the heat dissipation, compared to Joule losses, is facilitated by the fact that iron losses are distributed on the ferromagnetic material of the motor.
The motor speed and direction is controlled by the ECU through a high-frequency electrical switching current which is produced by power electronic devices, as IGBT or MOSFET. The main thermal constraint of the ECU comes from semiconductors, which generate power losses in the form of heat whenever the current is flowing or being switched. Two types of losses can be distinguished: conduction and switching losses. The former are due to resistive losses during forward conduction and are related to the duty cycle. The latter occur when the device is transitioning from the blocking state to the conducting state and vice-versa. This interval is characterized by a significant voltage across its terminals and a significant current through it. The energy dissipated in each transition needs to be multiplied by the frequency to obtain the switching losses. The high currents and switching frequencies required by high power density electric actuators lead to considerable heat output from the power electronics [42]. Although converter losses are generally lower than those of motor, they account for a large percentage of total losses. Until this heat is not dissipated, the resulting temperature will increase and it can permanently damage the temperature-sensitive electronic components. This should disable the motor and cause the loss of actuator control [42].

2.2.2 Operating temperature requirements

The thermal management of electrical actuators aims to ensure the compliance with permissible temperature limits of the device. This is very important since its temperature directly affects:

- The reliability and lifetime of the components that constitute the actuator.
- The reliability of airplane composite structures.

The electric motor and the ECU are the most sensitive elements of electrical actuators to high temperatures, as mechanical (for EMA) and hydraulic (for EHA) components are generally able to operate at high temperatures without severe reductions in performance

or lifetime [39] (although the oil in the EHA, or the lubricants in the EMA, can degrade at temperatures around 100°C). The maximum allowed temperature of an electric motor is strictly linked to the insulation class of windings. The temperature capability of each class specify the maximum allowable temperature of the motor winding insulation that will provide a life of 20000 hr (under continuous operation). Motor with Class F or Class H insulation are typically adopted for high power density applications because they allow respectively a winding temperature limit of 180 °C and 220 °C, as shown in Fig. 2.2.

Insulation Rating	Insulation Class	Average Winding Temperature Rise	Hot Spot Temperature Rise	Maximum Winding Temperature
Class 105	A	55 °C	65 °C	105 °C
Class 130	B	80 °C	110 °C	150 °C
Class 155	F	115 °C	145 °C	180 °C
Class 180	H	130 °C	160 °C	200 °C
Class 200	N	150 °C	180 °C	220 °C
Class 220	R	170 °C	200 °C	220 °C

Figure 2.2: Classes of winding insulation material [43]

Concerning power electronics, standard silicon components are designed for absolute maximum temperatures up to 125-175 °C. High temperature power electronics operating above 200°C has become possible with the recent availability of silicon carbide (SiC) devices [44]. Although the motor and power electronics are characterized by high operating temperature limits, the innovation of aircraft structure brings a new constraint on thermal design. A new trend is appeared, which consists of using composite technology for aircraft primary structures. Albeit the involved aerodynamic properties when using composite materials are well-known nowadays, papers on design temperatures for thermally loaded composite structures are very rare in the published literature. A study carried out by Petersen [45], concerning the thermo-mechanical design aspects of composite structures of aircraft, suggests to take a maximum temperature limit in a range between 70 °C and 110 °C as design driver. The fact these studies on thermal behaviour of these "new" materials are still under development, pushes aircraft manufacturers to consider a conservative temperature limit of 100 °C on the actuator skin.

2.2.3 Thermal environment and design scenarios

The energy losses generated by the actuator have to be dissipated in the confined environment allocated to them. The thermal environment in this confined space is highly influenced by the ambient conditions, both in flight and at the ground level. The aircraft flight is generally divided in eleven phases, as depicted in Fig.2.3, as a function of the operating altitude.

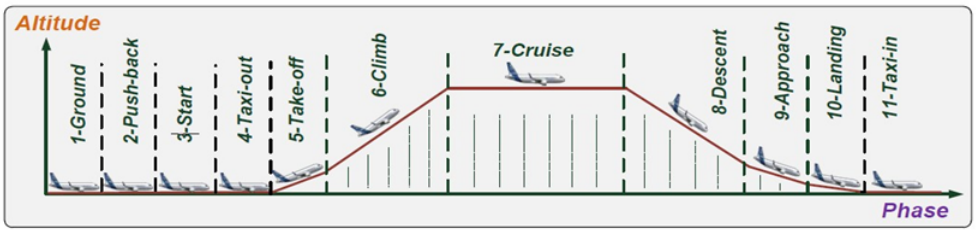

Figure 2.3: Aircraft flight phases [12].

The operating altitude affects the air properties (pressure, temperature, air density, etc.) and contributes to define the aircraft speed which influences how effective is air at cooling the aircraft skin. To determine the most severe design condition, three scenarios can be defined:

- The ground operations (phases number 1, 2, 3, 4 and 11 on Fig.2.3).
- The low altitude operations (phases number 5, 6, 8, 9 and 10 on Fig.2.3).
- The cruise phase (phase number 7 on Fig.2.3)

Which of this conditions is actually the most constraining for thermal management is essentially dependent on the relationship between ambient air temperature and the power delivered by the actuator. The latter is proportional to the aerodynamic load it holds, so it depends on dynamic pressure on the moving surface which itself depends on airspeed and air density. At ground level, aircraft moves very slowly or even not, so the aerodynamic loads on the control surfaces will be very small even if the control surfaces are fully deflected. On the other side, at ground level the air temperature is greater (e.g. $50°C$ or even more in the worst cases), which is clearly a demanding condition for thermal management. Control surface usage is usually greater at low altitudes, where air turbulence is most

severe and landing and takeoff require frequent control surface use compared to cruise. Moreover, the air temperature is still high in this scenario, and the low aircraft speed makes convection from the aircraft skin less effective. The cruise phase can also be severe for thermal management because although the air is cold at high altitudes, it is also far less dense, which makes it less effective for cooling. Clearly, it is straight forward to determine which of the conditions is the most severe for any given design. Because a large number of scenarios could not be accommodated within the preliminary design phase, a more simplified approach is generally adopted by industries. This consists of designing the actuator by considering laboratory conditions ($20°C$, sea level, natural convection) and successively validate the dynamic thermal performances along the entire flight scenario. If these performance are not satisfied, appropriate measures are taken either at individual components level, or alternatively the boundaries of the preliminary design are redefined. In this thesis a different approach is proposed. This is discussed in the next section.

2.2.4 Mission profile analysis and design approaches

The magnitude of the actuator losses is strictly related to the load profile of the actuator. This is difficult to determine as it depends on the usage of aircraft control surfaces, which is influenced by many variable factors including atmospheric turbulence and in particular by the specificity of the missions profile. Each of the flight control surface in fact has a distinct mission profile, as shown in Fig. 2.4, that requires a careful individual analysis. The analysis of the mission profiles in fact, is extremely important, as it allows the evaluation of the average and maximum load, and how this is distributed over time. In conventional designs, the actuator and the associated thermal management system are generally designed through a "static approach". This consists either in over-sizing the devices for the maximum load or in under-sizing them near the average load. If they are designed for the average load, a smaller and lighter weight system is achieved. The disadvantage, however, is that the operating temperature limits may not be guaranteed during peak or high load operations. This can significantly reduce the reliability of the temperature sensitive components. The design for the average load could be favourable for control surfaces as the Aileron, which has a relatively homogeneous load along the mission profile and a maximum load value close to the average load, as shown in Fig.2.4a. Less convenient might be for surfaces such as Rudder or Elevator, as figured in Fig.2.4b and Fig.2.4c, which operate at

very high torque during only very brief periods of the mission, while acting low or even null aerodynamic loads during cruise. As a result, in the latter cases, designing the system for the average load could not be sufficient to meet the temperature constraints during the peak phases.

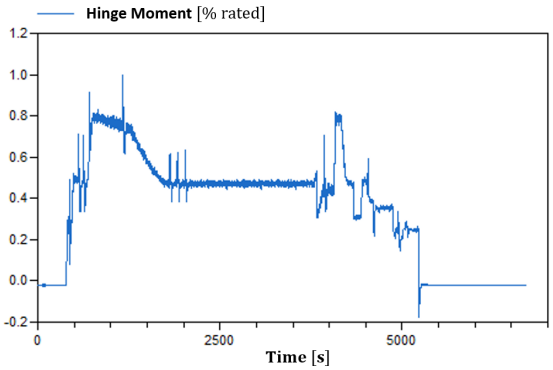

(a) Aileron

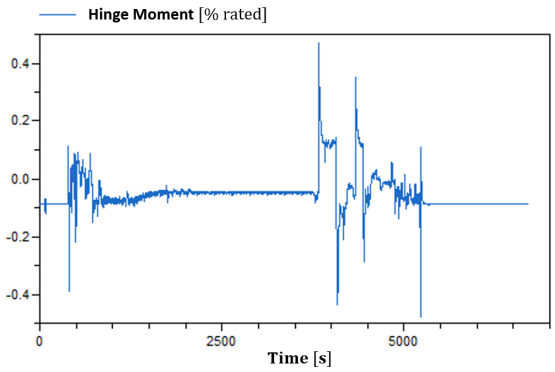

(b) Elevator

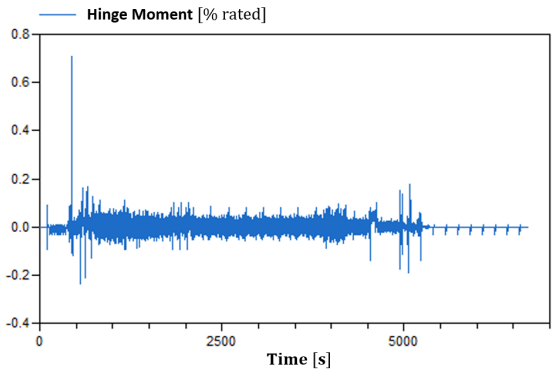

(c) Rudder

Figure 2.4: Examples of mission profiles for each primary flight control surface.

In these cases two solutions are possible. Either oversize the cooling device for a continuous peak load, so that it can guarantee that the temperature is maintained within the operational limits during the peak phase. Or oversize the electric motor, so that its nominal torque is equal to the maximal required peak torque, without using a cooling system. Oversizing at peak load, however, can be excessive in both cases. Excessive oversizing in fact allows to maintain component temperatures far below their operating temperature limits during the flight phase, at the expense of a larger, heavier and more costly system. At this point, one questions arises: how much do the devices need to be oversized in order to guarantee an optimal design? An optimal sizing ratio between maximum and average

load needs to be investigated. In this respect, a new sizing method is proposed in this thesis, based on a "dynamic approach". This consists of integrating a dynamic model of the system composed by the actuator and its cooling device (N.B. the term "system" will be used in this thesis to indicate the coupling between the actuator and the thermal management device), which allows the evaluation of its terminal behaviour along the mission, within the preliminary design procedure. In this way, it will be possible to design a system which optimally meets the operational thermal requirements. As a result, a lighter solution might be obtained and the preliminary dynamic validation phase will be earlier achieved. The implementation of such approach is discussed in further detail in Chapter 7.

2.3 State of the art of thermal management solutions

In the previous section a thermal analysis was carried out in order to highlight the main thermal constraints of EAs. In this section potential thermal management solutions are introduced. In this regards, three main strategies (depicted in Fig. 2.5) are investigated, in order to:

- **Improve the losses management** by designing the actuator so that it generates as less heat as possible.
- **Improve the heat transfer** from the actuator to the external environment by using additional thermal management systems in order to better evacuate it and thus lower the maximal temperature of system.
- **Improve the transient generation and storage** by minimizing the transient heat losses by an adapted control strategy and by designing the actuator/cooling device so that it efficiently stores transient heat.

For each of these strategies a state of the art of possible methods is provided. At the end of the section a mind map is illustrated in order to resume all the candidate solutions highlighted in the state of the art.

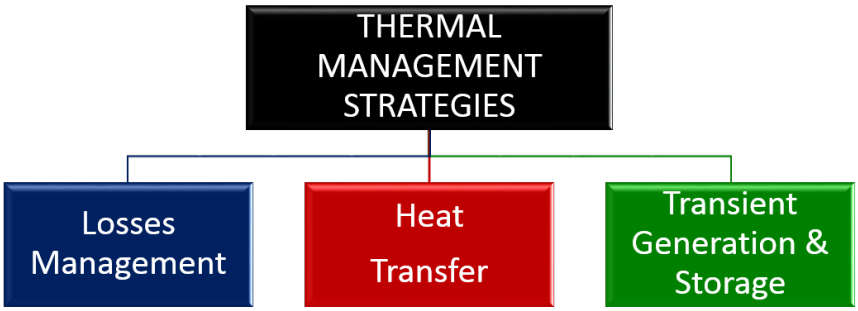

Figure 2.5: Strategies for improving the thermal management of EAs.

2.3.1 Improve the losses management

This strategy concerns the improvement of the actuator losses management. Several solutions, summarised in the diagram depicted in Fig. 2.6, can be adopted in this respect.

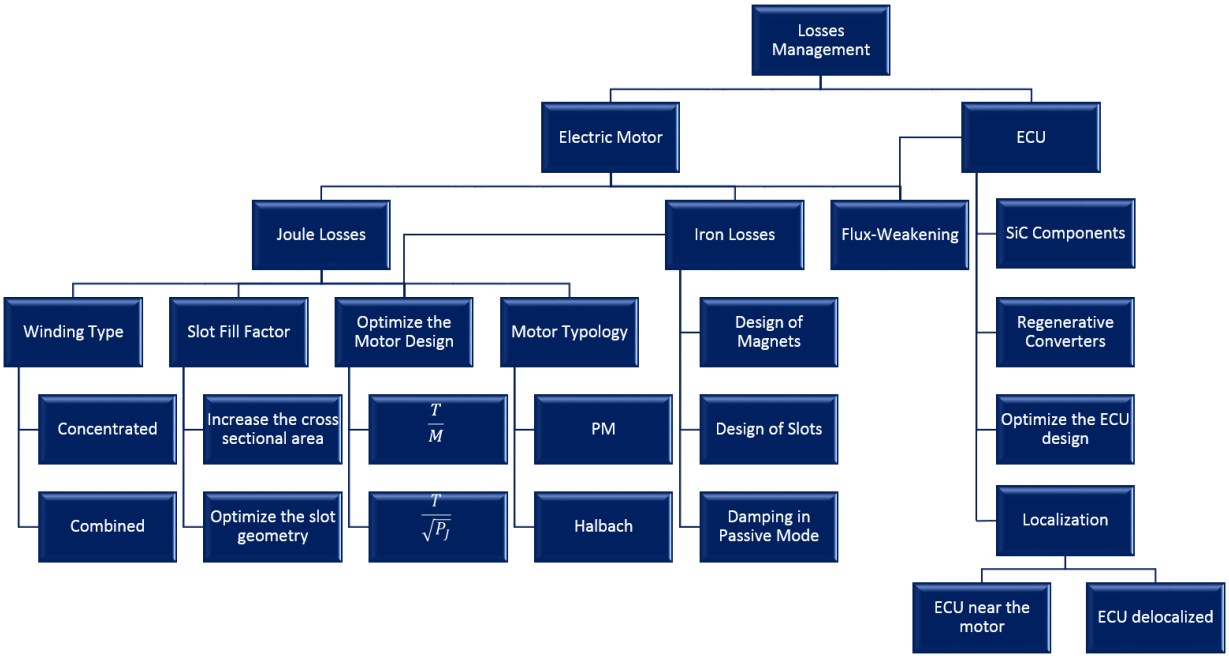

Figure 2.6: Strategies for improving the losses management.

In Section 2.2.1 the electric motor and power electronic have been identified as the main contributors to the generation of heat. Regarding the electric motor, the main sources of heat come from Joule losses and iron losses. The former generally reach the maximum value during stall load condition which occurs when the actuator is in position maintaining mode. This condition actually represents the fundamental role of primary flight control

actuator. From that, it follows the great importance of reducing these losses as they are generated along the entire mission profile. Methods, that are generally adopted for high power density applications, to reduce Joule losses consist in: increasing the cross-sectional area of windings using a higher slot-fill factor, optimizing the slot geometry or using concentrated winding. The concentrated windings (Fig. 2.7a) have potentially more compact designs compared to the conventional motor with distributed windings (Fig. 2.7c), due to shorter end-windings and axial build. One of the key advantages of concentrated winding, in comparison with distributed winding, is the ability to achieve significantly higher copper slot fill factor. This can have a significant impact on the machine power density. In addition, there is a significant gain in the weight of copper ($> 50\%$) and in the total cost. The Joule losses are so decreased and the efficiency is improved [46]. However, the dissipation of the Joule losses is complicated because the heat is highly concentrated inside the slots.

(a) Concentrated [47]

(b) Combined [48]

(c) Distributed [47]

Figure 2.7: Examples of different types of winding.

The change from one configuration to the other is shown in the scheme in Fig. 2.8. Makita et al. [48] proposed a new method to wind the electric motor, as shown in Fig. 2.7b, which combines the advantages of distributed and concentrated winding in order to obtain higher winding and slot fill factors.

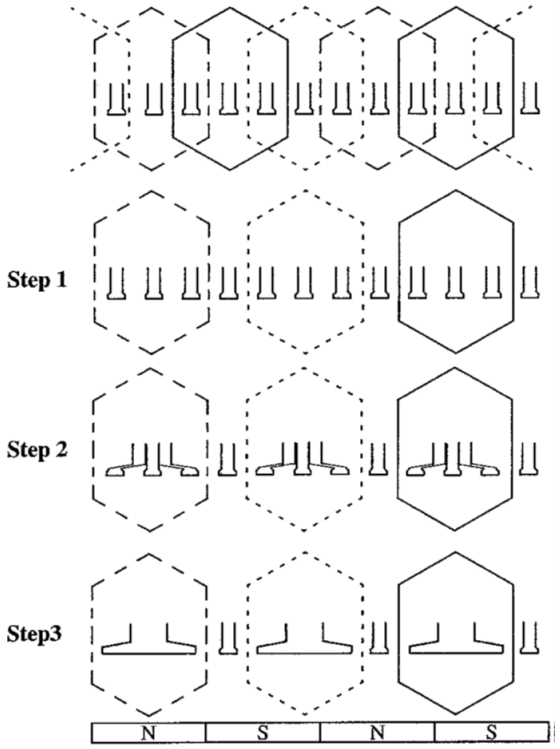

Figure 2.8: Determination of a machine with concentrated windings and an irregular distribution of slots from an initial machine with 12 slots and 4 poles [46].

A more ambitious approach consists in optimizing the motor design. To this purpose the motor design should be optimized according to one of these two criteria: the maximization of the torque density or the minimization of the ratio of the torque on the square root of Joule losses [49], [50], [51]. Halbach magnetized permanent magnets brushless machines can also be adopted to increase the power density [52] (Fig. 2.9).

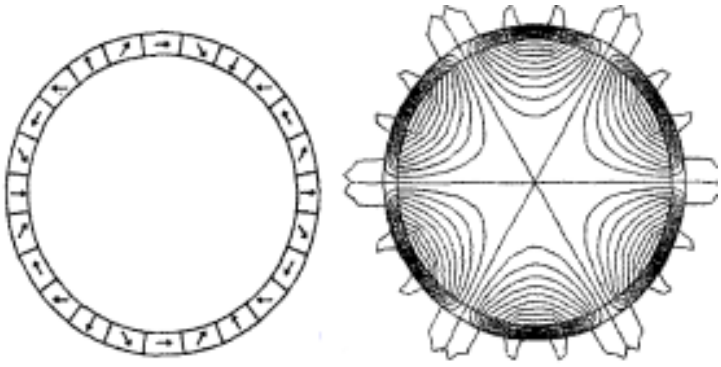

Figure 2.9: Example of Halbach magnet arrangement [52].

This typologies of motors presents a magnet arrangement which enables a significantly higher magnetic working point than equivalent radial or surface mounted magnets. This enables a better utilization of the magnet material and increases the power density. For better loss management, some measures regarding iron losses could be adopted. Prediction of iron losses of PM machines remains one of the most active topics of motor designers [53]. Several studies have been addressed to reduce these type of losses [54]. They involves design measures on magnets [55] and slots to limit the flux variations in the rotor [56]. Beveling of the magnet edges for example is a practical method adopted to reduce the slope of the tooth flux waveform and reduce the eddy losses. Small slot openings, as shown in Fig.2.10, are widely used in most small motor designs. This enables an increment of the magnetic flux and the developed torque, by allowing at the same time a leakage flux reduction in the shoes of the teeth. It is also important to note that, in reality, iron losses are not always a disadvantageous phenomenon, but can actually be helpful when the actuator is operating in passive mode. In fact, these losses, in particular eddy current losses, can be increased voluntarily to provide a load damping function when the motor is not powered (damped mode in the event of a failure of the electrical part).

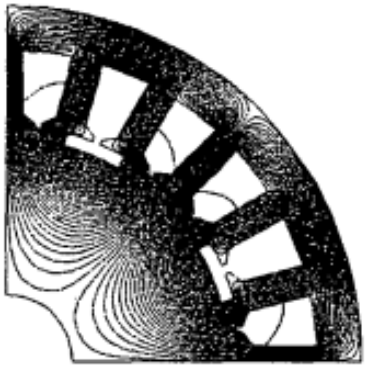

Figure 2.10: Example of partly slots opening [54].

Concerning the ECU, a number of possible solutions are available to improve the efficiency of power electronics that however currently is around 95% (at maximum power point). Power switching elements used with power drive electronics are silicon based Diodes and IGBTs. Now with the commercial availability of devices such as SiC based diodes, the losses in ECU could be reduced by approximately 30%. The main switching element IGBT can also be replaced by SiC based JFET. These components are currently being sampled and should help to reduce power dissipation by more than 50% for all next generation power electronics [57]. The power electronics may also be designed to allow regenerative power

back on the electric bus rather than dissipating it in the ECU. This would enable energy optimization and at the same time limit the temperature rise in the ECU. Matrix converter is one such topology but which needs further evaluation [57]. Specific design techniques for the thermal management of power electronics have been presented by De Jong et al. ([58]). They provide good interaction between the integration technologies implemented for converter miniaturization and the thermal management (Fig. 2.11). Higher power densities and reduced temperatures are obtained in this way.

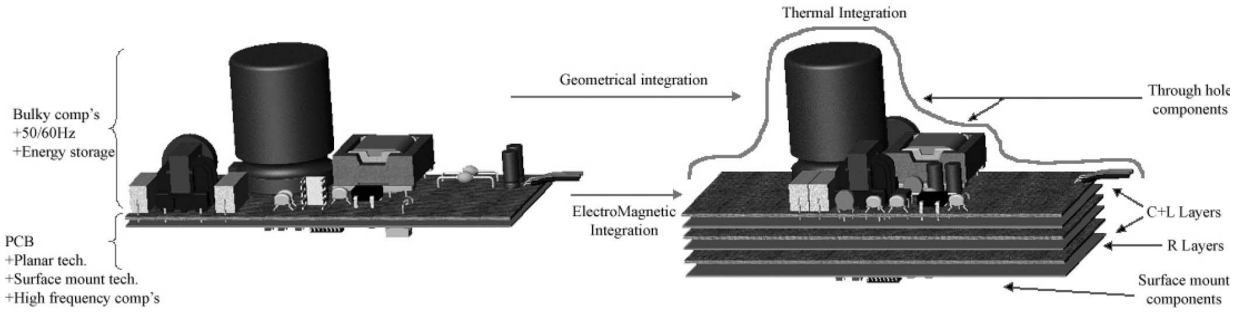

Figure 2.11: Conceptual integration process in switch mode converters from (left) discrete component design to (right) more integrated design [58].

Another interesting idea to improve the losses management is to dislocate the ECU module away from the actuator. It may be placed for example directly on wing skin access panels as has been suggested by Montero et al. ([59]). In this way the heat load generated by the ECU can be cooled by direct conduction to the aircraft skin. Another possibility is to locate all the actuator ECUs in one or several central fuselage locations in order to cool them by centralized cooling systems. Although this solution might be interesting for thermal management and mutualisation [7], the efficiency of electronics would be reduced due to the fact that longer wire transmission is needed. Moreover, the fact the motor is mounted far from its ECU can increase the electromagnetic-interference (EMI) effects from the high-intensity current flows between the electronics and EMA motor [60].
A flux-weakening control technique, is widely used in high-speed applications in order to exploit the motor maximum capability with minimum power consumption. This technique allows the best use of the supply voltage to produce speed. The increase in speed is then compensated by a rapid decrease in the torque produced per consumed current.

2.3.2 Improve the heat transfer

The second strategy concerns the improvement of the heat transfer. To this purpose several solutions, illustrated in Fig. 2.12, are industrially available nowadays and applied in a wide variety of engineering sectors.

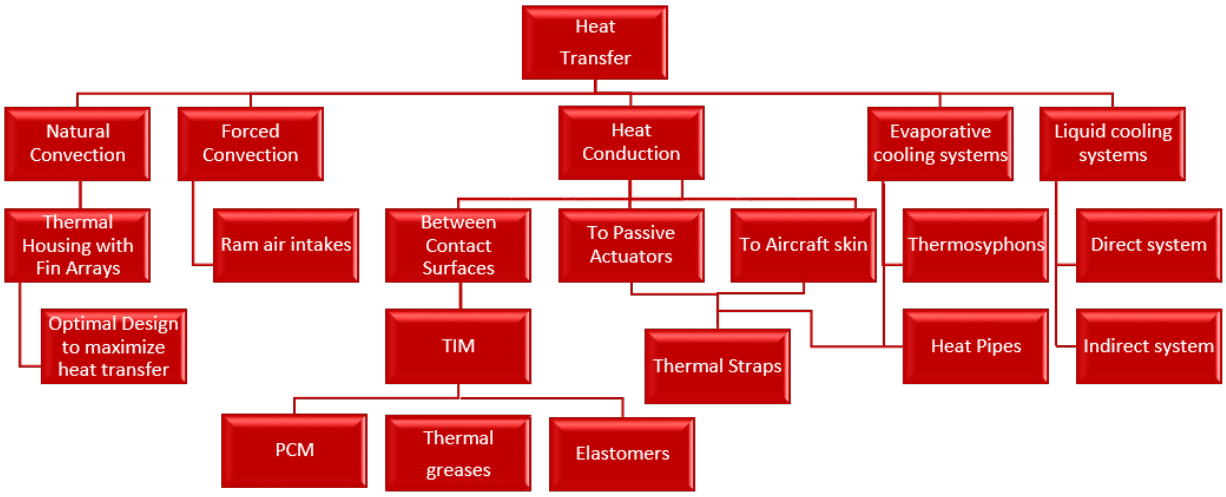

Figure 2.12: Strategies for improving the losses management.

One of the simplest and most available options for thermal management is natural convection. In this regard, thermal housings with fin arrays (Fig. 2.13) are widely used for air cooling of electronic and mechanical components.

Figure 2.13: Example of motor housing with fin arrays [61].

The use of these passive, natural convection heat sinks offers substantial advantages in terms of cost and reliability, but is often accompanied by relatively low rates of heat transfer (approximately 10 W/m^2K). Optimal design techniques have been developed [62][63] to

enhance the heat dissipation from such natural convection heat sinks. These studies have revealed that there is an optimal spacing between the fin arrays which maximizes the heat transfer rate for a given dimension of the base plate and operating environment. Moreover, relations have been introduced to determine the optimal fin thickness which minimises the mass of the heat sinks. Aluminum and copper are commonly used heat sink materials, but other materials such as magnesium can also be adopted. This latter material in fact presents the best ratio of heat conductivity per mass unit, with a ratio of 0.09 compared to 0.04 for aluminum and 0.045 for copper.
Forced convection by means of ram air can be an interesting and simple solution for improving the heat transfer. It can be readily available at the actuator locations on both the wing and empennage, and it could be canalized directly on the heat source by means of ram-air intakes (as shown in Fig.2.14). However, ram air creates an aerodynamic drag penalty with a resulting increase in fuel burn. Otherwise, forced convection could be supplemented by the use of fans or ejector pumps. But these devices require external power which can lead to an augmentation of mass and volume of the overall system and which can reduce its reliability.

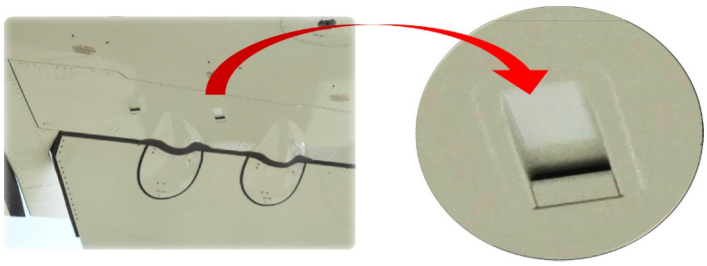

Figure 2.14: Underwing scoops for actuator cooling (EHA of the Airbus A350 aileron) [8].

Heat transferred toward an external body is another simple option for heat transfer but its effectiveness depends on the nearby availability of a medium being at low temperature. Airframe structure and aircraft skin are good candidates for heat sinks for actuators. Passive actuator located nearby could be used as passive heat sink as well. For effective heat transfer, the thermal resistance between the heat source and the sink must be as small as possible. Therefore high thermal conductivity materials with minimal number of interfaces along the thermal path are needed. In this regard thermal straps (Fig. 2.15), commonly referred to as "flexible thermal links", can be employed. They are heat transfer devices, popularly used in spacecraft application [64], consisting of end fittings (brackets/terminals), and a flexible conductive material such as copper foil, aluminum foil, graphite sheets or

fiber bundles. The heat is conducted from one terminal mounted on the heat source to the other one connected to the cold source by means of the conductive straps. They require no external power and their flexibility allows them to operate in severely constrained locations allowing relative movement between the heat source and sink. This is clearly advantageous for flight control actuators, which move relatively to the structure on which they are attached.

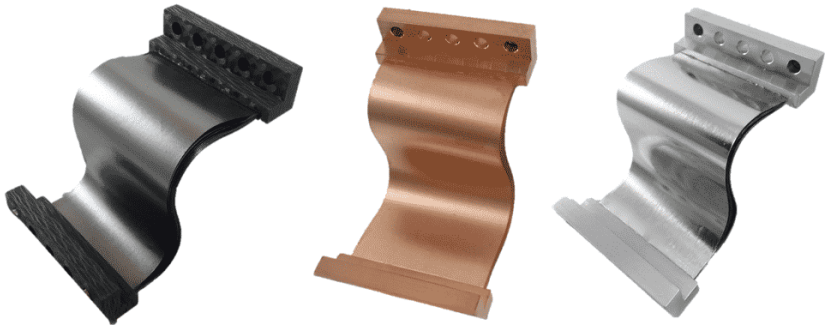

Figure 2.15: Example of flexible thermal straps [65].

Similar to thermal straps in geometry, heat pipes provide much higher heat transfer rates by means of evaporation. These devices, illustrated in Fig. 2.16, have two terminals called evaporator and condenser connected to each other via an "adiabatic" pipe, whose internal surface is lined with a thin layer of porous material, usually referred to as wick. [13][24][66].

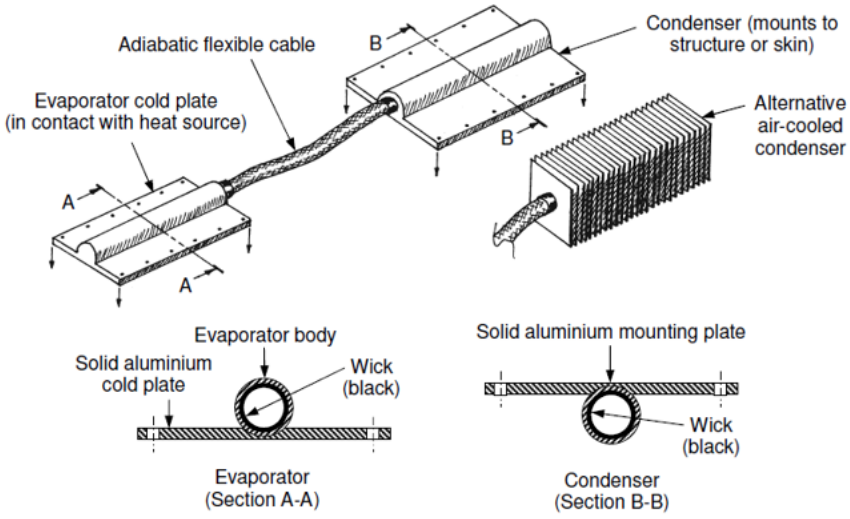

Figure 2.16: Geometry and structure of flexible heat pipes [26].

This wick is filled with a working liquid appropriated to the application. As heat is applied to the evaporator end, the working liquid evaporates from the wick, while the removal of heat from the condenser end causes the vapour to condensate on the wick. Due to capillary forces, the result is a pressure gradient in the liquid that causes the working liquid to flow through the wick towards the evaporator. The choice of material and working fluid varies depending on the application, and has led to pairings such as potassium with stainless steel, water with copper, ammonia with aluminum and so on. Effective thermal conductivities of heat pipes can range from 10000 to 100000 W/mK, in comparison with 400 W/mK for copper [26]. As thermal straps, they are widely employed for aerospace applications thanks to their advantages in terms of weight, flexibility and ease of installation. Ongoing studies are looking at heat pipes as a potential solution for thermal management of flight control EMAs

One of the problems of integrating devices such as heat pipes and thermal straps with the component to be cooled is to ensure a good thermal contact between the two surfaces across which heat transfer occurs. Imperfections as tool marks, warped or imperfectly-flat surfaces, surface porosity, etc. prevent actual physical contact between the two surfaces over much of their mating surface area (Fig. 2.17a), making the thermal resistance of the interface a lot higher than might be expected based on the apparent area of contact .

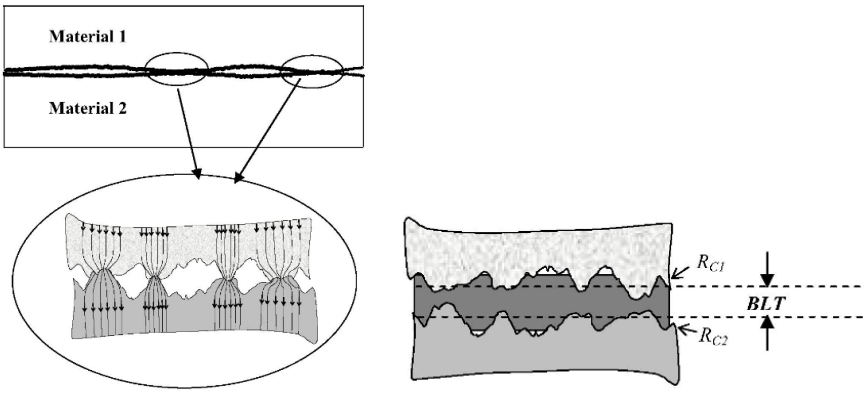

Figure 2.17: Example of the waviness and roughness of two contacting surfaces and how thermal interface material improve the contact area between the surfaces [67].

To overcome this problem, thermal interface materials (TIM) are employed. These are used to fill the spaces between the mating surfaces with a substance that has better thermal conductivity than air, which would otherwise fill those spaces (Fig. 2.17b). Thermal interface materials generally used include thermal greases, pastes, phase change materials

and advanced materials such as filled polymer matrices and particle-laden silicone materials (elastomers). The main advantages of fluid materials as greases and pastes are that they present a high thermal conductivity and they can easily fill the air gap between the contact surfaces with relatively low pressures. On the other hand, like any other greasy substance they can be extremely messy to handle, source of process contamination and probably not suitable for use in an aggressive environment (high temperature variation, humidity, vibrations, ...). Only certain particle-laden silicone materials, metal foils and polymeric TIMs are generally accepted in aircraft industry. These materials are normally easy to handle, can be easily cut to size of mounting surfaces, and keep their optimal performance over time (compared to thermal greases which dry-out over time by reducing the reliability). Compared to thermal fluids, however, they are more expensive and have a lower thermal conductivity [67].

Another evaporative system with a similar operation to heat pipes is the thermosyphon. The device, represented in Fig. 2.18, consists of a casing incorporating a working fluid inside which the heat source is immersed. The temperature increment causes the liquid to boil, so the vapor rises and condenses on the cooler surfaces at the top of the casing. Like heat pipes, the advantage of the thermosyphon is that the use of a two-phase fluid provides excellent heat transfer. It is also a passive system so it consumes no external power. The biggest drawback is that since the actuator is placed inside the container incorporating the fluid, its maintenance could be complex.

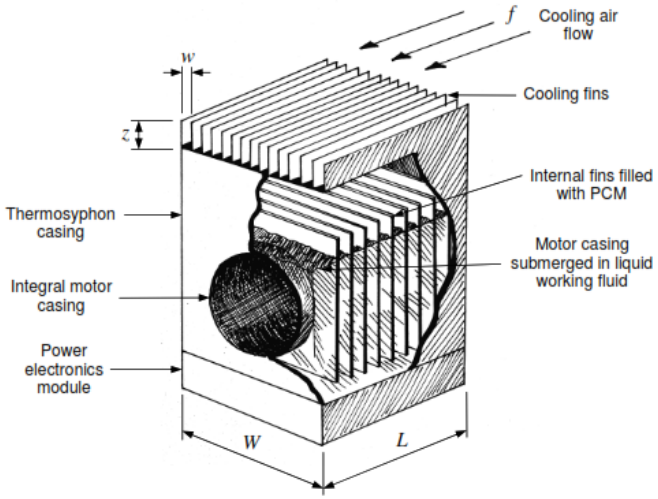

Figure 2.18: Geometry and structure of thermosyphon [13].

As evaporative systems, liquid cooling systems can achieve a greater heat transfer coefficient than air cooling systems, thanks to their higher thermal capacitance and density. This allows to accommodate heat sources with much higher power densities resulting in smaller system components.

Two types of liquid cooling systems are generally adopted as figured in Fig.2.19. A direct system allows heat to be dissipated by immersing the heat source in coolant or by spraying a jet of liquid onto the heat source components. This approach minimises thermal resistance, but the compatibility of the equipment with the coolant and maintenance accessibility must be attentively considered. In contrast, an indirect cooling system involves the conduction of heat from the source to a liquid-cooled cold plate. The liquid coolant is pumped through channels in the plate and the heat is dissipated to a heat sink through a separate heat exchanger. The main advantage of this method is that the heat source component can be easily removed from the self-contained liquid circuit. The main disadvantages of these approaches is that external power to drive the pump is needed, making the overall system mass generally greater than passive cooling systems. Maintenance, potential for leakage and fluid contamination are other important factors to be taken into account before considering the use of these solutions. Moreover, the system is made up of several (complex) components that can greatly reduce the overall reliability of the actuator.

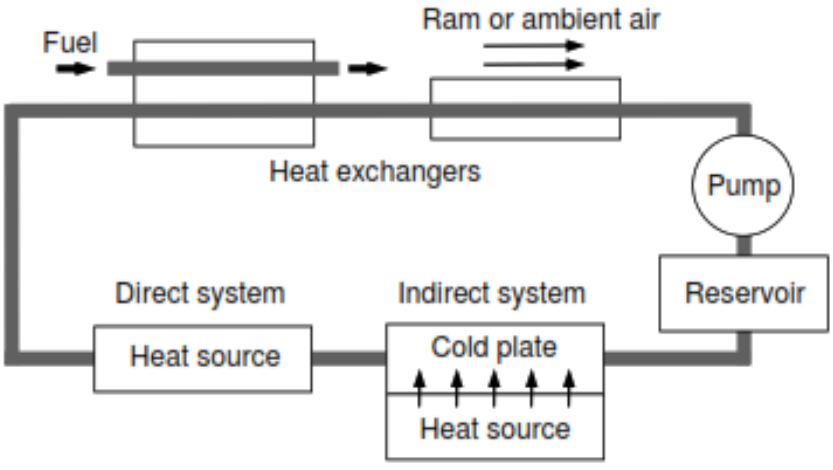

Figure 2.19: Liquid Cooling system circuit [13].

2.3.3 Improve the transient generation and storage

Another way to improve thermal management of electric actuators is to improve the transient storage and generation. In this regard, several solutions, illustrated in Fig 2.20, could be adopted.

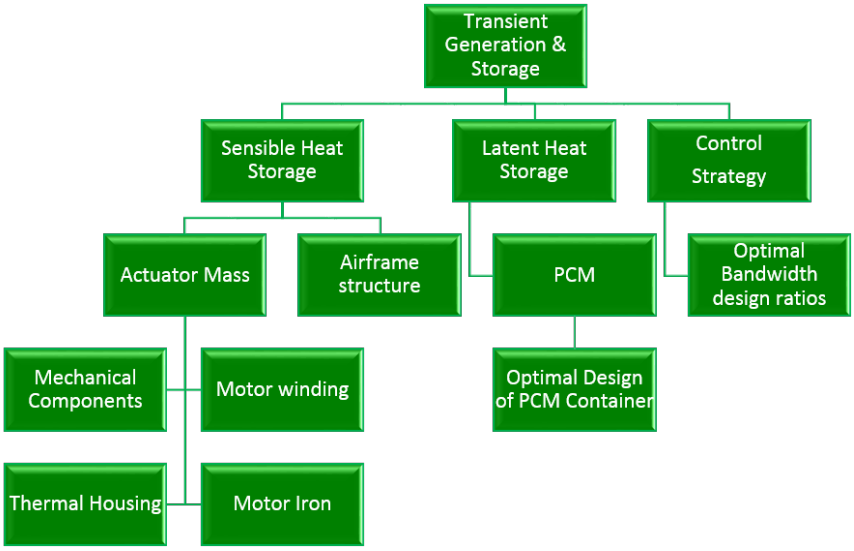

Figure 2.20: Strategies for improving the transient generation and storage.

The benefit of transient heat storage is that it allows to design the system for the average heat rejection requirements. This could allow to obtain a smaller and lighter system while maintain component temperature excursions during peak operations. There are essentially two methods to store thermal energy.

The first method is to store it by sensible heat storage, which uses the heat capacity of the sink material and results in a temperature rise as energy is absorbed without a phase change. The components of actuator, such as mechanical parts, thermal housing, copper and iron of motor could be used to store the heat load.

The second method consists in using phase change materials (PCM), involving either melting from solid to liquid or evaporation from liquid to gas. PCMs are materials which absorb large amount of energy in the form of latent heat within a narrow temperature range of phase transformation. Normally solid to liquid phase transformation would be preferred for aircraft applications, since vapor takes up more space and also induces other technical complexity on integration and reliability. The latent heat capacity of PCMs is 2 - 14 times greater than sensible heat capacity of most materials, leading in lighter solutions and

lower system temperatures. Typically the integration of PCMs in thermal systems could be challenging because of their low thermal conductivity. Therefore getting the heat into and successively out of the PCM can be a slow and inefficient process. Design techniques to embed the PCM within porous metallic foams [66] (Fig. 2.21a) or in finned structures [68] [13] (Fig. 2.21b) can lead to higher thermal performance and efficiency.

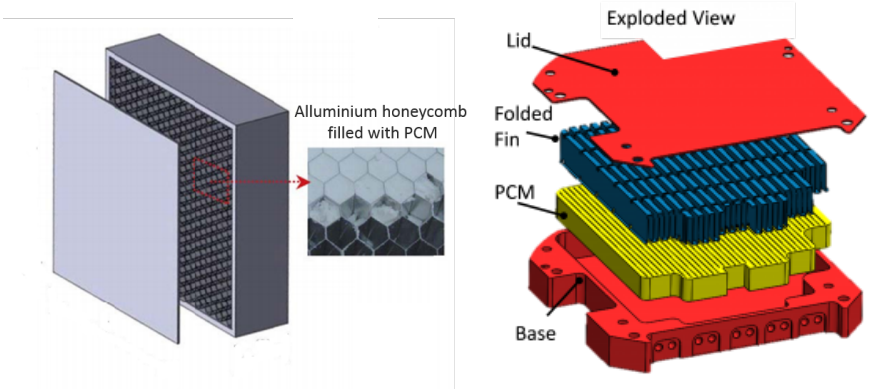

(a) PCM integrated in aluminium honeycomb [69]

(b) PCM integratated in aluminium fin arrays [70]

Figure 2.21: Examples of design techniques to embed PCM into aluminium heat sinks.

Control system design also plays a major role in altering the system's thermal behaviour, especially during transient operation. Different controller design methods to improve the system response, performance and efficiency have been explored by many researchers [71] [72]. The idea of controller tuning for heat minimization purpose still remains quite unexplored. Alternative control strategies could be investigated aiming to decrease the actuators's heat generation by careful selection and tuning of controller gains. With the final goal of limiting actuator temperatures, optimal ratios of current-to-speed and speed-to-position bandwidths can be examined.

With this last solution, the state of the art of the candidate solutions for improving the thermal management of flight control electrical actuators is concluded. A summary of these solutions is provided in the mind map depicted in Fig. 2.22.

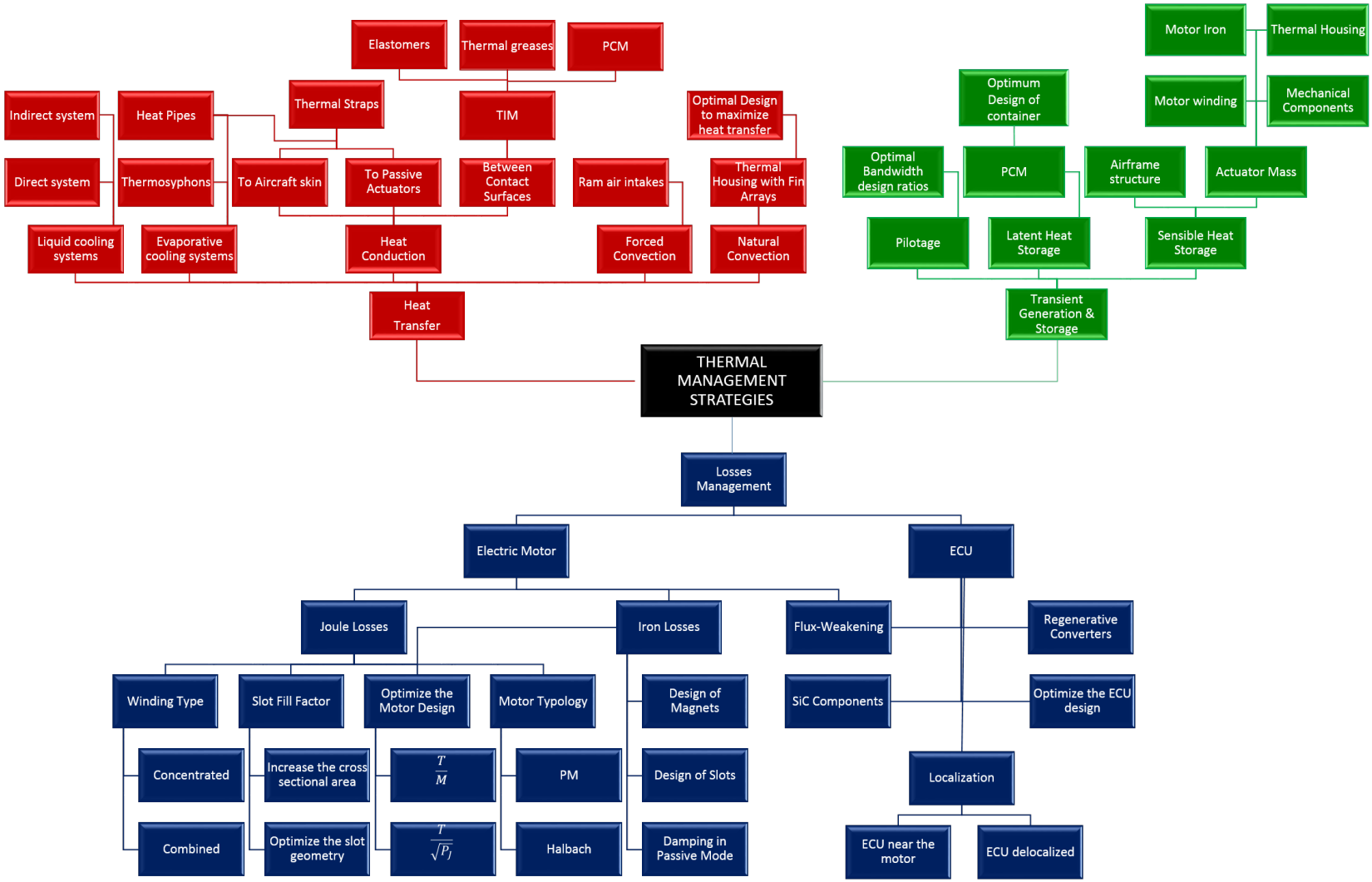

Figure 2.22: Mind map of all presented thermal management solutions for EAs.

2.4 Selected solutions for thermal management

A range of possible thermal management strategies and concepts were presented, many of which are currently being developed by industry for use with flight control actuators. The time available for this thesis project unfortunately did not allow for the exploration of the entire set of solutions presented. Therefore, for each of the three strategies introduced, it was decided to explore the following solutions, represented in the Fig. 2.23.

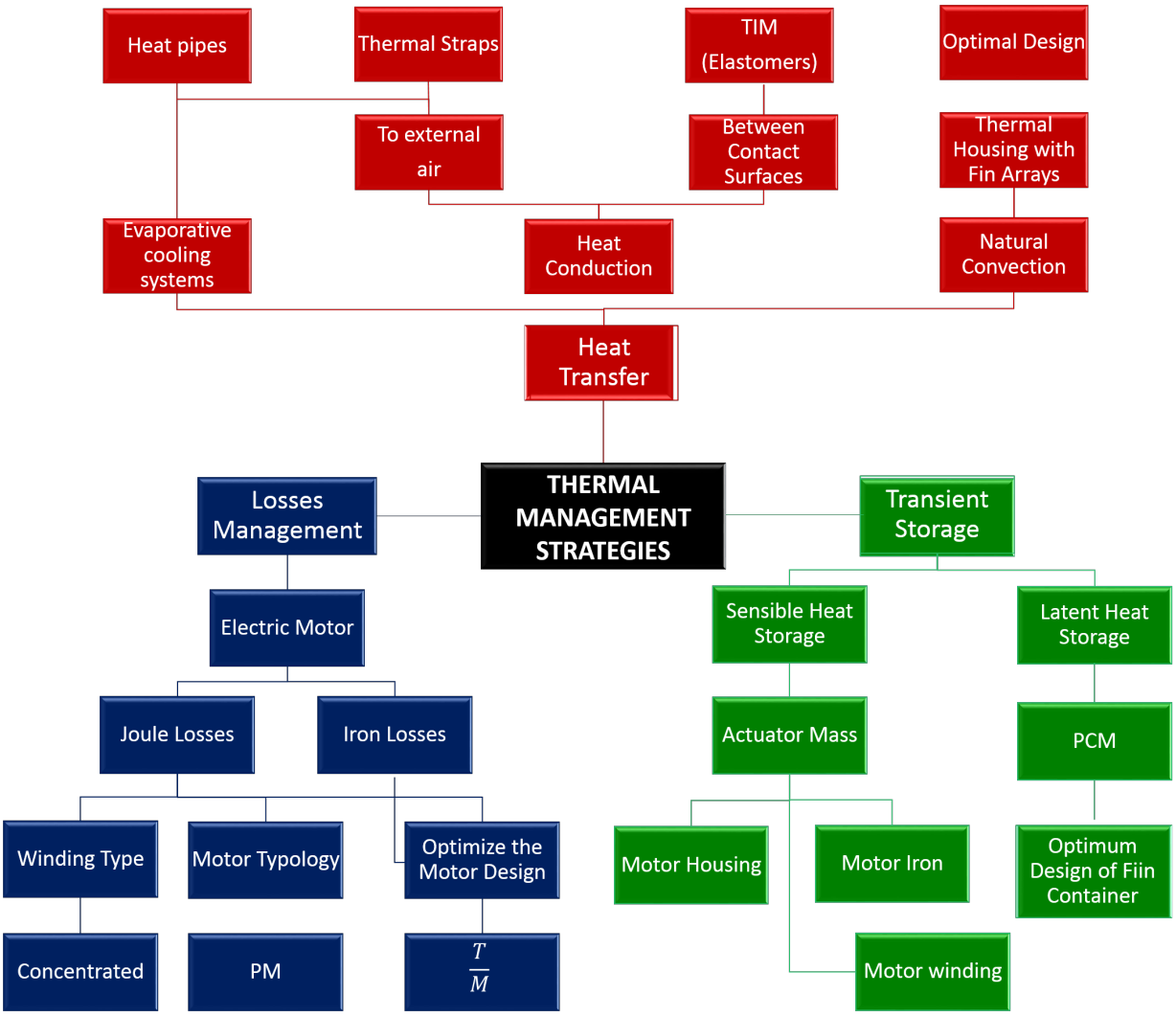

Figure 2.23: Selected solutions for thermal management of EAs.

With regard to the losses management axis, priority has been given to conventional motor typologies such as PM motors. This type of motor has by now reached a robust techno-

logical maturity and is widely used in the field of electrical actuators. Although Halbach motors represent an interesting technological development in the field of electric motors, they are extremely complex to manufacture, and at the time being resulting in considerably high costs that are not justified for these types of applications. The same considerations are also made regarding the winding. That is, the choice is directed towards conventional and technologically mature winding types, such as concentric windings. Since the preliminary design is a central theme of this thesis, modifications of the motor design that can be implemented at this stage are preferred. Hence, detailed design modifications, such as slot or magnet design improvements, are not considered. These are usually handled in the detailed design phase by experts in the field of electric motors. On the other hand, design modifications aimed at optimising the general geometry of the component (diameter, stator tooth size, slot size, magnet thickness, etc.) are investigated. The objective is to define a design aimed at maximising the torque density, while meeting the thermal constraints imposed by the application context. As the electric motor is the main responsible for the thermal problem of the actuator, it was decided to concentrate the efforts of this thesis on this device and the losses associated with it. The electronic control unit and the losses it generates will therefore not be analysed, assuming that the ECU is mounted away from the actuator and that its thermal management is handled separately. This choice significantly facilitates the thermal management and analysis of the actuator. However, this requires more in-depth studies concerning the possibility of locating the electronics of all the actuators in one or more central fuselage locations, so that they can be cooled by centralised cooling systems, and a particular analysis of the EMI effects induced. As a consequence of this choice, the flux-weakening control will not be treated either.

Regarding the heat transfer axis, passive, non-cumbersome and low-maintenance solutions are preferred. The chosen thermal management systems are: thermal housing with fin arrays, heat pipes and thermal straps. The finned thermal housing (Fig. 2.24) represents one of the most traditional and affordable methods of losses dissipation. Optimal designs aimed at maximising the heat transfer of the finned housing and at the same time minimising the mass of the device are envisaged. Thermal straps (Fig. 2.25a) and heat pipes (Fig. 2.25b) have the advantage of being able to transport large amounts of heat with a small temperature drop through the device, while being at the same time very lightweight. This temperature drop is important because it must be as small as possible to reduce the operating temperature of the actuator. Since these devices are much lighter than thermal housing with fins for the same amount of heat to be dissipated, they could be conveniently sized

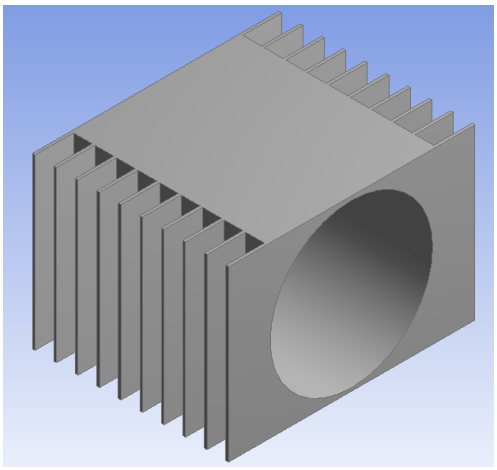

Figure 2.24: Motor thermal housing with fins arrays.

either for average load or for peak load rejections. They are also suitable for installation in confined spaces, which is an important consideration for actuator compartments. The heat conduction through these devices on the aircraft skin is not considered in view of the constraint arising from the low thermal conductivity of composite materials. A proposed mounting alternative considered here is to connect their terminal plates on an aluminum spreader plate installed on the outer side of the wing. This solution, represented in Fig. 2.25, allows the air flowing on the skin of the aircraft wing to be used as cold source, thus involving great benefits in terms of thermal management. This method will be further discussed in Chapter 5.

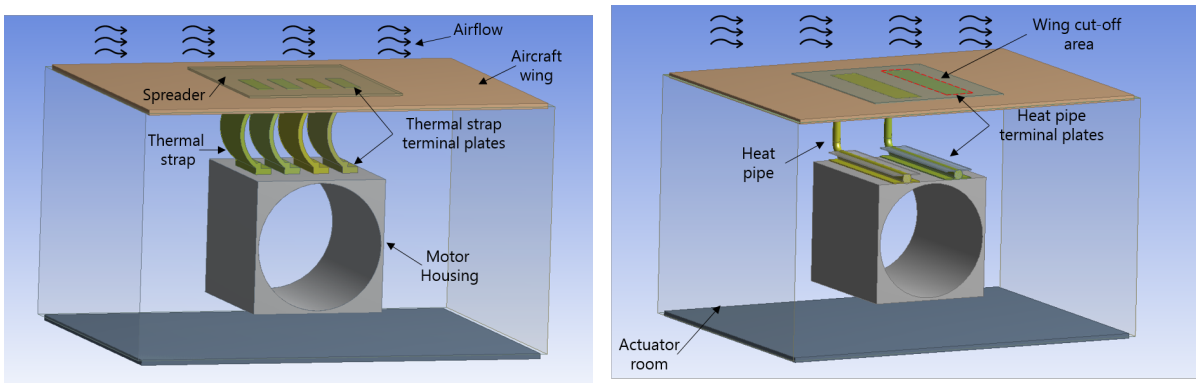

(a) (b)

Figure 2.25: Examples of thermal straps (a) and heat pipes (b) configurations.

Given their advantages of use for the applications discussed here, silicone elastomer materials will be used to interface these devices with the hot source (motor housing) and the cold surfaces (spreader plate).
With regard to transient storage through latent heat, PCMs are chosen. A configuration involving the integration of these materials in a finned plate is considered, as depicted in Fig. 2.26a. One or more plates can be placed on the surface of the motor housing to keep the temperature at the desired level, as shown in the example of Fig. 2.26b. The PCM plate can be also used in combination with the fined thermal housing, as shown in Fig. 2.27. This combination could be very useful in cases where the peak load is significant in relation to the average load and present for short periods of time. Their use would allow the peaks of heat to be absorbed through latent heat, allowing the use of lighter actuators and housing conveniently designed for the average load.

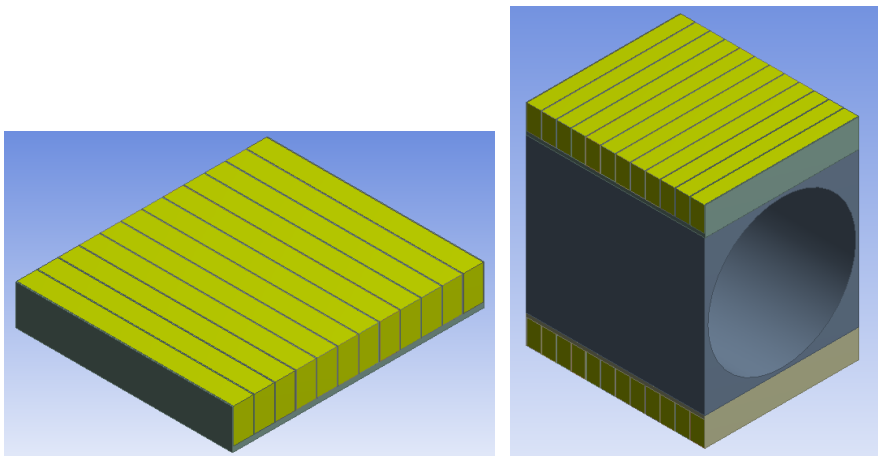

(a) PCM integrated in a finned plate (b) PCM plate mounted on the motor housing

Figure 2.26: Examples of PCM configuration and integration.

Sensible heat storage is taken into account by assessing the thermal capacities of the electrical motor and thermal components. Since, as announced in Section 2.2.2, the thermal problem does not particularly affects mechanical components, in order to simplify the studies carried out in this work, it has been decided not to consider the thermal analysis and evaluation of these devices. Nevertheless, this could result in a thermally conservative hypothesis, since the amount of sensible heat stored in mechanical devices is not taken into account.

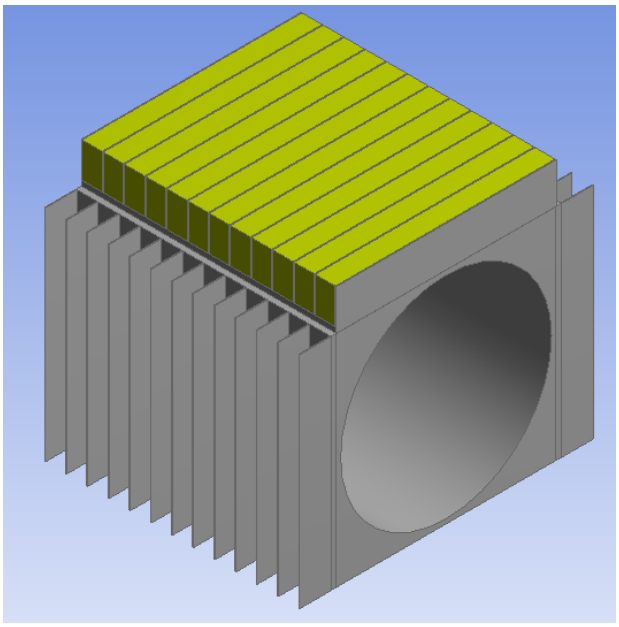

Figure 2.27: Coupling between finned thermal housing and PCM module.

Control strategies aimed at minimising the losses due to the actuator control, although very interesting and potentially promising, deserve a more in-depth discussion which will not be treated within this thesis for timing reasons.

2.5 Conclusion

In this chapter, the main candidates for thermal management of electric actuators have been presented. The main factors determining the major difficulties of thermal management have been introduced, and the related constraints induced in the design phase of the actuator and its associated cooling system have been highlighted. Electric motor losses firstly, and ECU losses have been identified as the main source of heat generation. The operating temperature requirements have been introduced according to the reliability and lifetime of the actuator components (motor winding: 180°C-200°C and ECU: 125°C-175°C) and airplane composite structures (actuator skin: 100°C). Mission profiles and flight scenarios were identified as dimensioning aspects of both the actuator and the cooling system. On the basis of these aspects, two design methodologies were introduced: a static approach consisting on extracting static design specifications directly from the mission profile, and

a dynamic approach involving the integration of the mission profile within the preliminary design phase. The sizing criterion adopted by industry manufacturer was also presented, consisting of sizing the actuator by considering laboratory conditions and successively validate the dynamic thermal performances along the entire flight scenario. A state of the art of possible solutions to improve the thermal management of electrical actuators has been subsequently presented. In this respect, three different strategies have been identified, for each of which different solutions applicable to the context under consideration have been proposed. The potentially most effective and applicable solutions, according to the resources available for this thesis project, have been subsequently selected. The solution chosen for improving the losses management is to define a design of the electric motor maximising the torque density. Since the motor has been individuated as the main actor to the generation of heat, it has been decided to concentrate the studies conducted in this thesis around this component and its associated losses, thus considering the actuator without the electronic control unit (assuming that the ECU is mounted away from the actuator and its thermal management is handled separately). In order to improve heat transfer, it has been decided to analyse passive, non-cumbersome and low-maintenance solutions such as the finned thermal housing, heat pipes and thermal straps. Concerning the transient heat storage systems, solutions for improving the sensible heat storage of component materials, as well as solutions using the latent heat storage by using phase change materials have been selected for the studies carried out in these thesis. The modelling, sizing and integration of these solutions are discussed in detail in the following chapters.

Chapter 3

Methodologies and Models for the Preliminary Design

Contents

3.1 Introduction **48**

3.2 State of the Art of Surrogate Modelling **49**

3.2.1 Surrogate Modelling Approaches for Multi-Disciplinary Design Optimization 49

3.2.2 Surrogate Modelling Techniques 51

3.3 VPLM Methodology **54**

3.4 Generalization of model reduction procedure via a sensitivity analysis based on optimization **58**

3.5 Generation of surrogate models of a PM brushless motor **61**

3.5.1 Dimensional Analysis 62

3.5.2 Sensitivity analysis for the selection of meaningful π numbers . . . 65

3.5.3 Model generation 67

3.6 Conclusion **70**

3.1 Introduction

This chapter introduces a new methodology for obtaining reusable surrogate models suitable for the preliminary design of electrical actuators. The methodology is based on a dimensional and sensitivity analysis adapted to the needs and constraints arising from multidisciplinary design. It enables simpler and lighter models to be obtained, with satisfactory predictive accuracy over a large range of validity. These surrogate models can cover a very large area of applications, where the components may vary from very small to very large sizes. As these models will be employed for the preliminary design of the electro-mechanical actuators used for the different primary control surfaces (Aileron, Rudder and Elevator), they are being conceived to be reusable. Avoiding the reconstruction of the model offers advantages in terms of capitalization and benefits from the concept of "reuse". In the first part of the chapter the state of the art of surrogate modelling is presented. After introducing the processes used for multidisciplinary design and the notion of disciplinary coupling, a brief summary of the different techniques for generating surrogate models is illustrated. Then, an original surrogate modelling methodology, called the VPLM (Variable Power Law Meta-model) technique, based on dimensional analysis and dimensionless numbers is presented. Although this method reduces the number of variables, models with complex geometries can lead to numerous aspect ratios. Hence, the model reduction procedure via a sensitivity analysis based on optimization is adopted to highlight and select those variables that:

- Represent optimal design of the considered component.
- Allow specific disciplinary coupling compromises during the phase of preliminary design and optimization.

To better understand the procedure, an example of an industrial application case is provided. It depicts the generation procedure for obtaining surrogate models of permanent magnet (PM) brushless motors.

3.2 State of the Art of Surrogate Modelling

3.2.1 Surrogate Modelling Approaches for Multi-Disciplinary Design Optimization

The design and optimization of electrical actuators involves selecting the dimensions and modelling the performance of the components and the interactions between them. Actually, a significant challenge arises in managing the mechanical-electromagnetic-thermal coupling between the various components of the actuator in order to satisfy some givens specifications and to optimize the performance of the system. Multidisciplinary Design Optimization techniques provide effective computational tools for optimal preliminary design of the multidisciplinary systems and to handle the problem of coupling between the system several disciplines. Although the use of MDO has increased greatly in the last decade, the aircraft industry [28] is still facing three major constraints related to this approach. The first concerns the calculation time needed to carry out the optimization. MDO needs a large number of iterations (efficient optimization requires an order of n^2 analyses, where n is the number of optimisation variables) and multiple discipline analysis tools. This can involve enormous computation burden and may even be non sustainable if the system relies on a large number of disciplines (especially if 2-D or 3-D finite element models are used). The second issue concerns the capitalization of knowledge. MDO requires knowledge and analysis of individual interconnected disciplines in order to optimize the whole system. However, the system design engineer is not a specialist in all the domains involved. Therefore, the capitalization of knowledge is a way to communicate, share and reuse knowledge, and adapt the complexity of the models to the level of design considered. The last difficulty of MDO implementation concerns the model capitalization, understood as the capability of the model to be reused for different system requirements with the least redevelopment or tuning effort. Reuse is key in capitalization as it implies time saving. Often, during the preliminary design phase, different architectures, configurations and specifications of the system can be evaluated in order to conduct trade-off analyses and comparisons. Hence, the numerical modelling of components needs to offer a wide domain of validity for reuse after new alterations of the system and needs to enable rapid decisions to be made. In addition, a model of a component can be reused in the preliminary design of a different multi-physical system. All the challenges mentioned above induce the necessity for models

not to demand too much computation time and to be easy for users to handle. Moreover, models need to take the combination of disciplines into account and guarantee a wide domain of validity if they have to be capitalized and reused. Surrogate models cover these needs, at least partially. A surrogate model is an engineering modelling method used when an output of interest cannot be easily directly measured, so a model of the outcome is used instead. Scientific literature offers several surrogate modelling techniques for building simpler and handier models suited for multidisciplinary design optimisation. They are essentially based on one of two approaches, represented in the example depicted in Fig. 3.1 (adapted to the context under consideration, i.e. the coupling between the different interacting disciplines between the actuator and the cooling device). The classical MBDO (Meta-model-Based Design Optimization) approach [32] (Fig. 3.1a) consists of generating one surrogate model for the output (y), composed of the overall single responses of the individual disciplines (x_{mecha}, x_{elec}, $x_{thermal}$) representing the system under consideration. This is done by Kriging methods [33] or related Gaussian processes, such as Efficient Global Optimization (EGO) [34]. The so called "online" surrogate models are very useful and are generally employed inside optimization framework for assisting and solving computationally expensive problems. These models are generally constructed through online learning to replace the computationally expensive objective function [73] [74] [75]. Although this technique is typically suited to map complex non-linear functions with a high degree of accuracy and prediction in a relatively limited range, it could be very time consuming in the case of system reformulation. This means that, if the system requires some internal modifications or if it has to satisfy some other kinds of specifications then the surrogate models must be reformulated. A more flexible approach (Fig. 3.1b), referred to as SBAO (Surrogate-Based Analysis and Optimization), [76] often associated with the concept of "offline" surrogate model, consists of generating models for individual responses (y_{mecha}, y_{elec}, $y_{thermal}$) of interest and successively employing them in design and optimization problems. In this way, simpler surrogate models are sufficient. They bring great advantages in terms of computational time and, mainly, capitalization. If the system changes, there is no longer a need to reformulate the entire problem: it is sufficient to modify or replace the discipline concerned. This approach is more suited to preliminary design, which is fundamentally a design stage that accepts low-fidelity models. The major challenges of this approach lie in defining a model that guarantees a wide domain of validity in order to be reusable and easily managed by users. To cover these needs, the existing VPLM methodology [77] [12] and a newly developed method of sensitivity analysis based on optimization [78] are

employed. To better understand these techniques, it may be necessary to describe and to compare the different methods used to build the surrogate models.

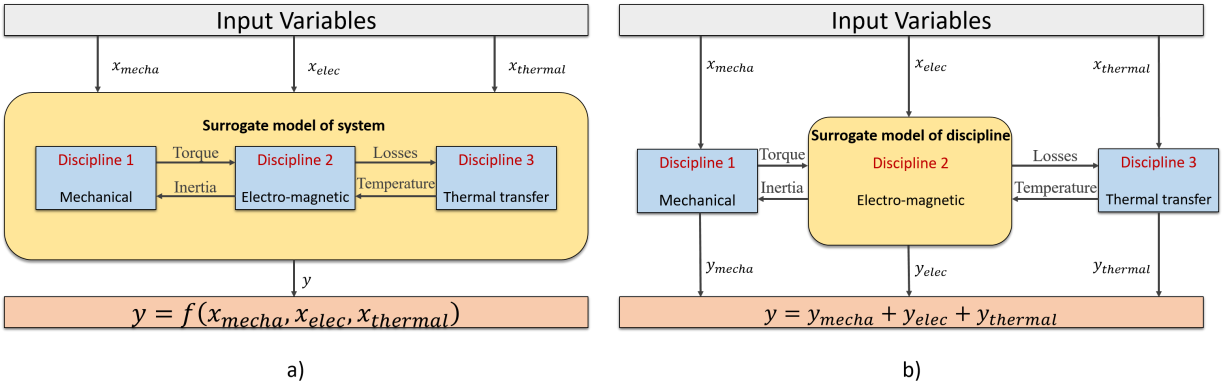

Figure 3.1: Surrogating approaches employed in MDO: a) MBDO and b) SBAO.

3.2.2 Surrogate Modelling Techniques

The surrogate model is a mathematical model, which aims to represent a physical characteristic (mechanical, chemical, electrical, electromagnetic, etc.) of a component or a system, usually estimated through 2-D or 3-D finite elements simulations. In this way, these latter can be easily replaced to obtain significant advantages in terms of computation time and ease of use, especially if, as previously said, these models are employed in an optimization process that involves a significant number of evaluations of numerous components.
A physical characteristic of a component, can be expressed in the following way:

$$y = f(d_1, d_2, \ldots, p_1, p_2) \tag{3.1}$$

where:

- y is the physical characteristic of a component that is useful for its selection in a system, such as the electro-magnetic torque of an electric motor, the thermal resistance of a component, etc.
- d_i are the geometrical dimensions of the component. These dimensions may vary

over large intervals during global system design, or from one application to another.

- p_i are boundary conditions and/or material properties used in the design of the components.

According to this formulation, two different approaches are distinguished to build the surrogate models: the mathematical approach and the approach based on dimensional analysis. The idea behind the mathematical approach is to generate a mathematical regression in order to describe the behaviours of a function with the following form:

$$y = f(x, \theta) \tag{3.2}$$

where:

- x is a vector of physical parameters $x_i, i = \{1, \ldots, n\}$ considered to be input variables and which can be design variables such as dimensions d_i, boundary conditions or material properties p_i;
- θ is a vector of parameters associated with the family of functions needed to construct the surface;

There are different methods, illustrated in Table 3.1, to generate such regressions. The very classical response surface methodology (RMS) and the common radial basis function (RBF) and Kriging methods, which are well suited to represent complex behaviours on well-defined and relatively small ranges of the input.

Table 3.1: Synthesis of mathematical forms of pure mathematical approaches [79].

Approaches	**Mathematical form of the model**
Response surface methodology (RSM)	$y = f(x,\theta) = \theta_0 + \sum_{i=1}^{n} \theta_i x_i + \sum_{i=1}^{n} \sum_{j=1}^{n} \theta_{i,j} x_i x_j$
Radial basis functions (RBF)	$y = f(x,\theta) = \mu + \sum_{i=1}^{n} \theta_i e^{-\frac{\|\|x - x_{(i)}\|\|^2}{\sigma^2}}$
Kriging functions	$y = f(x,\theta) = \mu + \sum_{i=1}^{n} \theta_i \prod_{j=1}^{k_x} e^{-\frac{\|x_j - x_j^{(i)}\|^{p_j}}{\sigma^2}}$
where μ is the mean value of y	

The approach based on dimensional analysis uses a more physical reasoning than the mathematical approach. It takes use of Buckingham theorem [80] to convert geometric and physical quantities into dimensionless ratios, thus reducing the number of inputs and consequently the complexity of the model. In this way, Eq. 3.2 is redefined in the form of:

$$\Pi_0 = F(\Pi_1, \Pi_2, \ldots, \Pi_q) \tag{3.3}$$

where:

- Π_i are dimensionless variables, also called dimensionless numbers.
- q is the number of dimensionless numbers, which depends on the m independent physical units (e.g. m, kg, s, etc.) and the n independent variables involved in the problem. It is calculated as: $q = n - m$.

The output response, y, is also modified to become dimensionless:

$$\Pi_0 = y \prod d_i^{a_i} p_i^{b_i} \tag{3.4}$$

This approach often uses products of power laws, widely used to solve many engineering and scientific problems, with dimensionless numbers Π_i, as illustrated in Table 3.2, to define the model. Very interesting in this regard is the SLAWMM (scaling law meta-models) method [81], which extends the validity of scaling laws by replacing the a and k constant coefficients by functions of Π_i numbers. The regressions obtained by this method

show a particular interest in the preliminary design because they are very easy to handle and remain valid over a wide range of sizes, for prediction and extrapolation purposes. Nevertheless, the mathematical expression is still dependent on a dimensional quantity L, representing the reference length. Often, the choice of the reference length is not obvious, and this may reduce the predictive capability of the model. For the preliminary design of complex multi-physics systems, a mathematical form of model that is more independent of the choice of characteristic quantity is essential. For this and the previously mentioned reasons, surrogate models generated by means of the VPLM methodology are used in this thesis.

Table 3.2: Synthesis of mathematical forms of dimensional analysis based approaches [79].

Approaches	**Mathematical form of the model**
Power laws with Π_i numbers	$\Pi_0 = a_0 \prod_{i=1}^{q} \Pi_i^{a_i}$
Power laws with x_i (SLAW)	$y = a_0 \prod_{i=1}^{n} x_i^{a_i}$
Scaling laws	$y = kL^a$
Scaling law meta-models (SLAWMM)	$y = f(L, \Pi_1, \Pi_2, \dots) = k(\Pi_1, \Pi_2, \dots) L^{a(\Pi_1, \Pi_2, \dots)}$
Polynomial meta-models with Π_i numbers	$\Pi_0 = a_0 + \sum_{i=1}^{q} a_i \Pi_i + \sum_{i=1}^{q} \sum_{j=1}^{q} a_{ij} \Pi_i \Pi_j$
Sum of power laws meta-model	$\Pi_0 = \sum_{j=1}^{m} \beta_j \prod_{i=1}^{q} \Pi_i^{\beta_{ij}}$
where k, a_i and β_j are numerical coefficients to be determined	

3.3 VPLM Methodology

The VPLM methodology [77] [82] is an original methodology of surrogate modelling that allows lightweight and compact substitution models to be obtained that are suitable for the preliminary design of multi-physical systems. In this phase, models need to be simple

and light in order to facilitate their implementation in multi-disciplinary optimization procedures and enable the preliminary design to be conducted in an optimal way with highly advantageous computational time. The methodology makes use of dimensional analysis [83], the Buckingham theorem [80] and response surface methods to extract compact models from finite element simulations. It relies on three main steps as depicted in Fig. 3.2: generation of the data necessary for the construction of the surrogate model, definition of the surrogate model and selection of the model. The first step starts with a dimensional

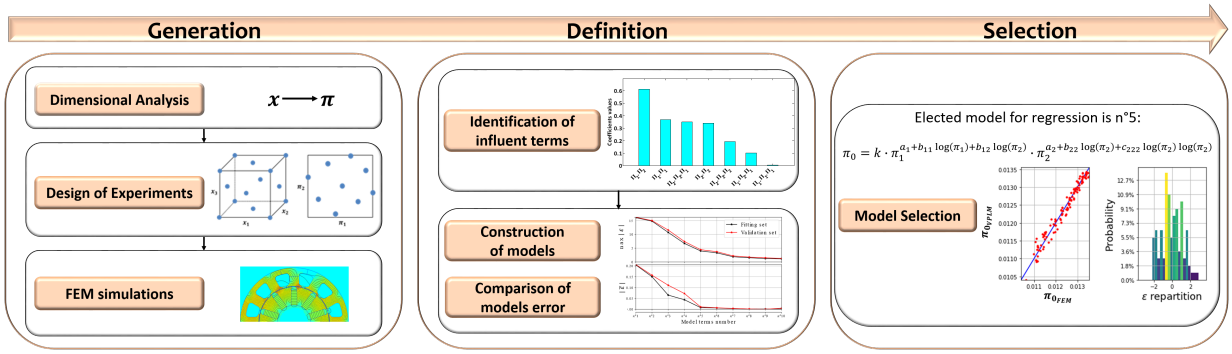

Figure 3.2: VPLM methodology flowchart

analysis. For instance, we consider a general system composed of several components and we are interested in estimating the performance y of a specific component which depends on $n-1$ parameters of interest:

$$y = f(x_1, x_2, \ldots, x_{n-1}) \tag{3.5}$$

The dimensional problem X can be transformed into a non-dimensional problem Π using the Vaschy–Buckingham theorem [80]. In this way, a reduction of the number of variables ($q < n$) as well as their range of variation is obtained without any loss of information:

$$\Pi_0 = f(\Pi_1, \Pi_2, \ldots, \Pi_{q-1}) \tag{3.6}$$

In fact, the dimensionless form generally reveals shape factors, which are typically ratios between geometrical variables with a range of variation usually smaller than that of the original dimensions. As long as the dimensionless variables are defined, a design of experiment (DoE) is set up [82] in order to generate the configurations to be simulated with finite element tools. Once the simulation results have been obtained, the surrogate models are defined. In this phase the algebraic form of the model is expressed. As the name of the

methodology suggests, the mathematical expression used for the description of the model is a product of variable power laws of dimensionless numbers. Compared to the traditional surrogate models such as polynomial response surfaces, Kriging, radial basis functions etc., it has the advantage of providing good predictive accuracy over a wide range of the design variables (several orders of magnitude) [77]. Moreover, this mathematical form is really suitable for engineering sizing problems because, as before said, their behaviour generally follows a power law:

$$\Pi_0 = k\Pi_1^{a_1}\Pi_2^{a_2}\dots\Pi_q^{a_q} \tag{3.7}$$

Eq. 3.7 written on a logarithmic scale becomes linear (first order polynomial) and allows a further reduction of the range of variables ($\log(\Pi_i)$):

$$\log\Pi_0 = \log(k) + \sum_{i=1}^{q} a_i \log(\Pi_i) \tag{3.8}$$

Since some problems require a high degree of accuracy, it can sometimes be useful to increase the order of the polynomial model:

$$\begin{aligned}\log\Pi_0 = \log(k) &+ \sum_{i=1}^{q} a_i \log(\Pi_i) \\ &+ \sum_{i=1}^{q}\sum_{j=1}^{q} b_{ij} \log(\Pi_i)\log(\Pi_j) \\ &+ \sum_{i=1}^{q}\sum_{j=1}^{q}\sum_{k=1}^{q} c_{ijk} \log(\Pi_i)\log(\Pi_j)\log(\Pi_k)\end{aligned} \tag{3.9}$$

By rewriting relation (3.9) on the linear scale, we obtain a variable power law model:

$$\Pi_0 = k\Pi_1^{a_1(\Pi_1,\Pi_2,\dots,\Pi_q)}\Pi_2^{a_2(\Pi_1,\Pi_2,\dots,\Pi_q)}\dots\Pi_q^{a_q(\Pi_1,\Pi_2,\dots,\Pi_q)} \tag{3.10}$$

where $a_i(\Pi_i)$ are polynomial functions of $log(\Pi_i)$. Most of the time, the model does not need to take all the higher order terms into account (those multiplied by b_{ij} and c_{ijk}) in Eq. 3.9. In order to identify the terms that need to be kept, a sensitivity analysis [84] is conducted using the simulation data obtained in the first step. Then, these terms are sorted in order of their significance (Fig. 3.3) and m models are automatically calculated where, for the i^{th} model, $i \in [1, ..., m-1]$, only the first i terms from Fig. 3.3 are considered. Note that for $i = 1$ the model obtained is identical to the one in Eq. 3.7.

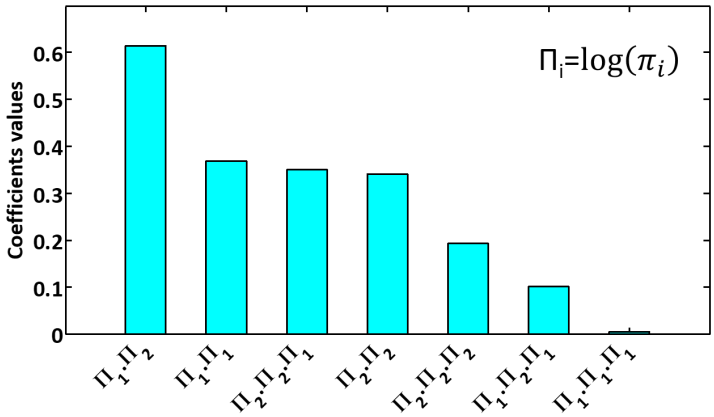

Figure 3.3: Example of results of sensitivity analysis after ranking the terms (in absolute value) according to their importance for the case of two dimensionless numbers [77].

Then the results are presented on a graph showing the maximal and the mean relative errors ($max|\varepsilon|$ and $\bar{\varepsilon}$ respectively) against the model terms numbers, as shown in Fig. 3.4.

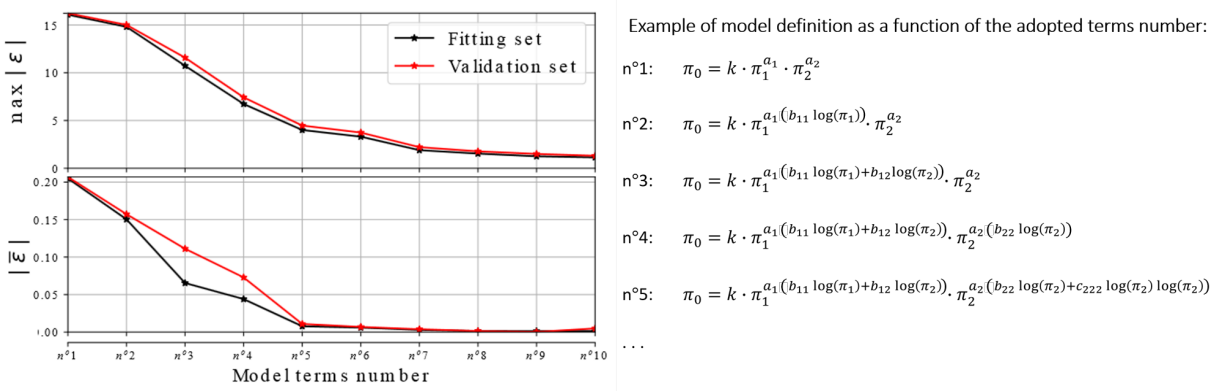

Figure 3.4: Example of evolution of maximum and mean relative errors as a function of the number of terms adopted for the definition of the model.

The last step of the methodology deals with the selection of the model (Fig. 3.5). The best candidate model may be chosen at the inflection point for the validation set, which is an average value of the leave-one-out cross-validation technique on the whole data set.
Although the dimensional analysis reduces the number of variables, components with complex geometry can lead to numerous aspect ratios. Moreover, since the surrogate models will be employed in system level design problems, attempts are made to obtain models with sufficient number of degrees of freedom to achieve the objective and the trade-offs of the preliminary design. For this reason, in this thesis we developed a method [78] which

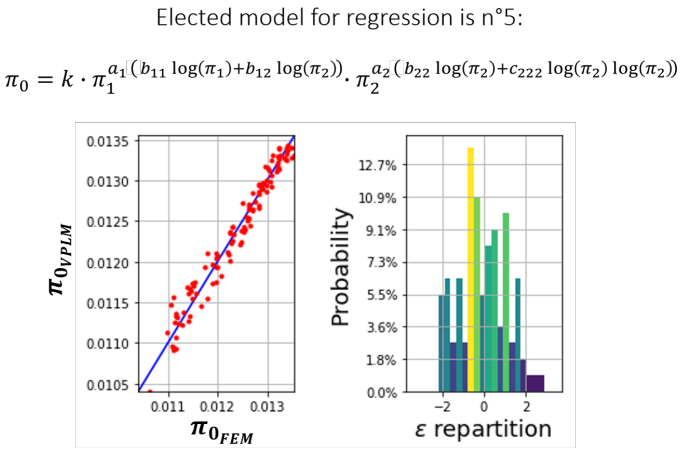

Figure 3.5: a) Comparison of VPLM model with finite element simulations for a selected model with 5 terms a b) error distribution.

allows to:

- Select the aspect ratios to be kept as variables.
- Achieve the necessary interdisciplinary coupling compromises.
- Determine the optimal numerical values of the aspect ratios that can be set as constants.

This method, explained in the next section, relies on a dedicated process of sensitivity analysis based on optimized designs.

3.4 Generalization of model reduction procedure via a sensitivity analysis based on optimization

The surrogate models must be as simple and compact as possible in order to estimate the component performance by means of a reduced number of design variables. In fact, the reduction of just one variable can lead to remarkable gains in terms of computational time during the phase of system design optimization. Although dimensional analysis reduces the number of inputs, there may still remain a high number of them, especially when the

component is described by many geometrical aspect ratios. One way to tackle this problem is to identify which aspect ratios can achieve multidisciplinary compromises at the system level and select them for the definition of the model, while leaving the remaining aspect ratios as constants. In this regard, the literature provides several methods for model order reduction [85] [86] and sensitivity analysis [87] [88]. Although they represent the state of the art, these techniques could be difficult to adapt to satisfy the trade-offs of the preliminary design, which is crucially dependent on the interactions between disciplines and components of the system. The preliminary design is facilitated and fulfils optimal results if the models of the components forming the system have already been optimized in accordance with particular specifications. Therefore the surrogate model not only has to describe the behaviour of a component with the fewest number of variables but also has to represent the optimal design satisfying specific requirements (i.e. mass minimization, maximization of the performances, etc.) and constraints over a wide range. In this regard we developed a new methodology of model reduction, which takes place immediately after the phase of dimensional analysis and is based on sensitivity analysis and optimization. In order to describe the methodology, the flowcharts of Fig. 3.6 and Fig. 3.10 (specific to the case study of the PM brushless motor) are used. The procedure developed for model reduction can be described by the following steps:

1. Identify the physical quantities (generally expressed in the form of dimensionless numbers as explained in Section 3.3) to be exchanged with other disciplines or components of the system.

2. Define a set of specifications, by means of a DoE, for the physical quantities of interest detected in step 1. These specifications should be representative of a full range of possible component uses. The specifications of a component are strictly linked to the characteristics of the system within which it is employed. Therefore, in order to guarantee the reuse of the model, different levels of specifications have to be taken into account. In more complex systems, the interconnected disciplines and the specifications involved are more numerous. In consequence, the dimension of the DoE increases, as does the number of configurations to be optimized. A Latin Hypercube Sampling (LHS) design of experiments is preferable, since it maximizes the number of levels and minimizes the correlation between the specifications. The number of configurations taken into account is strictly linked to the dimensionality of the problem. It has to be wisely chosen because a greater number of points

increases the number of optimizations, but without always increasing the efficiency of the sensitivity. For example, with a three-dimensional DoE in which four levels are taken into consideration for each factor with an equivalent Full-Factorial design, 27 points can be sufficient to cover the space of inputs sufficiently.

3. Set and solve an optimization problem for each of the configurations of the DoE defined in step 2.

4. Once the optimized components are found for the entire DoE, analyse the aspect ratios using an indicator of influence defined as:

$$\alpha_{\Pi_i} = \frac{\sigma(\Pi_i)}{\overline{\Pi}_i} \tag{3.11}$$

where $\sigma(\Pi_i)$ expresses the standard deviation and $\overline{\Pi}_i$ is the mean of the dimensionless variable Π_i.

A scatter matrix can be very useful to illustrate the variation of variables graphically and to support the user in choosing the variables. The most varying dimensionless numbers will be employed for the definition of the model, while the remaining dimensionless variables will be kept as constant and varied with geometrical similarity.
In order to give a practical example of an application, Section 3.5 shows how to use the developed methodology of model reduction to support the VPLM procedure in generating the surrogate models of a PM brushless motor.

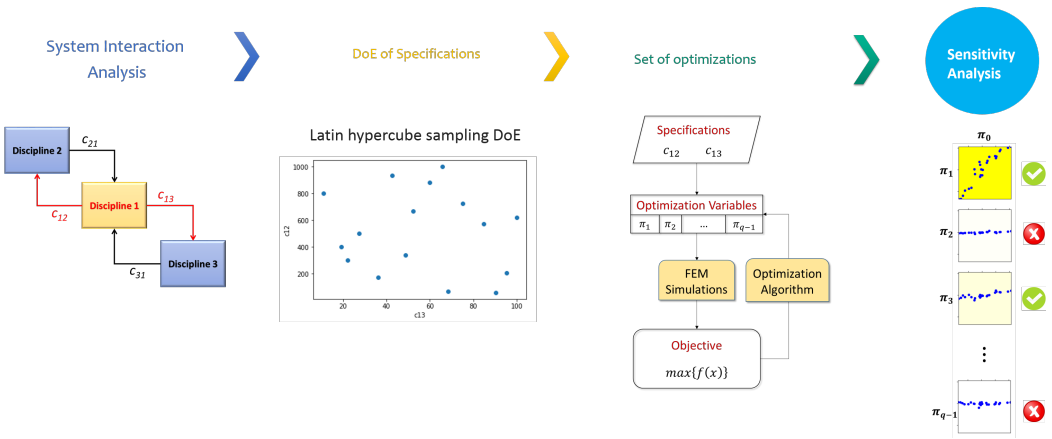

Figure 3.6: Flowchart of the proposed model reduction process.

3.5 Generation of surrogate models of a PM brushless motor

In this section, the different steps of the VPLM and model reduction methodologies are applied to build the surrogate models of a wide range of PM brushless motors (*PARKER NX servomotors* taken as reference) as depicted in Fig. 3.7a. A description of the Finite Element Method Magnetics (FEMM) model (Fig. 3.7b) adopted for the generation of the surrogate models is presented in **Annex A**. The methodologies are supported by the Python package *pyVPLM* which can be downloaded freely on Github (`https://github.com/SizingLab/pyvplm`).

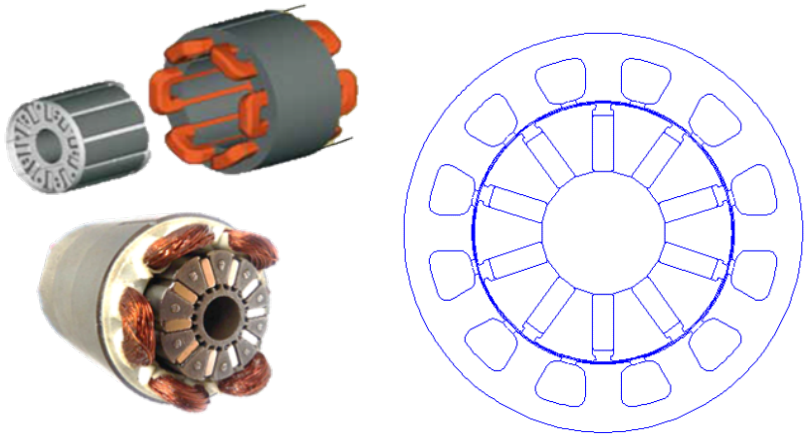

(a) (b)

Figure 3.7: a) Parvex NX 310 servomotor [89] and b) its representative finite elements model.

In the context of aeronautical design, an electric motor must be designed to satisfy an external load requirement without exceeding the operating temperature limits imposed by technology (e.g. motor winding temperature) and by aircraft manufacturers (e.g. to limit the aging of airplane composite structures). This leads to an electro-mechanical-thermal coupling between the motor, the heat sink and the mechanical components suitable for motion conversion (i.e. screw-nut, bearing, gearbox, etc.). The definition of the model should take this coupling into account in order to facilitate optimal compromises in system level design. Moreover, in the aircraft industry, there is a tendency to minimize the mass of the structure in order to decrease fuel consumption. Hence, the objective is to define the surrogate models of the electric motor optimized in terms of torque density.

3.5.1 Dimensional Analysis

The goal is to define the surrogate models expressing the performance of the motor in terms of electromagnetic torque T, Joule losses P_J and iron losses P_{Fe}. The first step deals with the dimensional analysis, which aims to identify all the geometrical (g) and physical (p) variables influencing such performances. For example, if we consider the electromagnetic torque expressed in form per unit length, these variables are (see Table 3.3 and in Fig. 3.8):

$$T/L_m = f(\overbrace{D_e, D_i, e_{tooth}, e_{yoke}, W_{PM}, R_i}^{g}, \overbrace{J, B_r, B_{sat}, \mu_0}^{p}) \tag{3.12}$$

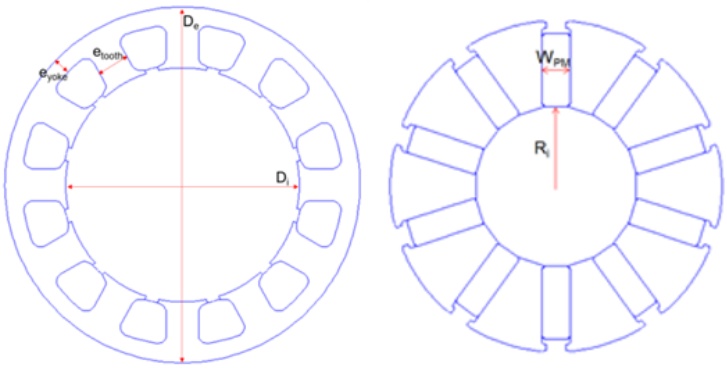

Figure 3.8: Stator and Rotor geometrical variables.

In the eleven identified quantities ($n = 11$), there are three independent dimensions $[N, m, A]$ ($k = 3$). According to the Buckingham-Pi theorem, eight dimensionless parameters, defined in Table 3.4, are necessary to completely describe the problem:

$$\Pi_{0_T} = f(\Pi_1, \Pi_2, \Pi_3, \Pi_4, \Pi_5, \Pi_6, \Pi_7) \tag{3.13}$$

where $\Pi_{0_T} = \frac{T}{L_m B_r J D_e^3}$.

Table 3.3: Dimensional variables

Variable	Definition	Range	Unit	$\frac{X_{max}}{X_{min}}$
D_e	Outer motor diameter	$[30-150]$	mm	5
D_i	Inner stator diameter	$[8.32-45.96]$	mm	5.52
e_{tooth}	Tooth thickness	$[1.21-12.09]$	mm	9.99
e_{yoke}	Yoke thickness	$[0.58-9.67]$	mm	16.67
W_{PM}	Permanent magnet thickness	$[0.96-11.97]$	mm	12.46
R_i	Inner rotor radius	$[3.38-26.61]$	mm	7.87
L_m	Motor length	$[21.77-108.87]$	mm	5
J	Current density	$[7-50]$	A/mm^2	7.14
f_{elec}	Electrical frequency	$[150-700]$	Hz	4
B_r	Residual induction	$[1.07]$	T	-
B_{sat}	Saturation induction	$[2.13]$	T	-
N_s	Slots Number	$[12]$	$[-]$	-
μ_0	Vacuum permeability	$[4\pi 10^{-7}]$	H/m	-
ρ_{Cu}	Electrical resistivity of copper $(20°C)$	$[1.68 \cdot 10^{-8}]$	Ωm	-
$\Delta_{P_{Fe}}$	Specific core losses	$[1.25]$	W/kg	-
γ_{Fe}	Density of iron	$[7.874]$	kg/m^3	-

Since Π_7 is constant for a given material, it will not be considered as an input of the model. Thus, the electromagnetic torque can be finally described by the remaining six dimensionless numbers. Following the same reasoning, we can obtain the dimensionless expressions for the Joule and iron losses, which are dependent on the following geometrical (g) and physical (p) variables:

$$P_J/L_m = f(\overbrace{D_e, D_i, e_{tooth}, e_{yoke}, W_{PM}, R_i}^{g}, \overbrace{J, B_{sat}, \rho_{Cu}, \mu_0}^{p}) \tag{3.14}$$

$$P_{Fe}/L_m = f(\overbrace{D_e, D_i, e_{tooth}, e_{yoke}, W_{PM}, R_i}^{g}, \overbrace{J, B_r, B_{sat}, \Delta_{P_{Fe}}, \gamma_{Fe}, f_{elec}, \mu_0}^{p}) \tag{3.15}$$

By applying the Buckingham-Pi theorem, the same dimensionless variables as obtained in Eq. 3.13 are found:

$$\Pi_{0_T}, \Pi_{0_{P_J}}, \Pi_{0_{P_{Fe}}} = f(\Pi_1, \Pi_2, \Pi_3, \Pi_4, \Pi_5, \Pi_6, \Pi_7) \tag{3.16}$$

where $\Pi_{0_{P_J}} = \frac{P_J}{L_m \gamma_{Fe} \rho_{Cu} J^2 D_e^2}$ and $\Pi_{0_{P_{Fe}}} = \frac{P_{Fe}}{L_m \Delta P_{Fe} \left(\frac{f_{elec}}{50}\right)^{1.5} B_r^2 D_e^2}$.

As can be seen by comparing the last column of Table 3.3 and Table 3.4, the transition to the dimensionless domain also reduces the range of the variables. Nevertheless,

Table 3.4: Dimensionless variables

Variable	Definition	Range	$\frac{\Pi_{max}}{\Pi_{min}}$
Π_1	$\frac{\mu_0 J D_e}{B_{sat}}$	$[0.62 - 4.42]$	7.12
Π_2	$\frac{D_i}{D_e}$	$[0.27 - 0.31]$	1.14
Π_3	$\frac{e_{tooth} N_s}{\pi D_e}$	$[0.15 - 0.30]$	2
Π_4	$\frac{e_{yoke} N_s}{\pi D_e}$	$[0.07 - 0.24]$	3.42
Π_5	$\frac{W_{PM}}{D_e}$	$[0.03 - 0.08]$	2.66
Π_6	$\frac{R_i}{D_e}$	$[0.11 - 0.17]$	1.54
Π_7	$\frac{B_{sat}}{B_r}$	$[1.99]$	1

if the number of inputs is high, the mathematical expression of the models may still be too complex and difficult to use in multidisciplinary optimization problems. In our case, among the six dimensionless ratios, five are purely geometric characteristics of the motor. During the phase of preliminary design, it is often convenient to vary the geometrical parameters of a component by conserving its geometrical similarity. This means that all the geometrical ratios are constant and the problem only depends on Π_1 (which express the magnetic saturation of the motor). In this way a very simple model can be obtained. However, when this is done, two problems arise. The first one concerns the value to be assigned to the geometrical ratios, which is normally dependent on the motor specifications. The second one deprives the designer of the possibility of having some meaningful aspect ratios as degrees of freedom during system design and optimization. Therefore, the model reduction methodology is applied here to:

- Highlight the dimensionless numbers representative of geometrical ratios which have the most impact on optimal designs. These Π_i numbers are considered as the inputs of the model.
- Find the numerical values for the rest of the Π_i numbers that can be assumed to be constant.

3.5.2 Sensitivity analysis for the selection of meaningful π numbers

The idea is to represent the model in terms of the only Π_i variables that represent significantly optimal designs in terms of torque density and take the interaction of the disciplines into account. For a given torque, a smaller motor has lower inertia but generates more heat, thus requiring a greater heat sink. Inversely, a larger motor generates less heat, so requiring a smaller heat sink, but it has greater inertia. For high acceleration applications (i.e. electrical propulsion systems of unmanned aerial vehicle [90]) or applications involving runaway scenarios (i.e. EMAs), the motor inertia is an important design driver to be taken into account. Once the interactions of the disciplines are defined, the idea is to define a set of optimizations by varying the physical quantities of the motor having a direct effect on couplings. More precisely the Π_i numbers representative of these coupling should be varied in a significant manner by acting on the dimensional quantities representable at motor level design. For these reasons, the optimization is done for motors specified in terms of:

1. Motor diameter: $D_e = [30 - 150]\, mm$, which is strictly linked to the motor torque and inertia.

2. Convective heat transfer coefficient: $h = [10 - 100]\, W/m^2K$, which represents the motor cooling capacity and consequently the level of losses that can be dissipated.

3. Motor speed: $\omega = [2100 - 8400]\, rpm$ which is strictly linked to the mechanical (choice of a reduction ratio) and thermal disciplines due to its dependence on the iron losses.

On the basis of these specifications, a 27 points DoE is generated. Each point of the DoE represents a specific motor configuration which has to be optimized in terms of torque density (to be maximized). In order to avoid solutions with magnetically saturated stator iron, a constraint on the maximal induction value on these surfaces is implemented ($1.8\, T$ on the yoke and tooth surfaces). Once the optimization has been carried out and the optimal Π_i found, the indicator of influence expressed in Eq. 3.11 is computed for each dimensionless number. A scatter matrix, as shown in Fig. 3.9, is adopted to graphically illustrate the variation of variables.
As expected from a physical point of view, the variable Π_1 embodying the current density and expressing the saturation shows the highest value of α. This is reasonable since the current density directly impacts the torque and the generated losses. On the other hand,

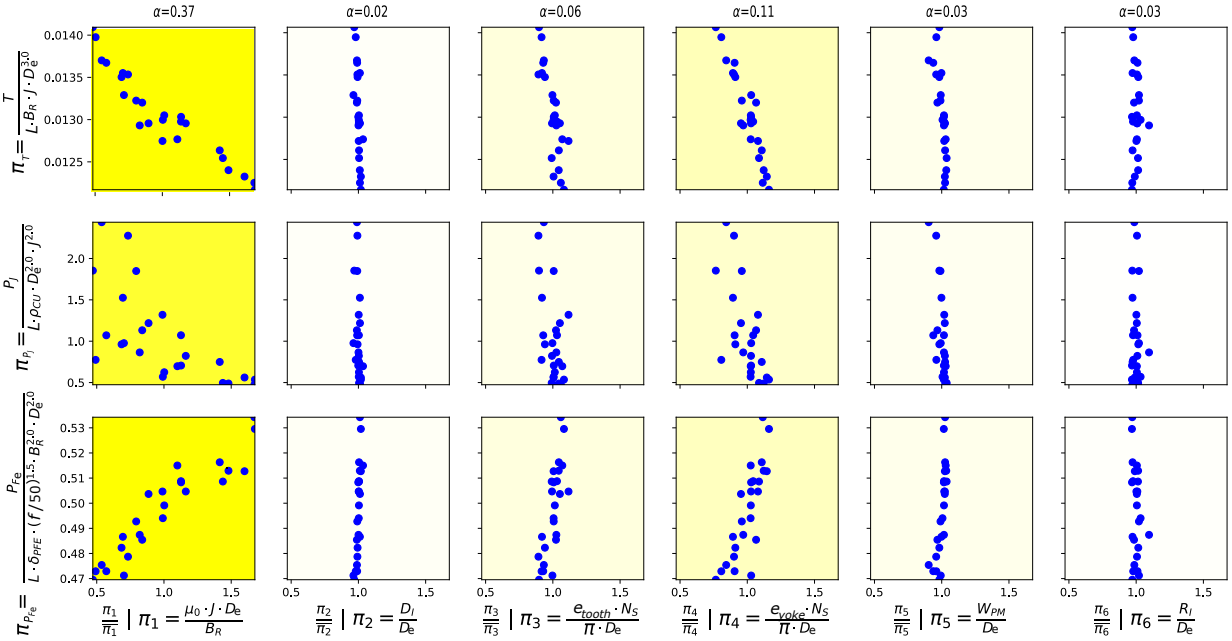

Figure 3.9: Results of sensitivity analysis.

Fig. 3.9 shows that the remaining dimensionless variables, representing the internal geometrical ratios of the motor, present a lower value of α. This means that these aspect ratios are roughly constant in a motor with optimal torque density. An exception is Π_4, incorporating the yoke thickness, which seems to have a certain degree of influence on the motor performance with a sensitivity indicator of 11%. This means that the yoke thickness does not conserve geometric similarity. This can be explained by the fact that for different motor velocities, the yoke thickness should be adapted in order to avoid its magnetic saturation, and consequently the rapid increment of the iron losses. From the results of this analysis (summarized in Table 3.5) it can be concluded that only two dimensionless variables, Π_1 and Π_4, are sufficient to describe the model. The remaining dimensionless numbers are constant, thus conserving geometrical similarity. In this way the number of inputs is reduced to the minimum and this enables the user to make the right compromises in the system level design.

The flowchart of Fig. 3.10 summarizes the different steps, methods and tools of the model reduction procedure applied to the case study described.

Table 3.5: Variables Π_1 and Π_4 selected for the surrogate model inputs and the value of the remaining dimensionless numbers that conserve geometrical similarity

Variable	Definition	Type	Value
Π_1	$\frac{\mu_0 J D_e}{B_{sat}}$	Design Variable	$[0.62 - 4.42]$
Π_2	$\frac{D_i}{D_e}$	Geometrical Similarity	0.29
Π_3	$\frac{e_{tooth}}{\frac{\pi D_e}{Ns}}$	Geometrical Similarity	0.27
Π_4	$\frac{e_{yoke}}{\frac{\pi D_e}{Ns}}$	Design Variable	$[0.1 - 0.21]$
Π_5	$\frac{W_{PM}}{D_e}$	Geometrical Similarity	0.07
Π_6	$\frac{R_i}{D_e}$	Geometrical Similarity	0.12

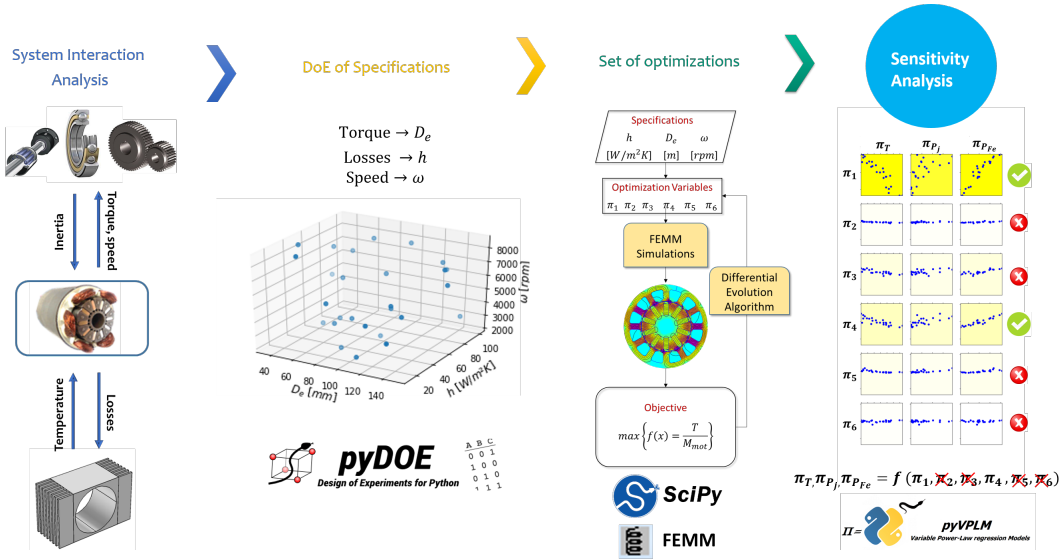

Figure 3.10: Model reduction process applied on the PM brushless motor model.

3.5.3 Model generation

Based on the results obtained with the sensitivity analysis, Eq. 3.16 can be simplified as follows:

$$\Pi_{0_T}, \Pi_{0_{P_J}}, \Pi_{0_{P_{Fe}}} = f(\Pi_1, \Pi_4) \tag{3.17}$$

Once the inputs of the model are defined, a DoE with 100 points generates the configurations to be simulated in FEMM. The number of configurations has to be chosen wisely in order to capture the magnetic saturation phenomenon, which is strongly non-linear. According to the results emerging from the sensitivity analysis, a variation range is defined for each variable (see Table 3.5). After the phase of data generation, the model selection phase is conducted. Starting from the results extracted from the simulations (outputs of

electromagnetic torque, Joule losses and iron losses), several surrogate models are built for each of the considered motor performance. The choice of an adequate model is a trade-off between precision and complexity of the model. The Python *pyVPLM* package assists the user by giving both the maximal and mean relative errors ($max|\varepsilon|$ and $\overline{\varepsilon}$ respectively), as well as the standard deviation (σ_ε), as a function of the number of terms employed in the model expression (Fitting set line in Fig. 3.11a) and the relative errors obtained by cross validation (Validation set line in Fig. 3.11a). Concerning the electromagnetic torque, for this application a model with five terms was chosen, which provides a $max|\varepsilon|$ around 5% and a $\overline{\varepsilon}$ close to 0%. Taking additional terms does not significantly decrease $max|\varepsilon|$.

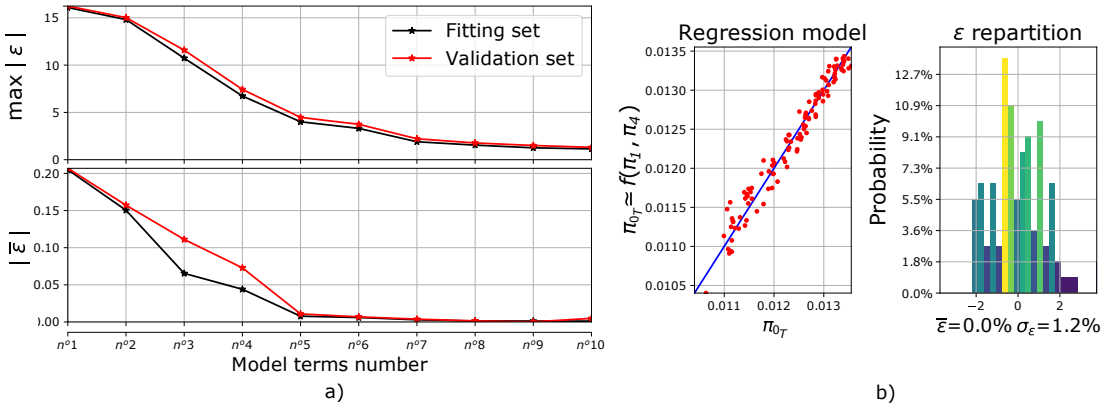

Figure 3.11: (a) Evolution of the error for the model of torque and b) comparison of VPLM model with FEMM model for the selected model with 5 terms.

The mathematical expression of the selected surrogate model of the torque is:

$$\Pi_{0_T} = \frac{T}{LB_rJD_e^3} = 10^{-2.55} \cdot \Pi_1^{-0.1\cdot(\log(\Pi_4))^2 - 0.14\cdot\log(\Pi_1)} \cdot \Pi_4^{0.45\cdot(\log(\Pi_4))^2 - 1.1} \tag{3.18}$$

Regarding the Joule losses, a model with 3 terms was selected (Fig. 3.12), which provides a $max|\varepsilon|$ and a $\overline{\varepsilon}$ close to 0%. The selected model provides the following expression:

$$\Pi_{0_{P_J}} = \frac{P_J}{L_m\rho_{Cu}J^2D_e^2} = 10^{-1.96} \cdot \Pi_1^{-0.07\cdot(\log(\Pi_4))^2} \cdot \Pi_4^{-0.08\cdot(\log(\Pi_4))^2} \tag{3.19}$$

Finally, for the iron losses a models with 5 terms has been selected (Fig. 3.13), characterised by a $max|\varepsilon|$ and a $\overline{\varepsilon}$ close to 0%. The mathematical expression of the model is:

$$\Pi_{0_{P_{Fe}}} = \frac{P_{Fe}}{L_m\Delta P_{Fe}\left(\frac{f_{elec}}{50}\right)^{1.5}B_r^2D_e^2} = 10^{-1.35} \cdot \Pi_1^{0.11+0.15\cdot\log(\Pi_1)} \cdot \Pi_4^{-1.67+0.62\cdot(\log(\Pi_4))^2} \tag{3.20}$$

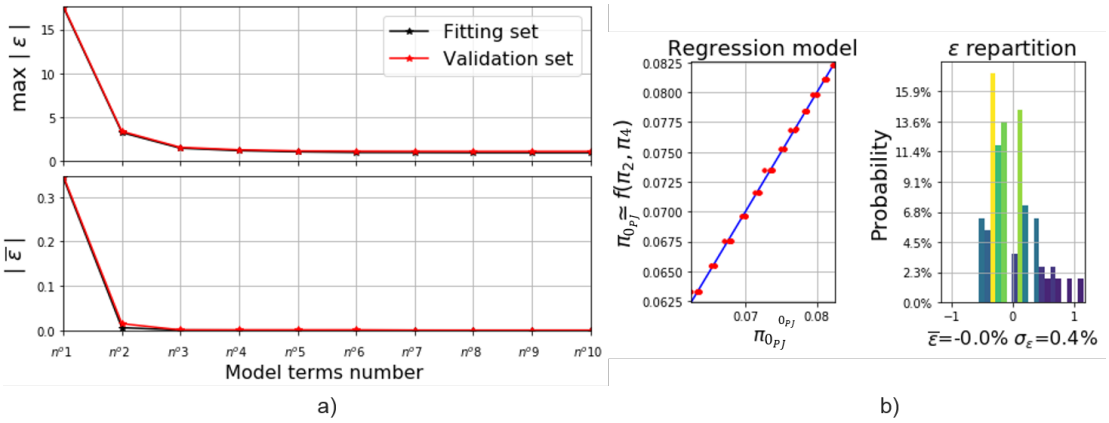

Figure 3.12: (a) Evolution of the error for the model of Joule losses and b) comparison of VPLM model with FEMM model for the selected model with 3 terms.

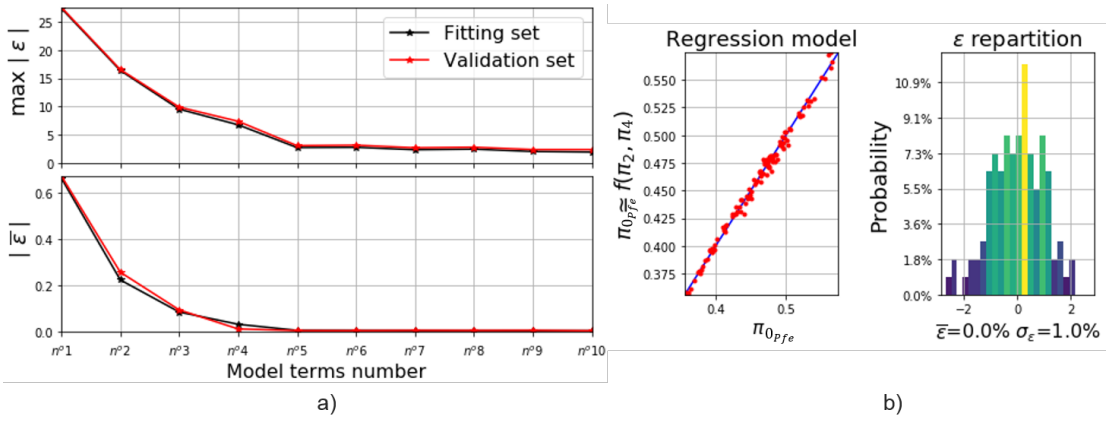

Figure 3.13: (a) Evolution of the error for the model of iron losses and b) comparison of VPLM model with FEMM model for the selected model with 5 terms.

3.6 Conclusion

To sum up, the problem is to represent functions of type $y = f(x_i)$ with light reusable surrogate models, as they are usually represented by high fidelity but costly models. The degree of complexity and the "weight" of a model are generally described, as shown in Fig.3.14, by two main factors: the number of variables N_b employed to define the model and the validity range of variables X^*, which is expressed by the ratio between their maximum value X_{max} and their minimum value X_{min}.

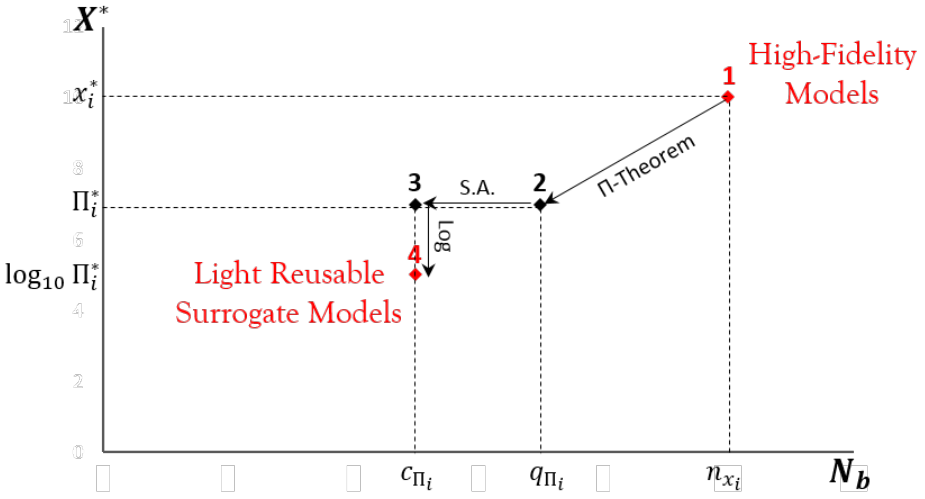

Figure 3.14: Variables representation space.

The transformation of the problem into the dimensionless domain, through the Buckingham theorem, involves a first reduction of the number of variables and their range of variation. The sensitivity analysis based on optimization allows to select the dimensionless variables that have the most influence on optimal designs of the component under consideration. This involves a further reduction of the model while guaranteeing a wide range of validity of application, as the optimization is performed for a large range of component specifications. This enables the reuse and thus capitalization, of models, a feature that distinguishes the VPLM surrogate models from surrogate models built with other approaches. Furthermore, it also simplifies the task of system engineers who can focus only on the variables of the components allowing the best compromises to be found at system level design. The definition of the model in logarithmic domains (characteristic of the VPLM methodology) allows an additional reduction of the range of variables and thus enforces additional lightness of the model. The proposed method has been illustrated by

the construction of three surrogate models describing the performances of a PM brushless motor. This method reveals that the ratio between the yoke thickness and outer motor diameter can provide a meaningful degree of freedom at system level design. Other surrogate models have been used in this thesis, for modelling some components characteristics such as: the vibration resistance of the fins of the thermal housing, the contact surface area of the thermal interface material and the motor thermal resistance. The following section of this manuscript will show how to use such models for the preliminary design of primary flight control EMAs.

Chapter 4

Primary Flight Control Actuation System Design Based on Static Approach

Contents

4.1 Introduction **74**

4.2 Overview of the design problem and description of the sizing procedure . . **74**

4.3 Definition of specifications for the established EMA architecture **76**

4.3.1 Definition of architectures 76

4.3.2 Design Drivers 79

4.3.3 Sizing scenarios 81

4.3.4 Mission profile analysis and extrapolation of design specifications . 82

4.4 Generation of component and system models **87**

4.4.1 Sizing scenario models 88

4.4.2 Component models 91

4.5 Definition of the sizing procedure **106**

4.6 Design and optimization **108**

4.6.1 Computation, capitalization and model construction times 113

4.7 Conclusion **114**

4.1 Introduction

In the previous chapters, two types of approaches, static and dynamic, for conducting the actuator preliminary design, were introduced, as well as the generation of the surrogate models necessary during this phase. In this chapter, the preliminary designs of electro-mechanical actuators for primary flight control applications (Aileron, Elevator, Rudder) are provided. A static approach is adopted and the surrogate models of the motor described previously are used. The first part of the chapter deals with setting up the specifications for the defined EMA architecture. Two different architectures are investigated: a gear drive and a direct drive system. The design is conducted by considering laboratory conditions, with cooling by natural convection only. Based on the mission profile of an Airbus A320 flight with a duration of 112 minutes, the static design specifications are extrapolated. Subsequently, the system and component models are generated and integrated into the sizing problem. In this case study, a thermal housing with fins is used as thermal management system. Its estimation model is therefore introduced. The preliminary design is performed via an optimisation procedure with a view focused on the mass minimisation and emphasis on thermal constraints satisfaction. The results emerging from the preliminary design are so analysed at the end of the chapter.

4.2 Overview of the design problem and description of the sizing procedure

Preliminary design of primary flight control actuators requires a specific approach. Indeed, these specific mechatronic systems are characterized by a strong coupling between the domains of their components while having to satisfy design constraints such as system requirements or component technological limits. The typical problems encountered while designing mechatronic systems can be summarized as follows [91]:

1. Conformity: Verify that the sizing problem considers all functions and requirements of the system in all its modes of operation.
2. Generate/Reuse knowledge: Enabling the implementation of knowledge in a reusable way.

3. Adapt knowledge: Adapt easily the implemented knowledge to specific design steps and needs.

4. Coordinate knowledge: Give the possibility to use component level knowledge at system level and vice versa.

5. Use different models: Easily integrate different types of models from different simulation environments.

6. Solve the sizing problem: Numerically solve the sizing problem by checking and correcting its solvability.

7. Optimize the design: Finding the optimal system design rapidly.

The preliminary design procedure proposed here aims to satisfy in an effectively way these design problems, through the implementation of four design steps, summarized in the Fig 4.1.
Firstly, the system specifications for the considered EMA architecture are defined. This involves individuating the component design drivers, sizing scenarios and system requirements extracted from mission profile analysis.
The second step consists in building system level models and component models. The former, based on analytical relationships, represent the link between sizing scenarios and components characteristics. The latter enable the estimation of the sizing characteristics of each component by means of analytical relationships, scaling laws, linear regressions or surrogate models.
The third step of the procedure aims to define the sizing procedure by representing the connections between the different system and component models and to graphically illustrate the design problem with a N^2 diagram representation.
The last step consists in solving the preliminary design problem via an optimization procedure implemented in a dedicated sizing framework.

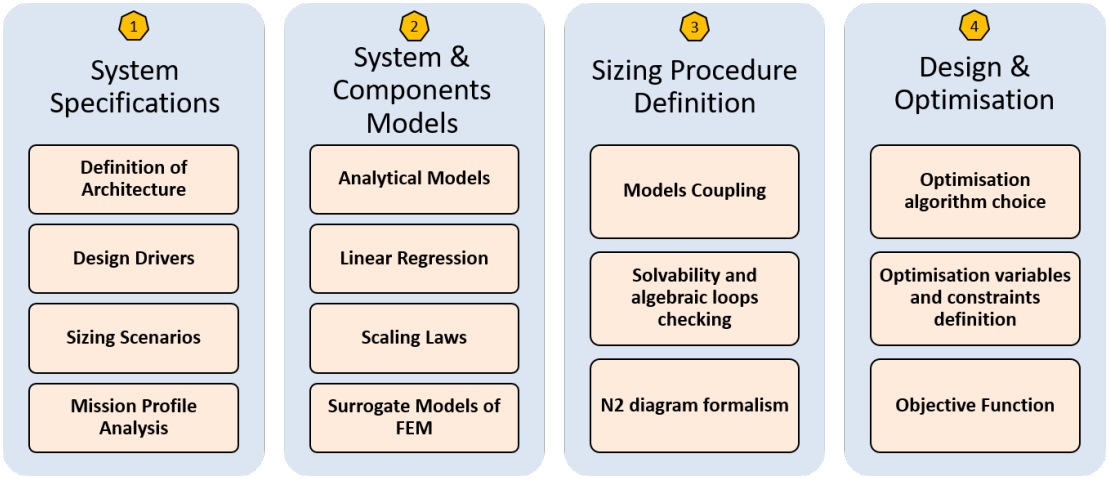

Figure 4.1: Methodologies and methods adopted for the preliminary design.

4.3 Definition of specifications for the established EMA architecture

4.3.1 Definition of architectures

The case study considered in this chapter relates to EMAs used for primary flight control applications. Two different architectures are investigated to this purpose, as shown in Fig. 4.3: a gear drive and a direct drive system. Both EMAs are linear, which means the rotational motion of the electric motor is transformed into linear motion by a mechanical assembly. The electro-mechanical chain is composed of (Fig. 4.2): a (PM) motor, a gearbox (in the case of gear drive), a screw-nut, a bearing and a thermal housing with two plate-fin heat sinks mounted sideways.

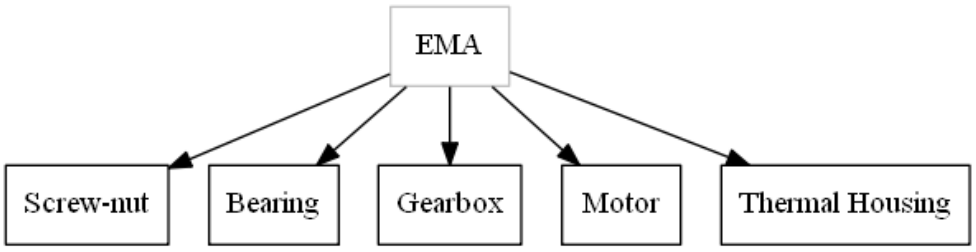

Figure 4.2: Actuator components considered for the case study.

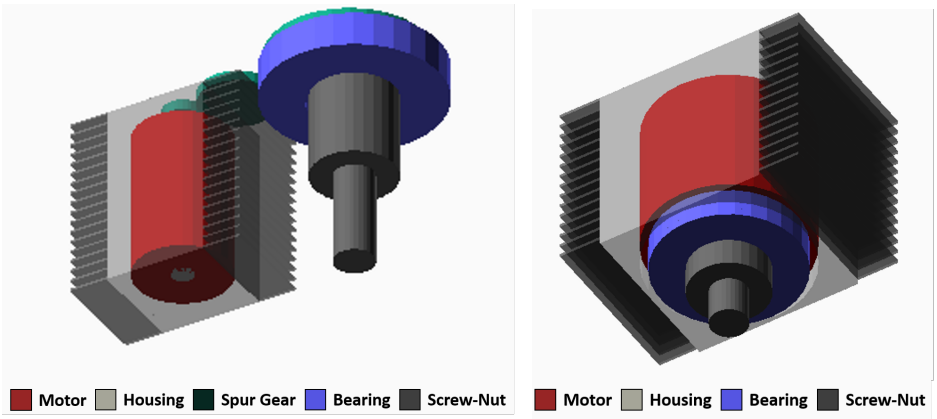

(a) Gear drive (b) Direct drive

Figure 4.3: Considered EMA architectures for the case study.

A PM motor is chosen for this application. All the advantages above the other motor types have been outlined in Chapter 2. The PM brushless motor (Fig. 4.4a) presented in Chapter 3 is taken as reference.

The main purpose of the gearbox is to reduce rotational speed while increasing torque in a mechanical system. Due to its simplicity and suitability, a low ratio spur gear with idler is used (Fig. 4.4b). The use of the idler is necessary to reduce the size of the input/output gears, in order to fit within the allocated space for the actuator, whilst maintaining the spacing of the shafts.

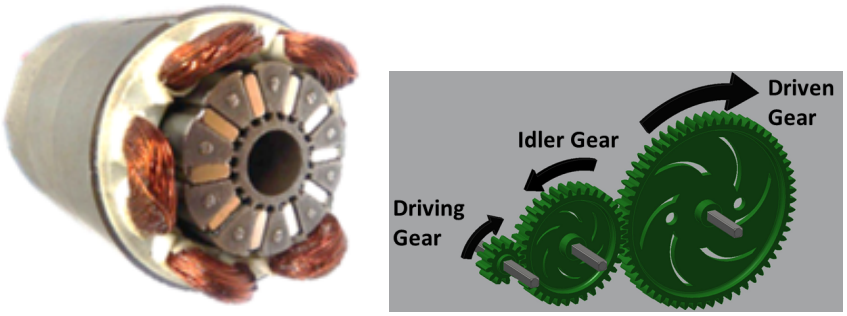

(a) PM brushless motor [89]. (b) Spur gear with idler [92].

Figure 4.4: Electric Motor and gearbox types considered for this study.

The screw nut mechanism is used to convert the rotatory motion of the motor to linear motion with a required force. By connecting the servo motor and external load, torque and speed are matched by the transitional mechanism. A planetary roller screw mechanism is used for this study. For a given load, it is made with a lower lead compared to ball screw

mechanism and its load capacity is higher.
A thrust bearing is a particular type of rotary bearing. Like other rotary bearings it allows rotation between parts, but it is mainly designed to support a high axial load. Different kinds of thrust bearings are used to support different amount of axial loads. A single four-point contact ball bearing is selected for this study. This makes it easy to simplify machine designs that have a combination of radial, thrust and moment loads because it can handle all three simultaneously, while providing some very important benefits in terms of space saving, weight, cost, installation, maintenance and so on.

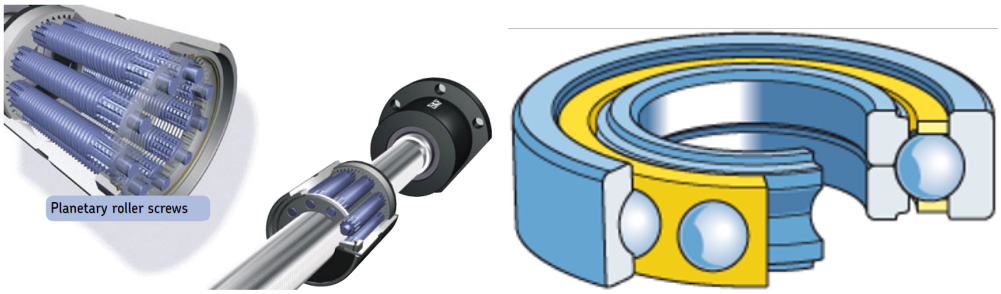

(a) Planetary roller screw [93]. (b) Four point contact bearing [93].

Figure 4.5: Screw nut and thrust bearing considered for this study.

The thermal housing is an aluminium body mounted around the motor surface which allows to dissipate the heat generated by the motor losses. The housing adopted here presents two finned plates heat sinks mounted on its sides useful to improve the heat dissipation with natural convection.

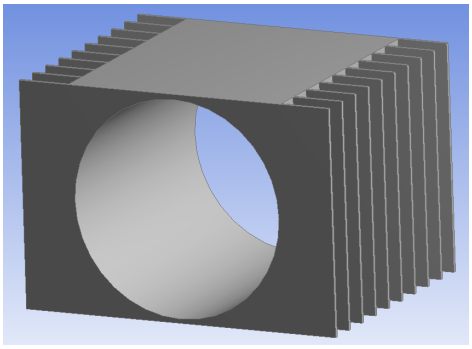

Figure 4.6: Thermal housing with fins.

4.3.2 Design Drivers

This part outlines the design drivers of actuator components, summarised in Fig. 4.7. It mixes selection parameters and technological limits of components that have to be considered to perform the preliminary design of the actuator. During the proposed design, emphasis is placed on thermal performances and system weight minimization.
Concerning the electric motor, the main design drivers are its nominal and maximum electromagnetic torque, as well as its maximal and average speed. The torque is either limited by the magnetic saturation of the iron core or by the maximum winding temperature. To determine the motor temperature, Joule losses and iron losses have to be evaluated. In addition, the equivalent conduction thermal resistance between the winding hot spot temperature and the external stator has to be determined. The motor inertia is also an important design driver, since it affects the runaway scenario and the reflected inertia (as explained in the next section).
With regard to mechanical components (bearing and screw-nut), the maximum and fatigue efforts are as well design drivers as they determine their sizes. In addition, as the reducer accounts for the shock of a runaway and for the reflected inertia, its reduction ratio is also a design driver for primary flight control actuators.
The thermal housing design drivers are its thermal and mechanical behaviour. The thermal behaviour of the device is represented by its thermal resistance. This is dependent on the temperature difference between the external environment and the housing skin, and on the losses it must dissipate. The device is designed considering laboratory conditions (20 $°C$, sea level), with cooling by natural convection only (referring to Fig. 4.3, with longitudinal direction to the fins). The mechanical behavior is represented by the vibration resistance of the fins. This is the design driver to take into account, since influence the size of fins and the heat dissipation capability of the thermal housing as a consequence.

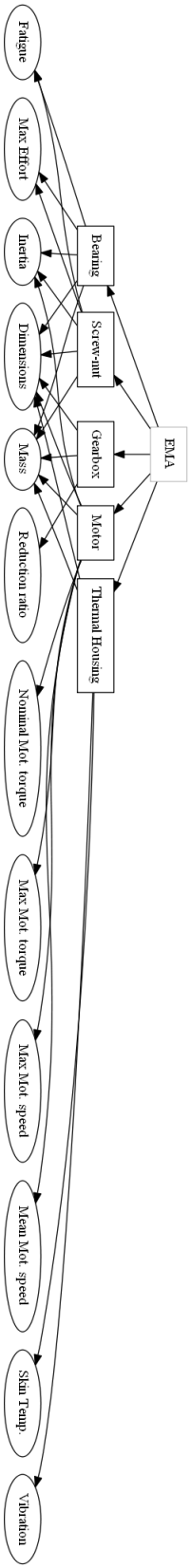

Figure 4.7: Component design drivers.

4.3.3 Sizing scenarios

The main scenario to which the actuator have to respond is the mission profile. Its analysis enables to determine the actuator load, intended as the operating torque and speed requirements for the brushless motor, as well as the equivalent fatigue and maximum effort for the mechanical components. This torque, effort and speed requirements enable to select the size of these components. However, the actuator has also to respond to other scenarios which will impact the sizing of its components. These additional sizing scenarios are listed here below:

- The maximum motor housing and winding temperatures. The hot spot winding temperature is a function of its thermal conduction resistance, the generated losses and the thermal housing temperature. The losses considered are Joule losses in the copper and the iron losses. The maximal temperature of the thermal housing is another constraint often imposed by the aircraft manufacturer, usually fixed at $100° C$.
- The reflected inertia. This is a function of the inertia of the EMA components and the reduction ratio (for gear drive). Taking this scenario into account is very important for the aerodynamic stability of the control surface (risk of flutter).
- The runaway scenario and arrival on end-stops. Runaway generates a higher load than a wind gust. Hence, only the load generated by a runaway is determined and used in the sizing. The runaway scenario is a function of inertia, stiffness, motor speed and torque.
- The vibratory scenario, which provides inputs for the vibratory analysis of the thermal housing.
- The geometric integration. It estimates the size of the overall actuator and verifies that it fits in the space given for a single actuator. Therefore, for the selected architecture, emphasis is placed on system compactness and simplicity.
- The system total mass, which is dependent on the mass of the thermal housing, the screw-nut, the reducer (for gear drive), the bearing and the motor.

In order to to check that all design features or drivers are covered by those scenarios, a verification matrix can be implemented, as illustrated in the Table below:

Table 4.1: Verification matrix.

Checking points		Sizing scenarios						
Type	Description	Mission profile	Components temperatures	Reflected inertia	Runaway	Vibratory scenario	Geometric integration	System mass
Function	No Flutter for aircraft stability			⊗				
Design driver	Max. Elec.magn. torque	⊗			⊗			
	Nominal Elec.magn. torque	⊗	⊗					
	Max motor speed	⊗			⊗			
	Mean motor speed	⊗	⊗					
	Max. mechanical effort	⊗						
	Fatigue effort	⊗						
	Reduction ratio			⊗	⊗			
	Housing temperature		⊗					
	Fins vibration		⊗			⊗		
	Components dimensions			⊗			⊗	⊗

4.3.4 Mission profile analysis and extrapolation of design specifications

This section shows how it is possible to define the actuator sizing specifications, from the mission profile analysis. These specifications, defined here at the level of the control surface, relate to the definition of the thermal specifications to design the electric motor and cooling device, and the mechanical specifications for designing the screw-nut and thrust bearing. The mission profiles analysed here are represented by the surface deflection order $\vartheta^*(t)$ and the aerodynamic torque $T_{aero}(t)$. The mission profile of the Aileron (normalised) is depicted in Fig. 4.8, while those of Elevator and Rudder are illustrated in **ANNEX B**. It must be taken into account, that these data are generated by a flight simulator with

autopilot. $\vartheta^*(t)$ is therefore the set-point received by the actuator and does not take into account the actuator own dynamics.

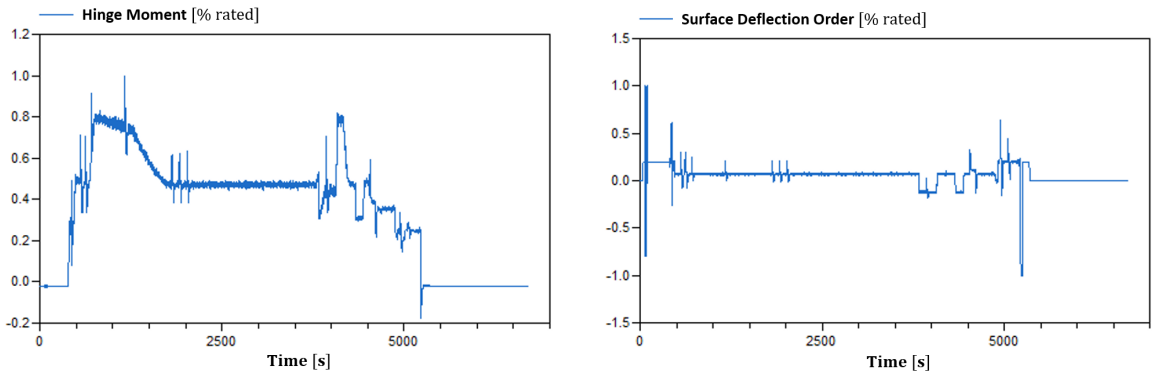

(a) Aerodynamic Torque (b) Surface deflection order

Figure 4.8: Mission profiles of an aileron surface of an Airbus A320 (NORMALISED DATA).

The position ϑ can be deduced from the time response of the actuator, which is assumed to follow the dynamics of a second-order system:

$$\vartheta^* = \vartheta + \frac{2\zeta}{\omega_0}\dot{\vartheta} + \frac{\ddot{\vartheta}}{\omega_0} \tag{4.1}$$

where ω_0 is the desired bandwidth of 2 Hz and ζ is the damping coefficient equal to 0.7071. By solving the differential equation, the position, speed and acceleration profiles are so obtained (Fig. 4.9). Once the different profiles are available, the design specifications of the actuator can be extrapolated. Concerning the thermal specifications, the root mean square and the maximum values of the aerodynamic load must be evaluated, as well as the average and maximum values of the mechanical speed. The torque the actuator must provide to move the control surface, is delivered by the electric motor through the generation of an electromagnetic torque. This is proportional to the square of the current intensity and therefore it is linked to the Joule losses, which represent the main source of heat generation. The RMS value of the load $T_{aero_{RMS}}$, expressed in Eq. 4.2, defines the equivalent continuous torque of the motor, which represents how much torque the motor can generate over an indefinite period of time without exceeding the thermal operating limits.

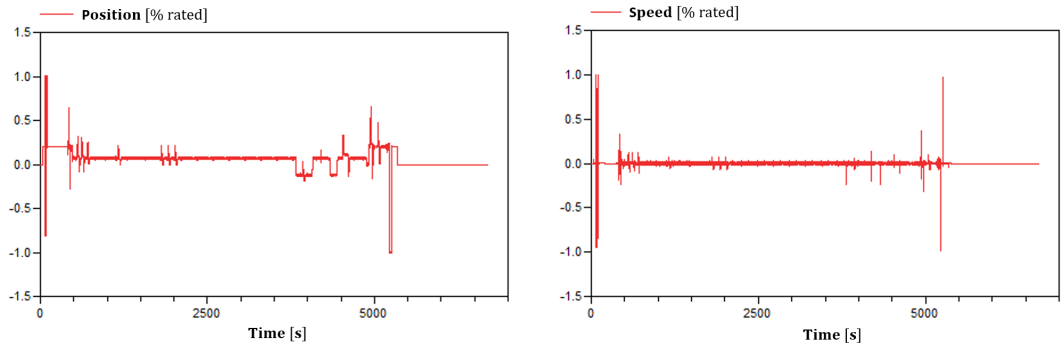

(a) Position (b) Speed

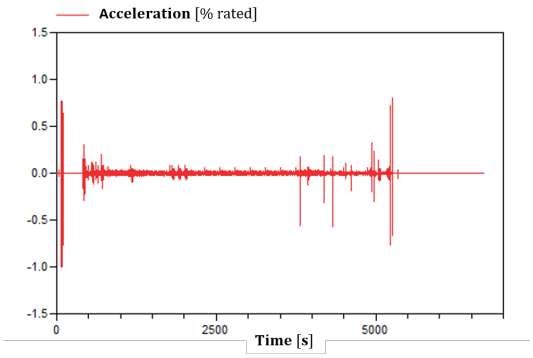

(c) Acceleration

Figure 4.9: Extracted mission profiles (NORMALISED DATA).

The maximum value of the load $T_{aero_{max}}$, expressed in Eq. 4.3, defines the peak torque of the motor, which is the maximum torque it can generate for a short period of time, typically few tens of seconds, without incurring in winding degradation.

$$T_{aero_{RMS}} = \sqrt{\frac{1}{T}\int_0^T T_{aero}^2(t)\,dt} \tag{4.2}$$

$$T_{aero_{max}} = \max\left(T_{aero}(t)\right) \tag{4.3}$$

The average $\overline{\dot{\vartheta}}$ and maximum $\dot{\vartheta}_{max}$ mechanical speeds required by the mission profile are important from a thermal point of view because they define the iron losses of the motor.

$$\overline{\dot{\vartheta}} = \left(\frac{1}{T}\sum_{i=0}^{T}|\dot{\vartheta}_i|^{1.5}\right)^{1/1.5} \tag{4.4}$$

$$\dot{\vartheta}_{max} = \max(\dot{\vartheta}(t)) \tag{4.5}$$

The factor 1.5 is used since it is the exponent used for the electric pulsation, which is proportional to the speed, when estimating the motor iron losses using the Steinmetz model [94].
Concerning the mechanical specifications, the equivalent rolling fatigue must be evaluated. The duration life of a rolling component is expressed by means of the following relationship:

$$Cd^3 \cdot L_{10} = K \tag{4.6}$$

which indicates that the product between the dynamic load to the third (Cd^3) and the lduration ife of component (L_{10}) is constant (K). Starting from this relationship, the cumulated damage can be described as follows:

$$|T_{fat}^3| \cdot N_{eq} = \sum_{i=0}^{T} |T_i^3| \cdot N_i = K \tag{4.7}$$

where T_{fat} is the equivalent fatigue load, N_{eq} is the equivalent number of revolutions, T_i and N_i are respectively the applied load and the number of revolutions at the time t_i. Considering the number of revolutions proportional to the speed, we could rewrite the previous equation in the form of:

$$T_{fat} = \left(\frac{1}{\int_0^T |\dot{\vartheta}(t)| dt} \cdot \int_0^T |T^3(t)| \cdot |\dot{\vartheta}(t)| dt \right)^{1/3} \tag{4.8}$$

It could be very interesting to identify the stroke range for fatigue, represented in Fig. 4.10, to specify the oscillatory magnitude δ in order to be more conservative. This diagram can be been constructed by repartitioning the damage per stroke interval. To have the right oscillatory cycles number n_{osc} for the specified equipment lifetime L_f, the following formula is adopted:

$$n_{osc} = L_f \cdot f_o = n_{flight} \cdot t_{flight} \cdot \frac{\bar{\dot{\vartheta}}}{2 \cdot \delta} \tag{4.9}$$

where n_{flight} is the number of flights, t_{flight} the flight duration and f_o the frequency oscillatory movement given by the ratio between the average deflection speed $\bar{\dot{\vartheta}}$ and the fatigue magnitude δ. This last calculation concludes the extrapolation of the specifications from the mission profile. The specifications extracted for the primary control surfaces analysed here are given in Tables 4.2 - 4.4. For reasons of confidentiality these have been normalised in relation to the Aileron specifications.

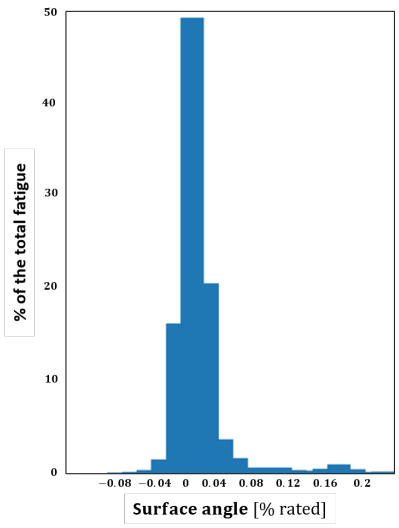

Figure 4.10: Fatigue distribution.

Table 4.2: Analysis of mission profile specifications of Aileron (normalised data).

Parameter	Value	Definition
$T_{aero_{RMS}}/(T_{aero_{max}})_{Aileron}$	0.43	RMS aerodynamic torque
$T_{aero_{max}}/(T_{aero_{max}})_{Aileron}$	1	Maximum aerodynamic torque
$T_{fat}/(T_{aero_{max}})_{Aileron}$	0.49	Rolling fatigue equivalent torque
$\bar{\dot{\vartheta}}/(\dot{\vartheta}_{max})_{Aileron}$	0.138	Average speed
$\dot{\vartheta}_{max}/(\dot{\vartheta}_{max})_{Aileron}$	1	Maximum speed
$\delta/(\delta)_{Aileron}$	1	Magnitude of the oscillatory movement
$n_{osc}/(n_{osc})_{Aileron}$	1	Oscillatory cycles number

Table 4.3: Analysis of mission profile specifications of Elevator (data normalised to Aileron specifications).

Parameter	Value	Definition
$T_{aero_{RMS}}/(T_{aero_{max}})_{Aileron}$	0.08	Root mean square aerodynamic torque
$T_{aero_{max}}/(T_{aero_{max}})_{Aileron}$	0.52	Maximum aerodynamic torque
$T_{fat}/(T_{aero_{max}})_{Aileron}$	0.15	Rolling fatigue equivalent torque
$\bar{\dot{\vartheta}}/(\dot{\vartheta}_{max})_{Aileron}$	0.0058	Average speed
$\dot{\vartheta}_{max}/(\dot{\vartheta}_{max})_{Aileron}$	0.97	Maximum speed
$\delta/(\delta)_{Aileron}$	6	Magnitude of the oscillatory movement
$n_{osc}/(n_{osc})_{Aileron}$	0.02	Oscillatory cycles number

Table 4.4: Analysis of mission profile specifications of Rudder (data normalised to Aileron specifications).

Parameter	Value	Unit
$T_{aero_{RMS}}/(T_{aero_{max}})_{Aileron}$	0.03	Root mean square aerodynamic torque
$T_{aero_{max}}/(T_{aero_{max}})_{Aileron}$	0.72	Maximum aerodynamic torque
$T_{fat}/(T_{aero_{max}})_{Aileron}$	0.09	Rolling fatigue equivalent torque
$\bar{\dot{\vartheta}}/(\dot{\vartheta}_{max})_{Aileron}$	0.01	Average speed
$\dot{\vartheta}_{max}/(\dot{\vartheta}_{max})_{Aileron}$	0.78	Maximum speed
$\delta/(\delta)_{Aileron}$	1.5	Magnitude of the oscillatory movement
$n_{osc}/(n_{osc})_{Aileron}$	0.24	Oscillatory cycles number

4.4 Generation of component and system models

The preliminary design problem of the electro-mechanical actuator consists in determining the dimensions and characteristics of the different components, belonging to different engineering domains, according to the specifications required by the system. The challenge then lies in enabling the heterogeneous disciplines to be assembled and computed in a computationally efficient manner. The design of such multi-domain systems can be decomposed into two different layers [95], that are supported by respective model types and analysis tools, as illustrated in Fig. 4.11. These modelling layers are represented by:

1. A System layer, to take into account the functional and physical coupling between components. This level of modeling is usually done using zero-dimensional and one-dimensional models generally represented by algebraic equations, ordinary differential equations (ODE) or differential algebraic equations (DAE). During the preliminary design, these models generally represent the sizing scenarios.

2. A component layer, to describe the performance limits and parameters necessary in the previous layer, according to the component dimensions. The specific domain phenomena are generally represented through partial differential equations (PDE). This level of modelling can be achieved, for simplified geometries by using analytical models based on analytical relationships, scaling laws or linear regressions, or, for complex two-dimensional and three-dimensional geometries by using numerical approximations, such as the finite element method (FEM).

To this purpose, analytical relationships are used for rapidly modelling the sizing scenarios, whereas estimation models based on surrogate models, scaling laws, linear regressions on datasheet catalogue and analytical relationships are employed to estimate the characteristics of the actuator components. The models of the foregoing components, and how they can be used according to the design case study, are shown in the following sections.

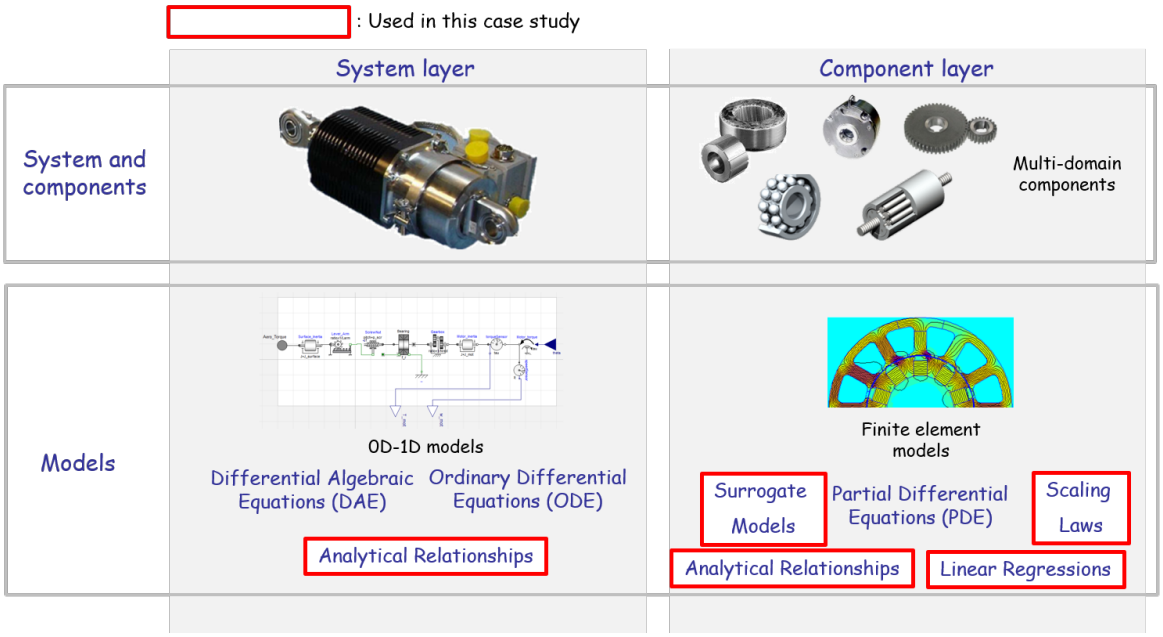

Figure 4.11: System layer and component layer modelling (adapted from [95].

4.4.1 Sizing scenario models

4.4.1.1 Actuator Load

The first scenario outlined was the actuator load. The mission profile analysis has enabled the computation of the actuator specifications at the level of the control surface. To define the actuator load, these specifications are therefore represented at actuator level, in order to define the torque requirements for the electric motor, as well as the efforts for the mechanical components.

The RMS T_{EMA} and maximum torque $T_{EMA_{max}}$ required from the motor are expressed as follows:

$$T_{EMA} = k_{s_{mot}} \frac{T_{aero_{RMS}} p_{sn}}{L_{arm} n_{red} \eta_{red} 2\pi} \tag{4.10}$$

$$T_{EMA_{max}} = k_{s_{mot}} \frac{T_{aero_{max}} p_{sn}}{L_{arm} n_{red} \eta_{red} 2\pi} \tag{4.11}$$

where L_{arm} is the lever arm of the actuator, p_{sn} the screw lead, while n_{red} and η_{red} represent respectively the reduction ratio and the gearbox efficiency. A security factor $k_{s_{mot}} = 1.3$ is considered. This coefficient allows to take into account certain unexpected events which are not considered in the mission profile, and it can be defined according to the reliability desired. In the context of numerical applications it is normally taken at 1.3 [96].
Concerning the mechanical components, as the screw-nut and the bearing, the mechanical rolling fatigue load F_{fat} and the mechanical maximal effort can be calculated as follow:

$$F_{fat} = k_{s_{mecha}} \frac{T_{fat}}{L_{arm}} \tag{4.12}$$

$$F_{max} = k_{s_{mecha}} \frac{T_{aero_{max}}}{L_{arm}} \tag{4.13}$$

where $k_{s_{mecha}}$ is the security factor assumed also in this case equal to 1.3.

4.4.1.2 Reflected Inertia

The EMA shall not exceed a maximum reflected inertia. This requirement strongly impacts the sizing of the motor and the mechanical components as it depends on their inertia, as well as the reduction ratio. The reflected inertia J_{ref} at control surface level is expressed as follows:

$$J_{ref} = \Big(\frac{J_{mot} n_{red}^2 + J_{red} + J_{sn} + J_b}{(\frac{p_{sn}}{2\pi})^2} \Big) {L_{arm}}^2 \tag{4.14}$$

where J_{mot} is the motor inertia, n_{red} is the reduction ratio, J_{sn} is the inertia of the screw-nut, J_b is the inertia of bearing and J_{red} the inertia of the gearbox. In this case study, the reflected inertia must respect a maximum limit fixed at $30\, kgm^2$.

4.4.1.3 Runaway

As mentioned previously, the runaway sizing scenario strongly impacts the electro-mechanical power chain design. It consists of the maximal torque capability of the EMA and the inertial torque due to the kinetic energy stored in the motor and mechanical components inertia, at maximum motor speed. This is transformed into elastic energy in an equivalent torsional stiffness when impacting end stops. This can be expressed, by equating kinetic energy and elastic energy, by means of the following equations:

$$F_{shock} = \sqrt{k_T J_{eq} \omega_{mot_{max}}^2} + \frac{T_{EMA_{max}} n_{red} \eta_{red}}{\frac{p_{sn}}{2\pi}} \tag{4.15}$$

where F_{shock} is the shock effort, $k_T = 10^7 Nm/rad$ is the torsional stiffness, J_{eq} represents the total components inertia at motor level and $\omega_{mot_{max}}$ is the maximum motor speed.

4.4.1.4 Geometric Integration

The geometric integration scenario verifies that the actuator must fit in the allocated volume delimited by its length L_e, width W_e and heigth H_e . The integration of the EMA in the operating volume environment is illustrated in Fig. 4.12.

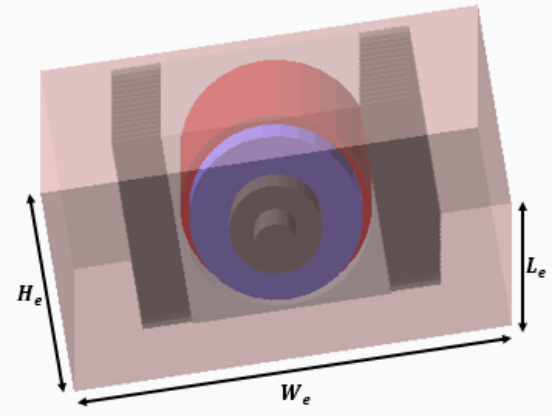

Figure 4.12: Aileron EMA integration.

4.4.1.5 System Mass

The mass of the system is obtained by adding up the masses of each component as follows:

$$M_{EMA} = M_{mot} + M_{sn} + M_b + M_{red} + M_{hous} \tag{4.16}$$

where M_{mot} is the motor mass, M_{sn} is the screw-nut mass, M_b represents the mass of the bearing, M_{red} is the mass of the gearbox and M_{hous} is the mass of the thermal housing.

4.4.2 Component models

4.4.2.1 Estimation model of Screw-Nut

The estimation models used for estimating the mass, dimensions and supported load of the screw-nut are based on the scaling laws. They are very useful to calculate the component characteristics without requiring a detailed design. They are based essentially on two key modelling assumptions [81]:

1. All material properties are assumed to be identical to those of the component used for reference: $E^* = \rho^* = \cdots = 1$.
2. The ratio of all the lenghts of the considered component to all the lenghts of the reference component is constant (geometric similarity): $D^* = T^* = \cdots = d^*$,
   where the generic quantity $x^* = \frac{x}{x_{ref}}$ is the ratio between the quantity under study x and the quantity taken as a reference x_{ref}.

In general, the main parameters of selection are both the static load $C_{0_{sn}}$ and the dynamic load $C_{d_{sn}}$. Taking the same stress limit σ [97] for a full product range yields:

$$\sigma^* = 1 \tag{4.17}$$

On the base of this consideration, a relation can be defined between $C_{0_{sn}}$ and the screw-nut geometry represented by a characteristic dimension d_{sn} [81]:

$$d^*_{sn} = C^{*1/2}_{0_{sn}} \tag{4.18}$$

So, starting from this relationship the others characteristic parameters can be defined:

$$C^*_{d_{sn}} = C^{*\frac{1.8}{2}}_{0_{sn}} \tag{4.19}$$

$$M^*_n = C^{*3/2}_{0_{sn}} \tag{4.20}$$

$$m^*_s = C^*_{0_{sn}} \tag{4.21}$$

where M_n represents the mass of nut, while the variable m_s is the linear mass of screw. In this context, the standard planetary roller screw "**SRC 25x5**" produced by SKF, depicted in Figure 4.13, is taken as reference.

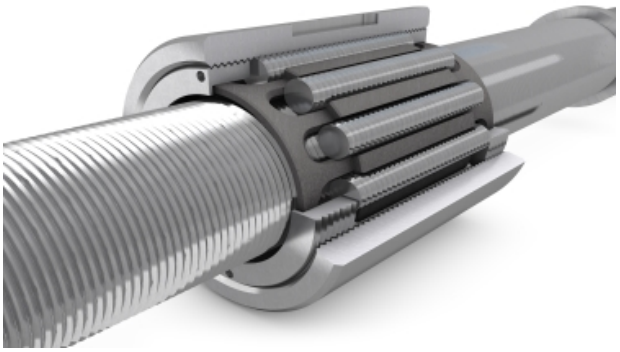

Figure 4.13: Screw nut model reference:"SRC 25x5" [93]

Table 4.5: Component reference for screw-nut (SRC 25x5) [93].

Parameter	Value	Unit	Definition
$C_{0_{sn_{ref}}}$	108.23	$[kN]$	Static Load
$C_{d_{sn_{ref}}}$	63.25	$[kN]$	Dynamic Load
$D_{n_{ref}}$	53	$[mm]$	Nut Diameter
$d_{s_{ref}}$	25	$[mm]$	Screw Diameter
$A_{n_{ref}}$	78	$[mm]$	Nut Length
$M_{n_{ref}}$	0.7	$[kg]$	Nut Mass
$m_{s_{ref}}$	3.9	$[kg/m]$	Screw linear Mass
p_{sn}	5	$[mm]$	Lead
n_r	10	$[-]$	Rollers number

Screw-Nut design

In this context, the static load is taken as definition parameter, while the dynamic load is considered as an operation limit linked to the duration life and reliability. The static load $C_{0_{sn}}$ can be defined as a function of the mechanical maximum load it has to support:

$$C_{0_{sn}} = k_{sn} F_{max} \tag{4.22}$$

where k_{sn} is a sizing coefficient defined during the phase of preliminary design. Once the static load has been computed, the dimensions (nut diameter D_n, screw diameter d_s, and nut length A_n), the mass of the nut M_n, the linear mass of the screw m_s and the dynamic load $C_{d_{sn}}$ are determined through the previously defined scaling laws. The resulting designed device must ensure the fatigue requirement $C_{d_{sn_{req}}}$, which is defined according to the following relationship:

$$C_{d_{sn_{req}}} = F_{fat}\Big(\frac{L_{10_{eqsn}}}{10^6}\Big)^{1/3} \tag{4.23}$$

where $L_{10_{eq_{sn}}}$ represents the duration life of the component, expressed by the following equation [93]:

$$L_{10_{eq_{sn}}} = \frac{2\Big(n_{osc} \cdot round_{inf}\Big(\frac{\gamma}{180} \cdot n_r\Big) + 1\Big)}{n_r/2} \tag{4.24}$$

where $\gamma = \frac{\delta L_{arm}}{p_{sn}}$ represents the screw oscillations and n_r is the roller number. The screw length l_s depends on the required race c of the application and for this reason no homothetic relations are applied for this variable. It is so calculated as follows:

$$l_{sn} = A_n + L_b + c \tag{4.25}$$

The mass of the component is given by the sum of the mass of the nut M_n, and the mass of the screw M_s:

$$M_{sn} = M_n + M_s = M_n + m_s l_{sn} \tag{4.26}$$

The efficiency of the system needs to be evaluated, as it affects the performance of the mechanical drive chain and consequently impacts the sizing of the actuation system. The losses resulting from the screw-nut functioning in fact, need to be compensated by a higher electro-magnetic torque delivered by the motor. Two efficiencies have to be taken into account. A direct efficiency $\eta_{sn_{dir}}$ which takes account of the system losses during the

extension phase, and an inverse efficiency $\eta_{sn_{inv}}$ which acts during the retraction phase. These are calculated as follows [93]:

$$\eta_{sn_{dir}} = 0.91 \frac{1}{1 + \pi d_s \frac{\mu}{p_{sn}}} \tag{4.27}$$

$$\eta_{sn_{inv}} = 2 - \frac{1}{\eta_{sn_{dir}}} \tag{4.28}$$

where μ is the friction coefficient provided by the manufacturer according to the type of the screw nut considered.
Finally, considering that in this case study the nut is rotating, the inertia of the device is calculated in this way:

$$J_{sn} = \frac{M_n(D_n^2 - d_s^2)}{8} \tag{4.29}$$

4.4.2.2 Estimation model of thrust bearing

As well as the screw-nut, the bearing is also modelled through scaling laws. In order to estimate the integration and simulation parameters over a wide range, it is possible to approximate the elements composing the bearing with a geometrical similitude. This hypothesis is quite reasonable given the fact this device are suitable for dimensions standardisation for the purpose of manufacturing economy. Based on the foregoing considerations, a relation can be defined between the static load C_{0_b} and the bearing geometry represented by a characteristic dimension d_b [81]:

$$d_b^* = C_{0_b}^{*0.5} \tag{4.30}$$

So, starting from this relationship the other characteristic parameters can be defined:

$$C_{d_b}^* = C_{0_b}^{*\frac{1.85}{2}} \tag{4.31}$$

$$M_b^* = d_b^{*3} = C_{0_b}^{*\frac{3}{2}} \tag{4.32}$$

where M_b^* represents the ratio between the mass of the considered component to that of the reference component. For this case study, the thrust bearing **"SKF QJ"** (shown in Figure 4.14) is taken as reference, which represents a four-point contact ball bearings.

Figure 4.14: Thrust bearing model reference: "SKF QJ" [93]

Table 4.6: Component reference for bearing (SKF QJ) [93].

Parameter	Value	Unit	Definition
$C_{0_{b_{ref}}}$	92	$[kN]$	Static Load
$C_{d_{b_{ref}}}$	86	$[kN]$	Dynamic Load
$D_{b_{ref}}$	110	$[mm]$	Outer Diameter
$d_{b_{ref}}$	60	$[mm]$	Inner Diameter
$L_{b_{ref}}$	22	$[mm]$	Length
$M_{b_{ref}}$	0.99	$[kg]$	Mass
n_b	14	$[-]$	Balls number

Bearing design

As it has been done for the screw-nut, the static load C_{0_b} is taken as definition parameter. This can be defined as a function of mechanichal maximum load F_{max}, as follows:

$$C_{0_b} = k_b s_0 P_0 = k_b s_0 Y_{0_b} F_{max} \tag{4.33}$$

where k_b is a sizing coefficient defined during the phase of preliminary design, s_0 is the static security coefficient (it is assumed equal to 1 for normal silence operational requirements),

P_0 is the equivalent static load and $Y_{0_b} = 0.58$ is a coefficient provided by the manufacturer for the bearing adopted. Once the static load has been computed, the dimensions (exterior diameter D_b, interior diameter d_b, and bearing length L_b), the mass M_b and the dynamic load $C_{d_{sn}}$ of the component are determined through the previously defined scaling laws. The resulting designed device must ensure the fatigue requirement, which is defined according to the following relationship [93]:

$$C_{d_{b_{req}}} = F_{fat}\Big(\frac{L_{10_{eq_b}}}{10^6}\Big)^{1/3} \tag{4.34}$$

where $L_{10_{eq_b}}$ represents the duration life of the component, expressed by the following equation:

$$L_{10_{eq_b}} = \frac{2\Big(n_{osc} \cdot round_{inf}\Big(\frac{\gamma}{180} \cdot n_b\Big) + 1\Big)}{n_b/2} \tag{4.35}$$

During its motion, the bearing generates a friction torque which counteracts the torque transmitted by the device. This friction moment therefore needs to be compensated by a higher torque delivered by the electric motor (although it helps in the braking quadrant), thus impacting on the design of this latter. This can be evaluated as follow [93]:

$$|T_{fric}| = f_r \, P_1^a \, d_m^b \tag{4.36}$$

where f_r is the friction coefficient dependent on the type of bearing, P_1 is the load determining the friction moment, $dm = 0.5(d_b + D_b)$ is the average diameter, a and b are coefficients depending on type of bearing.
For four point contact bearings, $a = 1$ and $b = 1$. The friction torque f_r and the load P_1 are expressed as follows:

$$f_r = 0.001\Big(\frac{P_0}{C_{0_b}}\Big)^{1.33} \tag{4.37}$$

$$P_1 = 1.5F_{mecha_{max}} \tag{4.38}$$

Lastly, the inertia of the bearing is evaluated as below:

$$J_b = \frac{M_b(D_b^2 - d_b^2)}{8} \tag{4.39}$$

4.4.2.3 Surrogate Models of PM motor

The surrogate models of the PM motor has been described in Section 3.5. These models, expressing the electric motor performances in terms of electromagnetic torque, Joule losses and iron losses, are summarised as below:

$$\Pi_{0_T} = 10^{-2.55} \cdot \Pi_1^{-0.1\cdot(\log(\Pi_4))^2 - 0.14\cdot\log(\Pi_1)} \cdot \Pi_4^{0.45\cdot(\log(\Pi_4))^2 - 1.1} \tag{4.40}$$

$$\Pi_{0_{P_J}} = 10^{-1.96} \cdot \Pi_1^{-0.07\cdot(\log(\Pi_4))^2} \cdot \Pi_4^{-0.08\cdot(\log(\Pi_4))^2} \tag{4.41}$$

$$\Pi_{0_{P_{Fe}}} = 10^{-1.35} \cdot \Pi_1^{0.11+0.15\cdot\log(\Pi_1)} \cdot \Pi_4^{-1.67+0.62\cdot(\log(\Pi_4))^2} \tag{4.42}$$

The value of the corresponding dimensionless variables are resumed in the following Table:

Table 4.7: Dimensionless variables of surrogate models of electric motor

Dimensionless Variable	**Definition**
Π_1	$\frac{\mu_0 J D_e}{B_{sat}}$
Π_4	$\frac{e_{yoke} N_s}{\pi D_e}$
Π_{0_T}	$\frac{T_{mot}}{L_m B_r J D_e^3}$
$\Pi_{0_{P_J}}$	$\frac{P_J}{L_m \rho_{Cu} J^2 D_e^2}$
$\Pi_{0_{P_{Fe}}}$	$\frac{P_{Fe}}{L_m \gamma_{Fe} \Delta P_{Fe} \left(\frac{f_{elec}}{50}\right)^{1.5} B_r^2 D_e^2}$

In order to evaluate the thermal performance of the motor, its thermal resistance R_{cd} has to be estimated. Similar to what has been done for the estimation of electromagnetic performances, the conduction thermal resistance model between the stator skin temperature and the winding hot spot temperature is obtained using a surrogate modelling approach and FEM simulations. The obtained surrogate model, which represents the motor conduction thermal resistance, is the following [77] [12]:

$$\Pi_{0_{Cond}} = 84.2 \cdot \Pi_{1_c}^{-1.077+0.164\log\Pi_{1_n}} \tag{4.43}$$

Where $\Pi_{0_{Cond}} = R_{cd} L_m \lambda_{ir}$, $\Pi_{1_c} = \frac{D_e}{e_N}$, e_N is the Nomex insulation thickness and λ_{ir} is the thermal conductivity of the iron.

Motor Design

The definition parameters of the electric motor are the stall load torque and the peak torque, as well as the average and maximum rotation speeds. The nominal torque of the motor T_{mot}, from a thermal point of view, is given by the composition of a direct torque $T_{mot_{dir}}$, operating during the extension phase, and an inverse torque $T_{mot_{inv}}$, operating during the retraction phase. These are defined as below:

$$T_{mot_{dir}} = \frac{T_{EMA}}{\eta_{sn_{dir}}} + \frac{T_{fric}}{n_{red}\eta_{red}} \tag{4.44}$$

$$T_{mot_{inv}} = T_{EMA}\eta_{sn_{inv}} - \frac{T_{fric}}{n_{red}\eta_{red}} \tag{4.45}$$

The nominal motor torque T_{mot} can be so calculated as follows:

$$T_{mot} = \sqrt{T_{mot_{dir}}^2 + T_{mot_{inv}}^2} \tag{4.46}$$

where n_{red} and η_{red} represent respectively the reduction ratio and the efficiency of the gear box. Note that the nominal motor torque has been defined here for a design of the RMS actuator load T_{EMA}. If the motor is intended to be sized for the maximum load $T_{EMA_{max}}$, this must be taken into account in Eq. 4.44 and Eq. 4.45.

The angular $\overline{\omega}_{mot}$ mean and maximum $\omega_{mot_{max}}$ velocities of the motor can be defined in this way:

$$\overline{\omega}_{mot} = \frac{2\pi\bar{\omega} L_{arm} n_{red}}{p_{sn}} \tag{4.47}$$

$$\omega_{mot_{max}} = \frac{2\pi\omega_{max} L_{arm} n_{red}}{p_{sn}} \tag{4.48}$$

Particular attention must be paid to the maximum speed of the motor, or more precisely to the associated electrical frequency. A functional limit of $750\,Hz$ is imposed, as beyond this frequency the magnetic performance of the iron is not guaranteed by the manufacturer.

Once the motor torque and speed have been determined, by taking the motor diameter D_e and the dimensionless variables Π_1 and Π_4 as input design parameters, the variables Π_{0_T}, $\Pi_{0_{P_J}}$ and $\Pi_{0_{P_{Fe}}}$ are calculated. The motor length is computed from Π_{0_T}, which is expressed in Table 4.7. Subsequently, the Joule and iron losses can be easily extracted from

the expression of $\Pi_{0_{P_J}}$ and $\Pi_{0_{P_{Fe}}}$ (see Table 4.7). With the same procedure adopted above, the peak motor torque and the related maximum Joule and iron losses can be determined. Concerning the thermal performance, the thermal resistance of the motor can be calculated from Eq. 4.43. So, the motor winding temperature Θ_{wind} is obtained as follows:

$$\Theta_{wind} = \Theta_{hous} + (P_{Fe} + P_J)R_{cd} \tag{4.49}$$

where Θ_{hous} is the temperature of the thermal housing (fixed here to 100°C). A functional temperature limits of $185°C$ is imposed in order to avoid degradation of the winding insulation. Note that in the equation adopted here for calculating the winding temperature, the resistance of the iron has not been taken into account, as it is considered negligible in relation to the resistance R_{cd} [79] (this will be explained later in Section 7.2.3). The mechanical behaviour of the motor is also needed to be evaluated in order to asses mass, geometric integration, inertia and maximum mechanical speed. The mass of the motor is given by the sum of its constituent parts: the mass of stator iron M_{Fe_s}, the mass of windings M_{Cu}, the mass of the rotor iron M_{Fe_r} and the mass of permanent magnets M_{PM}. Since the geometries (3.5) and properties (3.3) of the materials constituting the motor are known, the mass of each element can be estimated as below:

$$M_{mot} = M_{Fe_s} + M_{Fe_r} + M_{Cu} + M_{PM} \tag{4.50}$$

The motor inertia can be calculated approximately as follows:

$$J_{mot} = (M_{Fe_r} + M_{PM})\frac{(D_i^2 - 2r_i^2)}{8} \tag{4.51}$$

4.4.2.4 Estimation model of Gearbox

The estimation models of the gear box are based on analytical relations founded by Willis JR [98]. The method presented by Willis identifies the gear sizes and ratios that will permit the lightest possible design while meeting at the same time the power and contact surface durability requirements of the application. Moreover, it also gives a good estimation of total weight of the drive, including weight of the shaft, bearings and housing. Willis starts on the assumption that the weight of a gear system is approximately proportional to the sum of the solid rotor volumes of its gear:

$$\sum Fd^2 = Fd_p^2 + Fd_g^2 + Fd_i^2 \tag{4.52}$$

where F is the face width, d_p the pinion pitch diameter, d_g the gear pitch diameter and d_i the idler pitch diameter.

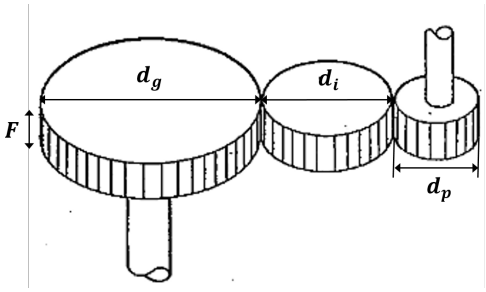

Figure 4.15: Gearbox geometry.

For a gear system with an idler, Willis provided the following relationships:

$$Fd_i^2 = \frac{2T_{mot}}{K}\Big(\frac{m_g + 1}{m_g}\Big)m_g^2 \tag{4.53}$$

where m_g is the ratio of pinion to idler diameter and K is the surface durability factor. By combining and re-formulating the two equations we obtain:

$$\sum \frac{Fd^2}{C} = 1 + \frac{1}{m_g} + m_g + m_g^2 + \frac{n_{red}^2}{mg} + n_{red}^2 \tag{4.54}$$

where $\frac{Fd^2}{C}$ represents the weight factor, $C = \frac{2T_{mot}}{K}$ and n_{red} is the total reduction ratio. Choice of K factor depends on materials, severity of service, desired life and application. In aircraft application, a value of $6.9 \cdot 10^6\,[N/m^2]$ is generally taken as guide [98]. Once obtained the weight factor, its value is after multiplied for C to obtain a numerical value of the total solid rotor volumes $\sum Fd^2$. Since the weight of a gear is proportional to the volume, a mean to estimate the reducer mass M_{red} is now available. To obtain the total weight of the component, the solid rotor volumes $\sum Fd^2$ has to be multiplied for the application factor A_f.

$$M_{red} = k_{SI} A_f \sum Fd^2 \tag{4.55}$$

where $k_{SI} = 6.1 \cdot 10^4$ is a conversion coefficient (as Willis refers to an imperial unit system). For aircraft application the application factor A_f (Fig. 4.16) is normally taken between 0.25 to 0.30 [98] and it takes into account the gearing, shaft, bearings and immediate support structure.

Application	Factor	Typical conditions
Aircraft	0.25 to 0.30	Magnesium or aluminum casings; limited-life design; high stress levels; rigid weight control.
Hydrofoil	0.30 to 0.35	Lightweight steel casings; relatively high stress levels; limited life design; rigidity desired.
Commercial	0.60 to 0.625	Cast or fabricated steel casings; relatively low stress levels; unlimited-life design; solid rotors and shafts.

Figure 4.16: Application factors for weight estimation [98].

Gearbox design

The reduction ratio n_{red} and the motor torque T_{mot} are taken as input design parameters. The pinion to idler ratio m_g can be calculated according to the minimum weight equation [98]:

$$2m_g^3 + m_g^2 = n_{red}^2 + 1 \tag{4.56}$$

In this way the rotor volumes $\sum Fd^2$ can be directly computed from Eq. 4.54. The mass of the gearbox can be therefore computed according to Eq. 4.55, by assuming $A_f = 0.30$. The pinion diameter d_p can be calculated according to the motor D_e, the fin width L_a and the bearing diameter D_b in the following way:

$$d_p = \frac{D_e/2 + D_b/2 + L_a}{1/2 + m_g + n_{red}/2} \tag{4.57}$$

Once calculated the pinion diameter, the gear and idler diameter can be computed as follows:

$$d_g = n_{red} d_p \tag{4.58}$$

$$d_i = m_g d_p \tag{4.59}$$

The contribution of the reflected inertia of the gearbox J_{red} (on the control surface level) can be approximately estimated as follows:

$$J_{red} = \frac{M_{d_g} d_g^2}{8} n_{red}^2 + \frac{M_{d_p} d_p^2}{8} + \frac{M_{d_i} d_i^2}{8} m_g^2 \tag{4.60}$$

where M_{d_g} is the mass of the gear, M_{d_p} the pinion mass and M_{d_i} the mass of the idler.

4.4.2.5 Estimation model of thermal housing

The thermal housing is an aluminium mass mounted around the motor which presents two finned plates heat sinks mounted on its lateral sides, as depicted in Fig. 4.6 and Fig. 4.17, to improve the heat dissipation with natural convection. Estimation models based on analytical relationships are used even in this case to estimate the heat transfer coefficients of the device. In order to compute the heat transfer coefficients of the fin h_{fin} and that of the surface situated between the fins h_{int}, formulations derived from Bar-Cohen and Rohsenow [62] are used. They extended the use of least-material single rectangular plate fin analysis to multiple fin arrays, using a composite Nusselts number correlation valid for different surface conditions:

$$\overline{Nu} = \left[\frac{576}{R_a\left(\frac{S}{H_c}\right)^2} + \frac{576}{R_a\left(\frac{S}{H_c}\right)^{1/2}}\right]^{-1/2} \tag{4.61}$$

where R_a is the Rayleigh number, S is the fin spacing and H_c is the fin height. The heat transfer coefficients at the fin and un-finned area are so obtained as follows:

$$h_{fin} = \overline{Nu}\frac{\lambda_{air}}{S} \tag{4.62}$$

$$h_{int} = \frac{0.59 R_a \lambda_{air}}{H_c} \tag{4.63}$$

where λ_{air} is the thermal conductivity of the air.

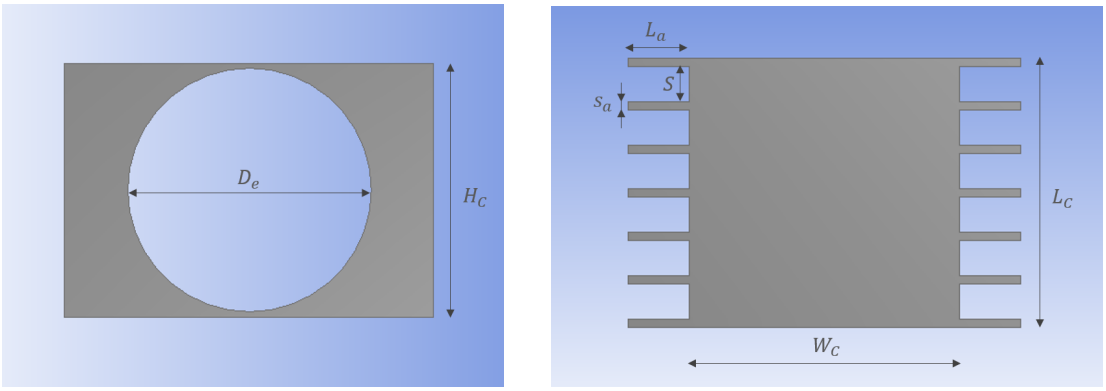

(a) Frontal view (b) Top view

Figure 4.17: Thermal housing geometry.

In order to compute the heat transfer coefficients on the top h_{top} and bottom h_{bottom} surfaces of the housing, reference can be made to the case of a free convention on horizontal plates. For this case, correlations for the average Nusselt number are provided by Bergaman et al. [99] [100]:

$$\overline{Nu}_{top} = 0.54 R_a^{1/4} \tag{4.64}$$

$$\overline{Nu}_{bottom} = 0.27 R_a^{1/4} \tag{4.65}$$

The heat transfer coefficients at the top and bottom surfaces are so obtained as follows:

$$h_{top} = \overline{Nu}_{top} \frac{\lambda_{air}}{L_{car}} \tag{4.66}$$

$$h_{bottom} = \overline{Nu}_{bottom} \frac{\lambda_{air}}{L_{car}} \tag{4.67}$$

where $L_{car} = \frac{L_c W_c}{L_c + W_c}$ represents the characteristic length of the considered surfaces.
The design of the thermal housing, in addition, is subject to mechanical constraints. In particular, the vibration resistance of the fins must be checked. As vibrations are very important [101] for aerospace embedded actuators, a sizing model is needed to estimate the vibration resistance of fins. To this purpose, surrogate models are adopted. As in the case of surrogate motor modelling, the use of Buckingham's theorem and dimensional analysis is adopted to reduce the number of variables expressing the physical problem in question. In this case, after analysing the maximum stress, the displacement and the resonant frequency, the maximum stress σ at the resonant frequency under a vibratory load can be expressed with the following dimensionless form:

$$\frac{\sigma}{Q_m a s_a \rho_a} = f\left(\frac{L_a}{s_a}, \frac{r}{s_a}\right) \tag{4.68}$$

where Q_m is defined as mechanical quality coefficient, a is the vibratory sinusoidal acceleration, ρ_a is the aluminium density and r represents the corner radius. A 2D-FEM modal analysis (Fig. 4.18) is conducted to obtain: the resonance frequency, the modal form and finally the maximum stress for given acceleration load and dimensions of fin. From this analysis, it emerged that starting from a ratio of $\frac{r}{s_a} = 0.4$, the corner radius no longer has any influence on the maximum stress. Therefore, a geometric similarity is adopted for this variable, assuming $\frac{r}{s_a} = 0.4$. The global expression of the dimensionless number expressing the stress is thus only function of one aspect ratios. The function f is thus approximated

with a surrogate model, built on the basis of FEM simulations defined by a dedicated DoE. The surrogate model expression takes the following mathematical form:

$$\frac{\sigma}{Q_m a s_a \rho_{al}} = 10^{0.72}\left(\frac{L_a}{s_a}\right)^{2.05} \tag{4.69}$$

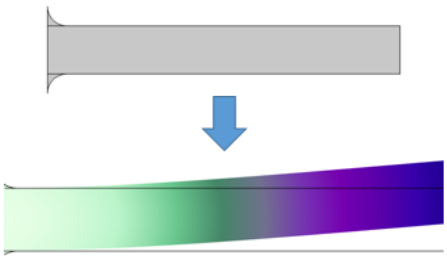

Figure 4.18: Fin modal analysis.

Thermal housing design

The definition parameters for the thermal housing are the skin temperature Θ_{hous} and the environmental temperature Θ_{ext}, which are assumed respectively equal to $100°C$ and $20°C$. The geometries defining the dimension of the component, expressed in Fig. 4.17, are taken as input design variables. In this way, based on the air thermal properties, the Rayleigh number is defined as below:

$$R_a = \frac{g\beta S^3(\Theta_{hous} - \Theta_{ext})}{\alpha v} \tag{4.70}$$

where g represents the gravity acceleration, β is the thermal espansion coefficient , α is the thermal diffusivity and v represents the kinematic viscosity. Hence, the Nusselts numbers related to the different surfaces are calculated by means of Eq. 4.61, Eq. 4.64, Eq. 4.65 and the heat transfer coefficients are so computed through of Eq. 4.62, Eq. 4.63, Eq. 4.66 and Eq. 4.67. The fins number, for fixed geometries, is calculated as follows:

$$n_{fin} = round\left(\frac{L_c + S}{S + s_a}\right) \tag{4.71}$$

The heat transfer rates of the fin plates can therefore be estimated, as well as the heat transfer contribution of top and bottom surfaces:

$$q_{fin} = n_{plate} n_{fin} h_{fin} 2(H_c\, L_a)(\Theta_{hous} - \Theta_{ext}) \tag{4.72}$$

$$q_{int} = n_{plate}(n_{fin} - 1) h_{int}(H_c\, S)(\Theta_{hous} - \Theta_{ext}) \tag{4.73}$$

$$q_{top} = h_{top}(L_c\, W_c)(\Theta_{hous} - \Theta_{ext}) \tag{4.74}$$

$$q_{bottom} = h_{bottom}(L_c\, W_c)(\Theta_{hous} - \Theta_{ext}) \tag{4.75}$$

where n_{plate} is the number of fin plates.
The last contribution of heat transfer is related to the radiation. Heat transfer by thermal radiation is the transfer of heat by electromagnetic waves. It is different from conduction and convection as it requires no matter or medium to be present. The radiative energy will pass perfectly through vacuum as well as clear air. The radiation heat transfer is proportional to the fourth power of the temperature and can be expressed with Stefan-Boltzmann Law as:

$$q_{rad} = \epsilon\sigma(\Theta_{hous}^4 - \Theta_{ext}^4) A_{rad} \tag{4.76}$$

where ϵ is the emissivity coefficient of the housing, here assumed equal to 0.85, σ is the Stefan-Boltzmann constant and $A_{rad} = H_c L_c(2L_a + W_c)$ is the area of the housing where radiation exchange takes place. The total heat transfer Q, can be so approximated by the sum of the heat transfer contributions of the different surfaces constituting the housing:

$$Q = q_{fin} + q_{int} + q_{top} + q_{bottom} + q_{rad} \tag{4.77}$$

The designed system must ensure that the total heat transfer Q is equal to or greater than the losses generated by the electric motor. The mass of the thermal management system can be simply estimated by the following formula:

$$M_{hous} = \rho_a V_{hous} \tag{4.78}$$

where ρ_a is the aluminum density and V_{hous} is the volume of the housing.
From the geometry of the fin (s_a, L_a), the vibration resistance can easily be calculated using Eq. 4.69. The maximum stress of the designed fins must not exceed $40\,MPa$.

4.5 Definition of the sizing procedure

The sizing procedure can be considered as a major part of the whole preliminary sizing process. It consists of gathering all the equations describing the system and component models (Fig. 4.19) and individuating the inequalities and algebraic loops involved in the problem. One of the biggest problems encountered during the coupling of the models, concerns the treatment of the constraints. Three types of constraints can be observed [102]: under-constrained singularities, over-constrained singularities and algebraic loops.

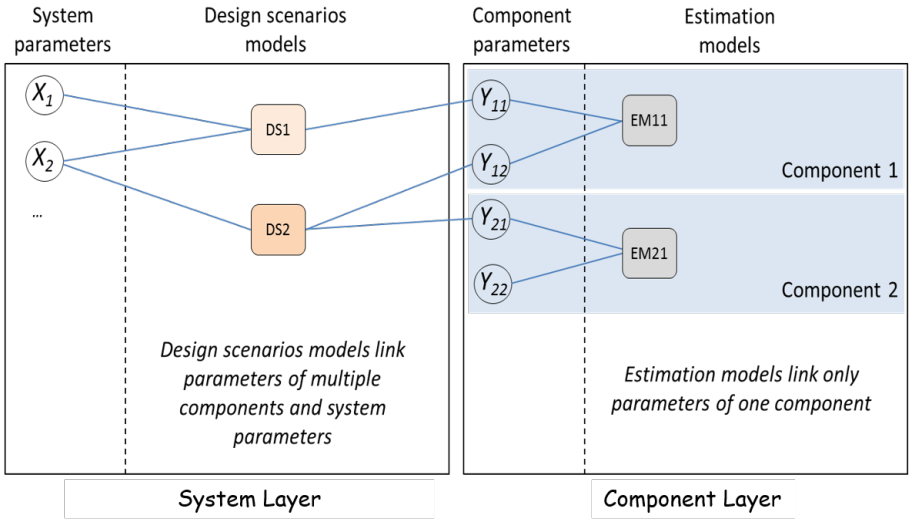

Figure 4.19: Problem graphical representation and orientation [95].

Under-constrained singularity This situation can occur when there are more unknowns than the number of equations involved in the system. In this case, some design assumptions have to be done by stating that some parameters are known. These new design parameters can be included in the optimization problem and their optimal value can be determined via the optimization algorithm. These assumptions allow to balance the number of equations available and the number of parameters to be determined by the calculation procedure. In this context, for example, the rotor volumes $\sum Fd^2$ of the gearbox is calculated from the reduction ratio n_{red} and the motor torque T_{mot}, whilst the latter in

turn depends on the reduction ratio n_{red}:

$$\sum Fd^2 = f(K, T_{mot}, n_{red}) \tag{4.79}$$

$$T_{mot} = f(T_{EMA}, n_{sn_{dir}}, n_{sn_{inv}}, n_{red}, \eta_{red}) \tag{4.80}$$

The parameter K and η_{red} were fixed, while the screw efficiencies $n_{sn_{dir}}$ and $n_{sn_{inv}}$ are input parameters coming from Eq. 4.27 and Eq. 4.28. By defining the reduction ratio as an optimisation variable ($n_{red} \in [0 - 4]$) the number of equations and unknowns can be therefore correctly balanced.

Over-constrained singularity If several equations of design scenarios have the same output, the problem may be over-constrained. One solution that can be applied in this case, consist in adding a safety factor and managing one of the equations as a constraint in the optimization problem. For the case of the finned thermal housing for example, the heat transfer rate Q must satisfy the motor losses constraint:

$$Q \geq (P_J + P_{Fe}) \tag{4.81}$$

where Q depends on the thermal resistance of the component and the temperature difference between the device and the external environment:

$$Q = f(R_{th}, \Delta\Theta = \Theta_{ext} - \Theta_{hous}) \tag{4.82}$$

Since the temperature difference was fixed ($\Theta_{ext} = 20°C$, $\Theta_{hous} = 100°C$) the only degree of freedom is on the thermal resistance. This depends on the housing dimensions, as shown in Section 4.4.2.5:

$$R_{th} = f(L_a, s_a, S, L_c, H_c, W_c) \tag{4.83}$$

Since La, sa, and S (Fig. 4.17) define the size of the finned plate, it is convenient to use them as optimisation variables to set the value of the thermal resistance, while L_c, H_c, and W_c, which define the size of the dimensions of the central body of the housing, can be fixed according to the size of the electric motor ($H_c = W_c \approx D_e$; $L_c = L_m$). The vibration constraint on the fins may, however, limit the value of R_{th}, thus involving the non satisfaction of the constraint of Eq. 4.81. For this reason, the over-sizing coefficients k_L, k_H and k_W, will be introduced as optimization variables in order to provide three degrees

of freedom on the housing dimensions and consequently on its thermal resistance:

$$L_c = k_L L_m \tag{4.84}$$

$$H_c = k_H D_e \tag{4.85}$$

$$W_c = k_W D_e \tag{4.86}$$

Algebraic loop An algebraic loop can be typically found in the selection of a component involving the use of characteristics of this same component. Adding once again a new design parameter, such as an over-sizing coefficient and a constraint to be checked by the optimization algorithm, makes the sizing procedure explicit. Here for example, for the computation of the static load C_0 of the bearing, expressed in Eq. 4.33, the coefficient design variable k_b has been introduced in order to oversize the static load. The additional consistency inequality (Eq. 4.87) is added to the design problem in order to verify that the static load is sufficient to withstand the shock effort F_{shock}, which is dependent on the other disciplines:

$$C_{0_b} \geq F_{shock} \tag{4.87}$$

where $F_{shock} = f(J_{eq}, \omega_{mot_{max}}, T_{mot_{max}}, n_{red}, \eta_{red}, \eta_{sn_{dir}}, p_{sn})$.

4.6 Design and optimization

Once the system and component equations have been formulated and coupled, they are integrated in a sizing framework in order to perform the preliminary design. To this purpose, a dedicated tool has been developed in Python programming language within which an optimisation procedure has been implemented with a view focused on minimising the mass of the system. An eXtended Design Structure Matrix (XDSM) [103] (Fig. 4.20) can be used to graphically highlight the interactions between the models. The optimization is performed by a differential evolution algorithm [104], by taking use of the Python package *SciPy*. This algorithm is very suited for more challenging objective problems in which there are a high number of optimisation variables and constraints, as in this case study. The optimisation problem is addressed in the following way:

$$
\begin{aligned}
\text{Minimize} \quad & M_{EMA} \\
\text{with respect to} \quad & D_e, \Pi_1, \Pi_2, k_b, k_{sn}, n_{red}, L_a, S, s_a, k_L, k_H, k_W \\
\text{subject to} \quad & \Theta_{wind} - \Theta_{wind_{lim}} \leq 0 \\
& \omega_{mot_{max}} - \omega_{max} \leq 0 \\
& C_{d_{sn_{req}}} - C_{d_{sn}} \leq 0 \\
& F_{shock} - C_{0_{sn}} \leq 0 \\
& F_{shock} - C_{0_b} \leq 0 \\
& C_{d_{b_{req}}} - C_{d_b} \leq 0 \\
& J_{ref} - J_{ref_{max}} \leq 0 \\
& P_{Fe} + P_J - Q \leq 0 \\
& \sigma - \sigma_{max} \leq 0 \\
& L_{EMA} - L_e \leq 0 \\
& W_{EMA} - W_e \leq 0 \\
& H_{EMA} - H_e \leq 0
\end{aligned}
\tag{4.88}
$$

The sizing problem is conducted for the entire set of primary control surfaces, for each of which, the direct and gear drive configurations are evaluated. On the basis of the considerations made in Section 2.2.4, for the Aileron application has been decided to size the motor to the RMS load T_{EMA}, while Rudder and Elevator applications are sized according to the maximum load $T_{EMA_{max}}$. The results obtained by optimization are summarized in Table 4.8. They are illustrated in more detail in **Annex C**.

Table 4.8: Results of optimizations

	Aileron		Elevator		Rudder	
	Gear	Direct	Gear	Direct	Gear	Direct
Motor Mass $[kg]$	1.26	4.12	1.22	3.62	1.46	4.93
Housing Mass $[kg]$	0.82	2.26	1	2.05	1.05	2.6
Screw-nut Mass $[kg]$	1.44	1.42	0.9	0.62	0.8	0.71
Bearing Mass $[kg]$	1.19	0.81	1	0.65	0.83	0.66
Gearbox Mass $[kg]$	0.9	-	0.65	-	0.88	-
Total Mass $[kg]$	5.6	8.61	4.77	6.94	5.02	8.89

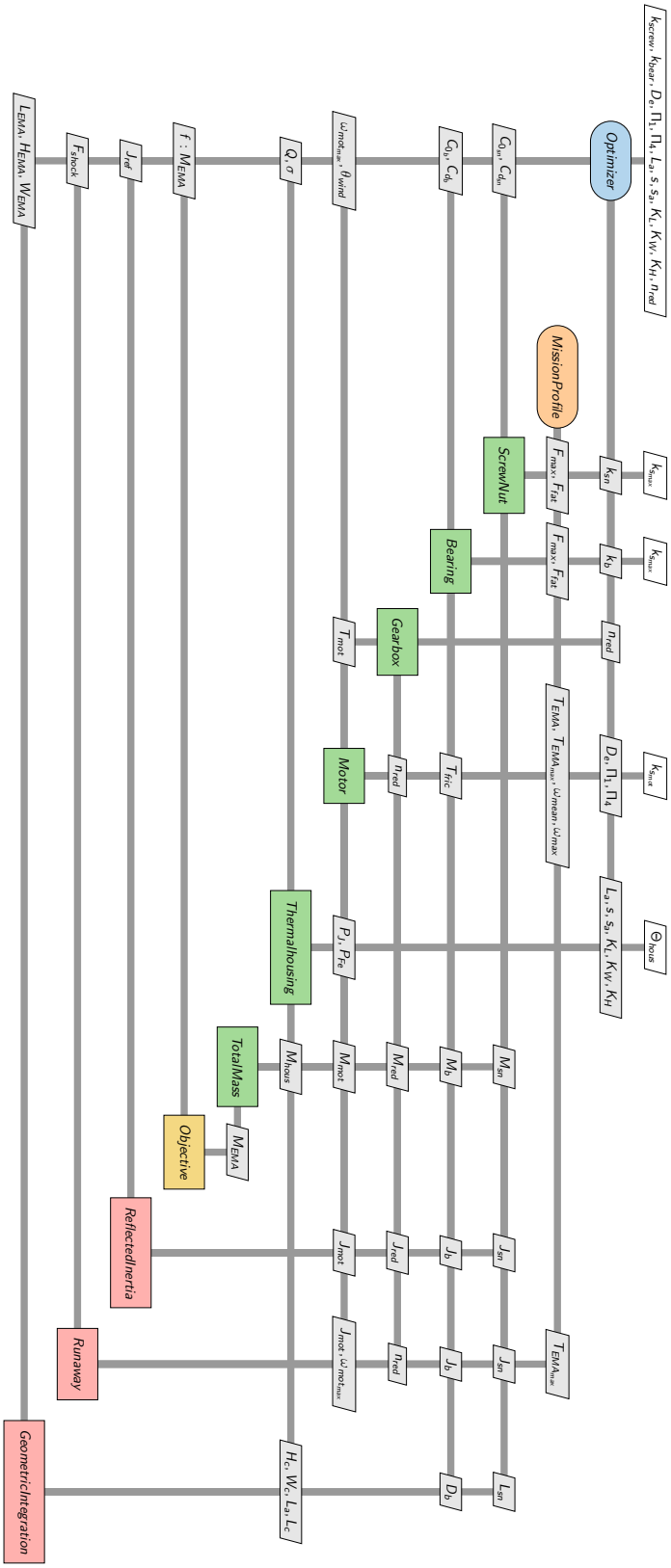

Figure 4.20: Extended design structure matrix of the EMA preliminary design.

In the designs obtained, the gear drive configuration proves to be lighter than the direct drive architecture. Thanks to the use of the gearbox, the motor is sized for a torque that is essentially four times lower (n_{red}) than that of the direct drive configuration. This results in a significant gain in mass, both at motor and system level. As it can be seen in the graph in Fig 4.21, in direct drive configurations the motor accounts for 50% of the total mass of the actuation system. Through the use of the gearbox, it was possible to reduce the mass of the motor between two and almost four times, depending on the type of application.

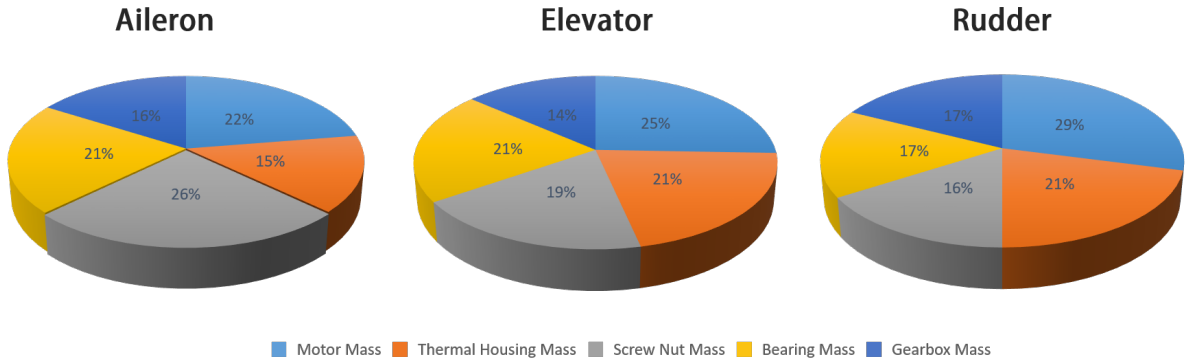

(a) Gear drive configuration

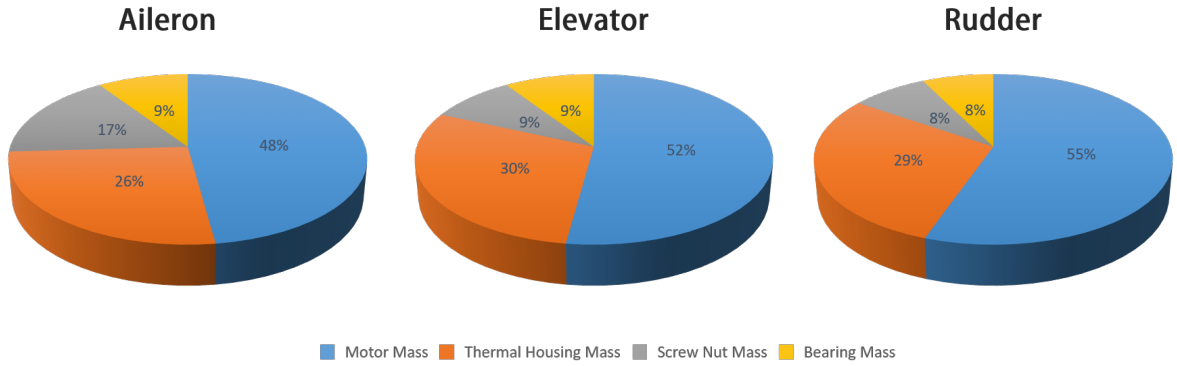

(b) Direct drive configuration

Figure 4.21: Mass distribution of EMA components for the different types of primary flight control application.

However, it is necessary to consider that the housing containing the mechanical components in the gear drive configuration is not considered for mass computation, as can be seen in Fig. 4.22. The thermal housing in fact, is sized according to the size and losses of the electric motor only. In the gear drive, the motor and mechanical transmission chain are separated. In direct drive, the transmission chain is integrated into the electric motor, so the thermal housing covers nearly the entire actuation device, as shown in Fig. 4.23.

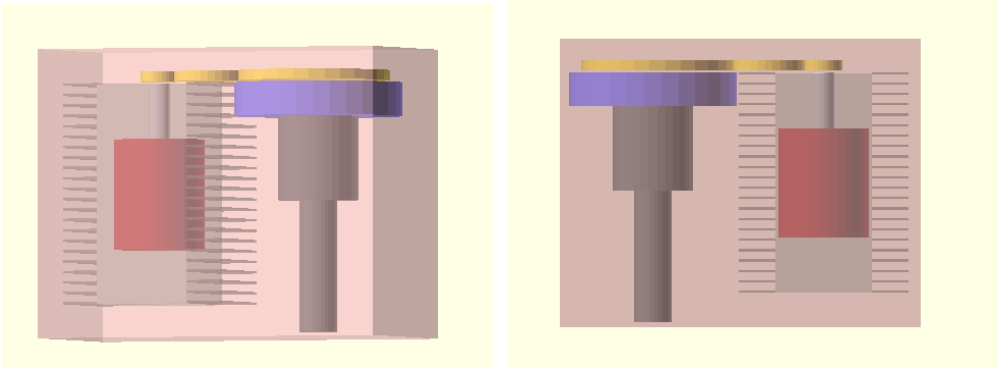

(a) Perspective view (b) Top view

Figure 4.22: Resulting geometry of Aileron EMA for gear drive configuration.

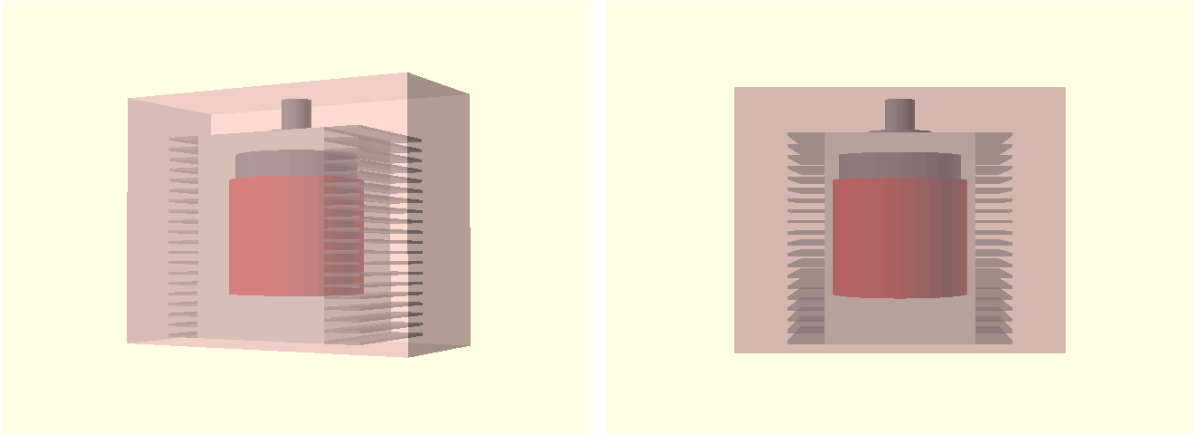

(a) Perspective view (b) Top view

Figure 4.23: Resulting geometry of Aileron EMA for direct drive configuration.

From Fig. 4.21, it can be seen that depending on the type of control surface, the optimum design involved a realisation of different mass compromises between the components. Rudder and Elevator applications are characterised by the masses of the electric motor and thermal housing being greater in percentage terms than those of Aileron application. This is because, for the first two applications, the motor has been sized according to the maximum load, resulting in an oversized motor. An increase in the size of the motor involves an increase in the dimensions of the housing into which it is integrated, thus justifying the percentage increase in the mass of the heat management device. However, the ratio between the mass of the motor and that of the thermal housing is different for all applications. This underlines the importance of using surrogate models that allow certain

degrees of freedom during the optimisation in order to set the right compromises between the interacting components. The constraint of the fins vibration is the most difficult from a thermal point of view, as it highly influences the geometry of the cooling system. In fact, the thermal housing tends to increase in length, thus extending the heat exchange surface by adding more fins, rather than increasing their width. This results, as can be seen in Fig. 4.22 and 4.23, in a thermal housing longer compared to the length of the electric motor.

4.6.1 Computation, capitalization and model construction times

The use of surrogate models allowed the preliminary design and optimization of the primary flight control EMAs to be carried out in a matter of seconds. This led to a significant gain in terms of calculation time compared to the use of FEMM models. However, how effective is this gain when compared to the time spent building the surrogate models? Put aside the process of model reduction, the temporal aspect of major relevance of VPLM regards the generation of the DoE and the FEMM simulations (step 1 of VPLM methodology, Fig. 3.10). For the DoE, the generation of the experiments depends on the number of variables considered. In this context, around 2 minutes were needed to generate 100 configurations (by using a *Intel i7* quad core processor). They were successively simulated in FEMM in around 50 minutes (30 seconds per simulation). Once the outputs of interest had been extrapolated (values of electromagnetic torque, Joule and iron losses) from FEMM, the definition of the models was generated instantaneously by using the Python package *pyVPLM*. Hence, the process of constructing the VPLM model is very inexpensive and it can be estimated at around one hour. The most expensive part lies in the procedure of model reduction. In fact, to conduct the sensitivity analysis, 30 FEMM optimizations were needed. For each of them, approximately 10 hours of simulation were spent, for a total of 300 hours of calculation. A single multidisciplinary optimization in the case of the preliminary design of the EMA requires between 190000 and 250000 function evaluations. This would involve around 1580 hours of simulations in the best of cases if FEMM models of brushless motor were used, which is 5 times the time needed to conduct the sensitivity analysis. Consequently, even in the case of evaluating a single system design optimization, the use of surrogate models built with the reduction methodology developed would be convenient from a computational point of view. Finally, the surrogate models can be reused for different sizing purposes [78], so the computational and capitalization gains become

remarkably significant.

4.7 Conclusion

In this chapter, an example of preliminary design of EMAs for primary flight control applications has been shown. Two types of architectures, gear and direct drive, have been investigated. After having defined the design drivers and sizing scenarios, the actuator sizing specifications were defined by analysing the mission profiles. Subsequently, the system and component models have been generated, showing the equations defining them and how they are interconnected according to the sizing case study. In order to conduct optimal designs, an optimisation procedure has been defined with the aim of minimising the mass of the actuator. The preliminary design has therefore been carried out for the primary control surfaces: Aileron, Elevator and Rudder. The obtained designs have been presented and analysed. They reveal the importance of the individual analysis of the mission profiles. As different specifications were defined for each of the applications considered, different EMA designs have been obtained. For each of the primary flight control applications, the compromises between the system components are highlighted in order to optimize the global mass of the actuator. These compromises are achieved thanks to the surrogate models utilisation, whose construction is based on the fundamental concept of providing specific degrees of freedom during the phase of preliminary design and optimisation. The optimisation also highlighted, for the considered case study, the advantage in terms of system mass achieved through a gear drive configuration compared to the direct drive configuration. The preliminary designs outlined the EMA Aileron as the heaviest actuator, followed by Rudder and finally Elevator. The use of surrogate models allowed the preliminary design of the primary flight control actuation systems to be carried out in a matter of seconds, thus highlighting the significant gains involved in terms of computation time, and especially capitalization, compared to other surrogate modelling methodology.

Chapter 5

Model Generation of Unconventional Thermal Management Systems: Solutions for Steady State

Contents

5.1 Introduction **116**

5.2 Characterization of aircraft heat sink **117**

5.2.1 Proposed installation method of the heat transfer devices 117

5.2.2 Computation of the heat transfer coefficient 119

5.3 Heat Pipe **121**

5.3.1 Heat transfer and temperature difference 124

5.3.2 Estimation model of heat pipe 126

5.3.3 Heat pipe design 129

5.4 Thermal Strap **130**

5.4.1 Estimation model of thermal straps 132

5.4.2 Thermal strap design 134

5.5 Thermal spreader **135**

5.5.1 Estimation model of a Thermal Spreader 136

5.5.2 Thermal spreader design 138

5.6 Thermal interface material **138**

5.6.1 Estimation model of TIM 139

5.6.2 TIM design 145

5.7 Conclusion **146**

5.1 Introduction

This chapter deals with the generation of models of unconventional thermal management systems, suitable for continuous operation over the entire duration of the mission. The term "unconventional" refers to systems which are currently not being used for the thermal management of flight control actuators. In this thesis, reference is therefore made to heat pipes (HP) and thermal straps (TS). The advantages of these devices have been introduced in Section 2.3.2. Their effectiveness depends essentially on three aspects, depicted in Fig. 5.1: the cold source used to dissipate the transported heat; the size of the heat exchange surface; and the interfacing with the surfaces on which they are installed.

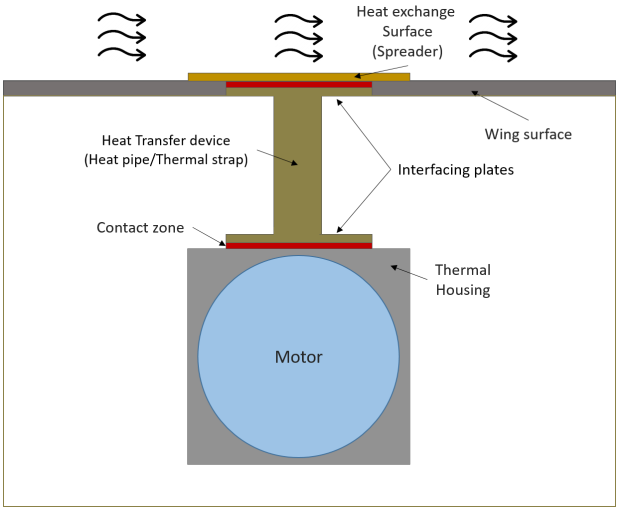

Figure 5.1: Representation of thermal aspects related to heat pipes/thermal straps.

The best available cooling medium is certainly the air that flows on the skin of the aircraft wing. Therefore, if it would be possible to expose the terminal plate of the considered thermal management system (TMS) outside the wing surface, the air flow can be used for heat dissipation and great benefits can be obtained in terms of thermal management. This subject is discussed in the first part of the chapter. The efficiency of this method can be quantified through the evaluation of the convective heat transfer coefficient. A method for its determination is therefore introduced.
In the second part of the chapter, the estimation models adopted for estimating the dimensions and performances of heat pipes and thermal straps are presented. How they are used in the design phase is also demonstrated.

In order to increase the heat exchange surface of the TMS, a thermal spreader can be adopted. The thermal analysis of the spreader is generally complex because the evaluation of its thermal resistance is computationally expensive. A method for rapidly evaluating the thermal resistance is therefore presented.
The last part of the chapter discusses the interfacing of heat transfer devices. The problem encountered with interfacing such devices is a degradation of the thermal performances mainly due to an imperfect contact with the surfaces on which they are mounted. This results in an increase of the thermal contact resistance. To overcome this problem, thermal interface materials (TIM) are used. The characterisation and modelling of TIM requires a good understanding of the contact zones. For this purpose, a surrogate model extracted from finite element simulations has been developed.

5.2 Characterization of aircraft heat sink

5.2.1 Proposed installation method of the heat transfer devices

One of the best available cold source for primary flight control actuators is the airflow over the aircraft skin, which, being characterised by a high air velocity during the flight, improves the heat transfer. The simplest method of using this source is to connect the heat pipes or thermal straps to the inner side of the wing structure, as shown in the example depicted in Fig. 5.2. In this way, the aircraft skin can be used as a thermal spreader, to absorb the heat load and slowly dissipate it to the ambient air.

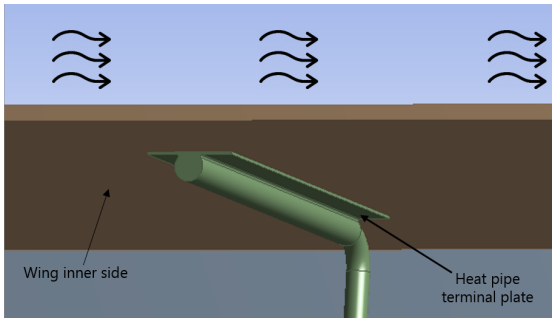

Figure 5.2: HP mounted on the inner side of aircraft wing skin.

The evolution towards the use of composite materials, however, makes aircraft manufactur-

ers reluctant to accept these types of solutions, as composites are characterized by a very low thermal tolerance, compared to metallic materials. In addition, the utilization of such materials is unfavourable for heat conduction, as most composites have a very low thermal conductivity (data from Pardini et al. [105] indicate that a typical carbon-fibre composite has a longitudinal and transverse thermal conductivity at 300 K of 8.40 W/mK and 0.84 W/mK respectively). To overcome this problem, an alternative solution is proposed in this thesis. The idea is to connect the end plate of the heat transfer devices to a thermal spreader (an aluminium plate) mounted on the outer side of the wing. This connection can be made either directly, as considered in this thesis, or indirectly. The first, illustrated in Fig. 5.3, involves removing a small section in the wing structure, corresponding to the size of the terminal plate of the device, so that it can be connected through direct contact with the thermal spreader. However, this solution may not necessarily be approved by the aircraft manufacturer, and should merit an extended analysis regarding possible mechanical degradation of the composite material. The other option, less invasive, could be drilling some holes in the concerned wing area in order to pass thermal drains and indirectly connect the device's terminal plate (situated inside the wing) to the spreader (situated outside the wing).

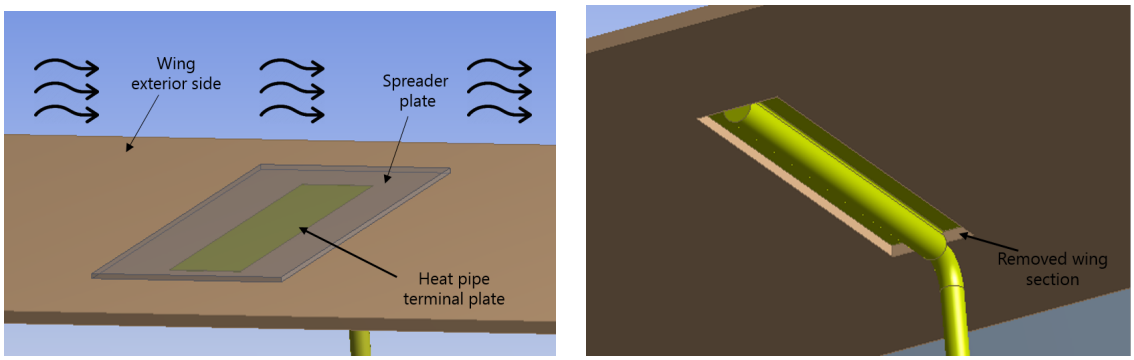

(a) Exterior side view of the wing (b) Inner side view of the wing

Figure 5.3: HP mounted on a thermal spreader on the exterior side of aircraft wing skin.

The effectiveness of this method can be quantified by means of the determination of the convective heat transfer coefficient. Its evaluation for this type of application can be complex, as it is closely dependent on the geometry of the heat exchange surface, on the air properties that are function of the atmosphere altitude and on the aircraft true speed which is continuously varying along the mission. An analytical formulation for calculating the convective heat transfer coefficient is outlined in the next section.

5.2.2 Computation of the heat transfer coefficient

The convective heat transfer coefficient characterises the amount of heat that can be exchanged between a solid surface and a fluid. It is generally calculated indirectly, out of the Nusselt number N_u, according to the following relationship:

$$N_u = \frac{h\,L}{\lambda} \tag{5.1}$$

where L is the characteristic length of the heat exchange surface, λ is thermal conductivity of the fluid and h is the convective heat transfer coefficient. Numerous empirical correlations can be found in the literature [99], providing equations to calculate the Nusselt number as a function of the profile type of the heat transfer surface. As the heat exchange takes place on the aircraft wing, it may seem convenient to take use of correlations established for flow patterns around a NACA (National Advisory Committee for Aeronautics) profile [106]. The problem with these correlation is that they have been developed by considering isothermal conditions over the whole surface of the wing. This is not the case for the applications discussed in this thesis, since the heat transfer occurs only over a reduced portion of the total surface of the wing, as shown in Fig. 5.4a. In order to consider this effect, it can therefore be convenient to refer to the method proposed by Ameel [107], which takes account of the average effects of forced convection over a flat plate with an unheated starting length. To better understand this method, refer to the representation shown in Fig. 5.4b. The velocity boundary layer growth begins at $x = 0$, while thermal boundary layer development begins at $x = \xi$. Hence, there is no heat transfer for $0 < x < \xi$. For a plate of total length L, with laminar or turbulent flow over the entire surface, Ameel [107] gives the following expression for the average Nusselt number over the heated length of the plate:

$$\bar{N_{u_L}} = \frac{L}{L-\xi} N_{u_L}\bigg|_{\xi=0} \frac{n+1}{n}\left[1 - \left(\frac{\xi}{L}\right)^{\frac{2n+1}{2n+2}}\right]^{\frac{2n}{2n+1}} \tag{5.2}$$

Where n is a coefficient that takes into account laminar or turbulent flow conditions, while the quantity $N_{u_L}|_{\xi=0}$ represents the average Nusselt number for a plate of length L when heating starts at the leading edge of the plate. This quantity is function of Reynolds number Re_L and Prandtl number Pr according to the equation below [99]:

$$N_{u_L}\Big|_{\xi=0} = C Pr^m Re_L^{\frac{n}{n+1}} \tag{5.3}$$

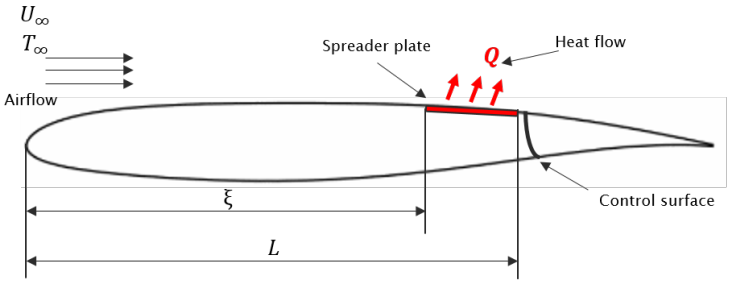

(a) NACA profile.

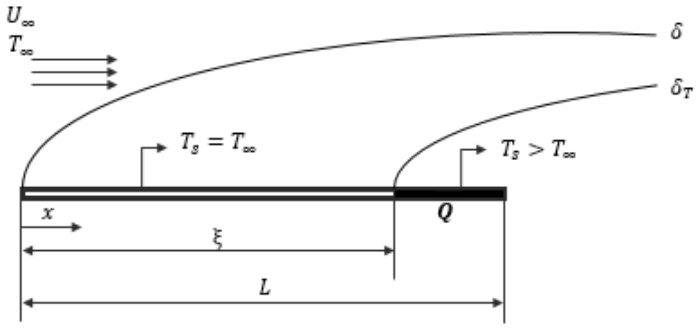

(b) Flat plate.

Figure 5.4: Heated surfaces with unheated starting length.

Typical values of the constants C, m, and n are given in Table 5.1, according to the type of flow and boundary conditions.

Table 5.1: Constants for use with Eq. 5.3 [107]

Case	Flow condition	Thermal Boundary condition	C	n	m
1	Laminar	Isothermal	0.332	1	1/3
2	Laminar	Isoflux	0.453	1	1/3
3	Turbulent	Isothermal	0.0287	4	3/5
4	Turbulent	Isoflux	0.030	4	3/5

Starting from the Nusselts number, the value of the average heat transfer coefficient over the heated length of the plate can be therefore calculated directly from relationship 5.1. Note that the Reynolds and Prandtl numbers depend on the properties of the air, which, being function of temperature and pressure, vary with the altitude. Correlation laws, presented in Section 7.2.4, have been developed to calculate the air properties within the temperature and pressure ranges encountered during the flight mission. For the applications considered

here, isoflux boundary conditions have been assumed for the calculation of the Nusselts number. We are aware that the heat transfer coefficient on a NACA profile is different from that on a plate. However, as there are no other studies in the literature (to our knowledge) with this specificity, the plate is the closest to our case.

5.3 Heat Pipe

The heat pipe is a very attractive solution for thermal management of primary flight control actuators because of its capability of transferring large amounts of heat with relatively small temperature differences. The main composition of a standard heat pipe is shown in Fig. 5.5. It is composed of an evaporator and condenser sections, connected to each other by an adiabatic pipe containing a wick. A working fluid is contained within the device, which is the main vehicle for heat transfer. The operating principle of the device is the following. The heat load coming from the heat source, vaporizes the working fluid in a liquid form at the evaporator section. The vapor flows through the adiabatic section toward the condenser section, mounted on a colder surface, where it condenses. Capillarity action then moves the condensed liquid back to the evaporator through the wick structure. The returning mechanism of the flow is assisted by gravity if the condenser is installed above the evaporator. This process of flow circulation continues as long as there is a temperature difference between the evaporator and condenser terminals. The fluid flow stops if the overall temperature is uniform, but starts moving again as soon as there is a temperature difference between the end plates.

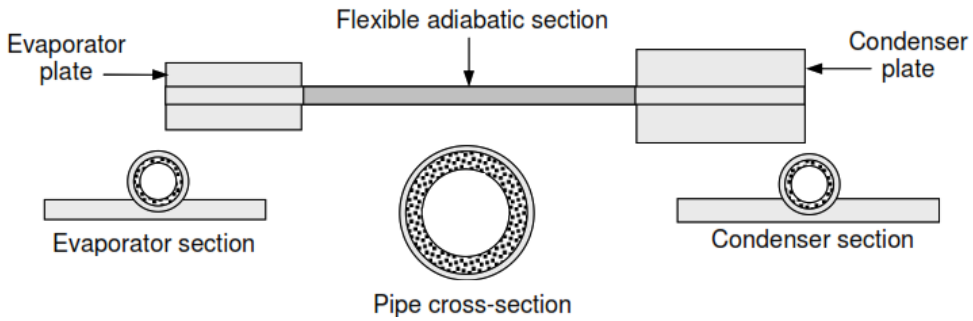

Figure 5.5: The main composition of heat pipe [108].

The main advantages of such devices are that they do not require external power to work and the working fluid is completely contained, so the device can be easily installed or removed. Other advantages include the compatibility of heat pipes to operate in highly constrained locations, and the ability to allow relative movement between the heat source and the heat sink. This is certainly advantageous for flight control actuators, which move relatively to the structure on which they are attached. The main selection parameters for heat pipes are related to the working fluid, which is selected according to the temperature range of application, and to the choice of the heat pipes container and wick materials, which essentially depend on their compatibility with the fluid.
Typical working fluids that could be adopted in this context and their temperature ranges are showed in Table 5.2.

Table 5.2: Example of Heat pipe working fluids usable in this context.

Medium	**Melting point** ($^\circ C$)	**Boiling point** ($^\circ C$)	**Useful range** $^\circ C$
Ammonia	-78	-33	-60 to 100
Pentane	-130	28	-100 to 120
Acetone	-95	57	-50 to 100
Methanol	-98	64	-60 to 130
Ethanol	-112	78	0 to 130
Heptane	-90	98	0 to 150
Water	0	100	30 to 200
Toulene	-95	110	-50 to 200

Within the same temperature ranges there might be several possible working fluids. Specific characteristics need to be examined in order to determine the most suitable fluid for the application considered. The main characteristics are: compatibility with wick and wall materials, high latent heat, high thermal conductivity, low fluid viscosity and good thermal stability. A convenient means to rapidly compare different working fluids is provided by the merit number, defined as:

$$M_r = \frac{\sigma L \rho}{\mu} \tag{5.4}$$

where σ is the surface tension, L the latent heat of vaporisation, ρ the liquid density and μ the liquid viscosity. An evident characteristic is the marked predominance of water, with its high latent heat and surface tension, compared to all organic fluids, such as acetone and alcohols. The selected final fluid is, of course, also dependent on cost, availability, compatibility and the other above-mentioned factors. At slightly lower temperatures , in

the range of $270-350\,K$, ammonia is a suitable fluid, although it demands careful handling to maintain a high degree of purity. Acetone and alcohols appear as good alternatives at lower vapour pressures. These fluids are frequently used in heat pipes for space applications. Water and methanol, both of which are compatible with copper, are often employed for cooling electronic equipment.

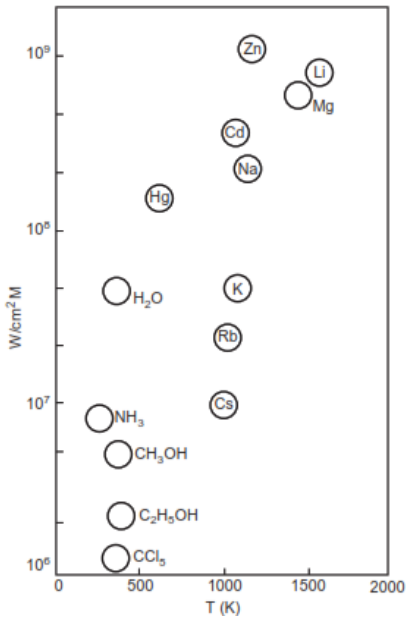

Figure 5.6: Merit Number vs Temperature for different working fluids [26].

The selection of the container wall material depends mainly on two factors: the compatibility with the working fluid and the thermal conductivity. The two main results of incompatibility are corrosion and non-condensable gas generation. The generation of non-condensable gases is the most common factor of heat pipe failure, as non-condensable agents tend to accumulate in the condenser section of the heat pipe, which gradually becomes blocked. An example of material compatibility with the working fluid is provided in Table 5.3. For the applications under investigation in this thesis, an operating temperature in the range from -30°C to 100°C is considered. This range was established according to the minimum atmospheric temperature encountered during the flight mission and the maximum temperature limit on the housing skin. On the basis of this operating range, the fluid/container material combinations shown in Tab. 5.4 could be considered. For the applications analysed here, aluminium heat pipes containing ammonia as working fluid have been selected. The choice of ammonia is motivated by the fact that it has a higher merit

factor than the other selectable fluids. Compared to other ammonia-compatible materials, aluminium is characterised by higher thermal conductivity and lower density.

Table 5.3: Material - Working fluid compatibility [26].

	Water	**Acetone**	**Ammonia**	**Methanol**
Copper	RU	RU	NR	RU
Aluminium	GNC	RL	RU	NR
Stainless steel	GNT	PC	RU	GNT
Nickel	PC	PC	RU	RL

RU, recommended by past succesful usage;
RL, recommended by literature;
PC, probably compatible;
NR, not recommended;
GNC, generation of gase at all temperatures;
GNT, generation of gas at elevated temperatures;

Table 5.4: Possible Material - Fluid combinations in the temperature range -30°C - 100°C.

Working fluid	**Container**
Ammonia	Aluminium
	Stainless Steel
	Nickel
Methanol	Copper
	Nickel
Acetone	Copper
	Aluminium

5.3.1 Heat transfer and temperature difference

In this section an overview of heat transfer and the associated temperature drops in the heat pipe is given. The thermal resistance of the heat pipe can be modelled by means of the equivalent circuit expressed in Fig. 5.7.

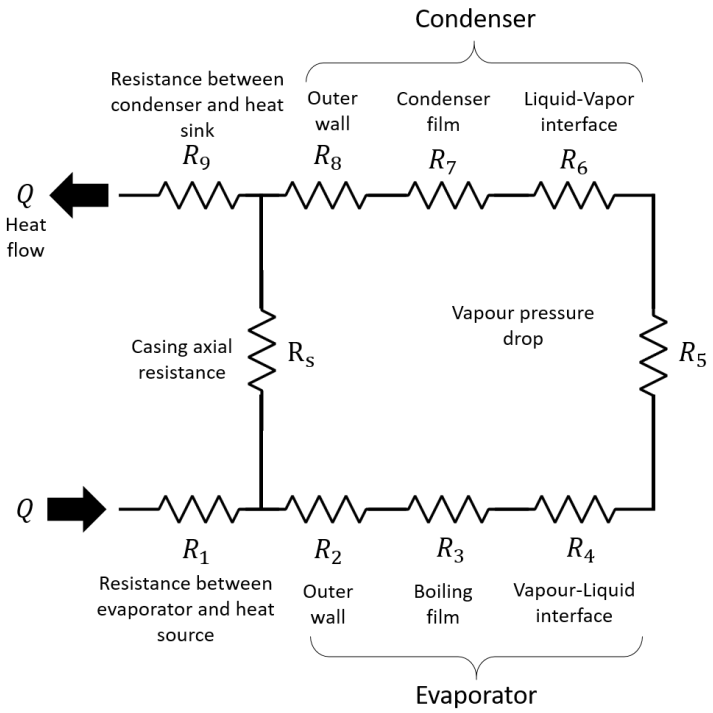

Figure 5.7: Heat Pipe Thermal Resistance Network.

The resistances representing the thermal circuit of the device are defined as follows:

- R_1 and R_9 represent the thermal contact resistances between the evaporator and the heat source and between the condenser and the heat sink.
- R_2 and R_8 represent the radial thermal resistances of the heat pipe wall at the evaporator/condenser level.
- R_3 and R_7 model the thermal resistances of the wick structure and explains any temperature difference between the wall and the liquid.
- R_4 and R_6 are the thermal resistances corresponding to the vapour-liquid surfaces. Their order of magnitude is around $10^{-5}\,°C\,cm^2/W$ and can usually be neglected.
- R_5 is modelling the temperature drop along the vapour column. It's order of magnitude is $10^{-8}\,°C\,cm^2/W$, so it can be neglected as well.
- R_s is the thermal resistance of the pipe connecting the evaporator to the condenser. This resistance is very large compared to all other resistances, which means that it can

be replaced by an open circuit. However, it may be important in other applications as the start-up of gas-buffered heat pipes [26].

On the basis of the above considerations, for the purposes of preliminary design, the resistive thermal circuit can be therefore simplified as shown in Fig. 5.8. In the next subsections, we will focus on the estimation of these resistances, leaving aside for a moment the evaluation of resistances R_1 and R_9, which will be discussed further in this chapter.

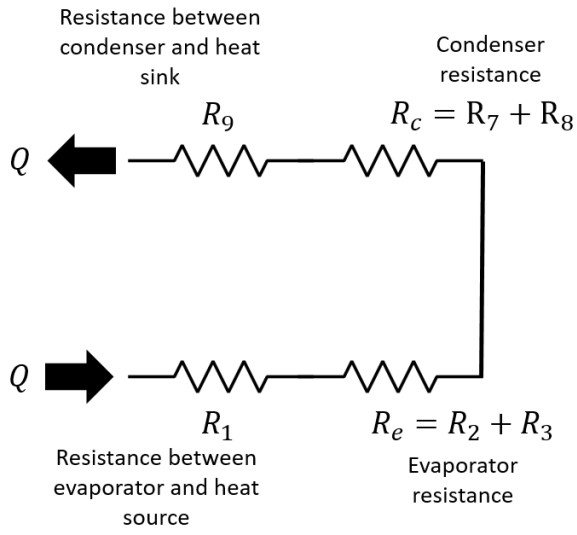

Figure 5.8: Simplified Heat Pipe Thermal Resistance Network.

5.3.2 Estimation model of heat pipe

The objective is to define a design model able to estimate the thermal resistances of the component, depicted in Fig. 5.8. The design of the heat pipe is rather complex, as besides sizing the liquid and the outer container, the wick has to be properly designed. The design of the wick is normally a detailed device design issue, usually performed by the heat pipe supplier. As a system design engineer, the preliminary design of a heat pipe should be limited to the choice of fluid, the number of tubes and their diameter, and the sizing of the evaporator(s)/condenser(s). Moreover, in the industrial sector, most companies propose their own solutions, based on their experience and mastery. The creation of a

customised heat pipe, even if accepted by the company, would require higher production costs. Especially if the product is made for prototyping purposes, and therefore cannot be industrialised in large quantities. In addition, from an industrial point of view, the choice of solutions commercially available may be more suitable during an initial investigation phase. For this reason, in this context, the design of the heat pipe has been carried out using linear regression on data-sheet catalogue of a commercially available heat pipe. In this regard, an aluminium grooved heat pipe produced by *EURO HEAT PIPES*, has been taken as reference. This heat pipe, depicted in Fig. 5.9, consists of an aluminium structure which contains ammonia as working fluid and which presents a capillary structure made up of extruded re-entrant grooves.

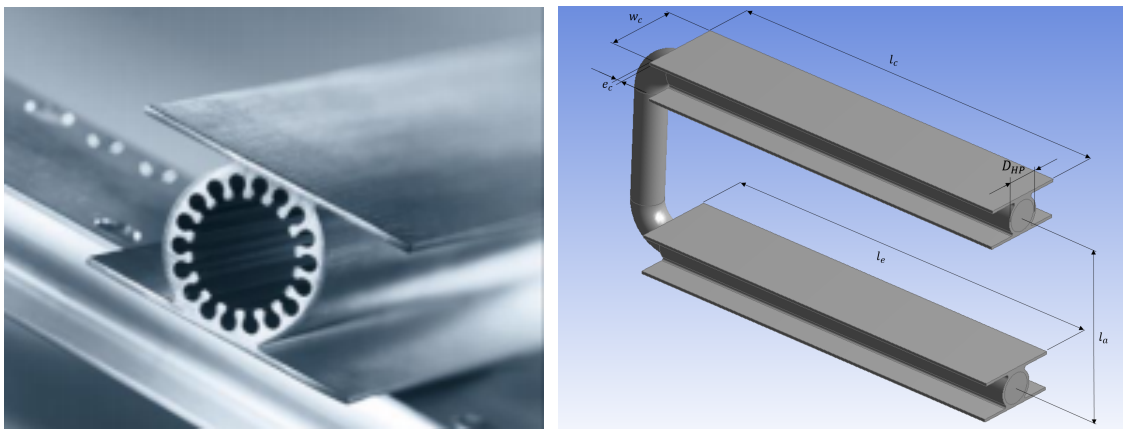

(a) EHP Heat Pipe. (b) Heat pipe dimensions

Figure 5.9: Heat pipe reference model [109].

The manufacturer provides the surface conductance values of the evaporator and condenser, which are useful for the computation of the thermal resistances of the component. The performances of the heat pipe is certified for gravity assisted operations. A summary of the characteristics of this heat pipe is given in Table 5.5. The supplier also provides the characteristic curves of the heat transport capability C_{HP} as a function of the working fluid temperature Θ_v, for the entire range of standardised diameters. On the basis of these curves, shown in Fig. 5.10, a mathematical regression has been established in order to determine the required diameter $d_{HP_{req}}$ of the heat pipe as a function of C_{HP} and Θ_v. The formulation obtained takes the following form:

$$d_{HP_{req}} = 8.74 + 0.021\, C_{HP} - 0.03018\, \Theta_v + 0.0005\, \Theta_v^2 \tag{5.5}$$

Table 5.5: Characteristics of the reference heat pipes.

Property	Value
Wall material	Aluminium
Working fluid	NH3
Capillarity structure	Extruded re-entrant grooves
Evaporator conductance, Λ_e	$5000\,W/m^2K$
Condenser conductance, Λ_c	$3500\,W/m^2K$
Heat transfer capability, C_{HP}	see Fig. 5.10
Maximum evaporator heat flux, $\Phi_{e_{max}}$	$7\,W/cm^2$
Maximum condenser heat flux, $\Phi_{c_{max}}$	$5\,W/cm^2$
Operating temperature range, Θ_v	$-60°C$ to $+100°C$

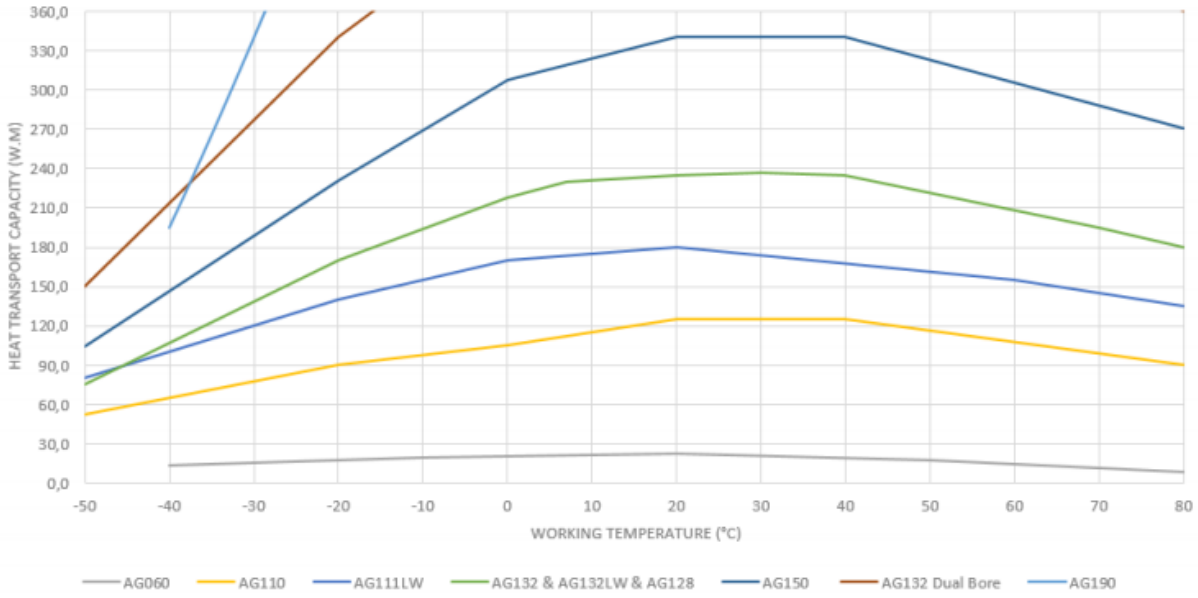

Figure 5.10: Heat transfer capability of heat pipes at given diameter and fluid temperature [109].

Similarly, a correlation law expressing the linear mass of the heat pipe m_{HP}, as a function of its diameter can be derived (according to the linear mass data provided by the manufacturer):

$$m_{HP} = 4.39\, {d_{HP}}^{0.61} \tag{5.6}$$

5.3.3 Heat pipe design

For the applications considered in this thesis, it has been planned to install one or more heat pipes between the top surface of the motor thermal housing and the top surface of the wing, as shown in Fig. 5.11.

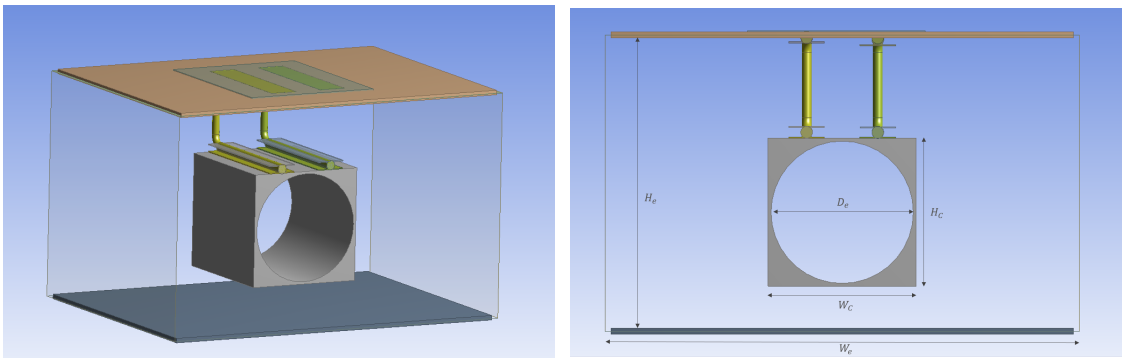

(a) 3-D view (b) Frontal view

Figure 5.11: Representation of the operating environment of heat pipes.

It is important to consider that, in this case, the housing only provides mechanical seal for the motor and support for the heat pipes. The convective heat exchange of the surface is therefore neglected, and only the phenomenon of thermal conduction/evaporation of the heat pipe is considered. The length of the housing L_c has been set equal to the length of the electric motor, while a width $W_c = D_e + 0.005m$ and height $H_c = D_e + 0.005m$ have been considered. Assuming that the housing is in the center of the volume allocated for the actuator, the adiabatic length l_a of the heat pipe can be estimated as follows:

$$l_a = \frac{H_e - H_c}{2} \tag{5.7}$$

In order to reduce the temperature gradient in the housing, we constrained the length of the evaporator l_e equal to that of the housing on which it is mounted. The length of the condenser l_c and the diameter of the heat pipes d_{hp} are set as design variables. The width and thickness of the end plates are fixed respectively to $w_c = 30\,mm$ and $e_c = 1.5\,mm$ (on the base of the data provided by the manufacturer). Once the characteristic dimensions of the heat pipe have been defined, the thermal resistance of the evaporator R_e and condenser R_c can be estimated as follows:

$$R_e = \frac{1}{\pi\, d_{HP}\, l_e\, \Lambda_e} \tag{5.8}$$

$$R_c = \frac{1}{\pi \, d_{HP} \, l_c \, \Lambda_c} \tag{5.9}$$

where Λ_e and Λ_c are respectively the evaporator and condenser surface conductance defined in Table 5.5.
The mass of the device, can be estimated as follows:

$$M_{HP} = m_{HP} \, (l_a + l_e + l_c) \tag{5.10}$$

It is necessary to verify that sized device complies with the minimum diameter requirements according to the the flow and temperature conditions encountered during operation. Moreover, the device must meet the maximum flow requirements, both on the condenser and evaporator sides, imposed by the manufacturer (Tab. 5.5).

5.4 Thermal Strap

The thermal strap provides a flexible and lightweight conduction path to move heat from the heat source to a cold surface. Widely used in aerospace applications [110] [111] [112], this advanced conduction solution consists of highly conductive and flexible materials connected to separate surface-mounted terminal plates that enable point-to-point heat transfer (Fig. 5.12 and Fig. 5.13).

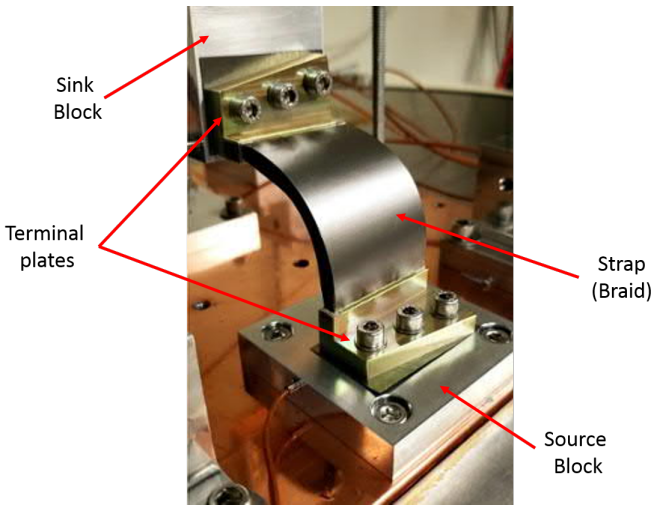

Figure 5.12: Thermal strap structure [113].

Thermal straps are completely passive equipments, eliminating maintenance costs and

providing lightweight solutions for low-dynamics and weight-sensitive applications. The thermal performance of a thermal strap is evaluated in terms of its thermal conductance G, expressed in (W/K). Aluminum and copper are common materials generally adopted due to their high thermal conductivity [114]. Pure copper straps provide excellent thermal performance, but are characterised by high mass and stiffness. The thermal conductivity of pure aluminium is 40% lower than that of pure copper at $300\,K$. On the other hand, pure aluminium has a density and stiffness that are respectively 30% and 60% lower compared to pure copper. Aluminium thermal straps often can fulfil the requirements in terms of mass, conductivity, flexibility and reliability with acceptable weight [115]. However, pyrolytic graphite foils (PGF) have recently emerged as new candidates for flexible material in thermal straps. [114].

Figure 5.13: Example of different types of thermal straps [113].

The thermal conductivity of pyrolytic graphite at 300 K is approximately 3.5 and 6 times greater than pure copper and pure aluminium, respectively [99]. In addition, its density is much lower than that of copper and aluminium. The specific thermal conductivity of a material, expressed as its thermal conductivity divided by its density, offers a figure of merit for comparing the thermal straps. The specific thermal conductivity at $300\,K$ of pyrolytic graphite, pure aluminum, and pure copper are respectively 0.63, 0.088 and 0.045 Wm^2/kgK. Besides being an excellent thermal conductor, PGF is highly flexible and has a modulus of elasticity of $23\,GPa$ at $300\,K$, as measured by beam deflection [116], which is 5 and 3 times lower than that of pure copper and pure aluminum, respectively [117]. Given the enormous advantages induced by these types of materials, PGF thermal straps are therefore selected for this project.

5.4.1 Estimation model of thermal straps

Scaling laws applied to an industrially available PGF thermal strap, depicted in Fig. 5.14, have been adopted for estimating the thermal resistance and mass of the component. A summary of the characteristics of this thermal strap is given in Table 5.6.

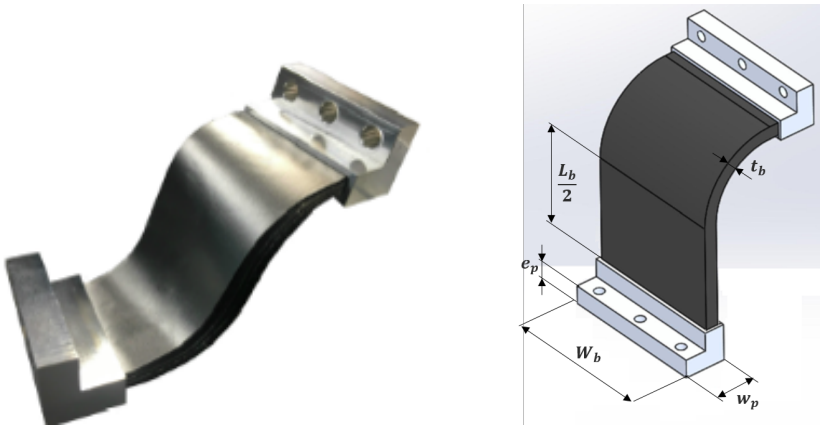

(a) PGF Thermal Strap [113]. (b) Thermal strap dimensions.

Figure 5.14: Thermal strap reference model.

Table 5.6: Characteristics of the reference thermal strap [113]

Property	**Value**
Strap length, $L_{b_{ref}}$	101.6 mm
Strap width, $W_{b_{ref}}$	50.8 mm
Strap thickness, $t_{b_{ref}}$	4.6 mm
Plate width, $w_{p_{ref}}$	15 mm
Plate thickness, $e_{p_{ref}}$	6.35 mm
Plates thermal resistance, $R_{plates_{ref}}$	0.242 K/W
Strap thermal resistance, $R_{braid_{ref}}$	0.272 K/W
Pyrolitic graphite conductivity at 300K, λ_{graph}	1700 W/mK
Plates mass, $M_{plates_{ref}}$	19.6 g
Strap mass, $M_{braid_{ref}}$	51.4 g

The thermal resistance of the device R_{TS} can be represented as a series connection of its constituent resistances [118]:

$$R_{TS} = R_{braid} + R_{plates} \tag{5.11}$$

where R_{braid} is the conduction thermal resistance of the strap and R_{plates} is the contact resistance between the ends of the braid and the strap end-lug. The calculation of the former is relatively simple, and can be determined through the relations established for the calculation of the conduction resistance in a plane wall [99]. The determination of R_{plates} is more complex, as it requires taking into account the contact phenomenon, which is difficult to estimate analytically. By analyzing the manufacturer's products, it was observed that all the dimensions of the connecting plates (except for the width, W_b) do not vary with the thickness of the strap. The plate width roughly equals that of the strap. Therefore, the product between the plate's resistance and its width is modelled by a scaling law:

$$R_{braid} = \frac{L_b}{\lambda_{graph} W_b t_{b_{ref}}} \tag{5.12}$$

$$R_{plates} = \frac{W_b}{W_{b_{ref}}} R_{plates_{ref}} \tag{5.13}$$

where λ_{graph} is the thermal conductivity of pyrolitic graphite, L_b and W_b are respectively the length and width of the braid, while $t_{b_{ref}}$, $W_{b_{ref}}$ and $R_{plates_{ref}}$ represent respectively the thickness, width and plates resistance of the reference component. The thermal conductivity λ_{graph} is temperature dependent and it can be extracted from the curve defined by Taylor [119], depicted in Fig. 5.15.

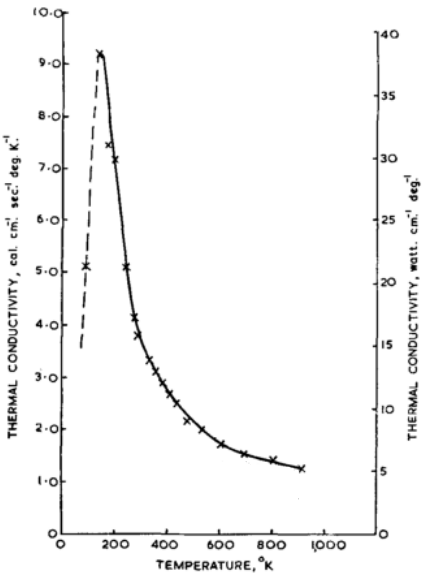

Figure 5.15: Thermal conductivity of pyrolitic graphite [119].

The total mass M_{TS} of the device is given by the mass contributions of the braid M_{braid} and the plates M_{plates}, which can both be estimated as follows:

$$M_{TS} = M_{braid} + M_{plates} = \frac{L_b}{L_{b_{ref}}} \frac{W_b}{W_{b_{ref}}} M_{strap_{ref}} + \frac{W_b}{W_{b_{ref}}} M_{plates_{ref}} \tag{5.14}$$

5.4.2 Thermal strap design

The design of the straps is similarly based on the considerations previously applied to the heat pipes. This means that, it has been planned to install one or more thermal straps between the top surface of the motor thermal housing and the closest surface of the wing, as shown in the example in Fig. 5.16. Also in this case, the same housing adopted for the heat pipes is used to provide mechanical seal for the motor and support for the thermal straps. Assuming that the housing is mounted in the middle of the actuator room, the length of the strap can be estimated as follows (assuming the same configuration of heat pipes illustrated in Fig. 5.11):

$$L_b = \frac{H_e - H_c}{2} \tag{5.15}$$

On the basis of the foregoing assumptions, the only degree of freedom on the design is given by the width of the strap W_b, while the remaining dimensions of the device are fixed to the dimensions of the reference component (Table 5.6). Once defined the dimensions, the thermal resistances and mass of the device can be estimated by means the defined relationships Eq. 5.11 - Eq. 5.14.

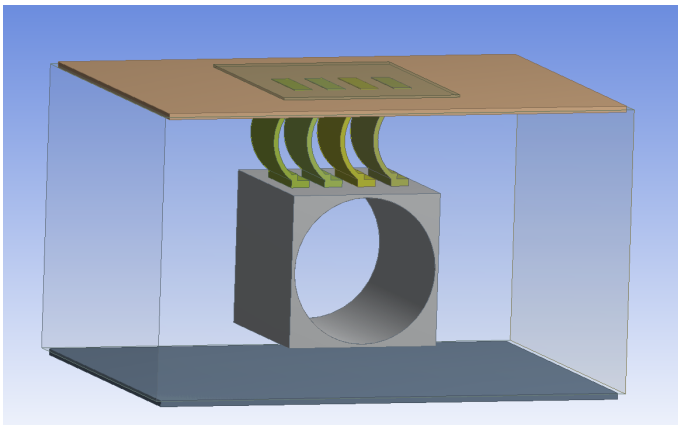

Figure 5.16: Representation of the operating environment of thermal straps.

5.5 Thermal spreader

To increase the effectiveness of the heat pipes and thermal straps, it is necessary to ensure a large heat exchange surface with air. Thermal spreaders can therefore be used to this purpose. In order to define the thermal model of the spreader, the case study represented in Fig. 5.17 and Fig. 5.18 is considered.

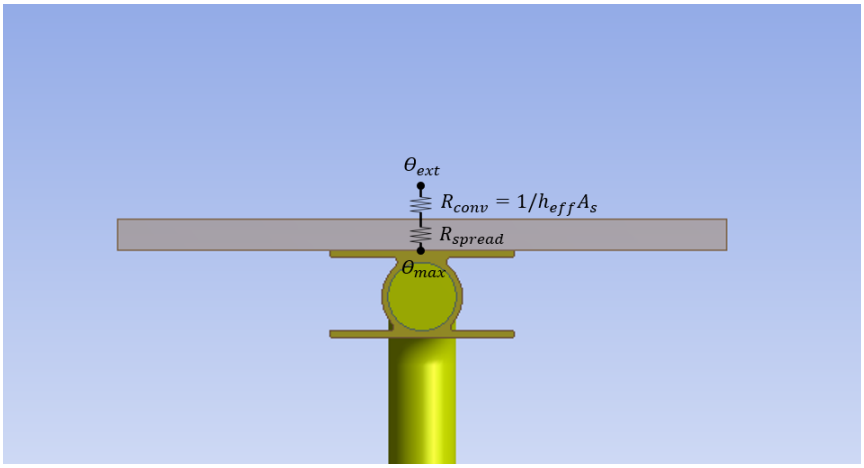

Figure 5.17: Connection of the spreader with the heat pipe.

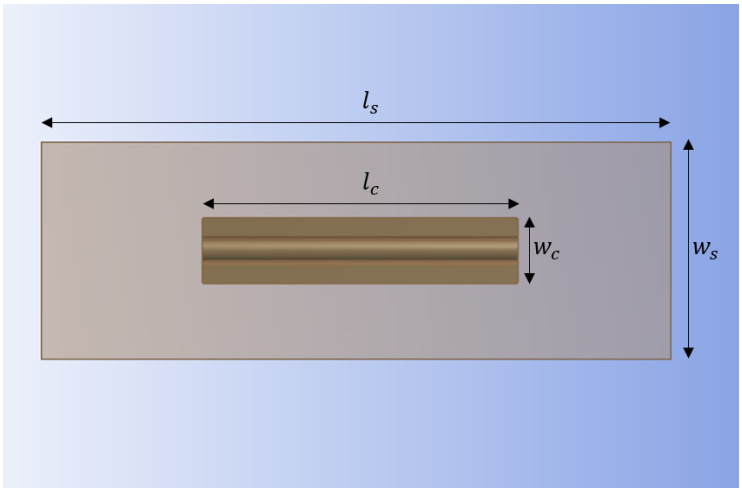

Figure 5.18: Spreader geometry of the considered case study.

This consists of a single rectangular spreader, mounted on a rectangular heat source representing the condenser plate of the heat pipe (or the connector of the thermal strap). The heat source is located at the middle of the lower side of the spreader plate, while a heat transfer coefficient h_{eff} is considered on the opposite side. The total thermal resistance from Θ_{max} to Θ_{ext} can be expressed as follows:

$$R_{tot} = \frac{\Theta_{max} - \Theta_{ext}}{Q} \tag{5.16}$$

where Θ_{max} is the temperature of the heat source, Θ_{ext} is the exterior temperature and Q represents the heat flow. The total thermal resistance is composed of a conduction/diffusion resistance R_{spread} and a convection resistance R_{conv}.

$$R_{tot} = R_{conv} + R_{spread} \tag{5.17}$$

The conduction/diffusion resistance, R_{spread}, includes diffusion effects and is affected by the effective heat transfer coefficient acting on the upper surface. Exact analytical solutions to the partial differential equations, for the computation of this resistance, have been reported in the literature [120] [121] [122]. Unfortunately, the solution can be obtained through a complicated infinite series with equally complicated coefficient terms, which is not easily adaptable to the context of this thesis. In the case of preliminary design, estimation models are needed in order to be able to rapidly predict the thermal resistance of the spreader.

5.5.1 Estimation model of a Thermal Spreader

The estimation model adapted here takes use of the formulations derived by Lee et al. [123]. The authors developed a closed-form solution which can provide results very close to the exact solution and easily implementable into computation spreadsheets or similar scheme. The solution is based upon a circular plate spreader with a circular heating area. Since the geometries involved in these context are rectangular, it becomes necessary to adopt transformations in order to apply these solutions. The transformation is based on the fact that the areas of the plate and the heat source are the same in both square and

circular geometry [124]. Thus, the equivalent radii in the rectangular case are given by:

$$r_1 = \sqrt{\frac{l_c w_c}{\pi}} \tag{5.18}$$

$$r_2 = \sqrt{\frac{l_s w_s}{\pi}} \tag{5.19}$$

where l_c and w_c are respectively the length and width of the condenser plate, while l_s and w_s represent the length and width of the spreader. By considering a spreader of thickness t and thermal conductivity λ_s, the thermal resistance can be estimated via the following set of equations:

$$\epsilon = \frac{r_1}{r_2} \tag{5.20}$$

$$\tau = \frac{t}{r_2} \tag{5.21}$$

$$Bi = \frac{h_{eff} r_2}{\lambda_s} \tag{5.22}$$

$$\lambda = \pi + \frac{1}{\epsilon\pi} \tag{5.23}$$

$$\Phi = \frac{tanh(\lambda\tau)\frac{\lambda}{Bi}}{1 + \frac{\lambda}{Bi} tanh(\lambda\tau)} \tag{5.24}$$

$$\Psi = \frac{\epsilon\tau}{\sqrt{\pi}} + \frac{1}{\sqrt{\pi}}(1-\epsilon)\Phi \tag{5.25}$$

$$R_{spread} = \frac{\Psi}{\lambda_s r_1 \sqrt{\pi}} \tag{5.26}$$

Thanks to the just outlined equations is so possible to rapidly estimate the thermal resistance of the spreader.
The mass of the spreader plate is easily computed as follows:

$$M_{spread} = \rho_a \, t \, l_s \, w_s \tag{5.27}$$

5.5.2 Thermal spreader design

In order to calculate the thermal resistance and mass of the spreader, it is necessary to define the geometry of the heat source and that of the spreader plate. The surface area of the heat source is fixed by the length and width of the end plates of the considered heat transfer device (for thermal strap: W_b, w_p; for heat pipe: l_c, w_c). The geometry of the spreader is represented by the width w_s and length l_s, which are considered design variables. For these variables a maximum range is defined as a function of the length L_e and width W_e of the actuator compartment, illustrated in Fig. 5.11b. An aluminum plate with a thickness of $t = 2\,mm$ has been considered. Having defined the dimensions concerned, and depending on the heat transfer coefficient introduced in Section 5.2.2, the resistances and mass of the spreader are then calculated according to Eq.5.26 and Eq. 5.27.

5.6 Thermal interface material

One of the problems of interfacing heat pipes and thermal straps, is to ensure a good thermal contact between the surfaces across which the heat transfer occurs. In general, these kinds of devices are commonly joined by bolts. The main problem with bolted joints is that due to the non-uniform distribution of stresses, the bodies in contact deform and the regions away from the bolts separate slightly, as shown in Fig. 5.19. Although very

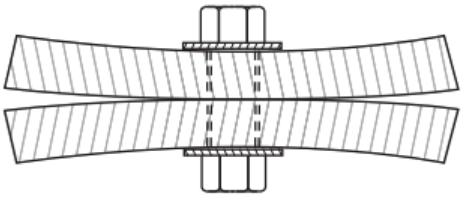

Figure 5.19: Example of surface deformation due to bolted joints [67].

small, this separation greatly influences the heat flow between the surfaces, and heat is mainly transferred through the regions under or near the bolts [125]. As the contact area increases and the thickness of the contact plates decreases, this problem intensifies and more bolts are required to maintain proper thermal conductance between the two parts. To overcome this problem, thermal interface materials can be used. In this way, by means

of these materials, it is possible to fill the gap between the mating surfaces. An increase of the contact area is so obtained and the heat transfer is improved as consequence. The effectiveness of these materials depends on the material type, and on the geometric and mechanical properties of the joints. But as a general rule, an improvement of 1.5 times in large, thin plates and 3 to 5 times in small, rigid plates can be obtained [125]. Fig. 5.20 illustrates an example of the result that can be obtained when a bare interface is confronted with an interface including TIM. For a bare interface, the contact is only located in the immediate area surrounding the fasteners. The interposition of a TIM can significantly expand the contact area [126].

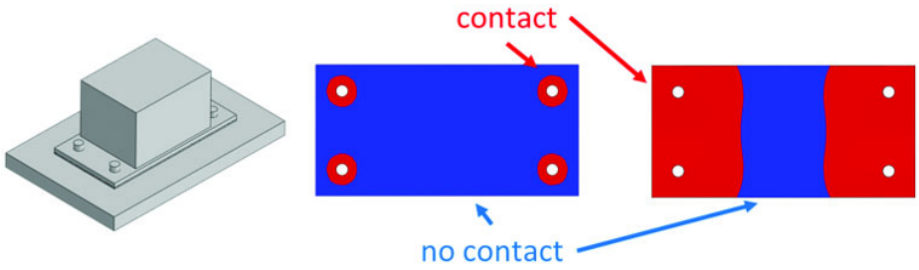

Figure 5.20: Contact zone of bare interface (left) and interface with polymeric TIM (right)[126].

Different types of TIMs are available commercially, such as thermal greases, gels, adhesives, phase change materials, metal foils, polymeric TIMs and even carbon nanotubes. However, the aircraft industry only allows the use of some of them, due to strict regulations on outgassing and fluid contamination. Only certain particle-laden silicone materials, metal foils and polymeric TIMs are accepted. In this thesis, the utilisation of a silicone elastomer TIM is considered.

5.6.1 Estimation model of TIM

The heat transfer through an interface is a complex process since it depends on many geometrical, mechanical and physical parameters [127] [128] (geometry of the contact surfaces, type of the thermal interface material, contact pressure, thermal conductivity of the contacting bodies, Young's modules of the two bodies etc.). If all these factors are known at a given joint, then reliable models are available to predict the thermal contact resistance. Otherwise, the most accurate method is to conduct experimental tests. Developing

a model to predict thermal resistance of such materials is therefore very challenging, in view of the large number of factors influencing the phenomenon. In achieving this objective, the approach adopted in this thesis is not to provide an extremely precise description of the system studied and the physical phenomena involved. Rather, it is to propose a model that is as synthetic as possible, to be effectively integrated and coupled in the preliminary design phase of the actuator. To this purpose, a surrogate model extracted from finite element simulations has been developed. The proposed model focuses mainly on the mechanical behaviour of the interfacing surfaces and the TIM, in order to obtain the contact areas and the pressure distribution in these regions. The mastery and optimisation of the TIM performance in fact, can only be obtained through a good understanding of the contact zones. Fig. 5.21 schematizes the level of abstraction used to build the model.

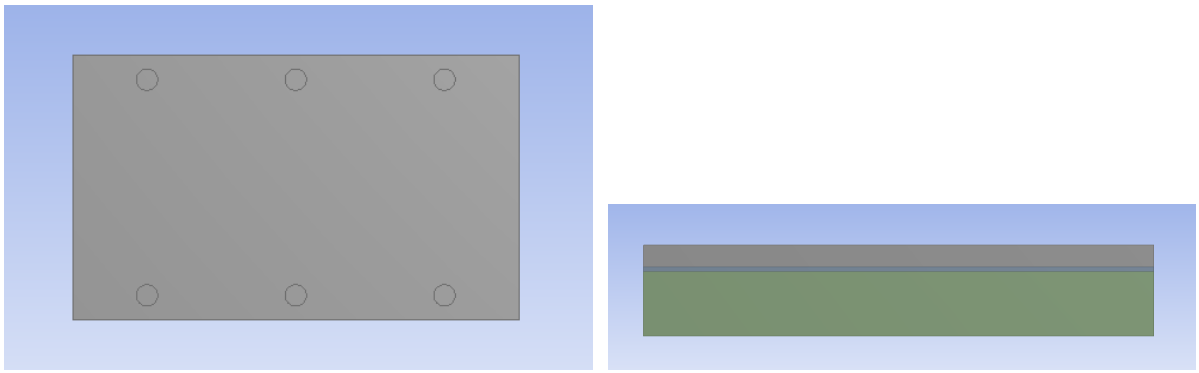

(a) Top view of the system (b) Frontal view of the system

Figure 5.21: Representation of interfacing surfaces.

A thin plate at the top of the assembly represents the aluminium end plate of the heat pipe or thermal strap. This plate is then placed on a thin layer of TIM. A Thermally Conductive Elastomer Insulators, manufactured by *Chomerics*, has been taken as reference. This TIM, largely used in aerospace applications, is a silicone elastomer filled with boron nitride particles and reinforced with fibreglass cloth. A summary of the material characteristics is shown in Table 5.7. The TIM is placed on a support that represents the thermal housing on which the heat transfer devices are mounted. In order to facilitate the analysis of the system and given its symmetry, it was chosen to analyse and model only the region of the system affected by a single bolt, as represented in Fig 5.22.

Table 5.7: "CHO-THERM 1671" TIM properties.

Properties	Characteristics
Binder	Silicone
Filler	Boron Nitride
Carrier	Fiberglass
Thickness e_{TIM}	$0.38\,mm$
Surface thermal resistivity r_{TIM}	$1.48e^{-4}Km^2/W$
Operating Temperature Range	$-60°C$ to $+200°C$
Young's modules E_{TIM}	$124\,MPa$
Optimum contact pressure range P_c	$2.07\,MPa$ to $3.45\,MPa$

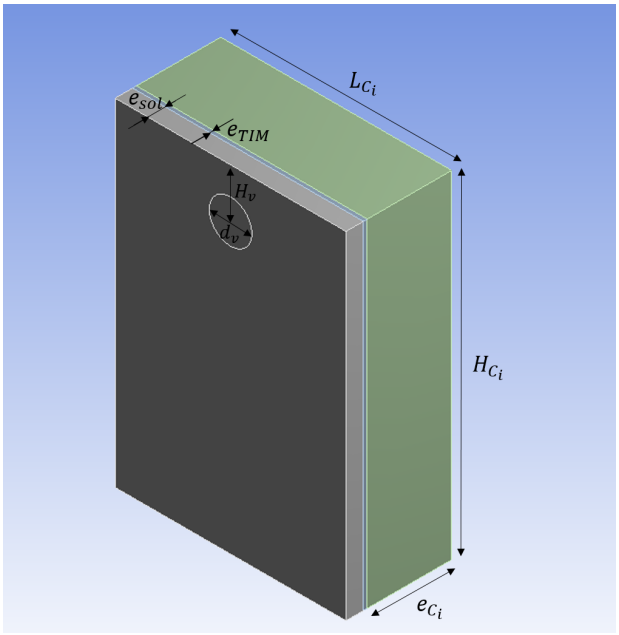

Figure 5.22: Geometry of the analysed model.

The composition of the total system will then be given by the union of the individual modeled parts, according to the number of bolts used. Moreover, fasteners are not modeled but replaced by uniform loads at the location of the contact zone between the bolt head and the fixing surface. The diameter of the bolt d_v is expressed as a function of the contact pressure P_c and the fastening pressure P_v, according to the following relationship:

$$d_v = \sqrt{\left(\frac{P_c L_{C_i} H_{C_i}}{\frac{\pi P_v}{4}}\right)} \tag{5.28}$$

A contact pressure $P_c = 2.75\,MPa$ is therefore taken as a reference in this study. With regards to the pressure exerted by the bolt, $P_v = 150MPa$ has been set according to COLLINS aerospace internal references for fastening pressures of actuator bolts. The aim is therefore to develop a surrogate model able to estimate the percentage of contact area S_c in relation to the total area S. The first step of surrogate model generation, deals with the dimensional analysis, in order to identify all the geometrical (g) and physical (p) variables influencing the phenomenon under consideration. These variables, which are defined in Table 5.8 and represented in Fig. 5.22, are:

$$S_c = f(\overbrace{H_{C_i}, L_{C_i}, e_{C_i}, H_v, e_{sol}, e_{TIM}, d_v}^{g}, \overbrace{E_{TIM}, E_{al}, P_c, P_v}^{p}) \tag{5.29}$$

Table 5.8: Dimensional variables of the system under study.

Variable	Definition	Range	Unit
L_{C_i}	Module length	$[20-60]$	mm
H_{C_i}	Module height	$[20-90]$	mm
e_{C_i}	Housing thickness	$[5-22.5]$	mm
e_{sol}	Plate thickness	$[1.5-5]$	mm
e_{TIM}	TIM thickness	$[0.38]$	mm
H_v	Bolt position	$[7-16]$	mm
d_v	Bolt diameter	$[4-10]$	mm
E_{TIM}	Young's module TIM	$[125]$	MPa
E_{al}	Young Aluminium plate	$[750000]$	MPa
P_c	Contact pressure	$[2.75]$	MPa
P_v	Fastening pressure	$[150]$	MPa

In the twelve identified quantities, there are two independent dimensions $[N, m]$. According to the Buckingham-Pi theorem, ten dimensionless parameters are necessary to completely describe the problem, as illustrated in Table 5.9.

$$\Pi_{0_{TIM}} = f(\Pi_{1_T}, \Pi_{2_T}, \Pi_{3_T}, \Pi_{4_T}, \Pi_{5_T}, \Pi_{6_T}, \Pi_{7_T}, \Pi_{8_T}, \Pi_{9_T}) \tag{5.30}$$

where $\Pi_{0_{TIM}} = \frac{S_c}{H_{C_i} L_{C_i}}$.

Table 5.9: Dimensionless variables of the system under study.

Variable	Definition	Range
Π_{1_T}	$\frac{L_{C_i}}{H_{C_i}}$	$[0.4 - 1.64]$
Π_{2_T}	$\frac{e_{sol}}{H_{C_i}}$	$[0.05 - 0.14]$
Π_{3_T}	$\frac{e_{TIM}}{H_{C_i}}$	$[0.005 - 0.011]$
Π_{4_T}	$\frac{H_v}{H_{C_i}}$	$[0.15 - 0.29]$
Π_{5_T}	$\frac{e_{C_i}}{H_{C_i}}$	$[0.25]$
Π_{6_T}	$\frac{d_v}{H_{C_i}}$	$[0.51 - 0.82]$
Π_{7_T}	$\frac{E_{al}}{E_{TIM}}$	$[6000]$
Π_{8_T}	$\frac{P_c}{E_{TIM}}$	$[0.022]$
Π_{9_T}	$\frac{P_v}{E_{TIM}}$	$[1.2]$

Among the ten dimensionless variables, the variables Π_{9_T}, Π_{8_T} and Π_{7_T} represent constant ratios, so they can be omitted from the description of the model. Regarding the variable e_{C_i}, since it represents the thickness of the thermal housing, it was decided to make it reasonably large in relation to the thickness of the plate and the TIM. In this way, it can be varied in geometric similarity with respect to H_{C_i} according to the relation $\frac{e_{C_i}}{H_{C_i}} = \frac{1}{4}$. Since the variable Π_{6_T} is intrinsically dependent on variable Π_{1_T}, it can consequently be omitted from the model. Its dependence on Π_{1_T} can be demonstrated as follows:

$$\frac{d_v}{H_{C_i}} = f\left(\sqrt{\frac{P_c L_{C_i} H_{C_i}}{P_v H_{C_i}^2}}\right) = f\left(\sqrt{\frac{L_{C_i} H_{C_i}}{H_{C_i}^2}}\right) = f\left(\sqrt{\Pi_{1_T}}\right) \tag{5.31}$$

The relation 5.30 can be therefore simplified in this way:

$$\Pi_{0_{TIM}} = f(\Pi_{1_T}, \Pi_{2_T}, \Pi_{3_T}, \Pi_{4_T}) \tag{5.32}$$

Once the inputs of the model are defined, a LHS DoE with 30 points generates the configurations to be simulated with finite element simulations in ANSYS software. The range of variables was chosen appropriately in order to obtain rectangular contact surfaces. In fact, during the simulation phase, two different behaviours were observed. Depending on the geometry of the system, the contact surface can take either a rectangular or a circular shape, as shown in Fig. 5.23. The problem that arises is that it is not possible to capture

the two phenomena through the use of a single surrogate model. A first DoE was then generated to analyse the different behaviours, and subsequently extract the configurations generating rectangular contact surfaces. The rectangular contact surfaces are preferred because the analysis carried out showed that they generate contact areas greater than 50% of the total surface area, while circular surfaces are present in contact areas of less than 50%. Once the configurations defined by the DoE are simulated, the surrogate model is built. The mathematical expression of the model takes the form of:

$$\Pi_{0_{TIM}} = 0.34 + 25.94\Pi_2\Pi_4 + 0.62\Pi_1\Pi_4 - 100.46\Pi_3\Pi_4 \tag{5.33}$$

From $\Pi_{0_{TIM}}$, the contact resistance can then be calculated as follows:

$$R_{th_{cont}} = \frac{r_{TIM}}{S_c} = \frac{r_{TIM}}{\Pi_{0_{TIM}} H_{C_i} L_{C_i}} \tag{5.34}$$

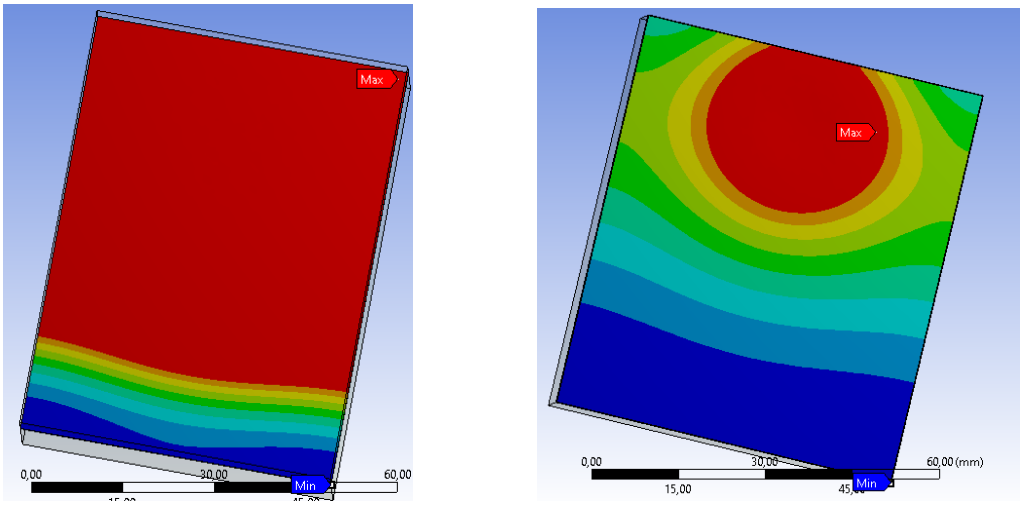

(a) Rectangular shape of contact surface

(b) Circlular shape of contact surface

Figure 5.23: Example of contact surfaces shape (red zone).

5.6.2 TIM design

The objective is to define the contact resistance of the TIM, which is used to interface the end plates of the heat pipes or thermal straps. For ease of discussion, we will consider in this paragraph the heat pipe interfacing, taking into account that in the case of thermal strap a different geometry of the end plates will be adopted. The interfacing of the device takes place in two different zones, as shown in Fig. 5.24: on the heat source side between the housing surfaces and the evaporator plate; and on the heat sink side between the thermal spreader and the condenser plate.

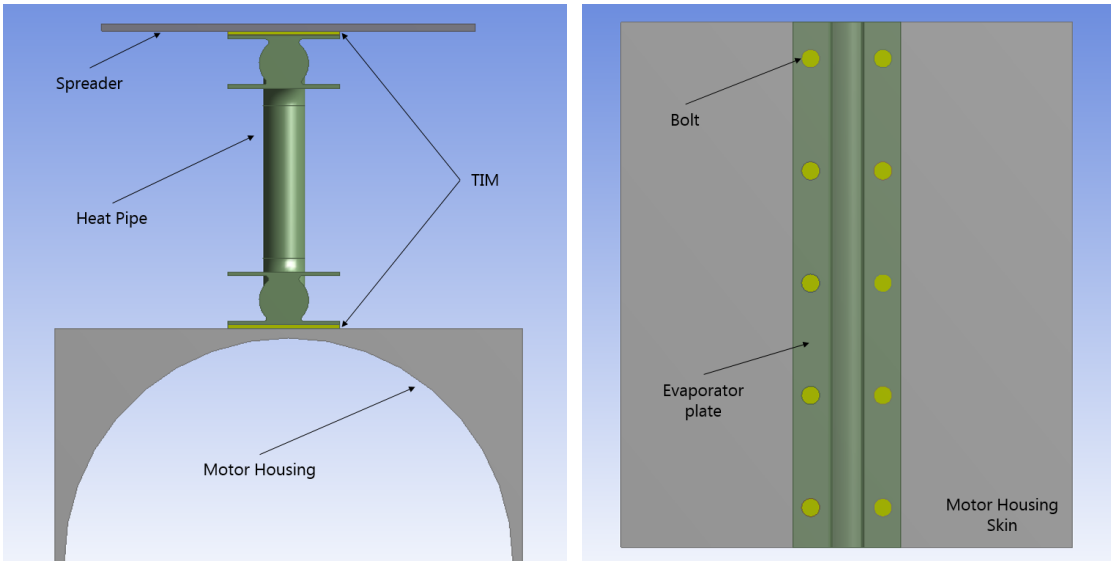

(a) Frontal view of the system (b) Top view of the system

Figure 5.24: Representation of the interfacing problem for the heat pipe case study.

The introduced surrogate model allows the estimation of the contact surface in the area affected by the individual bolt, as a function of the dimensionless variables $\Pi_{0_{TIM}}$, Π_{1_T}, Π_{2_T}, Π_{3_T} and Π_{4_T} (expressed in Table 5.9). The number of bolts k_{bt} as well as the variable Π_{4_T} are set as design variables, while the variables Π_{1_T}, Π_{2_T} and Π_{3_T} are calculated as a function of the geometry of the end plates. As far as the condenser plate is concerned, these are calculated as follows:

$$\Pi_{1_T} = \frac{2\,l_c}{w_c\,k_{bt}} \tag{5.35}$$

$$\Pi_{2_T} = \frac{2\,e_c}{w_c} \tag{5.36}$$

$$\Pi_{3_T} = \frac{2\, e_{TIM}}{w_c} \tag{5.37}$$

Starting from the values of the defined dimensionless variables, the variable $\Pi_{0_{TIM}}$ is computed according to Eq. 5.33 and the contact surface S_c is so extracted as follow:

$$S_c = \Pi_{0_{TIM}} \frac{l_c}{k_{bt}} \frac{w_c}{2} \tag{5.38}$$

The total contact surface $S_{c_{tot}}$ along the whole plate can then be calculated as below:

$$S_{c_{tot}} = 2\, k_{bt}\, S_c \tag{5.39}$$

As a function of the total contact surface, the thermal contact resistance is computed according to Eq. 5.34:

$$R_{th_{cont}} = \frac{r_{TIM}}{S_{c_{tot}}} \tag{5.40}$$

In the same way, the contact resistance on the evaporator side is determined, according to the geometry of the evaporator plate (the width w_c and thickness e_c of the evaporator plate are identical to those considered for the condenser, while the length of the plate instead is related to the evaporator length l_e).

5.7 Conclusion

In this chapter, the potential applications of heat pipes and thermal straps for the thermal management of flight control actuators have been discussed. Their operating principles, technological difficulties and methods for improving their efficiency have been described.
An installation technique, which allows the use of the airflow acting on the wing as cold source, has been proposed. This involves installing the end plate of the considered devices in direct contact to a thermal spreader mounted on exterior side of the wing.
A method for determining the convective heat transfer coefficient on the heated surface has been illustrated.
The estimation models of heat pipes and thermal straps have been subsequently presented. As far as heat pipes are concerned, linear regressions on data-sheet catalogue have been carried out in order to calculate the required diameter according to the thermal specifications. A commercially available heat pipe made of aluminium and containing ammonia as

working fluid has been taken as reference for the realisation of the model.
With regard to thermal straps, devices made of pyrolitic graphite foils have been considered and modelled by means of scaling laws.
Techniques to increase the heat transfer area and to minimise the contact resistance of the interfacing surfaces have been subsequently presented. In the first case, the use of a thermal spreader has been proposed and an analytical model representing its thermal resistance has been established. In the second case, the use of thermal interfacing materials has been considered. A surrogate model enabling the calculation of the contact surface in the interfacing zone has been developed.

Chapter 6

Model Generation of Unconventional Thermal Management Systems: Solutions for Transient Regime

Contents

6.1 Introduction **149**

6.2 Characterisation and classification of mission profiles **150**

6.2.1 Analysis of PST and PSE indicators for the considered mission profiles 153

6.3 Sensible heat storage **155**

6.3.1 Design techniques to improve sensible heat storage 157

6.4 Phase Change Materials **158**

6.4.1 Mathematical representation of the phase transition of a PCM Slab 160

6.4.2 Application of the mathematical formulations 163

6.4.3 Model of the PCM integrated in a finned plate 166

6.4.4 PCM-Fin module design 170

6.5 Conclusion **172**

6.1 Introduction

Solutions to improve transient storage were previously introduced in Section 2.3.3. It has been outlined how, using them, it is possible to design a smaller and lighter system, while at the same time allowing the operational thermal limits to be met during peak heat load

phases. Two storage methods were presented: the sensible heat storage, which uses the thermal capacity of the material to absorb heat without involving a phase change, and the latent heat storage, achieved through phase change materials (PCM), which absorb thermal energy during their phase transition. In this chapter, solutions aimed at implementing these two methods are discussed in more details.
In the first part of the chapter, a procedure to identify the most favourable mission profiles for the use of thermal storage systems is presented. This procedure, is based on the calculation of two coefficients defining the thermal storage potential (PST) and the energy storage potential (PSE) according to the type of the mission profile.
Subsequently, design techniques to improve sensible heat storage are discussed. These methods rely on altering the geometries and dimensions of the actuator components, in compliance with the admissible technological limits, in order to increase their heat capacities.
The second part of the chapter deals with the phase change materials. Their operating principles, constraints and methods for enhancing their thermal performances are illustrated. Successively, mathematical formulations are introduced in order to represent the thermal behaviour of a PCM slab during the phase transition. These formulations have then been re-adapted and implemented in *Dymola* [129] modelling environment, in order to define the model of a PCM integrated within an aluminium finned plate container. This model is then compared and validated with respect to a finite element model simulated in *ANSYS* [130].

6.2 Characterisation and classification of mission profiles

The feasibility of using a thermal storage system depends mainly on the duty cycle of the heat load. There is therefore the need, to characterise and classify the different mission profiles, in order to identify those which are most favourable to the use of heat storage systems. To this purpose, a reference is made to the power hybridisation potential (PHP) and the energy hybridisation potential (PHE) indicators used to assess the feasibility of energy storage systems in railway hybridisation [131]. By re-adapting these indicators to the context under consideration, the thermal storage potential (PST) and the energy

storage potential (PSE) are thus defined.
The PST reflects the potential size reduction of the actuator that the use of the thermal storage system would allow. It can be determined as follows:

$$PST = 1 - \frac{T_{aero_{RMS}}}{T_{aero_{max}}} \tag{6.1}$$

where $T_{aero_{RMS}}$ and $T_{aero_{max}}$ are respectively the RMS and maximum values of the aerodynamic torque. This definition implies that, whatever the mission considered, PST $\in$ [0, 1]. If the PST value is close to zero, there is little (no) change in the heat flow and it would be better to address the thermal management with solutions for the permanent regime. On the contrary, PST close to one characterises a mission strongly favourable for transient heat storage. Despite its relevance and even its intuitive nature, thermal storage potential does not cover all the aspects of the form of the mission. If, for example, we consider the two theoretical missions shown in Fig. 6.1, we can see that they both have the same amplitude and, above all, the same PST. Nevertheless, they are very different from one another. Intuitively, we can note that in comparison to mission m_1 (Fig. 6.1a), the multiple cycles of mission m_2 (Fig. 6.1b) would facilitate thermal storage better.

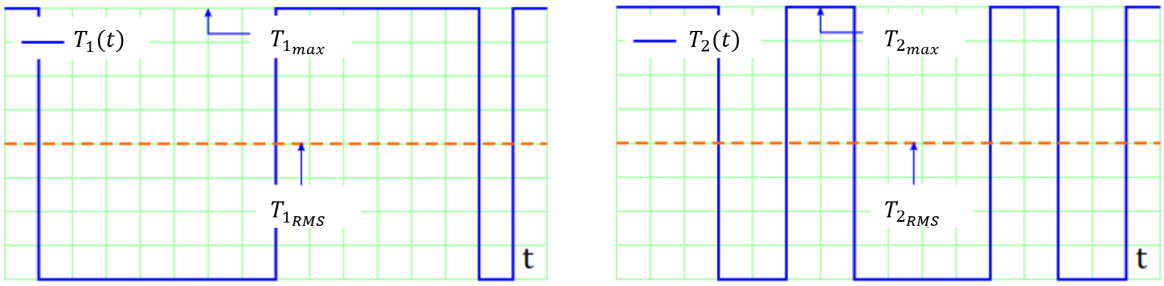

(a) Mission m_1: PST=0.5 (b) Mission m_2: PST=0.5

Figure 6.1: Two examples of theoretical missions and the associated PST .

In order to demonstrate this observation, the energy aspect of the missions should be considered. For this reason, the energy storage potential is introduced. In order to compute this indicator, it is necessary to calculate the useful thermal energy E_u that would be stored by the storage system to perform the mission. This can be defined as follows:

$$E_u = max\Big(E(t)\Big) - min\Big(E(t)\Big) \tag{6.2}$$

where $E(t)$, is expressed by the following relationship:

$$E(t) = \int_0^t \left(T^2_{aero}(t) - T^2_{aero_{RMS}}\right) dt \tag{6.3}$$

Note that the notion of "energy" used here does not respect the corresponding unit of measurement ($[J]$). The energy should in fact be formally expressed as $E(t) = \int_0^t \left(P(t) - P_{RMS}\right) dt$, where $P(t)$ represents the power losses over time and P_{RMS} the RMS value of these losses. As they are essentially due to the motor Joule losses (main source of heat), which are proportional to the square of the electromagnetic torque (current intensity), the energy has been expressed as shown in Eq.6.3.

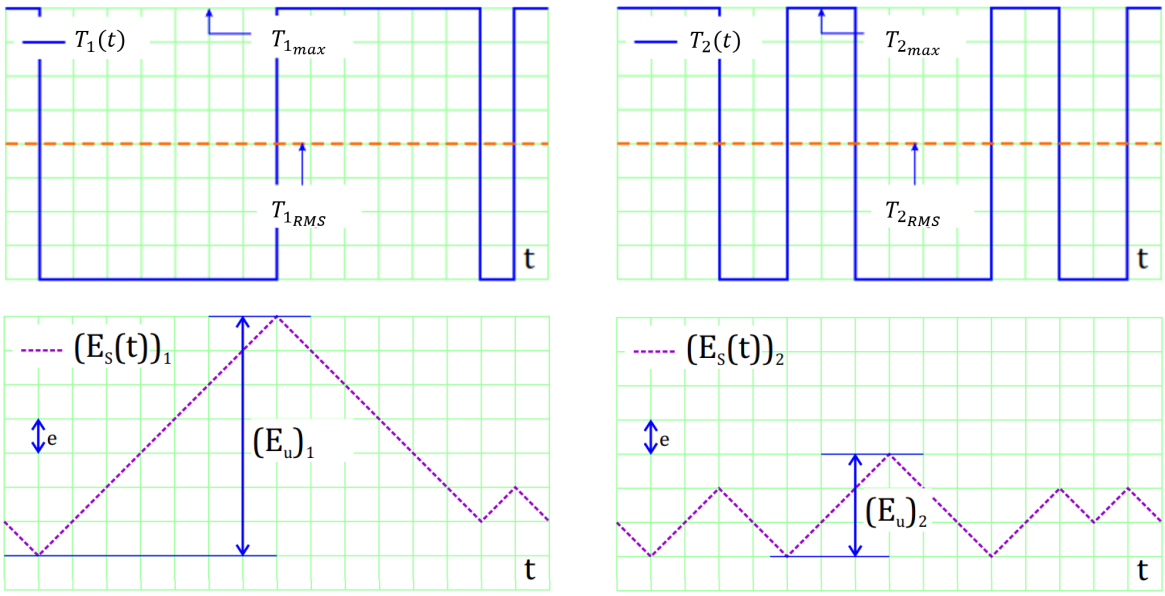

(a) Mission m_1: $PST = 0.5$; $E_u = 7e$. (b) Mission m_2: $PST = 0.5$; $E_u = 3e$.

Figure 6.2: Two examples of theoretical missions differentiated by their PST and E_u.

From the expression of the useful energy E_u, it can be deduced that, the longer the mission involves charging/discharging phases, the more is the energy stored. Conversely, the higher the frequency and regularity of the mission's charge/discharge cycles, less energy transits through the storage device. This led to the idea of formulating the energy storage potential (PSE) so as to illustrate these two notions of frequency and regularity. To do this, the PSE is assimilated to a fictitious frequency defined by:

$$PSE = \frac{T^2_{aero_{max}}}{E_u} \tag{6.4}$$

This definition implies that PSE $\in [0, +\infty]$, regardless of the mission under consideration. The indicator PSE is thus dissociated from any consideration related to the duration of the mission and assesses the higher (large PSE) or lower (small PSE) favourability of employing storage systems. Referring to the example of the missions previously introduced (see Fig. 6.2), the m_1 mission requires a larger storage volume (smaller PSE) than the m_2 mission (higher PSE). In fact, it is the frequency and regularity of the cycles of the m_2 mission that justifies its low useful energy to store.

6.2.1 Analysis of PST and PSE indicators for the considered mission profiles

At this point it becomes interesting to evaluate the expressions of PST and PSE indicators for the mission profiles of the primary flight control actuators considered in this thesis (depicted in Fig. 6.3). In addition, as mentioned in the introduction in Chapter 1, the mission profile of the Spoiler will also be analysed in this section.

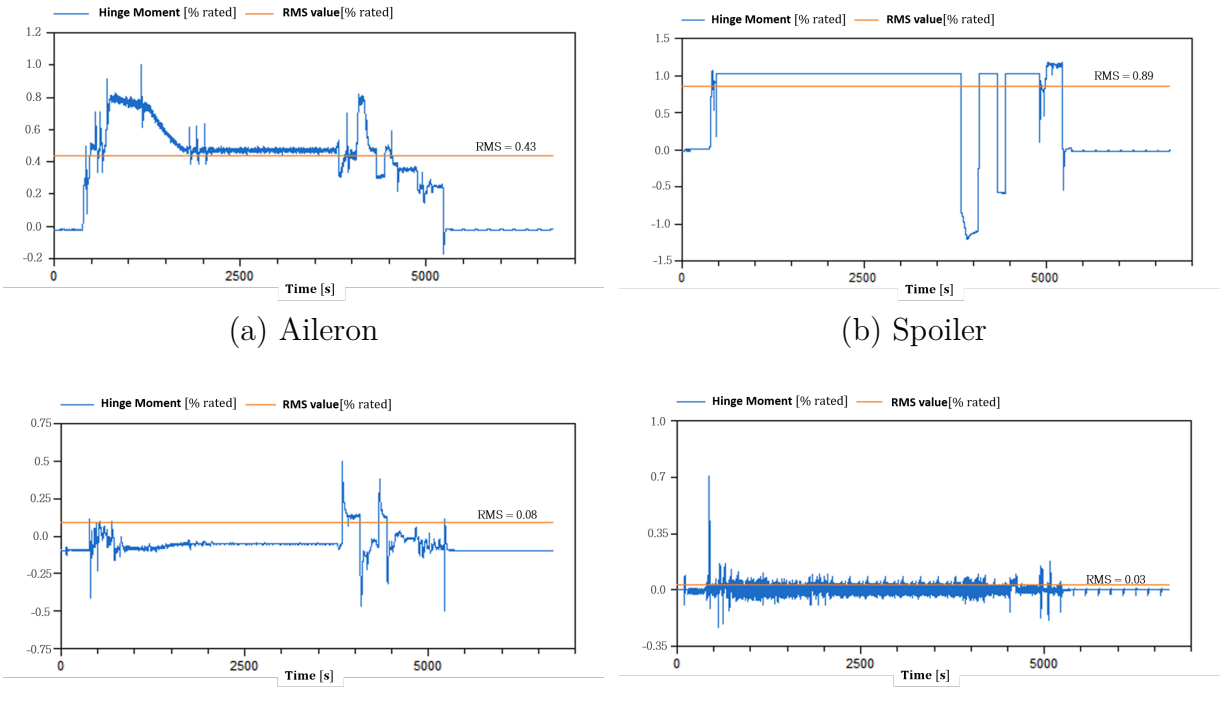

(a) Aileron (b) Spoiler

(c) Elevator (d) Rudder

Figure 6.3: Aerodynamic torque profile of the considered applications.

The values obtained for the two indicators, for each mission profile, are represented in Tab. 6.1.

Table 6.1: PST and PSE values for the considered mission profiles.

	PST [-]	PSE $[Hz]$	t_c $[s]$	$3\tau_{th}$ $[s]$
Rudder	0.95	0.144	6.93	30-54
Elevator	0.84	0.0233	42.91	27-45
Aileron	0.56	0.0023	436.12	57-69
Spoiler	0.28	0.001	999.84	42-66

In order to facilitate the interpretation of the results, the parameters t_c and τ_{th} have been introduced. The first, being the inverse of the PSE, can be assimilated to a characteristic time for which a torque greater than the RMS torque is present over the mission. This is used to give us an idea of the operation time of the heat storage device. The latter represents the thermal time constant of the motor, expressed as the product of thermal resistance and capacity of the copper windings. For each application, the τ_{th} values have been defined according to the results we observed during the design phases for EMA gear drive configurations. $3\tau_{th}$ is approximately the time reponse of the copper winding to reach the maximum temperature starting from the reference temperature (i.e. 20°C). Taking τ_{th} and t_c into account is essential in order to properly analyse the results outlined in Table 6.1.

In fact, if we only focus on the PST and PSE, we would say that the Rudder results to be the most favourable application for thermal storage. As a matter of fact, a huge peak aerodynamic torque is present for a very short mission time ($t_c = 6.93\,s$), which is lower than the thermal time constant of the motor windings ($3\tau_{th} > 30\,s$). This means that, the thermal capacity of the copper windings could allow to store the thermal energy by sensible heat during this phase. The use of storage systems may be therefore unnecessary or less favourable than expected.

Similarly, the analysis of the Elevator application can be conducted. In this case, slightly lower PST and PSE indicators are observed. The characteristic time is slightly greater (but approximately of the same order) than the thermal constant of the motor windings. Also in this case the thermal capacity of copper can be sufficient to store the heat load during peak phases, or alternatively, the sensible heat stored in the iron thermal capacity

of the motor, or the use of a small cooling system, may ensure the compliance with the temperature requirements.
A different scenario is obtained for the Aileron, where a moderate aerodynamic peak torque takes place over a larger time interval ($t_c = 436.12\,s$). This application is characterised by a slightly higher than average PST and by a characteristic time which is almost one order greater than the thermal constant of windings. In this case, it is difficult to conclude with certainty the benefits that can be obtained by using thermal storage systems. A larger storage device may be required, which can put a mass penalty at system level. The thermal requirements could also be achieved by over-sizing the motor or by using larger thermal management systems. A trade-off analysis should be conducted among the possible outlined strategies, in order to find the solution that provides the optimal mass compromise. This trade-off is explored in Chapter 7.
The Spoiler application is certainly the least favourable for the use of storage systems, given its low PST and PSE values. As can be seen from the mission profile shown in Fig. 6.3b, the RMS torque is practically close to the maximum torque. This indicates that the electric motor sized at RMS torque will operate at its nominal performance for the entire mission duration. There is therefore no interest in using storage systems, or particular cooling devices for this type of application.
It must be noted that during this phase of mission analysis, the nature of the storage systems is not taken into account, thus assuming that energy storage takes place in ideal storage systems. This assumption was necessary to decouple the mission analysis from the technological constraints associated with the different storage systems and application cases. For the application discussed here, these constraints are mainly due to the efficiency of the phase change materials and their installation constraints. Efficiency is mainly limited by their very low thermal conductivity, which represents one of the major barriers to the wide application of most PCMs. In addition, for greater operational effectiveness, the PCM should be installed as close as possible to the heat source, located at the electric motor windings. This represents a vary challenging aspect from an implementation point of view.

6.3 Sensible heat storage

The most direct way to store thermal energy is represented by sensible heat storage. Although this method is currently less efficient compared with latent heat storage, it has

the advantage of being less complicated and inexpensive. The amount of thermal energy a material can store by sensible heat depends on: the specific heat of the material c_p, its mass m and the temperature variation $\Delta\Theta$. This can be expressed according to the following relationship:

$$Q = \int_{\Theta_f}^{\Theta_i} mc_p(\Theta)\, d\Theta = mc_p(\Theta_f - \Theta_i) \tag{6.5}$$

where Θ_f and Θ_i represent respectively the initial and final temperature of the material. Since the material mass is given by the product of its volume V and its density ρ, Eq. 6.5 can also be written as follows:

$$Q = \rho V c_p(\Theta_f - \Theta_i) \tag{6.6}$$

Similarly to the definition of material density, the thermal density ρ_{th} of a thermal storage medium can be defined as:

$$\rho_{th} = \rho c_p \tag{6.7}$$

The thermal storage density is an important parameter when choosing a a storage material. In fact, it is important to have a material with a high ρ_{th} value in order to reduce the volume of the heat storage system. However, in the field of electrical actuators, there are very few degrees of freedom in the choice of materials to adopt, as the materials of the components making up the system are defined by their technology. For example, the electric motor is made up of materials to guarantee certain electrical and magnetic performances, as well as the mechanical components are composed of materials chosen according to their mechanical properties, etc. An approximate example (for illustrative purposes only) of material types commonly used for actuators, is summarised in Table 6.2.

Table 6.2: Illustrative example of materials used for actuator.

Material	Component	Density $[kg/m^3]$	Specific heat $[J/kgK]$	Thermal density $[J/Km^3]\cdot 10^6$
Steel Stainless	Mechanical components	7897	452	3.56
Copper	Electric motor	8960	385	3.44
Electrical steel	Electric motor	7650	502	3.84
Aluminium	Thermal Housing	2700	921	2.48

6.3.1 Design techniques to improve sensible heat storage

Since the thermal densities of actuator components are pre-established, the only possibility of increasing the storage capacity for sensible heat is to affect the size of the components. It is clear that any increase in the size of components must be made in accordance with the envelope, mass and technological limits of the application. Leaving aside the mechanical components, whose thermal behaviour is not analysed in this project, the components on which changes can be made are the motor and the thermal housing. It is important to remember that the thermal design of these devices is aimed at satisfying the operating thermal limits, such as the maximum temperature of the motor winding and the maximum skin temperature of the actuator. In the first case, it may therefore be advisable to act, for example, on the mass of the copper winding. In the second on the mass of the motor iron and/or on the mass of the thermal housing. As a matter of facts, since the dimensions of the components are interdependent, it is not possible to act on the dimensions of one without affecting the thermal behaviour of the other. To better explain this point, we can refer to the example of the electric motor model defined in Chapter 4. The developed surrogate model allows us to act on two parameters: the outer diameter D_e and the thickness of the yoke e_{yoke} (see Fig. 6.4).

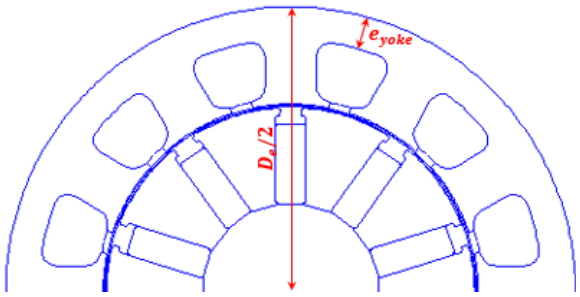

Figure 6.4: Geometry of the adopted electric motor model.

Increasing the motor diameter, by assuming geometrical similarity, leads to an overall increase of sensible storage heat in all the different materials composing the device. On the other hand, a high mass penalty is obtained, considering the fact that the mass is a function of the squared diameter. In addition, the dimensions, mass and heat capacity of the motor housing augment as well. For equal diameter, by varying the yoke thickness, it is possible to act directly on the masses of the copper winding or the stator iron, without significantly affecting the overall mass of the system. An increase in the mass of iron,

achieved by augmenting the yoke thickness, might be more interesting at first sight, as it is characterised by a higher thermal density (see Table 6.2) compared to copper. A larger yoke, nonetheless, leads to a reduction of the slot cross-section area, so the amount of heat stored in the windings is reduced and the winding temperature will rise more rapidly. In addition, a reduction in the cross-section of the windings increases the electrical resistance which, for the same generated torque, leads to more Joule losses. The opposite effect would therefore be achieved by reducing the yoke thickness. The negative effect in this case is an increase in iron losses and an higher risk of magnetic saturation, since the magnetic flux cross-section area is reduced. Also in this case, a need arises to investigate optimal mass compromises in order to better exploit the potential for sensible heat storage. These compromises will be investigated during the actuator sizing phase, performed in Chapter 7.

6.4 Phase Change Materials

Latent heat storage by means of phase change materials is one of the most effective ways of storing thermal energy. In contrast to the sensible heat storage method, the latent heat storage approach provides a much higher storage density, with a smaller temperature difference. The phase transition of a material can occur either through the transition from solid to liquid phase, or through the phase change from liquid to gas. The solid-liquid phase change of a material is generally more interesting for such applications because of the higher energy storage density and the smaller volume change compared to liquid-gas transformations [132]. The working principle of these materials, adapted to a simplified duty cycle of an actuator, is illustrated in Fig. 6.5. The system temperature increases as the actuator faces maximum load conditions (A-B). Once the melting temperature of the PCM is attained (point B), which is specifically chosen according to the operational limits of the actuator, the system temperature continues to rise, but at a very low rate, with the PCM absorbing much of the excess heat as it melts. At the end of the maximum load condition (point C) the system starts to cool down (C-D). Once the freezing temperature of the PCM is reached, the PCM starts to solidify. The PCM at this point acts as an additional heat source by releasing its stored heat energy. The system then continues to dissipate heat and cool-down until steady state conditions are achieved or the next peak heat rejection period (point E) occurs.

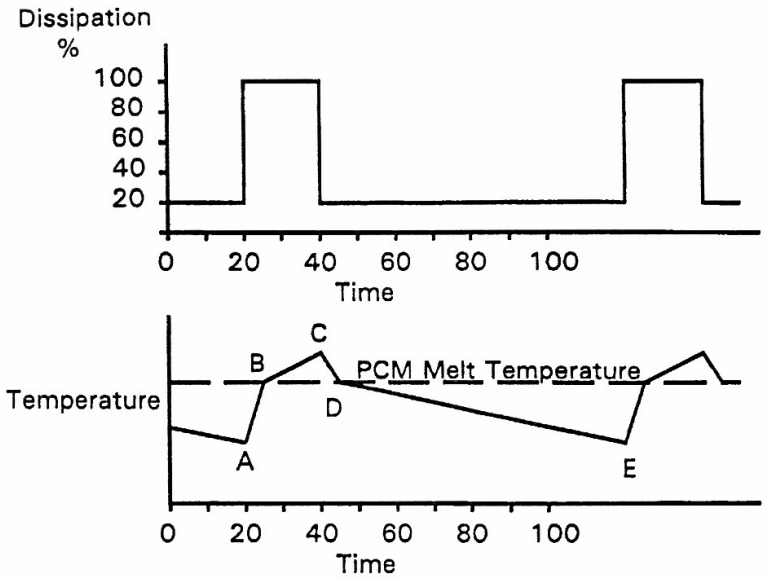

Figure 6.5: Temperature Variation in a TMS with PCM [133].

The choice of the type of PCM to be used depends on the type of application, but above all the first selection criterion is certainly based on the melting temperature. Therefore, the first requirement is to select a material which has a melting temperature within the practical application range. Secondly, other selection criteria include [132] [134]:

- High latent heat of fusion per unit mass, whereby a smaller amount of material stores a given amount of energy.
- High specific heat to provide additional sensible heat storage effects.
- High thermal conductivity, so that the temperature gradients for loading and unloading the storage heat are small.
- Small volume changes during the phase transition, so a simple container and heat exchanger geometry can be used.
- Containing non-poisonous, non-flammable and non-explosive elements/compounds.

A wide variety of PCMs are commercially available. A comprehensive review of the different types of phase change materials in use, their classification and characteristics, benefits and

drawbacks, as well as the experimental studies are widely available in the literature [135] [136] [137] [138]. Some examples of PCMs typically used in various industrial applications are provided in Table 6.3.

Table 6.3: Thermophysical properties of PCMs investigated for different applications [135].

Compound	Melting Temperature $°C$	Heat of fusion kJ/kg	Specific heat capacity kJ/kgK	Thermal Conductivity W/mK	Density kg/m^3
Water	0	335	4.2	2.4 (liquid) 0.6 (solid)	1000
RT25	24	232	1.8 (liquid) 1.41 (solid)	0.18 (liquid) 0.19 (solid)	749
PEG900	34	150	2.26	0.188	1100
P116 wax	46.7	209	2.89	0.277(liquid) 0.140 (solid)	786
Commercial paraffin wax	52.1	243.5	-	0.15	809
Palmitic acid	60	185	-	0.162	850 (liquid) 989 (solid)
$Mg(NO_3)_26H_2O$	89	162	-	0.490 (liquid) 0.611 (solid)	1150 (liquid) 1636 (solid)
RT100	99	168	2.4 (liquid) 1.8 (solid)	0.2	770
Erythritol	117	339.8	2.61 (liquid) 2.25 (solid)	0.326 (liquid) 0.733 (solid)	1330 (liquid) 1480 (solid)

One of the major barriers to the wide application of most PCMs is related to their very low thermal conductivity. Hence, internal heat transfer enhancement techniques are required in latent heat thermal storage applications. Among the most commonly used techniques, very interesting in this context are design methods which consist of encapsulating the PCM within finned plate heat exchangers [68] [139]. The integration and modelling of a PCM module integrated in an aluminium finned container is discussed in the next section.

6.4.1 Mathematical representation of the phase transition of a PCM Slab

For an accurate and efficient estimation of the heat storage capacity of the PCM, it is essential to develop a suitable approach to solve a moving boundary problem (the so-called Stefan problem). One-dimensional phase change heat conduction problems have been explored by various analytical, numerical and experimental methods [140] [141] [142] [143], some of which have also been tested within this project. Given the context of application, and in view of the satisfactory results obtained, a re-adaptation of the lumped parameter model of a PCM slab, developed by An et al. [144] has been used in this thesis. This model is based on Hermite approximations for integrals [145], used to estimate the averaged temperature for both the liquid and solid phases during melting of PCM. In order to describe the mathematical formulation of the model, the 1-D melting problem illustrated in Fig.6.6 is considered. Within the PCM, during the melting process, the material is present in both liquid and solid phases. The x_f frontier therefore delimits the

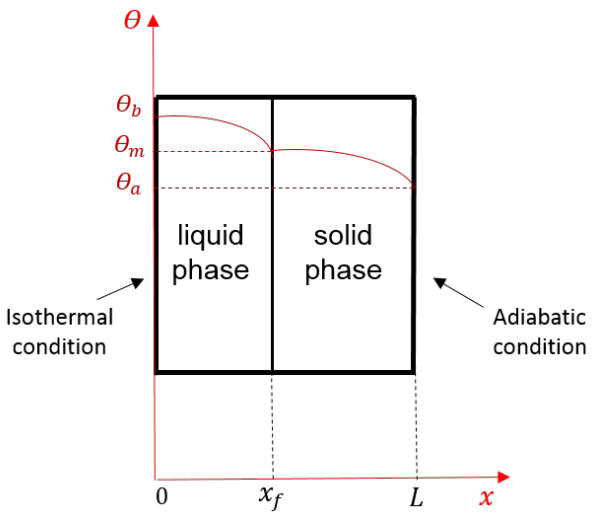

Figure 6.6: Geometry and temperature coordinates representing the melting process of a PCM slab.

two states. The length L represents the width of the slab. The ends of the slab are subject to: adiabatic conditions on the right side and isothermal conditions on the left side. During the entire melting process, a temperature Θ_b, higher than the melting temperature Θ_m, is presents on the left side of the slab, whereas a temperature $\Theta_a \leq \Theta_m$ is encountered on the right side. To model the melting process, the following assumptions are used to simplify the analysis: (1) All physical properties within a phase are independent of temperature; (2) Volume change associated with phase change is neglected; (3) Melting occurs at a discrete temperature of Θ_m; (4) No convective heat transfer is considered in the liquid phase of the PCM. On the basis of the above assumptions, the heat conduction equations governing the temperatures in the liquid and solid phases are provided by the following mathematical formulations:

$$\frac{\delta\Theta_l(x,t)}{\delta t} = \alpha_l \frac{\delta^2\Theta_l(x,t)}{\delta x^2}, \quad \text{in} \quad 0 < x < x_f(t) \tag{6.8}$$

$$\frac{\delta\Theta_s(x,t)}{\delta t} = \alpha_r \frac{\delta^2\Theta_s(x,t)}{\delta x^2}, \quad \text{in} \quad x_f(t) < x < x_0 \tag{6.9}$$

where $\Theta_l(x,t)$ and $\Theta_s(x,t)$ are respectively the temperatures of the liquid and solid phases, x is the space variable, t the time, $\alpha_l = \frac{\lambda_l}{\rho c_{pl}}$ and $\alpha_s = \frac{\lambda_s}{\rho c_{ps}}$ are the thermal diffusivities of the liquid and solid phases, ρ the density, c_p the specific heat and λ the thermal conductivity. By expressing an energy balance between the solid and liquid phases across the phase

change edge, the following interface heat flux equation is obtained:

$$\lambda_l \frac{\delta \Theta_l(x,t)}{\delta x} + \rho H \frac{dx_f(t)}{dt} = \lambda_s \frac{\delta \Theta_s(x,t)}{\delta x}, \quad \text{at} \quad x = x_f(t) \tag{6.10}$$

where H is the latent heat of fusion. The spatially averaged temperatures for the liquid Θ_{lav} and solid phases Θ_{sav} can be defined as follow:

$$\Theta_{lav}(t) = \frac{1}{x_f(t)} \int_0^{x_f(t)} \Theta_l(x,t)\, dx \tag{6.11}$$

$$\Theta_{sav}(t) = \frac{1}{L - x_f(t)} \int_{x_f(t)}^{L} \Theta_s(x,t)\, dx \tag{6.12}$$

So, by applying the operators defined in Eq.6.11 and Eq. 6.12 on the governing equations for the liquid (Eq. 6.8) and solid (Eq. 6.9) phases, the following formulations are obtained:

$$\frac{d}{dt}\Big(\Theta_{lav}(t) x_f(t)\Big) - \Theta_l(x,t)\Big|_{x=x_f(t)} \frac{dx_f(t)}{dt} = \alpha_l \frac{\delta \Theta_l(x,t)}{\delta x}\Big|_0^{x_f(t)} \tag{6.13}$$

$$\frac{d}{dt}\Big(\Theta_{sav}(t)(L - x_f(t))\Big) + \Theta_s(x,t)\Big|_{x=x_f(t)} \frac{dx_f(t)}{dt} = \alpha_s \frac{\delta \Theta_s(x,t)}{\delta x}\Big|_{x_f(t)}^{L} \tag{6.14}$$

By using Hermite's approximation of the first order [144] [145] on the definitions of average temperatures, the following expression are obtained:

$$\begin{aligned} \Theta_{lav}(t) \approx & \frac{1}{2}\left(\Theta_l(x,t)\Big|_{x=0} + \Theta_l(x,t)\Big|_{x=x_f(t)}\right) + \\ & + \frac{x_f(t)}{12}\left(\frac{\delta \Theta_l(x,t)}{\delta x}\Big|_{x=0} - \frac{\delta \Theta_l(x,t)}{\delta x}\Big|_{x=x_f(t)}\right) \end{aligned} \tag{6.15}$$

$$\begin{aligned} \Theta_{sav}(t) \approx & \frac{1}{2}\left(\Theta_s(x,t)\Big|_{x=x_f(t)} + \Theta_s(x,t)\Big|_{x=L}\right) + \\ & + \frac{L - x_f(t)}{12}\left(\frac{\delta \Theta_s(x,t)}{\delta x}\Big|_{x=x_f(t)} - \frac{\delta \Theta_s(x,t)}{\delta x}\Big|_{x=L}\right) \end{aligned} \tag{6.16}$$

Whereas Hermite's approximation of order zero [144] [145] are used for the computation of the heat fluxes:

$$\int_0^{x_f(t)} \frac{\Theta_l(x,t)}{\delta x}\, dx = \Theta_l(x,t)\Big|_{x=x_f} - \Theta_l(x,t)\Big|_{x=0} \approx \frac{x_f(t)}{2}\left(\frac{\delta\Theta_l(x,t)}{\delta x}\Big|_{x=0} + \frac{\delta\Theta_l(x,t)}{\delta x}\Big|_{x=x_f(t)}\right) \tag{6.17}$$

$$\int_{x_f(t)}^{L} \frac{\Theta_s(x,t)}{\delta x}\, dx = \Theta_s(x,t)\Big|_{x=L} - \Theta_s(x,t)\Big|_{x=x_f} \approx \frac{L-x_f(t)}{2}\left(\frac{\delta\Theta_s(x,t)}{\delta x}\Big|_{x=x_f(t)} + \frac{\delta\Theta_s(x,t)}{\delta x}\Big|_{x=L}\right) \tag{6.18}$$

Starting then from the equations obtained, the lumped model which provides the average temperatures in the phases and the heat fluxes can be defined. The inverse process of freezing, i.e. when the material starts to solidify from a completely liquid state, can be represented by the same equations with some inversions, i.e. $\Theta_b < \Theta_m$ and a frontier that also moves from the left to the right. These inversions are explained in more detail in Section 6.4.2.1.

6.4.2 Application of the mathematical formulations

The analytical formulations described in the previous section define a system consisting of four algebraic equations (Eq. 6.15 - 6.18), plus three differential equations (Eq. 6.10, Eq. 6.13, and Eq. 6.14). In order to solve this system of equations, the following boundary conditions are defined:

$$\Theta_s(x,t) = \Theta_l(x,t) = \Theta_m, \quad \text{at} \quad x = x_f(t) \tag{6.19}$$

$$\Theta_l(x,t) = \Theta_b, \quad \text{at} \quad x = 0 \tag{6.20}$$

$$\Theta_s(x,t) = \Theta_a, \quad \text{at} \quad x = L \tag{6.21}$$

The solution of the system of equations can then be easily obtained using computational software environments. To this purpose, the mathematical problem has been implemented in *Dymola* simulation environment [129], as shown in Fig. 6.7. The thermal characteristics of the PCM, defined in Table 6.4, have been chosen by taking as reference the material *0500- Q100 BioPCM*, produced by "Phase Change Energy Solutions".

Table 6.4: Functionalized Bio-PCM *0500- Q100 BioPCM*.

Characteristic	Value
Melting temperature, $\Theta_m\,[°C]$	100
Latent heat of fusion, $H\,[kJ/kg]$	247
Density, $\rho\,[kg/m^3]$	1250
Thermal conductivity (for both liquid and solid phase), $\lambda\,[W/mK]$	0.7
Specific heat (for both liquid and solid phase), c_p $[kJ/kgK]$	4.3

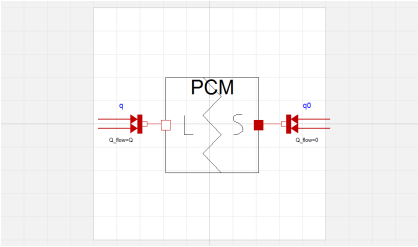

(a) Model diagram.

```
equation
  Theta_l_x_0 = port_Theta_b.T;
  Theta_s_x_L = port_Theta_a.T;
  // Equations
  Theta_lav = 0.5 * (Theta_l_x_0 + Theta_l_x_Xf) + Xf/12 * (dTheta_l_dx_0 - dTheta_l_dx_Xf);
  Theta_sav = 0.5 * (Theta_s_x_Xf + Theta_s_x_L) + (L - Xf)/12 * (dTheta_s_dx_Xf - dTheta_s_dx_L);
  Theta_l_x_Xf - Theta_l_x_0 = Xf/2 * (dTheta_l_dx_0 + dTheta_l_dx_Xf);
  Theta_s_x_L - Theta_s_x_Xf = (L - Xf)/2 * (dTheta_s_dx_Xf + dTheta_s_dx_L);
  // ODE
  lambda_l * dTheta_l_dx_Xf + roh_s * H * der(Xf) = lambda_s * dTheta_s_dx_Xf;
  der(Theta_lav * Xf) - Theta_l_x_Xf * der(Xf) = a_l * (dTheta_l_dx_Xf - dTheta_l_dx_0);
  der(Theta_sav * (Length - Xf)) + Theta_s_x_Xf * der(Xf) = a_s * (dTheta_s_dx_L - dTheta_s_dx_Xf);

  port_Theta_b.Q_flow = - dTheta_l_dx_0 * lambda_l * (Lc * H_fin);
  port_Theta_a.Q_flow = dTheta_s_dx_L * lambda_s * (Lc * H_fin);
```

(b) Model code.

Figure 6.7: Dymola model of the PCM slab *Dymola*.

In order to test the model, it has been chosen to set a heat flow $q = 0,020\,W$ at $x = 0$ and a heat flow $q_0 = 0$ (representing the adiabatic conditions) at $x = L$. The length and height of the slab were fixed respectively to $L = 3.05\,mm$ and $H_{fin} = 3.74\,mm$, while a thickness $L_c = 1\,mm$ is considered. Initial temperature conditions of $100°C$ have been set, in order to start the simulation at the beginning of the melting process. The simulation model not only provides values for the temperatures in the liquid and solid phases, but also makes it possible to extrapolate the time it takes for the material to completely melt, as shown in the graphs depicted in Fig. 6.8. From this we can see that the material took about 250s to melt completely (when the x_f frontier equals the value of L). At the end of the melting process, the temperature Θ_b=117°C, which is 17°C higher than the melting temperature (Θ_m=100°C), while the average temperature of the liquid Θ_{lav}=108°C. The average temperature of the solid Θ_{sav}, as well as the temperature Θ_a, are reasonably equal to the melting temperature Θ_m during the entire melting process (note that the temperature Θ_{sav} in Fig. 6.8a is not noticeable as it is equal to the temperature Θ_a).

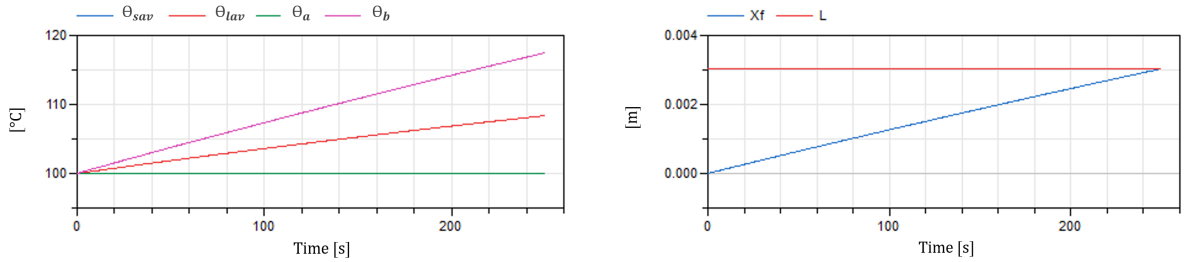

(a) Temperatures evolution (b) Frontier evolution

Figure 6.8: Example of thermal behavior of the Dymola model.

6.4.2.1 Representation of the PCM out of the melting phase

There is still a further step to be accomplished before this model can be used in a complete thermal duty cycle. The model defined so far represents the behaviour of the PCM during the phase transition. It is therefore necessary to define its behaviour out of transition phase (i.e. when the material is completely in the solid or liquid state) and its behaviour during the inverse transition (i.e. during the freezing phase, when the melted material starts to solidify again). For this reason, the model needs to represent each of the four possible phases. In this respect, the formulations described so far have been adapted as follows:

- In Dymola, instead of representing the two liquid/solid phases explicitly, we chose to represent two left/right sides defining the liquid/solid phases during the melting process and the solid/liquid phases during the freezing process. Thus, in both phase transition processes the frontier between the two phases moves from the left to the right side.
- During purely liquid ($\Theta_b > 100$) or purely solid ($\Theta_b < 100$) phases, the boundary conditions $x_f = 0$ and $dx_f/dt = 0$ have been set.
- For reasons of continuity of the model, during the solid and liquid phases the right hand side has been modelled as identical to the left hand side. This does not represent anything physically but it allows the solver to resolve the implemented equations.

Through these adaptations, it has been possible to use the PCM slab model within a complete thermal duty-cycle, as shown in the example in Fig. 6.9.

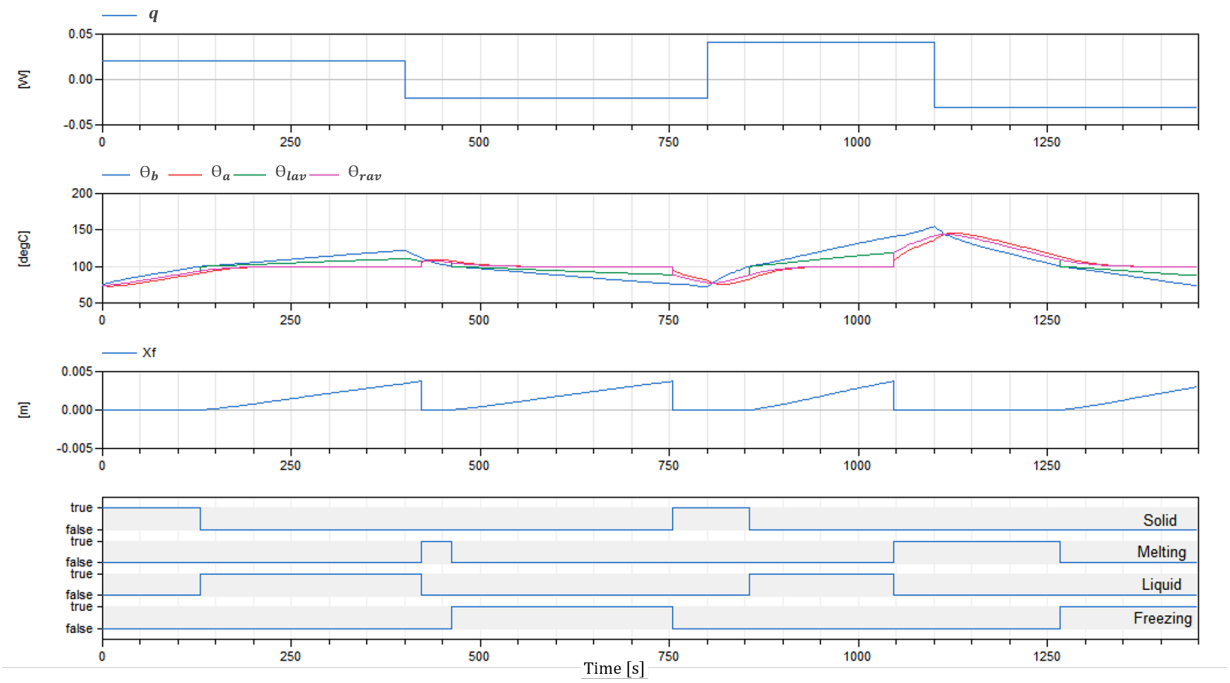

Figure 6.9: Thermal Behavior of PCM with a heat flux duty-cycle.

6.4.3 Model of the PCM integrated in a finned plate

Once the model of the PCM slab has been defined, it has to be adapted for the coupling with the fin structure. The representation of such a system is shown in Fig. 6.10. For ease of discussion, given the symmetry of the module, it is possible to analyse only half of the distance between two fins, as shown in Fig. 6.11.

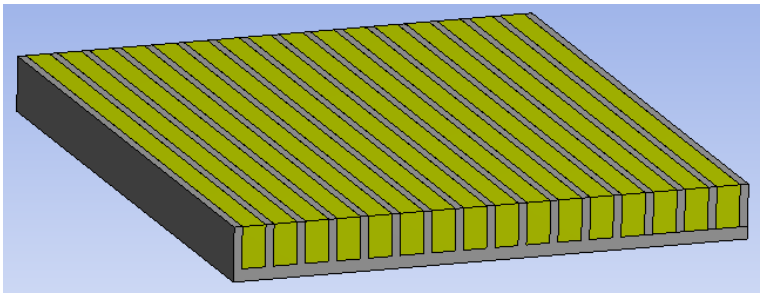

Figure 6.10: PCM embedded in a plate-fin container.

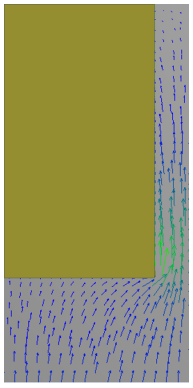

Figure 6.11: 2-D representation of the problem.

Modelling the PCM-fin plate is more complicated, since, compared to the previous case, the heat exchange does not only take place at the lateral side of the PCM, but also at the bottom side. In fact, if the plate is placed on the top and/or bottom surface of the thermal housing of the electric motor, the heat generated by the motor losses is transferred to the base of the PCM plate and then distributed in the fins, as illustrated in Fig. 6.11. Because of this effect, the melting process of the material does not only occur at the lateral boundary of the PCM, as illustrated previously, but also at the bottom boundary, as can be seen in the example in Fig. 6.12.

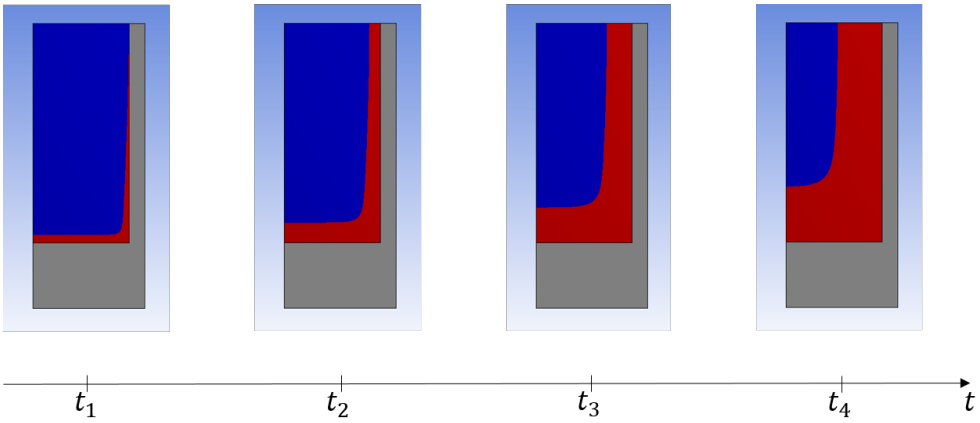

Figure 6.12: Evolution of the liquid frontier (red area representing the liquid phase) of PCM during the melting process.

In order to take this phenomenon into account, it is therefore necessary to make some re-adaptations to the model described before hand. The problem can therefore be represented by decomposing the system into two modules:

- A module integrating the effect of heat exchange along the fin, defined as "side module".
- A module integrating the effect of heat exchange along the base of the plate, defined as "bottom module".

The thermal behaviour of the system is therefore defined by the superposition of the effects of the two modules. To better understand this concept, reference should be made to the illustration shown in Fig. 6.13. The heat flow coming from the system is distributed within the two modules, which are basically connected in parallel. As the temperature of the liquid increases, the liquid boundary x_f moves, both in the bottom and side modules.

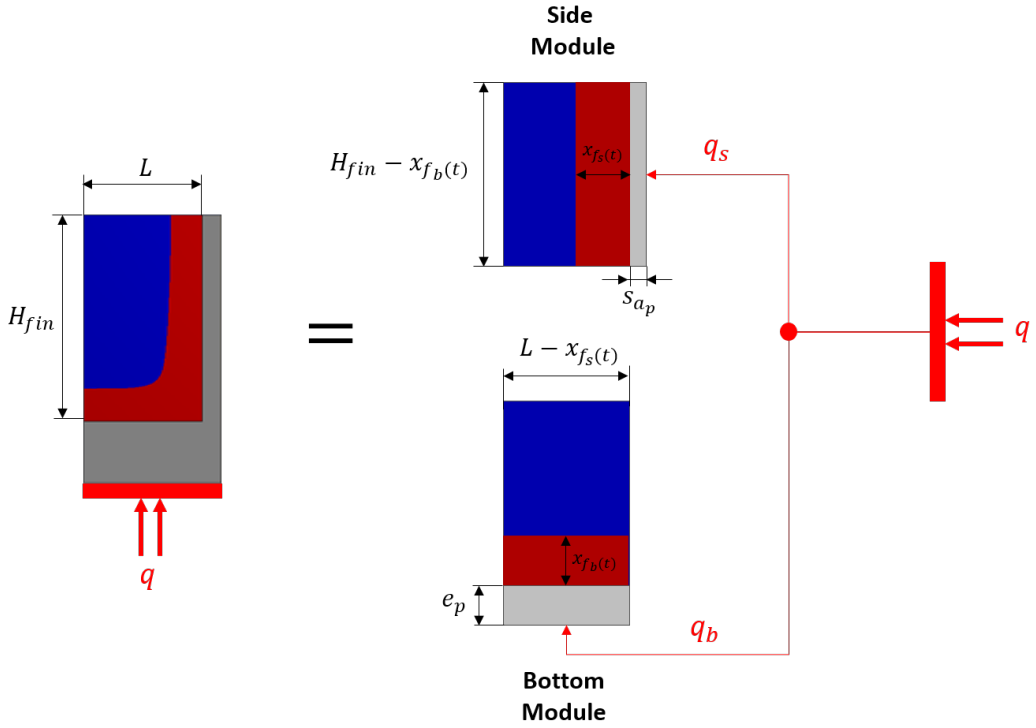

Figure 6.13: Decomposition of the PCM-Fin problem.

Therefore, the behaviour one module automatically affects the dimension of the other. Consequently, the side module during the phase transition is faced with a lower heat exchange surface defined by $(H_{fin} - X_{f_b})$, and in the same way the bottom module sees an exchange surface reduced as $(L - X_{f_s})$ (Fig. 6.13) . Therefore, the temperature change at the boundary in $x = 0$ for the two modules can be determined as follows:

$$\left.\frac{\delta\Theta_{l_s}(x,t)}{\delta x}\right|_{x=0} = \frac{-q_s}{\lambda L_c(H_{fin} - X_{f_b}(t))} \quad \text{at the side module} \tag{6.22}$$

$$\left.\frac{\delta\Theta_{l_b}(x,t)}{\delta x}\right|_{x=0} = \frac{-q_b}{\lambda L_c(L - X_{f_s}(t))} \quad \text{at the bottom module} \tag{6.23}$$

where the dimensions L_c, L and H_{fin} represent respectively the PCM thickness, the PCM width, and the fin heigth, $X_{f_b}(t)$ and $X_{f_s}(t)$ represent the frontiers of the bottom and side modules, $q = \frac{Q}{N_{blocks}}$ is the part of the plate heat flow acting on the portion of the system considered and N_{blocks} is the number of PCM slabs composing the system. Based on the foregoing considerations, the model of the PCM embedded in the finned plate is therefore

newly developed on Dymola, as shown in Fig. 6.14.

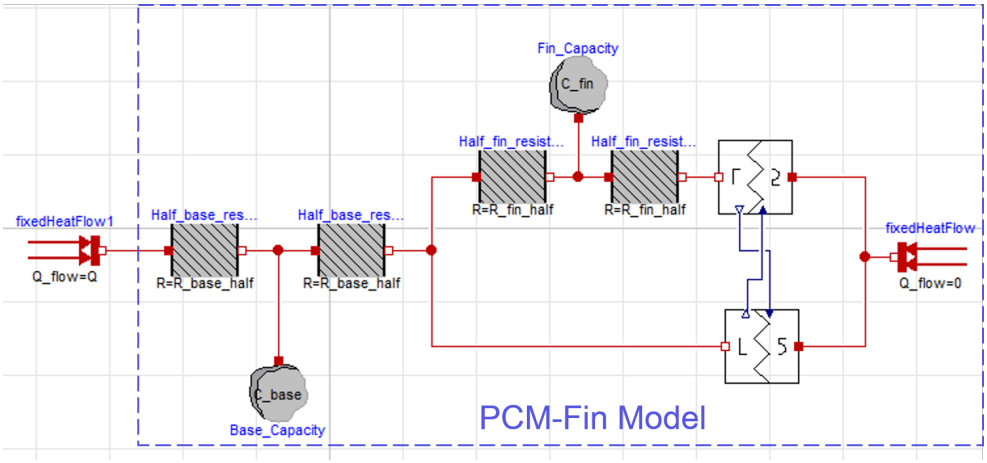

Figure 6.14: PCM-fin model implemented in Dymola.

Note that the thermal capacities and resistances of the base of the plate (C_{base}, R_{base}) and those of the fin (C_{fin}, R_{fin}) have been taken into account in the model. In order to validate it, an equivalent FEM model developed in *ANSYS* simulation software has been implemented. The model is then validated on the basis of 16 different geometrical configurations and flow conditions, generated through an LHS DoE. For each of the configurations, the fin temperature Θ_b and the average temperature of the liquid phase Θ_{lav} at the end of the melting time t_m are calculated with the two simulation models (ANSYS and Dymola). The comparison of the results is given in Fig. 6.15. As it can be seen from the figure, the Dymola model allows estimating the behaviour of the system with a good approximation with respect to the FEM simulations.

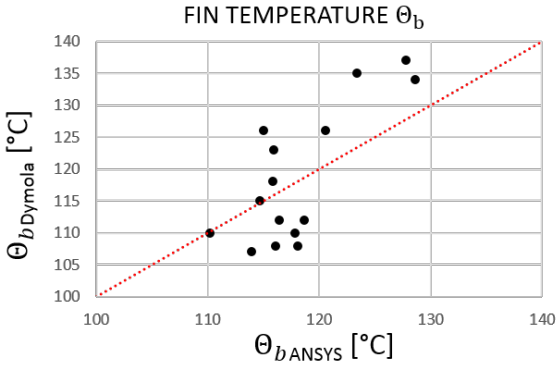

(a) $max|\epsilon| = 9.5\%$; $\bar{\epsilon} = 5.4\%$

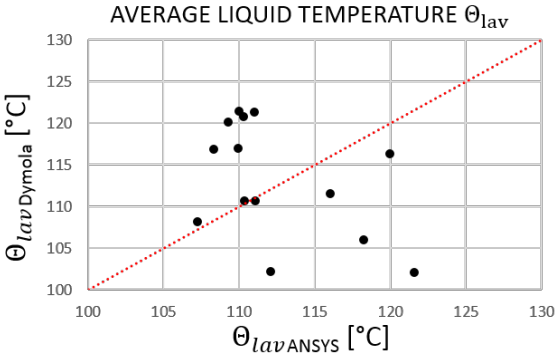

(b) $max|\epsilon| = 16\%$; $\bar{\epsilon} = 7.2\%$

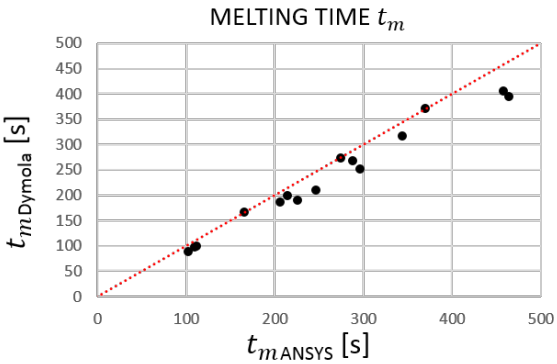

(c) $max|\epsilon| = 15.8\%$; $\bar{\epsilon} = 9.3\%$

Figure 6.15: Comparison of the results obtained with Dymola and Ansys models of the PCM.

6.4.4 PCM-Fin module design

For the applications considered in this thesis, it has been planned to install two PCM modules on the top and bottom surfaces of a finned thermal housing, as shown in Fig. 6.16. In this way, the PCM modules can be used to assist the heat transfer during the transient phases, while the finned housing can be used to dissipate heat during steady state operations. In order to design a more compact system, it has been decided to install only one finned module on one side of the thermal housing. With a view of maximizing the heat transfer, a design of the PCM plate directly integrated on the finned housing has been considered. On the basis of the results obtained from the simulations previously performed (both on Dymola and Ansys), it was decided to use a material with a melting temperature of 90°C. It was noted that, after the melting process is complete, the average temperature

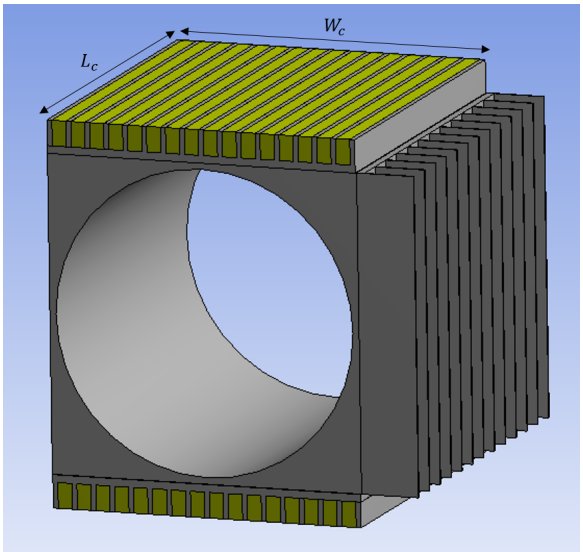

Figure 6.16: PCM module integrated in the finned thermal housing.

of the material increases by approximately 10°C-20°C (depending on the geometry configuration and heat flow inputs) compared to the melting temperature. The material *0500-Q91 BioPCM* has been therefore selected, as it has the same properties of the *0500- Q100 BioPCM*, with the exception of its melting temperature of 91°C. Concerning the module geometry, the dimensions of the plate are fixed equal to those of the surface of the housing on which it is mounted (W_c, L_c in Fig. 6.16). A plate base thickness $e_p = 2.5\,mm$ and a fin thickness $s_{a_p} = 0.75\,mm$ (Fig. 6.14) are assumed. The fins height H_{fin} and the half-width of the PCM L are set as design variables. Once the module dimensions have been defined, the number of PCM slabs N_{blocks} can be calculated as follows:

$$N_{blocks} = rounds\left(\frac{W_c - 2s_{a_p}}{2s_{a_p} + 2L}\right) \tag{6.24}$$

The mass of the module $M_{PCM_{module}}$ is estimated according to the geometries and densities of the PCM and the aluminium container as follows:

$$\begin{aligned} M_{PCM_{module}} &= M_{plate} + M_{PCM} = \\ &= \rho_a L_c \Big(H_{fin} 2s_{a_p} (N_{blocks} + 1) + W_c e_p \Big) + \rho_{PCM} L_c 2L H_{fin} N_{blocks} \end{aligned} \tag{6.25}$$

where M_{plate} is the mass of the aluminium plate container, M_{PCM} the PCM mass, ρ_a the aluminium density and ρ_{PCM} the PCM density.

6.5 Conclusion

In this chapter, solutions to improve the thermal storage of primary flight control actuators have been discussed. A method for classifying the mission profiles according to their suitability for using thermal storage systems has been provided. This method, based on the calculation of the thermal storage potential (PST) and the energy storage potential (PSE), and assuming an ideal storage system, has been applied to the mission profiles considered in this thesis. Analyses of these indicators and the thermal time constants of the motor windings revealed that, for Rudder and most probably also for Elevator applications the sensible heat stored in the copper windings capacity can be sufficient to absorb the heat load during the peak load phases of the mission. They also shown that the Spoiler application is not suitable for the use of storage systems, while for the Aileron no definitive conclusion could be deduced. For the latter, the potential benefits obtained through the use of storage materials need to be further investigated.

The concept of storage through sensible heat in actuator components has been discussed. Design techniques to improve sensible heat storage of components were illustrated, showing how the geometric interdependence between components pushes towards the search for optimal size and mass compromises.

Storage by latent heat by means of phase change materials has been presented. Their advantages, material selection requirements and techniques to improve their efficiency through the use of aluminium finned containers were illustrated. Analytical formulations describing the behaviour of a PCM slab during the phase transition process have been introduced. Using these formulations, a dynamic model of the PCM slab has been developed on Dymola. This allows to provide the average temperatures in the liquid and solid phases, as well as the evolution of the frontier between the two phases, during the entire melting process. This model was subsequently adapted to represent the PCM thermal behaviour outside the phase transition. The model thus defined was then used to represent the behaviour of the material when inserted into an aluminium finned structure. The generated model was finally validated, by means of finite element simulations, over different geometric configurations and heat flow conditions.

Chapter 7

A Dynamic Approach for the Preliminary Design of Primary Flight Control Actuators

Contents

7.1 Introduction **174**

7.2 Actuator dynamic model for thermal behaviour **176**

7.2.1 Electro-mechanical transmission chain model 177

7.2.2 Motor Losses Model 178

7.2.3 Motor Thermal Model 179

7.2.4 Atmospheric model 181

7.2.5 Thermal management system models 183

7.2.6 Validation of the electro-mechanical actuators designed with the static approach 187

7.3 Preliminary design and evaluation of the discussed TMS concepts **189**

7.3.1 Model integration in the preliminary design framework 189

7.3.2 Case study 1: Finned thermal housing 190

7.3.3 Case study 2: Heat pipe 196

7.3.4 Case study 3: Thermal Strap 200

7.3.5 Case study 4: PCM 203

7.3.6 Trade-off analysis 205

7.3.7 Computational times and design compromises 209

7.4 Conclusion **210**

7.1 Introduction

Preliminary design plays a key role in the product development process (Fig. 7.1) [146] [147]. This is in fact a challenging stage with complex requirements, which has a significant impact and repercussions in the overall design process [148]. The ever-increasing industrial pressure to produce a product in the shortest possible time pushes systems engineers to evaluate the effect of a potential idea or solution in advance to speed up the design process, especially when there are multiple design alternatives [149]. It is therefore in the preliminary design phase where the technical feasibility of a product becomes a critical issue in time. For this reason, it becomes essential to develop more original and effective solutions from this stage at a higher rate, in order to predict the effects on subsequent design phases. Adapting the foregoing considerations to the actuator development process, graphically expressed through the V-Cycle depicted in Fig. 7.1, an effective preliminary design could predict the effects of the subsequent stages of detailed design and virtual prototyping.

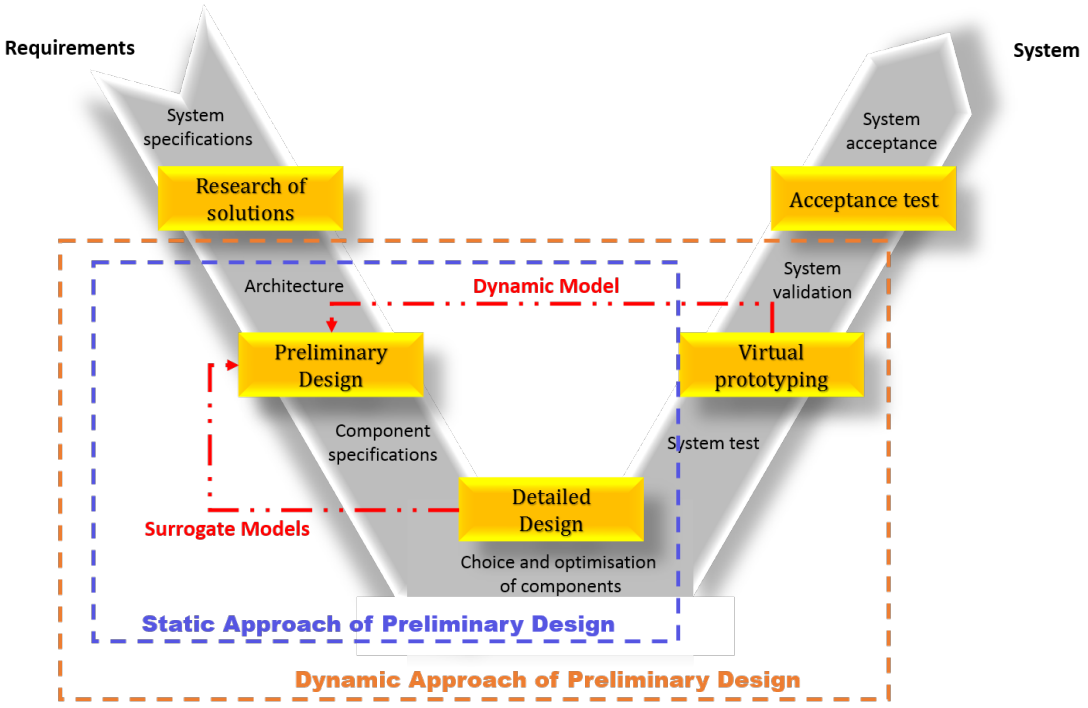

Figure 7.1: V design cycle.

Detailed design aims to define each component in detail in order to refine the results of the preliminary design. The numerical tools generally used at this stage are finite or volume element simulation softwares (ANSYS, COMSOL, FEMM, etc.). In Chapter 3 and Chapter 4, it has been shown how the effects of this phase can be integrated into the preliminary design through the use of surrogate models, which allowed to effectively replace computationally heavier finite element models.
Virtual prototyping aims to test and validate the choices made on actuator components and subsystems, before committing to making a physical prototype. Complex dynamical models or non-linear models are adopted at this stage, and implemented in system simulation software (Matlab Simulink, Dymola, AMESim etc), in order to analyse the behaviour of the actuator under real-world operating conditions. From a thermal point of view, the temperature behaviour of the actuator is observed along the mission, and the system is validated if the operational thermal requirements are fully satisfied. The use of dynamic models in preliminary activities, where only steady-state models are used, is generally unusual as it may involve substantial computation times. On the other hand, their use would allow the design of an actuator sized specifically according to the mission profile (Fig. 7.2), thus avoiding loops between the preliminary design and the validation step.

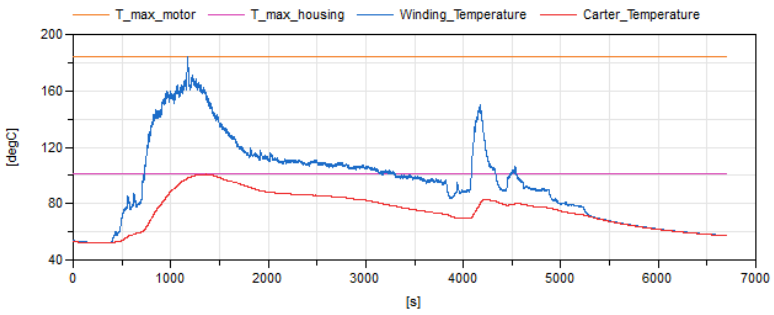

Figure 7.2: Examples of thermal profile of an optimally-sized system.

In this regard, Sanchez et al. [150] proposed an innovative approach using dimensionless numbers, built from computational fluid dynamic simulations, to predict system thermal risk for the conceptual design of aircraft equipment bays. In this thesis, a different strategy aimed to effectively integrate the dynamic model of the actuator within the preliminary design phase is proposed. Through this, it will be therefore possible to size the actuator by means of a "dynamic" design approach. The idea is to perform the preliminary design of the EMA according to its flight profile, so that the thermal behaviour of the sized system optimally meets its operational thermal requirements (the maximum windings and housing

skin temperatures perfectly meet the permissible limits, as shown in Fig. 7.2). The steps and tools necessary for its implementation are described in the first part of the chapter. This approach is subsequently used to perform the preliminary design for the entire set of primary flight control EMAs. The sizing is conducted for the four types of thermal management systems discussed so far, namely: the thermal finned housing, the heat pipe, the thermal strap and the PCM plate. A trade off analysis is conducted at the end of the chapter according to the results obtained from the preliminary designs.

7.2 Actuator dynamic model for thermal behaviour

The dynamic model of the actuator must reproduce and interconnect the key aspects that determine the thermal dynamics of the actuator along the mission profile. Hence, receiving the mission profile as input, it must represent all those elements of the actuator and the external environment that affect the motor losses and consequently the motor winding hot spot temperature and housing skin temperature. These elements are represented by means of the modules illustrated in Fig. 7.3, which are:

- The electro-mechanical transmission chain model.
- The motor losses model.
- The motor thermal model.
- The thermal models of the TMSs.
- The atmospheric model.

Since this model will later be used within the optimization framework built to conduct the preliminary design (as made in Chapter 4), it is essential to only consider those characteristics that have an influence on the thermal dynamics, thus neglecting all the parameters describing the components or the system, which do not influence the analysed behaviour and would therefore slow down the simulations. The dynamic model developed here has been implemented in Dymola simulation environment ([129]), represented in Fig. 7.3. The construction of the model is detailed in the following sections.

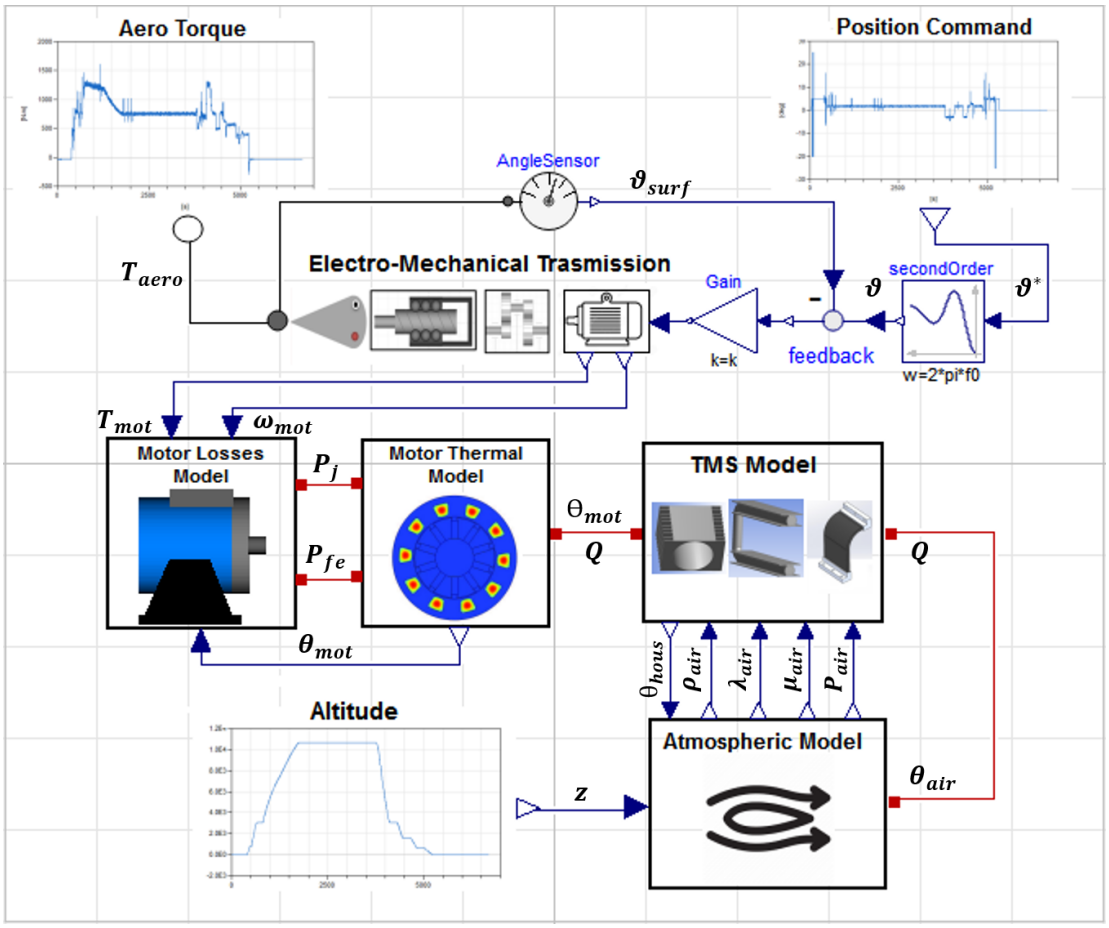

Figure 7.3: Actuator dynamic model architecture and interfaces.

7.2.1 Electro-mechanical transmission chain model

The electro-mechanical transmission chain model, depicted in Fig.7.4, must allow the determination of the torque and speed generated by the motor to be sent to the motor losses model. The inputs of this model are the aerodynamic load T_{aero} and the angular deflection command ϑ^* profiles. In order to meet the computational requirements defined previously, the model must only include aspects relating to the thermal behaviour of the actuator, and therefore the parameters which consequently have an impact on the generation of electromagnetic torque and motor speed. As seen in Section 4.4.1.1, the mechanical parameters influencing the motor torque are: the lever arm L_{arm}, the screw lead p_{sn}, the direct $\eta_{sn_{dir}}$ and inverse $\eta_{sn_{dir}}$ efficiency of the screw-nut device, the friction torque of the bearing which is dependent on the friction coefficient f_r and its average diameter d_m, the gearbox ratio

n_{red} and its efficiency η_{red}. The mechanical components shown in Fig.7.4 are therefore represented by means of the parameters just mentioned. The motor torque and speed are defined through a control loop necessary to automatically adjust the value of a measured angular deflection ϑ_{surf}, dependent on the inertia of the system J_{surf} and J_{mot}, to equal the value of the position command ϑ^*. The latter is calculated by determining the time response of the actuator, approximated to a second-order system.

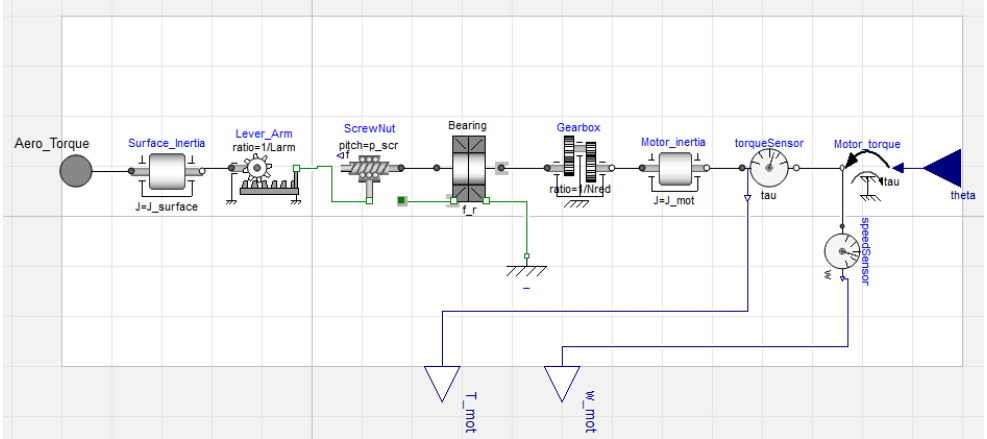

Figure 7.4: Electro-mechanical transmission chain model.

7.2.2 Motor Losses Model

The motor losses model, represented in Fig. 7.5, enables to express the Joule and iron losses of the motor as a function of the torque and speed provided. In both cases, it is possible to use the surrogate models of motor losses developed in Section 3.5. These models are described through the dimensionless variables Π_1, defining the magnetic saturation, and Π_4, expressing the ratio between the yoke and the motor diameter. The variables Π_1 depends on the current density J, which varies along the mission as a function of the torque generated by the motor. This is so derived by interpolation from the motor saturation curve (for a defined motor size, the saturation curve is generated through the surrogate model of the electromagnetic torque defined on several points at the variation of Π_1). In order to take account of the effect of the temperature on Joule losses, the electrical resistivity of copper

ρ_{Cu} is evaluated as follows:

$$\rho_{Cu} = \rho_{Cu_{\theta_{ref}}}\Big(1 + (\Theta_{wind} - \Theta_{ref})\alpha_{co}\Big) \tag{7.1}$$

where Θ_{ref} is the reference temperature $(20°C)$, Θ_{wind} is the winding temperature, $\rho_{Cu_{\Theta_{ref}}}$ the equivalent copper resistivity at Θ_{ref} and α_{co} is the temperature coefficient.

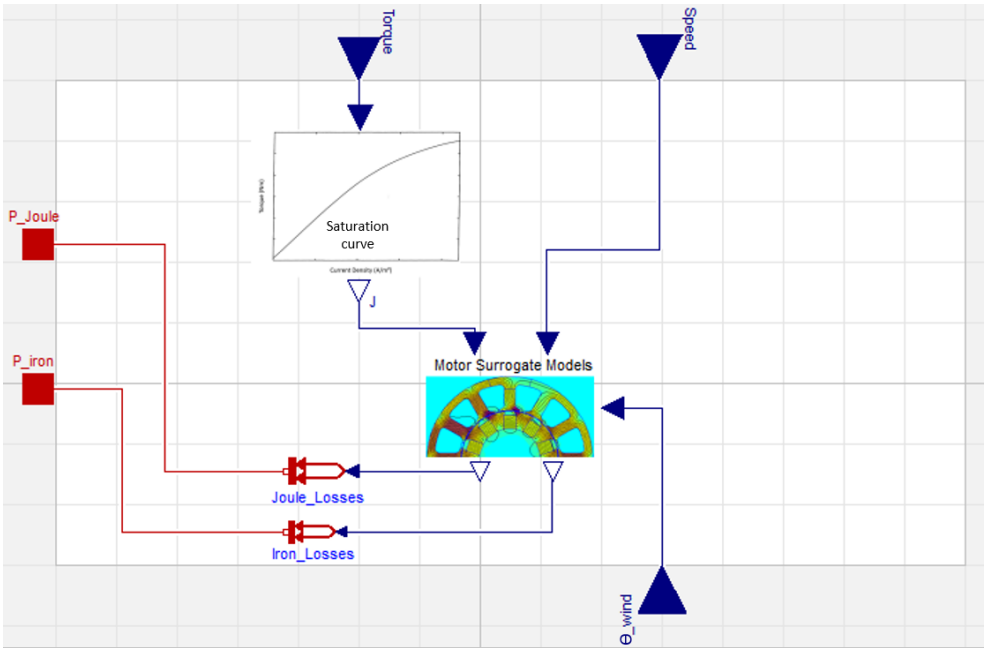

Figure 7.5: Motor losses model.

7.2.3 Motor Thermal Model

The construction of a 1-D thermal model of the electric motor, enabling the satisfaction of the computational requirements, is quite challenging. Complex resistance and capacity networks, such as those described by Sciascera et al. [151], are very difficult to parametrise and lead to quite long simulations. For this reason, a simpler model using two resistance-capacitance pairs (for copper and iron respectively) is often used in the preliminary design phase (Fig. 7.6).

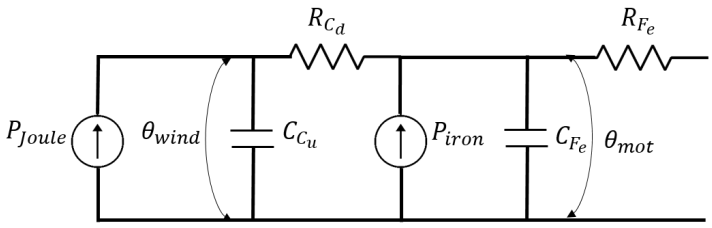

Figure 7.6: Example of 2-body thermal motor model.

An accurate estimation of the thermal resistances of the motor can be obtained through the surrogate model introduced in Section 4.4.2.3. This model, developed by Sanchez [12] [152], allows the estimation of the thermal resistance R_{cd} between the hot spot temperature in the motor slot and the temperature of the exterior surface of the stator iron, as a function of the motor diameter, its length and the electrical insulation layer thickness. The use of this model also permits an important approximation, allowing the thermal resistance of the motor iron R_{F_e} to be neglected. This has proved negligible when compared to that of the winding R_{cd} [152], as the latter takes into account an equivalent homogenisation of the copper, potting resin and insulation. The thermal model of the motor can be so defined as shown in Fig. 7.7.

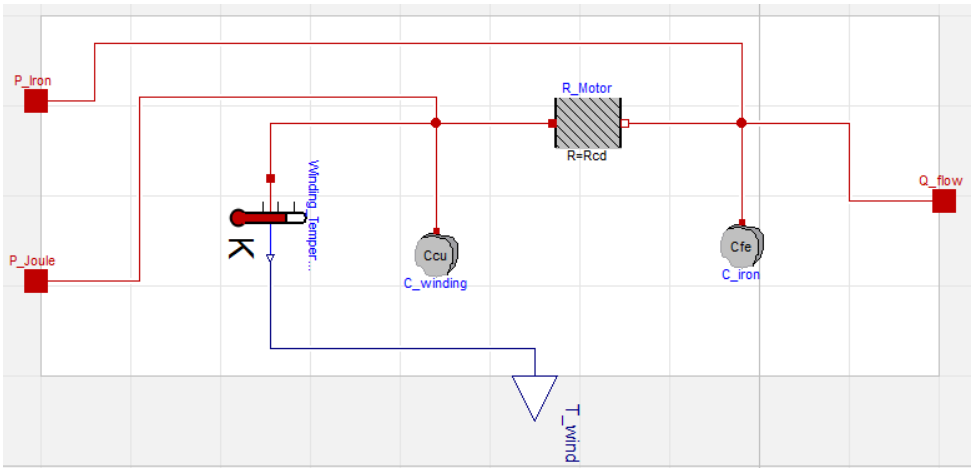

Figure 7.7: Motor Thermal Model.

7.2.4 Atmospheric model

The atmospheric model depicted in Fig. 7.8, is used to determine the temperature, pressure and air properties as a function of the flight altitude. Firstly, the air temperature Θ_{air} and pressure P_{air} can be computed by means of the relationships established by Cavcar et al. [153]:

$$\Theta_{air} = T_0 - 6.5\frac{z}{1000}, \quad [K] \tag{7.2}$$

$$P_{air} = P_0\Big(1 - 0.0065\frac{z}{\Theta_0}\Big)^{5.2561}, \quad [Pa] \tag{7.3}$$

where the variable z represents the altitude, Θ_0 ($[K]$) is the ground temperature ($15°C$) and P_0 is the atmospheric pressure at sea level ($101.33\,kPa$). In order to consider the most severe scenario from a thermal point of view, a standard hot day condition in the International Standard Atmosphere (ISA +35°C) is considered. The reference temperature Θ_0 can then be reformulated as follows:

$$\Theta_{0_{ISA}} = \Theta_0 + \Theta_{0_{ISA+35}} = 15°C + 35°C = 50°C \tag{7.4}$$

Air properties are determined as a function of the corresponding temperature and pressure conditions. These can generally be determined from specific tables [154] or numerical calculators, which provide values for density ρ_{air}, dynamic viscosity μ_{air}, thermal conductivity λ_{air} and specific heat $c_{p_{air}}$ according to the pressure and temperature. However, an automatic approach is needed in this context to evaluate the air properties continuously throughout the duration of the mission profile. Consequently, it becomes necessary to express a mathematical formulation that correlates the air properties as a function of the atmospheric conditions of temperature and pressure along the flight phase. In order to determine these relationships, correlation laws have been developed. To do this, a LHS DoE defining 100 temperature and pressure values has been generated, chosen within a range of minimum and maximum values detected within the altitude spectrum considered. For each point of the DoE the corresponding values of ρ_{air}, μ_{air}, λ_{air} and $c_{p_{air}}$ have been extracted through the Python package "CoolProop" [155], which provides the thermophysical properties of a wide variety of fluids according to the temperature and pressure conditions. Based on the values obtained, linear regressions have been implemented, which provide the followings relationships (with a maximum $max|\epsilon|$ and mean $\bar{\epsilon}$ relative errors close to 0%

compared to the data from CoolProop):

$$\rho_{air} = (17.42 + 0.24P_{air} - 0.0004\Theta_c P_{air}) \cdot 10^{-4}, \quad [kg/m^3] \tag{7.5}$$

$$\lambda_{air} = (3.86 + 0.075\Theta_c) \cdot 10^{-3}, \quad [W/m/K] \tag{7.6}$$

$$\mu_{air} = (3.89 + 0.048\Theta_c) \cdot 10^{-6}, \quad [kg/m/s] \tag{7.7}$$

$$c_p = 1005, \quad [J/kg/K] \tag{7.8}$$

where $\Theta_c = \frac{\Theta_{air}+\Theta_s}{2}$ is the mean film temperature between the heat exchange area and the external environment. It should be noted that for the altitude range considered, the specific heat is the only parameter that is independent of temperature and pressure, while the density is the only variable that is dependent on pressure.

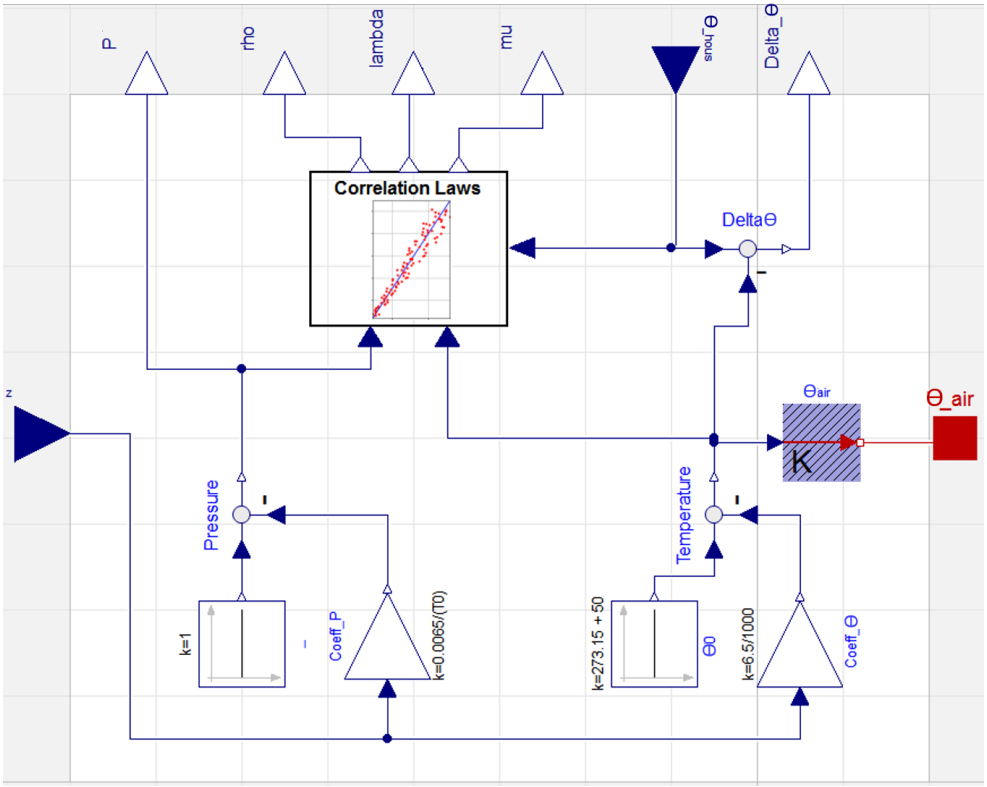

Figure 7.8: Atmospheric Model.

7.2.5 Thermal management system models

7.2.5.1 Finned thermal housing model

The thermal model of the finned housing considers its capacity and thermal resistances, as depicted in Fig 7.9. The thermal resistance is defined by the parallel connexion of 5 thermal resistances, discussed in Section 4.4.2.5, depending on the different convective heat transfer surfaces and radiation of the component. It is important to keep in mind that the values of the convective heat transfer coefficients must be updated along the mission, depending on the values of air properties described in the previous subsection.

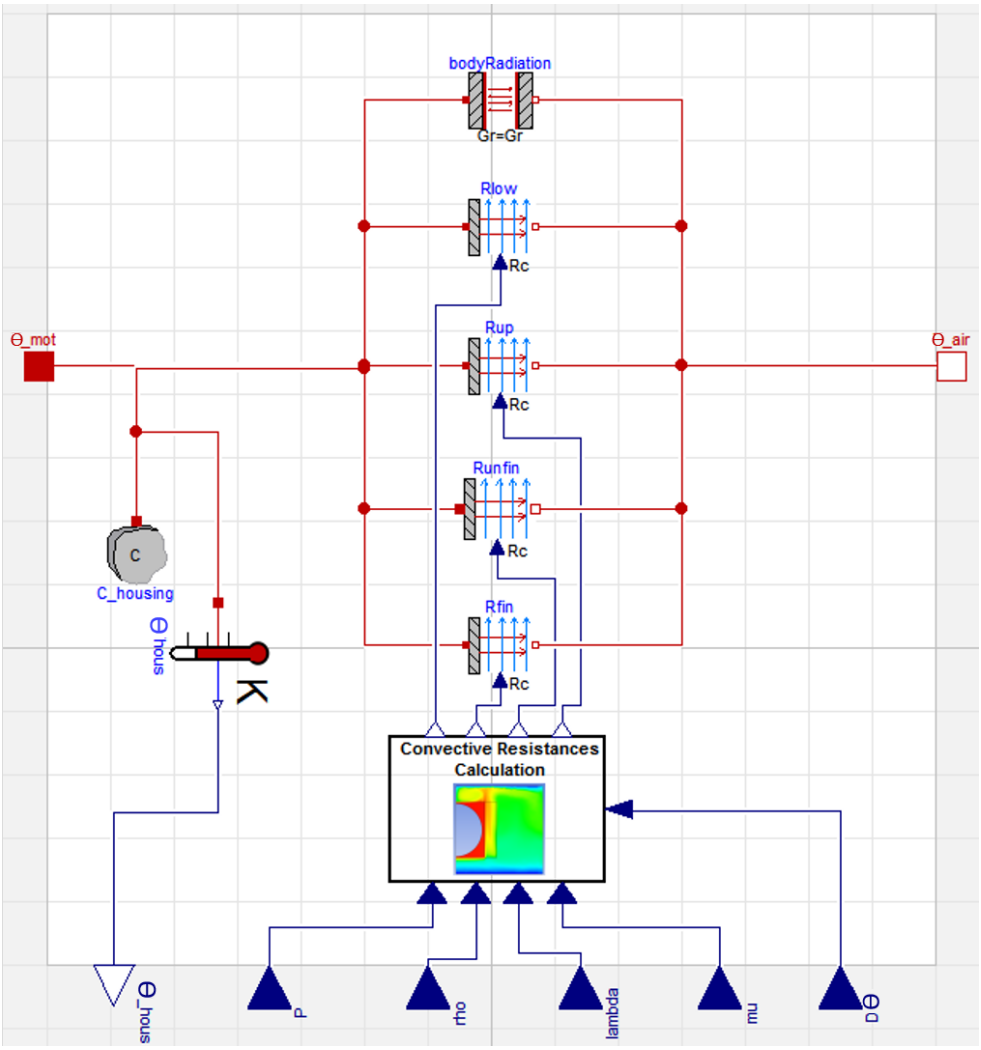

Figure 7.9: Thermal Housing Model.

Effect of the actuator compartment

The resistance models developed so far are defined for the case of free convection in open space. On the other hand, the actuator is located in a semi-confined space[1] inside the wing, which is detrimental for natural convection. The evaluation of the effects of this semi-confined volume on natural convection can only be achieved by means of fluid-dynamic simulations, whose implementation within an optimisation procedure would require inhibitory computation times. To this purpose, Sanchez et al. [156] investigated the relations between the aircraft systems' locations within an equipment bay and the characteristics of the ventilation sources. They established an accurate model based on dimensionless numbers validated by computational fluid dynamic simulations.

In order to take this aspect into account, a conservative multiplication coefficient $k_{room} = 0.5$ has therefore been adopted for the calculation of the convective resistances. The value of this coefficient has been determined according to the results provided by finite volume method simulations applied to a representative case study, depicted in Fig. 7.10. In this case study, the confinement environment of the actuator is represented by a volume which dimensions are fixed to those of the actuator envelope. A finned thermal housing has been placed within this volume. The motor losses are simulated through a 100 W heat source distributed on the interior walls of the housing. Isothermal temperature conditions (20 °C) have been placed on the top and bottom of surfaces of the volume. The results obtained from the simulation, revealed a convective heat transfer coefficient $h_{eq} = 2.99\,W/m^2K$ (weighted on the whole exchange surface).
The same housing configuration was subsequently simulated for the case of natural convection in open space (Fig. 7.11). The results obtained from this study indicated $h_{eq} = 6.04\,W/m^2K$, pointing out that a 53% reduction of the heat transfer coefficient occurs in EMA location with respect to the free convection case. Hence, the choice to use the multiplicative coefficient $k_{room} = 0.5$ in the calculation of convective resistances.

7.2.5.2 Heat pipe model

The thermal model of the heat pipe, shown in Fig. 7.12, is composed of the heat capacity of the motor housing and the series of resistances described in Chapter 5: the resistance

[1]The term semi-confined refers to the fact that the airflow re-circulation is mainly bounded vertically by the upper and lower surfaces of the wing, while it is more free to circulate along the horizontal directions within the wing.

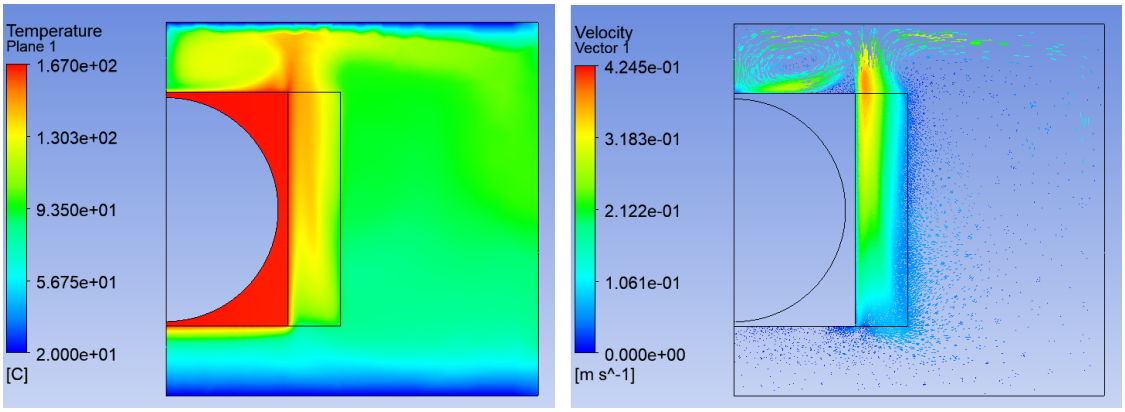

(a) Temperature distribution (b) Airflow velocity distribution

Figure 7.10: 2-D visualisation of the results obtained with finite volume method simulation for the case study of confined space.

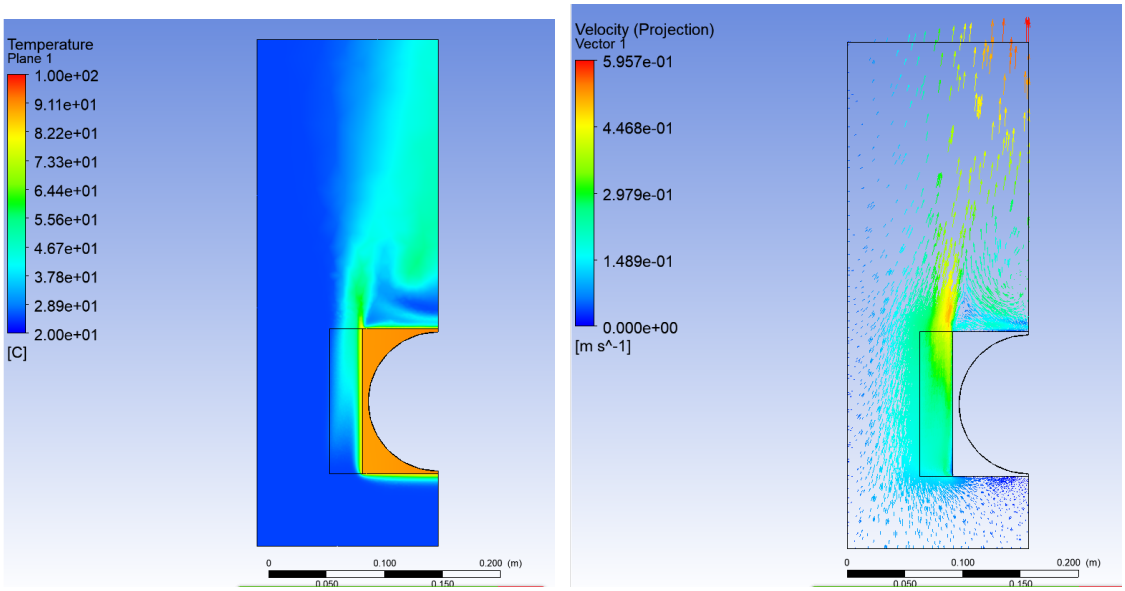

(a) Temperature distribution (b) Airflow velocity distribution

Figure 7.11: 2-D visualisation of the results obtained with finite volume method simulation for the case study of open space.

of the TIM interposed between the heat source and the evaporator, the resistance of the evaporator, the resistance of the condenser, the resistance of the TIM inserted between the condenser and the spreader, the resistance of the spreader and the convective resistance with the external environment. With regard to convective resistance, the formulations of

Ameel [107] are implemented to determine the value of the heat transfer coefficient on the heated surface of the wing (spreader surface). To this purpose, the aircraft speed profile and the air properties enable the calculation of Reynolds and Prandtl numbers along the flight mission. The obtained value of heat transfer coefficient is also used to calculate the thermal resistance of the spreader (according to Eq. 5.22).

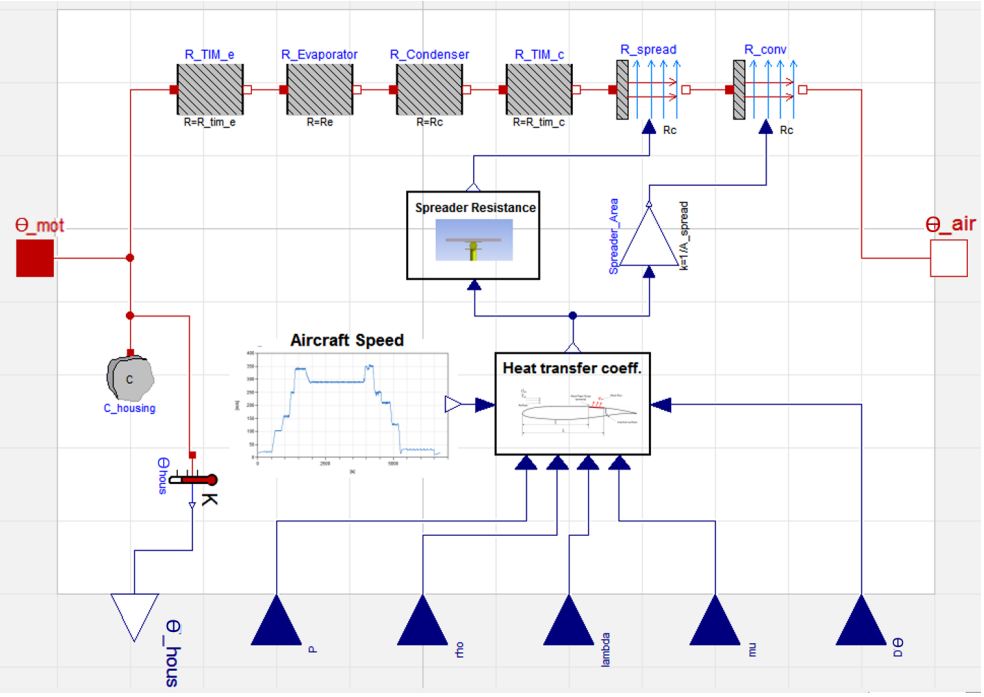

Figure 7.12: Heat Pipe Model.

7.2.5.3 Thermal strap model

Similar to the heat pipe, the thermal model of the thermal strap is defined. The only difference is that the evaporator and condenser resistances are replaced by the strap and plates resistances of the thermal strap, as show in Fig. 7.13. The value of the conduction resistance of the strap is updated along the mission as a function of the value of the pyrolitic graphite conductivity, which depends on the temperature.

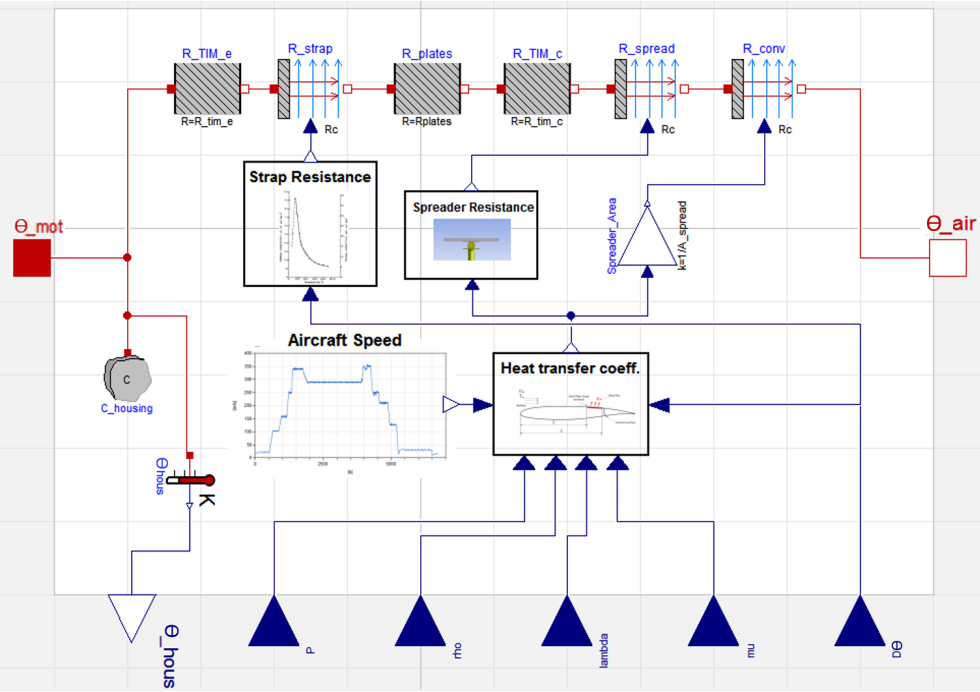

Figure 7.13: Thermal Strap Model.

7.2.5.4 PCM plate model

The model of the PCM plate has been described in Section 6.4.3.

7.2.6 Validation of the electro-mechanical actuators designed with the static approach

Once the dynamic model of the actuator has been assembled, it may be convenient at this point to observe the thermal behaviour of the electro-mechanical actuators designed in Chapter 4. In this way, it is possible to verify how effective were, from a thermal point of view, the sizing choices made for the different primary flight control actuators and, above all, if the integration of the dynamic model in the design procedure could be convenient or not. The output parameters of interest emerging from the obtained design are so passed to the dynamic model, and the thermal behaviour along the mission profile is thus analysed. When analysing the dynamic thermal response, for the three sized gear drive EMAs, two

completely different aspects emerge, as illustrated in Fig. 7.14. The Aileron design at average load resulted to be undersized from a thermal point of view, as the temperature limits of the device have been exceeded. On the other side, the Elevator and Rudder designs at maximum load were too conservative, since the operating temperatures, both in the motor windings and in the housing skin, are well below the permissible technological limits. As a result, the Elevator and Rudder are excessively oversized, making the actuator heavier and more cumbersome. The observed dynamic thermal profiles therefore justify the interest of implementing the dynamic sizing approach, aiming to design the actuator so that it can maximise the thermal performance while ensuring the lightest solution.

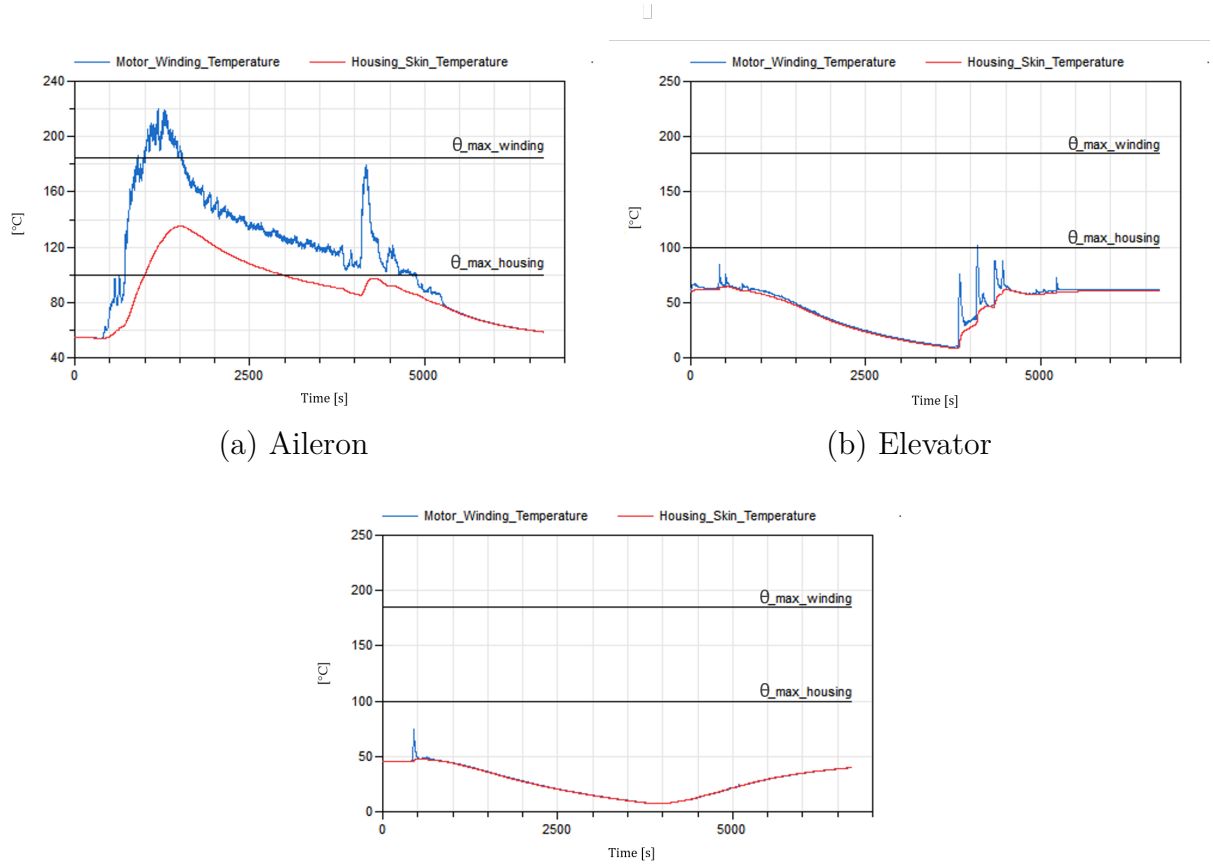

(a) Aileron

(b) Elevator

(c) Rudder

Figure 7.14: Dynamic thermal profile of EMAs designed with the static approach.

7.3 Preliminary design and evaluation of the discussed TMS concepts

In this section, the models and methods developed so far are implemented to evaluate the most suitable thermal management solutions according to the types of application considered in this study. To this purpose, the preliminary design of the electro-mechanical actuator is performed for the entire set of primary control surfaces. The dynamic approach is therefore adopted and the sizing procedure is conducted according to the four types of thermal management solutions considered in Chapter 5 and Chapter 6: the thermal finned housing, the heat pipe, the thermal strap and the PCM plate. As far as the EMA architecture is concerned, a gear drive configuration, identical to that described in Chapter 4, is adopted. The actuator specifications are defined according to the same mission profiles and sizing scenarios considered for the preliminary design based on the static approach. The design procedure is identical to that adopted in Chapter 4. The only difference consists in the introduction of the dynamic model used to evaluate the thermal sizing scenario, previously modelled by means of algebraic equations. In order to implement the sizing problem by means of an optimisation procedure aimed at minimising the mass of the system (composed by the actuator and its associated TMS), a dedicated framework has been developed in the Python environment. Within this framework, a library containing all the generated models (system and components models, as well as the dynamic models) has been defined. In this way, depending on the case study, the framework selects the modules of interest directly from the library.
In the next sections, the integration of the dynamic model within the design framework is first illustrated. The preliminary design problems are subsequently presented and the obtained results for the different case of studies are finally analysed.

7.3.1 Model integration in the preliminary design framework

In order to include the dynamic model in the design phase, it is necessary to define a method for integrating the Dymola model within the Python sizing framework. This integration is achieved by converting the Dymola model into a FMU (Functional Mock-up Unit). This generated model conforms to the FMI (Functional Mock-up Interface) standard

[157], which enables the exchange and the co-simulation of models generated in different simulation environments. Then, the pyFMI package [158] is used in the design framework for modifying inputs and parameters, simulating the model and accessing the simulations results as it is required to perform the optimization problem. The interaction between the sizing models and the dynamic model contained in the FMU, can be graphically illustrated with the XDSM, as depicted in Fig. 7.15, adopted for the case study of the finned thermal housing. The optimizer integrated in the sizing framework coordinates the preliminary design problem, by sending the design variables to the sizing models for the computation of the dimensions, mass and performances of the system. Subsequently, the sizing models send to the FMU the parameters of the actuator affecting the thermal performances. Then the FMU provides the motor winding hot spot temperature and housing skin temperature. These temperatures are analyzed and their maximum values are passed as constraints to the optimizer. A FMU simulation is so performed for each optimizer iteration, until the optimum system requirements are achieved.

7.3.2 Case study 1: Finned thermal housing

The Preliminary design of this case study is conducted similarly to that carried out in Chapter 4. However, some adaptations have been made, as the integration of the dynamic model of the actuator involves a different coordination of the design problem. Firstly, the treatment of the thermal constraints is different. In the static design, the housing temperature $\Theta_{hous_{max}}$ was fixed at $100°C$ and the thermal constraints considered were:

$$\Theta_{wind_{max}} \leq \Theta_{wind_{lim}} \tag{7.9}$$

$$Q \geq (P_J + P_{Fe}) \tag{7.10}$$

Since the maximum temperature of the housing is now evaluated with the dynamic model, Eq. 7.10 is no longer necessary. Consequently, this is replaced by the following constraint:

$$\Theta_{hous_{max}} \leq \Theta_{hous_{lim}} \tag{7.11}$$

where $\Theta_{hous_{max}}$ is the maximum temperature of the housing observed along the mission profile and $\Theta_{hous_{lim}}$ is the temperature limit on the housing skin fixed at $100°C$.

In addition, in order to provide an additional degree of freedom for the definition of the motor sizing torque, the oversize coefficient $k_{d_{opt}}$ has been introduced:

$$T_{EMA} = k_{d_{opt}} \frac{T_{aero_{RMS}} p_{sn}}{L_{arm} n_{red} \eta_{red} 2\pi} \tag{7.12}$$

where the torque design coefficient $k_{d_{opt}} \in \left[1; \frac{T_{aero_{max}}}{T_{aero_{RMS}}}\right]$ is taken as optimization variable. Note that in the case of static designs, the aileron actuator has been sized for the RMS aerodynamic torque, while the Rudder and Elevator actuators have been sized for the maximum torque. In order to make a comparison between the two types of sizing approaches, we could then consider for the static design cases, $k_{d_{opt}} = 1$ for the aileron, $k_{d_{opt}} = 6.5$ $(\frac{T_{aero_{max}}}{T_{aero_{RMS}}})$ for the Elevator and $k_{d_{opt}} = 24$ $(\frac{T_{aero_{max}}}{T_{aero_{RMS}}})$ for the Rudder.
In order to graphically illustrate the optimization problem, the XDSM depicted in Fig 7.15 is used. The optimization problem is formulated in the following way:

$$\begin{aligned}
\text{Minimize} \quad & M_{EMA} \\
\text{with respect to} \quad & k_{d_{opt}}, D_e, \Pi_2, k_b, k_{sn}, n_{red}, L_a, S, s_a, k_L, k_H, k_W \\
\text{subject to} \quad & \Theta_{wind_{max}} - \Theta_{wind_{lim}} \leq 0 \\
& \Theta_{hous_{max}} - \Theta_{hous_{lim}} \leq 0 \\
& \omega_{mot_{max}} - \omega_{max} \leq 0 \\
& C_{d_{sn_{req}}} - C_{d_{sn}} \leq 0 \\
& F_{shock} - C_{0_{sn}} \leq 0 \\
& F_{shock} - C_{0_b} \leq 0 \\
& C_{d_{b_{req}}} - C_{d_b} \leq 0 \\
& J_{ref} - J_{ref_{max}} \leq 0 \\
& \sigma - \sigma_{max} \leq 0 \\
& L_{EMA} - L_e \leq 0 \\
& W_{EMA} - W_e \leq 0 \\
& H_{EMA} - H_e \leq 0
\end{aligned} \tag{7.13}$$

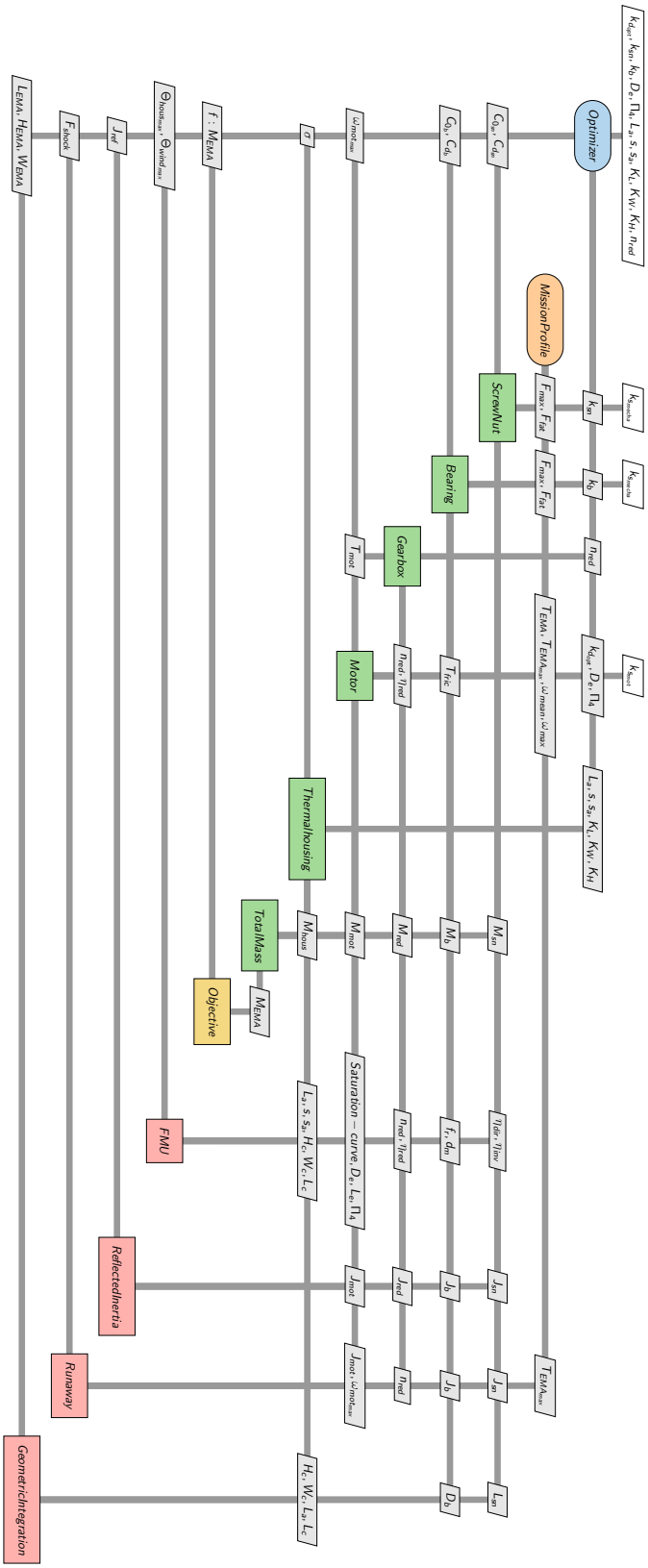

Figure 7.15: Extended design structure matrix of the EMA preliminary design of case study 1.

The results obtained from the optimisation are summarised in Table 7.1, and compared to those obtained with the static design approach. Details of results are shown in **Annex D**. The temperatures evolution of the motor windings and the housing skin are shown in Fig. 7.16.

Table 7.1: Results of optimizations for case study 1

	Static Design			Dynamic Design		
	Aileron	Elevator	Rudder	Aileron	Elevator	Rudder
Design coefficient, $k_{d_{opt}}$ $[-]$	(1)	(6.5)	(24)	1.25	3.2	10.2
Motor diameter, D_e $[mm]$	62.9	53.29	62.55	61.57	40.25	38.87
Motor length, L_m $[mm]$	76.62	98.33	91.22	99.76	76.14	102
Motor Mass, M_{mot} $[kg]$	1.26	1.22	1.46	1.58	0.5	0.62
Fin width, L_a $[-]$	25.25	30	31.64	21.73	22.76	5
Housing/Motor length ratio, k_L $[-]$	2	2	2	2	1	1
Fins mass, M_{fin} $[kg]$	0.16	0.30	0.32	0.12	0.03	0.005
Housing body mass (no fins), M_{body} $[kg]$	0.65	0.69	0.74	1.55	0.17	0.21
Housing mass, M_{hous} $[kg]$	0.82	1	1.05	1.67	0.2	0.215
Screw-nut mass, M_{sn} $[kg]$	1.44	0.9	0.8	1.44	0.35	0.36
Bearing mass, M_b $[kg]$	1.19	1	0.83	1.28	0.37	0.38
Gearbox mass, M_{red} $[kg]$	0.9	0.65	0.88	0.9	0.33	0.4
EMA Mass, M_{EMA} $[kg]$	5.6	4.77	5.02	6.87	1.75	1.98

For the EMA Aileron, the thermal constraints have been fulfilled through a 23% increase in the mass of the device, with respect to the static design case. This is due to an increase of both the electric motor ($k_{d_{opt}} = 1.25$; +24% of mass) and the finned thermal housing (+103% of mass). The most critical flight phase is during climb, where the peak aerodynamic load is present for the entire duration of this phase. The cooling system adopted is limiting for this type of application, due to the encumbrance and fins vibration constraints, which negatively affect the design of the finned housing. Since the device cannot further increase the heat exchange surface area by increasing the size of the fins, it is forced to increase in length of the housing ($k_L = 2$), thus generating a major mass penalty. The limitations of the thermal management system result in an under-use of the electric motor (the winding temperature is $30°C$ below the permitted thermal limits), which is forced to increase its size in order to limit the generated power losses. The resulting system so does not will operate at its full thermal capability.

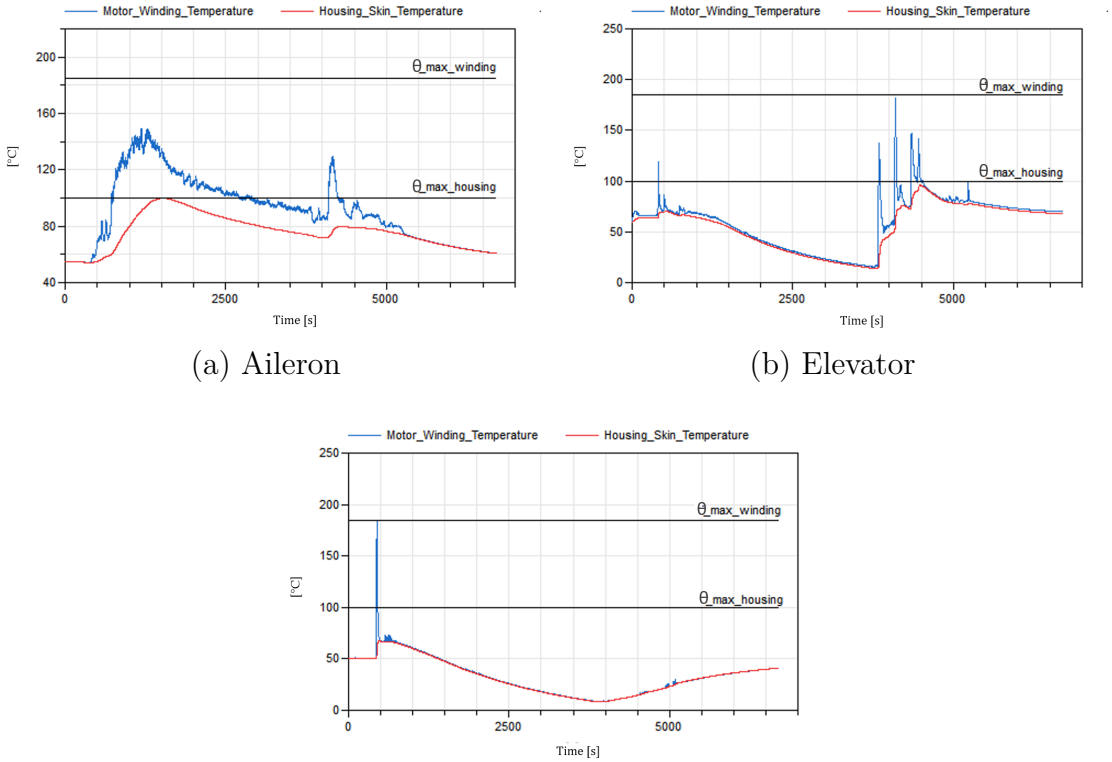

(a) Aileron

(b) Elevator

(c) Rudder

Figure 7.16: Thermal profile of EMAs designed with the finned thermal housing.

Regarding the Elevator, significant mass benefits have been achieved through the dynamic optimisation. By designing the actuator with a sizing coefficient $k_{d_{opt}} = 3.2$, a mass decrease of 64% is achieved with respect to the static design at the maximum load. The thermal performance of the device is in this case limited by the maximum temperature limit of the motor winding, reached during the descent phase. During this phase, an instantaneous load peak produces a drastic rise in the winding temperature. This means that the thermal capacity of the copper winding is only responsible for keeping the temperature below the operating thermal requirements. A minimum of cooling device is however necessary ($k_L = 1$, $M_{fin} = 30\,g$), in order to contain the temperature along the mission. A decrease in fins size, for example, would result in higher temperature levels reached during the flight. The peak load would then start at a higher temperature point, leading to the non-compliance of the operational thermal requirements (see Fig.7.17). It should also be noted that reducing the size of the electric motor leads to a decrease of the shock on stops, allowing the masses of the screw-nut and bearing devices to be reduced.

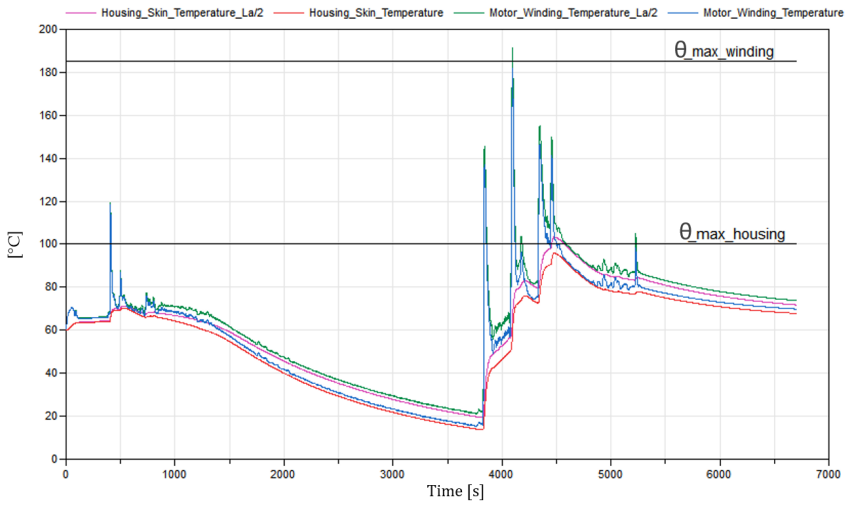

Figure 7.17: Effect of a reduced fins size ($L_a = 11.38\,mm$) on the thermal profile of the sized EMA Elevator.

The EMA Rudder design is the most favourable from a thermal point of view. Also in this case the dynamic optimisation has allowed a considerable decrease of 60% of the mass of the system ($k_{d_{opt}} = 10.2$) compared to the mass obtained with the static design at maximum load. The mission profile shows a huge load peak of very short duration that takes place at the beginning of the flight, while a very low average load is present for the entire duration of the mission. In this case, the only thermal capacity of the motor is sufficient to maintain the winding temperature under the required limit, thus making the use of the cooling system unnecessary whatever the type of TMS considered (the dimensions of the finned thermal housing are set to the lower bound of the defined variables' range). Given the results obtained, the use of thermal management systems such as heat pipes and thermal straps is therefore superfluous for this application. As a consequence, the preliminary design of the EMA Rudder for case study 2 and case study 3 is not considered.

7.3.3 Case study 2: Heat pipe

The sizing problem for this case study is achieved by simply replacing the thermal model of the finned housing with the heat pipe module. The interconnection between the sizing models and the FMU models is thus altered as shown in the XDSM depicted in Fig. 7.18. The implementation of the heat pipe model leads to the introduction of new optimisation variables and constraints. These variables concern geometrical design parameters of the heat pipe (n_{HP}, l_c, d_{HP}), spreader (w_s, l_s) and TIM (k_{bt}, Π_{4_T}), introduced in Chapter 5. The added constraints take into account the heat pipe limits ($d_{HP_{req}}$, Φ_{max}). The optimization problem is so formulated as below:

$$
\begin{aligned}
\text{Minimize} \quad & M_{EMA} \\
\text{with respect to} \quad & k_{d_{opt}}, D_e, \Pi_2, k_b, k_{sn}, n_{red}, n_{HP}, l_c, d_{HP}, w_s, l_s, k_{bt_e}, k_{bt_c}, \Pi_{4_{T_e}}, \Pi_{4_{T_c}} \\
\text{subject to} \quad & \Theta_{wind_{max}} - \Theta_{wind_{lim}} \leq 0 \\
& \Theta_{hous_{max}} - \Theta_{hous_{lim}} \leq 0 \\
& \omega_{mot_{max}} - \omega_{max} \leq 0 \\
& C_{d_{sn_{req}}} - C_{d_{sn}} \leq 0 \\
& F_{shock} - C_{0_{sn}} \leq 0 \\
& F_{shock} - C_{0_b} \leq 0 \\
& C_{d_{b_{req}}} - C_{d_b} \leq 0 \\
& J_{ref} - J_{ref_{max}} \leq 0 \\
& d_{HP} - d_{HP_{req}} \leq 0 \\
& \Phi_c - \Phi_{e_{max}} \leq 0 \\
& \Phi_e - \Phi_{c_{max}} \leq 0 \\
& L_{EMA} - L_e \leq 0 \\
& W_{EMA} - W_e \leq 0 \\
& H_{EMA} - H_e \leq 0
\end{aligned}
\tag{7.14}
$$

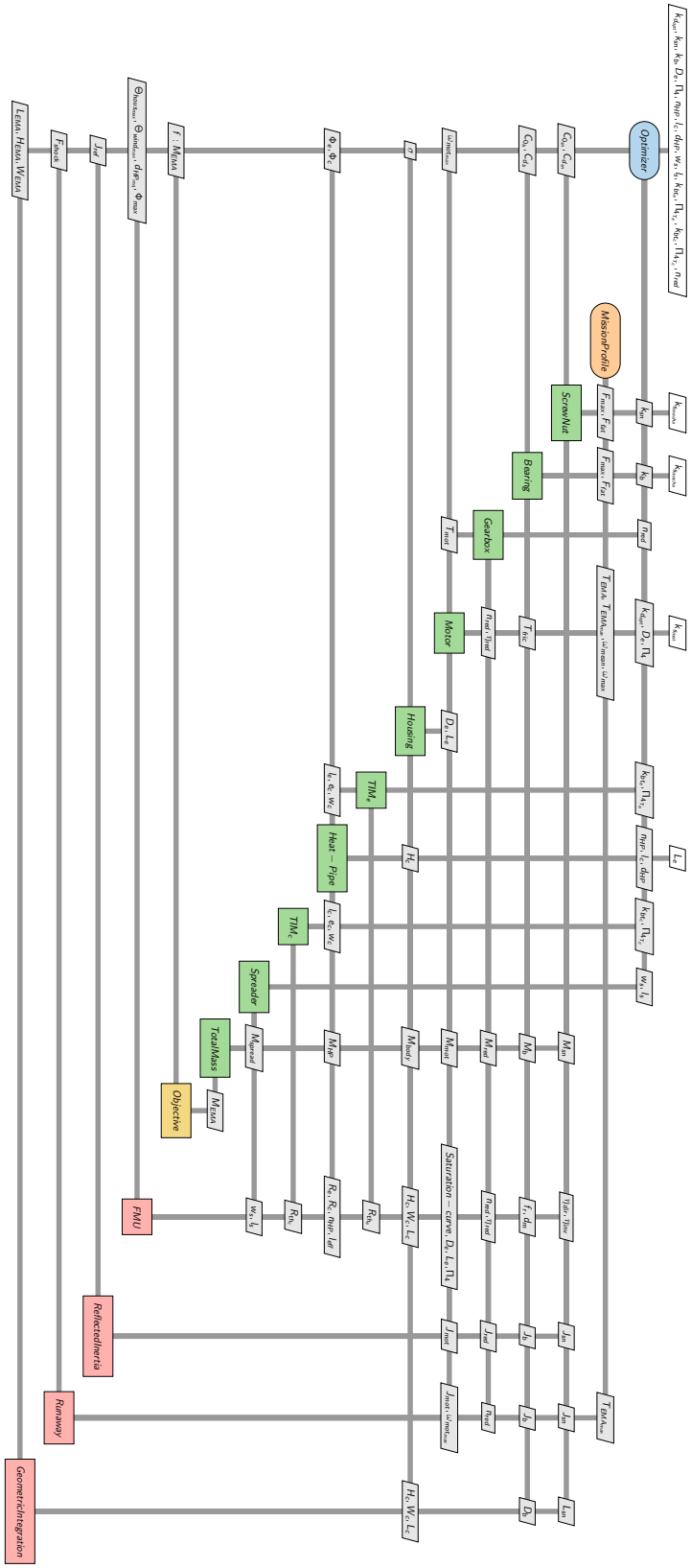

Figure 7.18: Extended design structure matrix of the EMA preliminary design of case study 2.

The results obtained from the optimisations are shown in Table 7.2, while the temperature profiles of the motor windings and skin housing are showed in Fig. 7.19. Details of results are shown in **Annex D**.

Table 7.2: Results of optimizations for case study 2

	Aileron	Elevator
Design coefficient, $k_{d_{opt}}$ $[-]$	1.15	3
Motor diameter, D_e $[mm]$	51.66	36.46
Motor length, L_m $[mm]$	124	90.57
Motor Mass, M_{mot} $[kg]$	1.35	0.49
HP number, n_{HP} $[-]$	2	1
HP diameter, d_{HP} $[mm]$	10.49	10
Condenser length, l_c $[mm]$	151.5	42
Effective length, l_{eff} $[mm]$	235	170
Hp mass (per unit), M_{HP} $[kg]$	0.1	0.06
Spreader length, l_s $[mm]$	182.6	50.75
Spreader width, w_s $[mm]$	212	48.21
Spreader mass, M_{spread} $[kg]$	0.31	0.02
Housing body mass, M_{body} $[kg]$	0.35	0.16
Screw-nut mass, M_{sn} $[kg]$	1.44	0.32
Bearing mass, M_b $[kg]$	0.94	0.34
Gearbox mass, M_{red} $[kg]$	0.83	0.31
EMA Mass, M_{EMA} $[kg]$	5.42	1.70

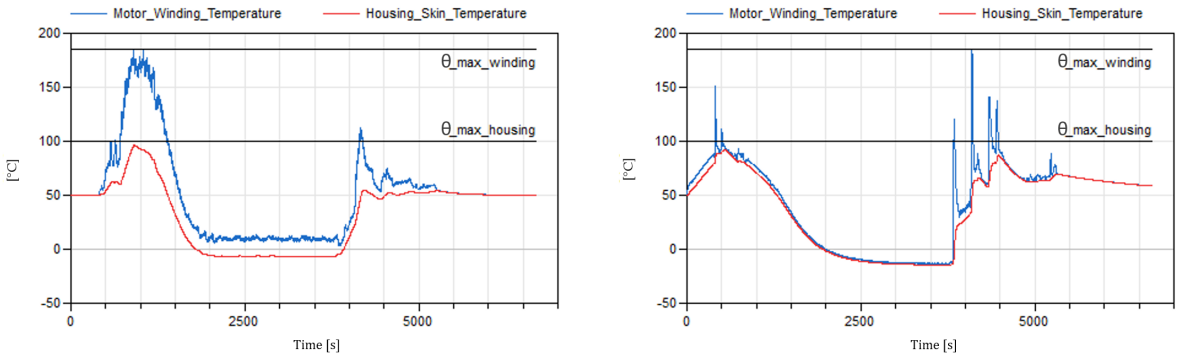

(a) Aileron (b) Elevator

Figure 7.19: Thermal profile of EMAs designed with the heat pipes.

For the Aileron application, significant benefits in terms of mass (-22%) and thermal performances have been achieved through the use of 2 heat pipes, compared to case study 1. These benefits are mainly due to the fact the heat pipe offers greater thermal performances compared to the finned housing, which means that for the same temperature difference, a higher heat transfer rate can be obtained. This enabled a system design characterised by:

- A smaller electric motor (-14.56% of obtained mass), operating at maximum admissible thermal capabilities.
- Lighter mechanics, as less shock on stops is generated due to the reduced size and inertia of the motor (the bearing mass reduced by 26.56%; the screw-nut mass is unchanged as the fatigue effort is predominant for this device from a design point of view).
- A lighter TMS (-48.44% of obtained mass) (Case study1: $TMS_{mass} = M_{hous}$; Case study 2: $TMS_{mass} = M_{body} + n_{HP}M_{HP} + M_{spread}$) which allows to dissipate the higher amount of power losses generated by the electric motor.

Concerning the EMA Elevator, the same levels of mass have been obtained as in case study 1. This seems quite reasonable, since, as seen previously, the TMS is used to better cooling the housing skin, while the temperature constraint for this application is at the motor winding. And since the finned housing were already very light in case study 1, there is no further mass gain involved by using heat pipes instead. In fact, with the same housing obtained for the two case studies, the mass contribution of the heat pipe and the associated spreader to the total system is practically of the same order as that of the fins.

7.3.4 Case study 3: Thermal Strap

The preliminary design concerning the thermal straps is similar to the previous case study, given the analogy of the configurations. This is performed by simply replacing the heat pipe module with the thermal strap model, as shown in the XDSM depicted in Fig. 7.20. This involves replacing the optimisation variables defining the heat pipe geometries with those of the strap (n_{TS}, W_b). The only constraint introduced by this module concerns the maximal width W_b, which has to be lower than the length L_c (or width W_c) of the housing on which it is mounted. The optimisation problem is thus implemented as follows:

$$
\begin{aligned}
\text{Minimize} \quad & M_{EMA} \\
\text{with respect to} \quad & k_{d_{opt}}, D_e, \Pi_2, k_b, k_{sn}, n_{red}, n_{TS}, W_b, w_s, l_s, k_{bt_1}, k_{bt_2}, \Pi_{4_{T_1}}, \Pi_{4_{T_2}} \\
\text{subject to} \quad & \Theta_{wind_{max}} - \Theta_{wind_{lim}} \leq 0 \\
& \Theta_{hous_{max}} - \Theta_{hous_{lim}} \leq 0 \\
& \omega_{mot_{max}} - \omega_{max} \leq 0 \\
& C_{d_{sn_{req}}} - C_{d_{sn}} \leq 0 \\
& F_{shock} - C_{0_{sn}} \leq 0 \\
& F_{shock} - C_{0_b} \leq 0 \\
& C_{d_{b_{req}}} - C_{d_b} \leq 0 \\
& J_{ref} - J_{ref_{max}} \leq 0 \\
& W_b - W_c \leq 0 \\
& L_{EMA} - L_e \leq 0 \\
& W_{EMA} - W_e \leq 0 \\
& H_{EMA} - H_e \leq 0
\end{aligned}
\tag{7.15}
$$

The results obtained from the optimisation are shown in Table 7.3. Details of results are shown in **Annex D**. The temperature profiles of the motor windings and skin housing are shown in Fig. 7.21. The design obtained with the thermal straps reasonably follows the trend introduced by heat pipes. In fact, it should be noted that the obtained masses of the actuator components broadly reflect the component masses resulting from the previous case study. The same considerations can therefore be adopted.

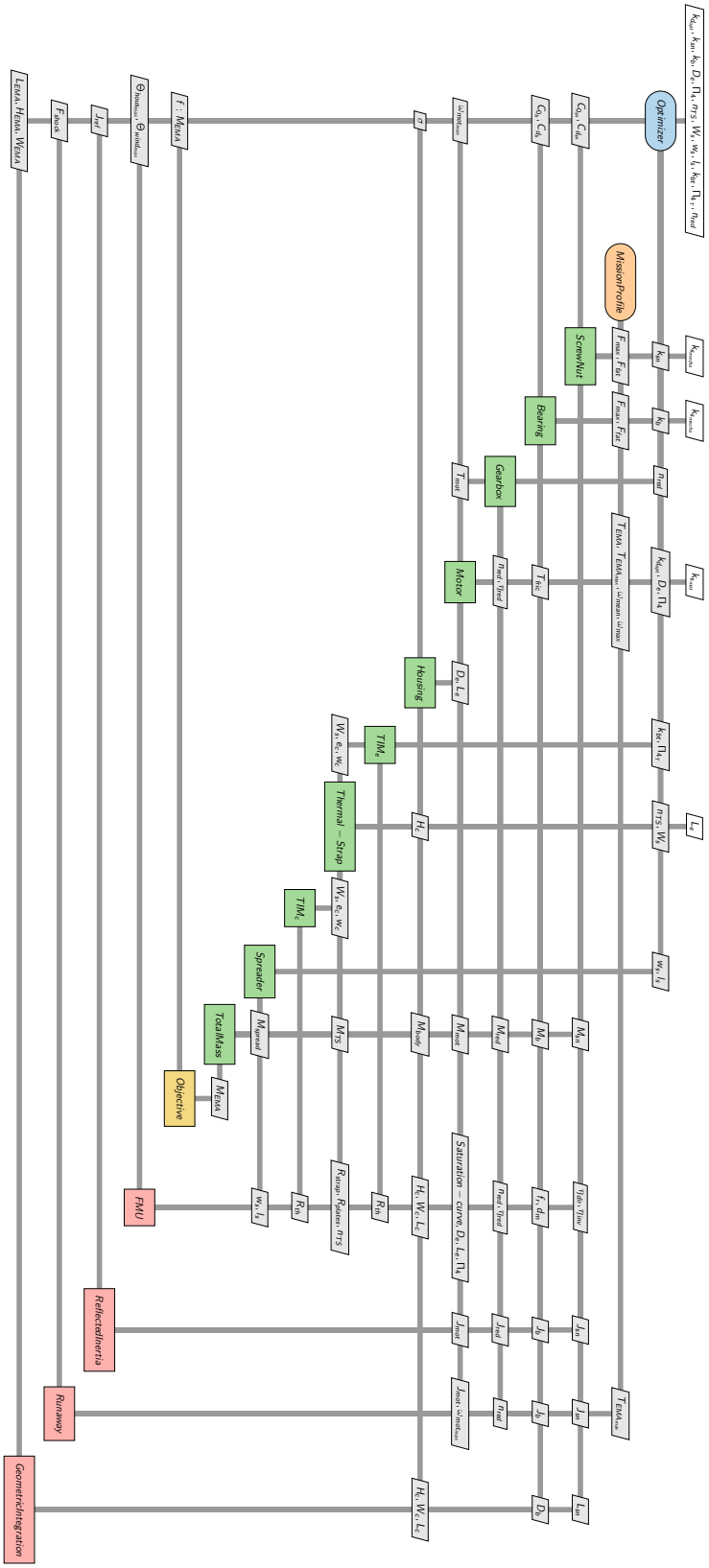

Figure 7.20: Extended design structure matrix of the EMA preliminary design of case study 3.

Note in particular that, compared to the previous case, the TMS mass is slightly higher since more heat transfer devices are used: 6 thermal straps are employed for the Aileron application and 2 for the Elevator.

Table 7.3: Results of optimizations for case study 3

	Aileron	Elevator
Design coefficient, $k_{d_{opt}}$ $[-]$	1.15	3
Motor diameter, D_e $[mm]$	58.11	42.41
Motor length, L_m $[mm]$	97.63	67.19
Motor Mass, M_{mot} $[kg]$	1.34	0.49
TS number, n_{TS} $[-]$	6	2
TS length, L_b $[mm]$	93.44	101.29
TS width, W_b $[mm]$	35.88	30.73
TS mass (per unit), M_{HP} $[kg]$	0.05	0.04
Spreader length, l_s $[mm]$	142	63.65
Spreader width, w_s $[mm]$	229	51.60
Spreader mass, M_{spread} $[kg]$	0.27	0.026
Housing body mass, M_{body} $[kg]$	0.35	0.15
Screw-nut mass, M_{sn} $[kg]$	1.44	0.34
Bearing mass, M_b $[kg]$	1.07	0.36
Gearbox mass, M_{red} $[kg]$	0.83	0.31
EMA Mass, M_{EMA} $[kg$	5.6	1.75

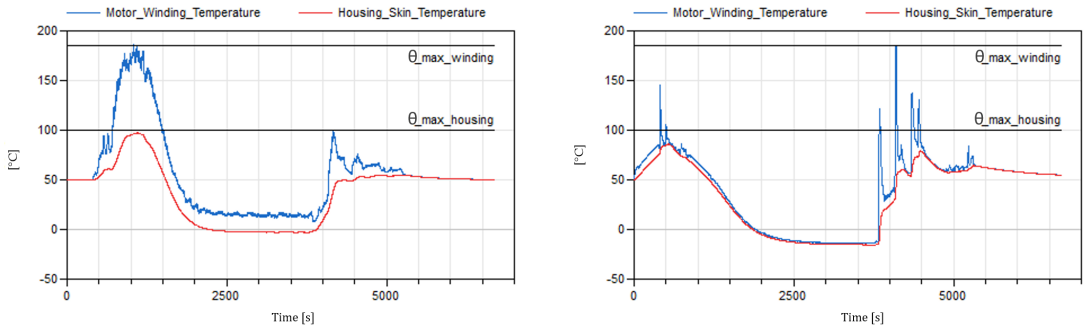

(a) Aileron (b) Elevator

Figure 7.21: Thermal profile of EMAs designed with the thermal straps.

7.3.5 Case study 4: PCM

In view of the results obtained from the previous case of studies, the utilisation of the PCM modules for the thermal management of Elevator and Rudder applications will not be investigated. This is because, when observing the temperature evolution of the housing for these applications, it appears to be practically always below the melting temperature of the PCM. Consequently, the application of the PCM plate installed on the housing is useless, as the phase transition would never takes place. For these applications, as mentioned above, the temperature constraint is mainly encountered in the motor windings. In order to evaluate the benefits of the PCM for Elevator and Rudder, it would therefore be necessary to install the PCM in proximity of the motor slots. This solution cannot be implemented using the type of PCM module here developed, in view of the reasons previously explained in Section 6.2.1. Consequently, the preliminary design of this case study is conducted uniquely for the Aileron application.
The sizing problem basically follows the same patterns of the case study 1. It can be therefore formulated as made in Eq. 7.13, by taking into account two additional optimization variables defining the geometry of the PCM (H_{fin}, L). The results obtained from the optimisation are shown in Table 7.4, while the temperatures of the motor windings and the skin housing encountered along the mission are shown in Fig. 7.22.

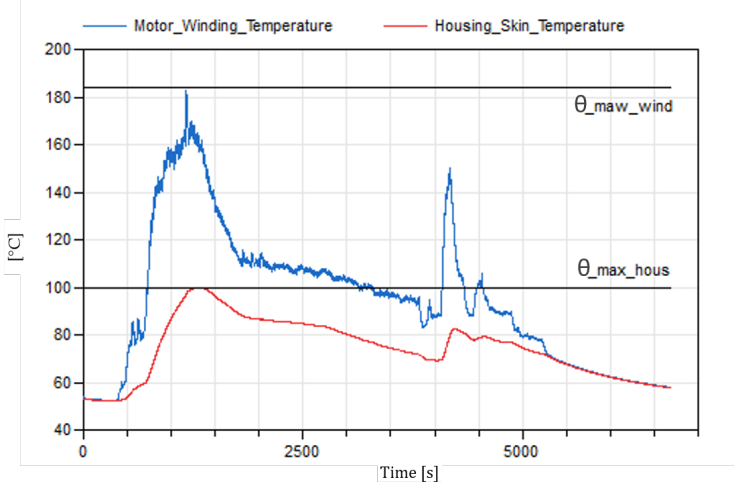

Figure 7.22: Thermal profile of EMA Aileron designed with PCM module.

As can be seen from the results obtained, the use of the PCM plate enabled a decrease of 20% of the system mass compared with that obtained in the case study 1. The use of

this module has made it possible to design a lighter motor (-15% in mass) operating at maximum thermal capability, thus enabling a lower inertia. As a result, a lower shock on stops in case of runaway is produced, allowing to design a lighter bearing (-10% in mass). The mass of the thermal management system, consisting of the semi-finned housing plus the PCM plate, is of the same order as the finned housing used in case study 1.

Table 7.4: Results of optimizations for case study 4

	Aileron
Design coefficient, $k_{d_{opt}}$ $[-]$	1.2
Motor diameter, D_e $[mm]$	61.39
Motor length, L_m $[mm]$	86.54
Motor Mass, M_{mot} $[kg]$	1.35
Fin width, L_a $[mm]$	30.45
Housing/Motor length ratio, k_L $[-]$	1.57
Fins mass, M_{fin} $[kg]$	0.06
Housing body mass (no fins), M_{body} $[kg]$	0.56
Housing mass, M_{hous} $[kg]$	0.61
PCM slab height, H_{fin} $[mm]$	15.11
PCM slab half width, L $[mm]$	1.34
PCM mass, M_{PCM} $[kg]$	0.06
Aluminium container mass, M_{plate} $[kg]$	0.14
PCM module mass (per unit), $M_{PCM_{Module}}$ $[kg]$	0.2
Screw-nut mass, M_{sn} $[kg]$	1.44
Bearing mass, M_b $[kg]$	1.15
Gearbox mass, M_{red} $[kg]$	0.87
EMA Mass, M_{EMA} $[kg]$	5.82

7.3.6 Trade-off analysis

This section summarizes the results obtained from the preliminary designs, outlined in the graph depicted in Fig. 7.23, and it discusses the relative advantages and disadvantages of the TMS concepts analyzed.

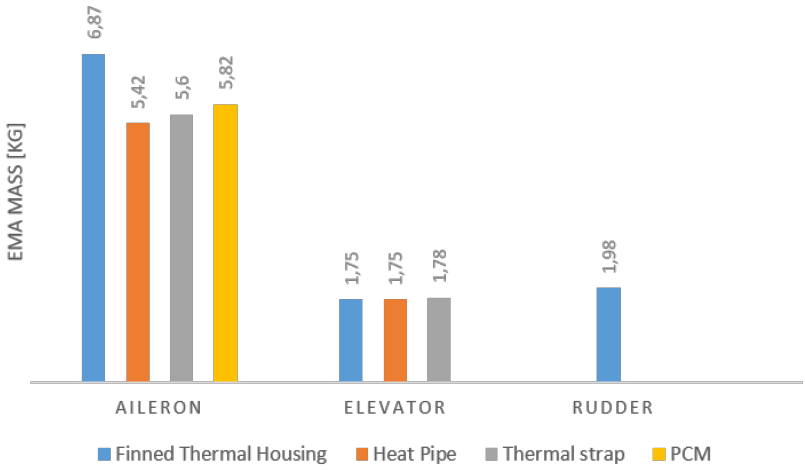

Figure 7.23: Summary of the results obtained from the performed preliminary designs.

The Rudder application has proved to be the least demanding from a thermal point of view. The results obtained indicated that the thermal capacity of the motor is sufficient to ensure keeping the temperature of the device below the limits. The cooling device is therefore not necessary. A phase change material, however, if installed in proximity of the motor windings, could lead to a further reduction in the mass of the electric motor.
The EMA Elevator also appears to be thermally favorable. Unlike the Rudder, however, a minimum cooling device is required. Conventional TMS, such as finned thermal housing, can be sufficient for this type of application. The use of non-conventional systems, such as heat pipes and thermal straps, does not result in additional gains in system mass. Also in this case, the use of phase change materials installed close to the windings could involve a further system mass reduction.
The Aileron application has proved to be thermally the most challenging. The use of a finned thermal housing, although effective in guaranteeing compliance with temperature requirements, is limiting from the point of view of performances and mass of the system. The encumbrance and vibration constraints preclude a conveniently sized finned thermal

housing. The result is an oversized motor operating below its maximum thermal capability. This limitation can be overcome through the use of non-conventional heat transfer devices, such as heat pipes and thermal straps. Their high ability to transfer large amounts of heat with small temperature differences and reduced masses, has made it possible to achieve a more compact motor operating at its maximum thermal potential. Compared to the finned thermal housing, a system mass gain of 22% and 19% is achieved by using 2 heat pipes or 6 thermal straps respectively. In response to the question raised in Section 6.2.1 regarding the convenience of using storage systems for the Aileron application (PST=0.56; PSE=0.0023), the use of PCM induced significant benefits on system mass. The two PCM modules installed above and below the finned housing have made it possible to obtain a system 25% lighter than the system not using the PCM.

The analysis conducted so far has been developed around a discussion of the mass benefits induced by the different TMS. The choice of the most suitable solution, however, deserves a broader discussion, as this depends on other relevant aspects, summarized in Tab 7.5.

One the most important aspects to take into account is surely the ease of integration of TMS. From this point of view, the finned housing is the most favorable, since its installation and use does not alter in any way the surrounding aircraft structure. The same cannot be said for heat pipes and thermal straps. As described in Chapter 6, their installation requires the removal of small sections of the airframe in order to connect the terminal plates with the thermal spreader. The effects of possible performance degradation of composite materials need to be investigated thoroughly. Especially in the case of thermal straps, where more devices are required. The acceptance of the aircraft manufacturer for this solution must also be verified. The indirect installation solution described in Section 5.2.1, could be considered as a possible alternative. Moreover, the interfacing of these devices via the spreader with the external environment makes them subject to exposure to lightning. Their resistance to lightning impact should therefore be evaluated. The PCM module is either designed as an integral part of the housing, as in this case, or as a stand-alone module. The first case is actually beneficial for maximising the heat transfer rate, even if it is less prone to the concept of modularity, intended as the opportunity to have a housing on which it is possible to install different types of TMS. The stand alone module fully respects this concept, but is penalizing from a thermal point of view, especially in view of the fact that the mechanical interfacing by bolting, with the strategy adopted for the interfacing the heat pipes and thermal straps, would be complicated.

The ease of maintenance and removal is another important aspect to take into account.

Also in this case, the finned housing is the most advantageous, as it does not require particular maintenance. The heat pipes and thermal straps should be relatively easy to install and remove, as they are mechanically fixed to the actuator by bolting. In order to ensure maintenance of the PCM module, a removable cap should be designed. It will be important to ensure that such a lid provides perfect containment of the liquid that will prevent it from spilling. For ease of maintenance and removal, the stand alone module is advantageous in this case.
Another important aspect to consider is the orientation of the device. This strongly constrains the heat pipes to be installed with the condenser facing the top surface of the wing, in order to ensure optimal performance of the device. Thermal straps offer a better alternative in this regard, as they are independent of orientation and could be installed, for example, on the trap door, or eventually on the passive actuator housing skin placed in the adjacent chamber. The performance of the fins is also strictly related to their orientation. For proper operation, as seen in Chapter 5, they need to be arranged sideways to the housing, (along the trajectory of the airflow), thus constraining the architecture of the actuator. For the PCM module adopted here, there should be no particular constraints on the performances relating to its orientation.
The potential for failure through leakage of the working fluids should be considered too. This interests the heat pipe and PCM module. The leakage of the contained working fluids could degrade the performance of these devices, thus involving a temperature increase of the EMA components. In the worst case (a winding degradation), this can cause the failure of the actuation system. Moreover, the ammonia contained in heat pipes is also classified as a toxic and flammable refrigerant. The PCM material here adopted should not be affected by these problems, as it is made of bio-degradable raw materials.
Cost will be the ultimate factor in determining which TMS concept is the best for use on a real aircraft. Developing a sufficiently detailed cost estimate is very challenging at a preliminary sizing stage. First, the unconventional TMS modules analyzed here represent a niche in the industrial world, so it becomes difficult to perform a large-scale cost comparison. Secondly, according to our experience, most industries tend to sell these types of products by stock, and not by individual units. The unit prices are therefore generally much higher than the effective cost of the device (order fees, delivery fees, design fees, etc.). The cost analysis carried out here is based on different quotes obtained from different manufacturers. The cheapest option found is the aluminium finned housing, characterized by a unit cost around 500€. Regarding heat pipes, it has been difficult to identify a well-

defined price. Depending on the materials and the type of wick used, the price of a single unit in the catalog ranges from 250€ - 3000€. The price of an out-of-print heat pipe, i.e. produced according to the required geometry, could increase dramatically by 5-6 times or more. Surprisingly, thermal straps are among the most expensive devices. The quotations we obtained from different manufacturers, oscillate in a range between 2000€ and 9000€ per unit. These vary mainly according to the country of production (most of the companies identified are located in the United States) and the type of material used (from copper to graphite foils). However, the price is between two and four times lower if purchased in large quantities (usually more than 10-100 units). The price of the PCM material itself is quite cheap (a few tens of euros per kilo), the problem is the cost for the encapsulation of the material. For the PCM modules we requested, two quotations were obtained from two different companies, respectively worth 2500€ and 20000€ per module (the higher price, however, foresees an encapsulation of the PCM in an aluminium honeycomb structure). On the basis of all the above aspects, it is clear that it is difficult to identify the most advantageous TMS solution. A detailed analysis of all these factors would deserve to be carried out. The preliminary sizing, however, has allowed to provide a qualitative and quantitative idea on the technological advantages and disadvantages provided by the different cooling solutions, which is almost certainly the most influential aspect in the selection criteria.

Table 7.5: Summary of Case studies TMS concepts.

	Finned Housing	**Heat Pipes**	**Thermal Straps**	**PCM Module**
System mass gains *	⊕	⊕ ⊕ ⊕ ⊕	⊕ ⊕ ⊕	⊕ ⊕
Minimal airframe integration *	⊕	⊕ ⊕ ⊕	⊕ ⊕	⊕
Ease of maintenance / removal *	⊕ ⊕ ⊕ ⊕	⊕ ⊕	⊕ ⊕ ⊕	⊕ ⊕ ⊕ ⊕
Orientation dependency	⊕ ⊕ ⊕	⊕ ⊕ ⊕	×	×
Possibility of leakage	×	⊕	×	⊕
Exposure to lightning impact	×	⊕	⊕	×
Cost	⊕	⊕ ⊕	⊕ ⊕ (⊕)	⊕ ⊕ (⊕)
* weighted on aileron application				

7.3.7 Computational times and design compromises

As we have seen in the previous sections, the dynamic sizing approach allowed to design an actuator sized specifically for the mission. In this way, it was possible to obtain a system (actuator + TMS) as light as possible and operating at its maximum thermal potential. The advantages over the static sizing approach have been demonstrated and found to be significant. A question at this point arises: what are the computational times required to perform the preliminary design? The computational time depends essentially on two aspects: the type of mission profile and the type of TMS analyzed.

The Aileron and Rudder mission profiles are the most computationally favourable. For these types of applications, the maximum aerodynamic torque is present towards the beginning of the mission and consequently the maximum temperature levels are reached during this phase. There is therefore no need to simulate the entire mission profile, but only the initial part concerned. This strategy, however, is not applicable to the Elevator profile, since the Elevator is subject to load peaks both at the beginning and at the end of the mission. It is therefore necessary to simulate almost the entire mission profile.

The type of TMS adopted affects the computational time as a function of: the number of optimisation variables and constraints involved and the number of elements and parameters used in the dynamic model. The thermal housing is favorable under this point of view. The heat pipe instead is characterized by a higher number of design variables and constraints and at the same time is modeled by a higher number of elements within the dynamic model.

In conclusion, the calculation times required are in a range between 4 hours (approximately 20000 function evaluations) in the most favorable case (Rudder-Finned housing) to about 12 hours (approximately 50000 function evaluations) for the least favorable case (Elevator-HP), by using a *Intel i7* quad core processor. Although the time required seems to be high for a preliminary design problem, it is in reality quite reasonable considering that this approach allows to anticipate, automate and optimize the effects of the 2 subsequent phases of the V-Cycle, namely, the phase of detailed design and the phase of dynamic pre-validation by virtual prototyping.

A very important outcome, which deserves to be highlighted, concerns the different design compromises obtained according to the type of TMS used. If we analyze the graph illustrated in Fig. 7.24, we can realize that for each of the analyzed solutions, different geometries of the components forming the system have been obtained. This information

is very important as it highlights the main hypothesis on which this thesis was conducted, that is, the need to integrate the design of the thermal management system when designing the actuator. In fact, during the sizing phase, it was seen that the thermal capability of the different cooling solutions had a significant impact on system performance and on the size of the electrical and mechanical components. The methodology developed here, has pushed towards the search for these optimal design compromises, in order to maximize the thermal performance of the actuator and to minimize its mass.

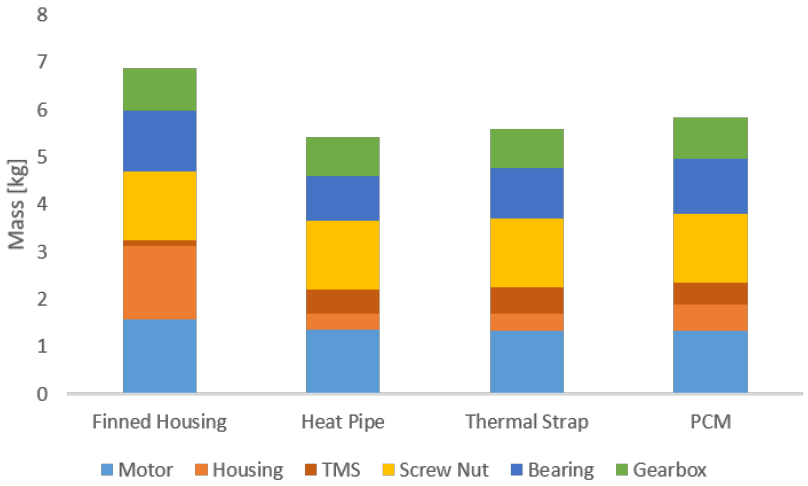

Figure 7.24: Evolution of the component masses for the designed Aileron EMAs.

7.4 Conclusion

In this last chapter, the thermal management system models developed during the thesis were finally used to conduct the preliminary designs of the primary flight control electro-mechanical actuators. In order to evaluate the effectiveness of these devices along the mission, a methodology based on a dynamic sizing approach has been implemented. In this regard, a dynamic model of the actuator has been developed on Dymola, able to provide the thermal behavior of the actuation system along the flight profile. This model was then transformed into FMU and integrated into the preliminary sizing framework implemented in Pyhton environment. The dynamic sizing was then performed for each of the case studies of TMSs analyzed, applied to the different primary flight control EMAs. The results

emerging from the sizing problems were then used to conduct a trade off analysis. From this, it emerged that the performance and mass of the Elevator and Rudder actuators do not seem to be affected by the type of cooling system adopted. The latter could even avoid the utilization of a cooling system, by using the thermal capacity of the motor as heat sink. On the opposite side, the Aileron resulted to be the most thermally constraining application. The use of non-conventional cooling systems, such as (in increasing order of mass) heat pipes, thermal straps and PCM, has been shown to provide significant advantages in terms of the overall system mass and performances over the conventional finned housing, which performances are limited by vibrational and space constraints. It was subsequently pointed out that the TMS selection criterion also depends on other important factors such as installation, airframe integration, cost etc. Each of these aspects would merit a further detailed analysis. The computational times required to conduct the preliminary design through the dynamic approach were discussed at the end of the chapter, and they were identified within a range of 4 to 12 hours. These times can be considered acceptable because of the fact that through this methodology it was possible to predict and optimize the effects of the subsequent phases of detailed design and dynamic validation by virtual prototyping.

Chapter 8

Conclusions and Perspectives

8.1 Summary

This thesis mainly focused on a topic that has not yet been fully explored in the literature, which concerns the optimal design and coupling of the thermal management solutions with primary flight control electrical actuators. A classic approach commonly adopted in the industry consists to design the thermal management systems after sizing the actuator. The fundamentals of this thesis are rather based on the assumption that, if thermal devices are optimally integrated during the preliminary design phase of the actuator, a lighter actuation system characterised by improved thermal performances can be obtained.
The main objective of this thesis was to provide effective methods and tools suited for the preliminary design of electrical actuators, with a particular attention to the thermal management. This objective has been decomposed into a series of scientific (S1-S4) and industrial (I1-I3) objectives, summarised in Tab. 8.1, in order to consolidate the interactions between the research laboratory Institut Clément Ader and the company COLLINS Aerospace.

Table 8.1: Industrial and scientific objectives.

Industrial Objectives		**Scientific Objectives**	
I1	Identification of potential thermal management solutions	S1	Generation of a surrogate modelling methodology
I2	Perform the preliminary design of primary flight control EMAs with a static approach	S2.	Model development of selected thermal management solutions
		S3.	Implementation of a preliminary design procedure and an associated sizing tool
I3	Perform the preliminary design of primary flight control EMAs with a dynamic approach	S4.	Development of a virtual prototype

In Chapter 2, potential thermal management solutions suitable for primary flight con-

trol electrical actuators have been identified (Objective I1). This was achieved in two phases: the individuation of design constraints on both the actuator and the cooling system (Phase 1) and the research of thermal management solutions aimed to satisfy the outlined constraints (Phase 2).

In Phase 1, the analysis of the thermal problem has been carried out. Electric motor losses have been identified as the main source of heat generation and the studies conducted in this thesis have focused on them. The decision was therefore made to focus entirely on the actuator without the electronic control unit. The operating temperature requirements have been identified according to the reliability and lifetime of the actuator components and airplane composite structures. The electric motor has been identified as the most sensitive element of the actuator to high temperature, as it is subject to degradation of the winding insulation. Taking into account that for the applications considered here, high power density motors are used, a hot spot temperature limit of 185°C has been considered. With regard to composite materials, a temperature limit in the range of 70°C to 110°C was highlighted. The uncertainty of the studies concerning the thermal behaviour of these materials led us to consider a conservative temperature constraint of 100 °C on the actuator skin. Mission profiles and flight scenarios were identified as dimensioning aspects of both the actuator and the cooling system. The flight scenarios showed that depending on the altitude, the atmospheric properties affect the thermal performance of the system differently, leading to the possibility of sizing the actuator according to the most constraining flight scenario. The industrial sizing criterion adopted by aircraft makers was then presented, consisting of sizing the actuator by considering laboratory conditions and successively validate the dynamic thermal performances along the entire flight scenario. The relevance of the mission profile analysis was highlighted, since by means of this, the design specification of the actuator can be determined. On the basis of these aspects, two design methodologies applied during the thesis were introduced: a static approach consisting on extracting static design specifications directly from the mission profile, and a dynamic approach involving the integration of the mission profile within the preliminary design phase.

Within Phase 2, a state of the art of potential thermal management solutions has been conducted. Three strategies, representing the axes of the thesis, to improve the thermal performance of the actuator were presented: 1. Improve the losses management by designing the actuator so that it generates as less heat as possible; 2. Improve the heat transfer from the actuator to the exterior environment by using additional cooling systems to better

evacuate it and thus lower the maximal temperature; and 3. Improve the transient storage by designing the actuator/cooling system so that it efficiently stores transient heat. The solution chosen for the first axis was to define a design of the electric motor maximising the torque density while respecting the operating thermal limits of the device. In order to improve heat transfer, it was decided to analyse conventional TMS, generally used for flight control applications, such as the finned thermal housing, and non-conventional TMS, such as heat pipes and thermal straps. Concerning the transient heat storage systems, solutions for improving the sensible heat storage of component materials, as well as solutions using the latent heat storage by using phase change materials have been considered.

In order to integrate and evaluate the solutions selected in the preliminary design phase of the actuator, modelling methods have been identified. They allow the realisation of estimation models (scaling laws, linear regressions, analytical relationships etc.) which permit to rapidly estimate the performance of the components according to their dimensions. In some cases, such as the modelling of the electric motor, a higher degree of fidelity was sought, with a view at the same time, to ensure the computational time required for the preliminary design. This choice was driven by the fact that an optimal motor design was considered. The need of using the motor model within different sizing problems has also pushed towards the necessity to dispose a reusable model, valid over a wide range and which allows the effects of other disciplines to be taken into account in order to make optimum sizing compromises. For these reasons, a new methodology for obtaining reusable surrogate models has been generated. This method, based on dimensional and sensitivity analysis adapted to the needs and constraints arising from multidisciplinary design, has been presented in Chapter 3 and it allowed the achievement of the scientific objective S1.

The generated surrogate models of the electric motor were then used in Chapter 4 to conduct the preliminary design of primary flight control electro-mechanical actuators. The sizing approach defined here as static has been adopted. In this respect, a design methodology developed in four steps (1. system specifications, 2. model generations, 3. sizing procedure definition and 4. design & optimization) has been defined. Two different actuator architectures, gear and direct drive, have been investigated and the design have been performed under laboratory conditions. The finned thermal housing has been used as thermal management system and its estimation model has been so developed. The generated model allowed to estimate the convective resistances, radiation and mass of the device as a function of its dimensions and the temperature conditions between the

housing skin and the external environment. A dedicated sizing tool was also generated in the Python environment, within which an optimisation procedure was implemented. This allows the scientific objective S3 to be achieved. The obtained designs revealed the importance of the individual analysis of the mission profiles. As different specifications were defined for each of the applications considered (Aileron sized for the RMS load, while Elevator and Rudder sized for the maximum load) different EMA designs were obtained. In addition, space and vibration constraints on the fins revealed an ineffective use of finned housing, resulting in a reconfiguration of the actuator architecture penalising the system mass. The surrogate models utilization enabled different optimal compromises between component dimensions in order to minimize the mass of the system. Moreover, the use of surrogate models allowed the preliminary design of the primary flight control actuation systems to be carried out in a matter of seconds, thus highlighting the significant gains involved in terms of computation time, and especially capitalization, compared to other surrogate modelling methods or to the use of finite element models. With the realisation of the static design, the industrial objective I2 has been achieved.

Chapter 5 dealt with the potential applications and modelling of heat pipes and thermal straps, and the thermal devices used to enhance their efficiency. The factors limiting their use for the thermal management of primary flight control actuators have been identified as: 1. the availability of the cold source used to dissipate the transported heat; 2. the size of the heat exchange surface; and 3. the interfacing with the surfaces on which they are installed. For each of these factors, a solution has been proposed.
The airflow over the skin of the aircraft wing has been identified as the best cold source available. In order to be able to use it, and in view of the constraint arising from the low thermal conductivity of composite materials, the solution proposed and considered in this thesis was to connect the end plate of the thermal transfer devices in direct contact with a spreader plate mounted on the outer side of the wing. This method involves removing a small section in the wing structure, corresponding to the size of the terminal plate of the device, so that it can be connected through direct contact with the thermal spreader. However, this solution would require additional analysis to verify the possible degradation of the mechanical performance of the composite materials, and the availability of the aircraft manufacture to accept the installation of these devices on the wing. An alternative option was also proposed and should be investigated. This solution, less invasive on airframe structure, could be to drill some holes in the concerned wing area in order to pass

thermal drains and indirectly connect the device terminal plate (situated inside the wing) to the spreader (situated outside the wing). A method for determining the convective heat transfer coefficient on the heated surface has been illustrated. The adopted method is based on the calculation of the average effects of forced convection over a flat plate with an unheated starting length.
The use of the thermal spreader has been envisaged with a view to increasing the available heat exchange surface area. This has therefore been modelled by simple formulas for estimating the thermal resistance of a rectangular spreader plate on which a rectangular heat source is located in the middle.
In order to minimize the contact resistance of the interfacing surfaces, the use of thermal interfacing materials has been considered. A surrogate model enabling the calculation of the contact surface in the interfacing zone has been developed.
As far as heat pipes are concerned, their representative resistive thermal circuit has been presented. A range of possible combinations of materials and working fluids was identified according to the temperatures involved during the flight mission. Among the possible solutions available, the choice of the configuration to be analysed in this project was made according to the thermal requirements and the commercially available options. An aluminium heat pipe containing ammonia as working fluid has been taken as a reference. The heat pipe model was then developed by means of mathematical regression on data-sheet catalogue.
With regard to thermal strap, a device made of pyrolitic graphite foils has been considered and it has been modeled by means of scaling laws applied to a reference commercially available component.

The third axis of the thesis, concerning the improvement of transient heat storage with either sensible or latent heat storage, was discussed in Chapter 6.
Design techniques to improve sensible heat storage of components have been presented, by illustrating how the geometries of components can be altered in order to enhance the thermal capacities of their constituent materials. It has also been highlighted the fact that the geometric interdependence between components pushes towards the search for optimal compromises.
The operating principles, material selection criteria, constraints and methods for enhancing the performance of the phase change materials have been discussed. The use of an aluminium finned container was considered in order to increase the low thermal conductivity

of the PCM. On the basis of industrially available materials and depending on the required melting temperature and the thermal properties, a bio PCM, made up of biodegradable materials has been selected for this study. Analytical formulations describing the behaviour of a PCM slab during the phase transition were presented. These formulations were then adapted to take into account the integration of the PCM in the finned structure and a dynamic model of the PCM was realised in Dymola. The PCM modelling concludes the modelling work of the selected cooling solutions, allowing the achievement of the scientific objective S2.
A method for classifying the mission profiles according to their suitability for using thermal storage systems has also been provided. This method, based on the calculation of the thermal storage potential (PST) and the energy storage potential (PSE), showed that the Rudder (first), and the Elevator applications, are more favorable from a thermal management point of view compared to the Aileron.

Chapter 7 made it possible to implement the models and methodologies developed here, necessary to achieve the satisfaction of the thesis objectives.
A virtual prototype of the actuator, allowing the evaluation of its thermal behaviour along the mission profile was developed (objective S3). This model, developed in Dymola environment, firstly allowed the electro-mechanical actuators designed with the static approach in Chapter 3, to be thermally tested along the flight mission. In the case of the Aileron EMA, sizing at average load was found to be insufficient to meet the operational thermal limits of the system. On the other hand, the design at maximum load considered for the Elevator and Rudder EMAs resulted in excessively oversized systems.
For this reason, the so-called dynamic design approach was implemented, fulfilling the last remaining objective I3. This involves integrating the generated dynamic model of the actuator within the sizing phase, so that the actuators are designed taking into account their actual thermal behaviour along the mission profile. The preliminary design with dynamic approach was thus conducted for the entire set of primary flight control applications, for each of which the different cooling solutions considered were analysed, namely: the finned thermal housing, the thermal strap, the heat pipe and the PCM module.
The finned housing case study outlined the significant benefits of the dynamic approach over the static approach. In the case of the Aileron, a slightly heavier system was obtained but the required thermal limits were satisfied, while in the case of the Elevator and Rudder, substantial mass benefits were obtained by using the actuator at the maximum thermal

performances.
The results obtained from the sizing of the other thermal management systems allowed a trade-off analysis to be carried out.
This showed that for Elevator applications, and in particular for the Rudder, the thermal management was not a particular technological constraint. For the former, a simple finned housing is sufficient to maintain the temperature of the device under the desired temperature levels. For the latter, it could even do without a cooling device, since the thermal capacities of the motor are sufficient to ensure compliance with the operating temperature limits. The use of the PCM for these applications has not been analysed as the temperature in the housing is below the melting temperature of the material for the entire duration of the mission. Its use at the motor windings could prove beneficial in further reducing the mass of the device.
The EMA Aileron proved to be the most thermally demanding. The finned thermal housing system has proved to be penalising from a mass point of view. The overall dimensions and vibration constraint of the fins prevent an effective sizing of the thermal device. Given these constraints, a larger electric motor is needed to generate fewer losses. This results in an oversized system. Significant benefits in terms of mass and thermal performance were obtained through the use of 2 heat pipes or 6 thermal straps. The use of PCM has also proved beneficial to the mass and performance of the system, offering a viable alternative if the installation constraints of heat pipes or thermal straps prevent their use.
In the selection of the potential cooling solution, further factors need to be taken into account, such as installation, airframe integration, cost etc.
The computational times required for dynamic design have been illustrated and placed in a range between 4 and 12 hours depending on the application analysed. These times, although substantial for a preliminary design, can be considered satisfactory considering that this method has made it possible to foresee and optimise the effects of the subsequent phases of detailed design and dynamic validation tests.

8.2 Limitations and propositions for future works

The work carried out within this thesis has shown how the integration of the design of the cooling systems within the actuator sizing has provided significant benefits in obtaining an optimised system in terms of thermal performance and mass. However, the time constraints

related to the realisation of the project did not allow us to consider other interesting aspects and solutions that could be integrated into the design methodology defined here.

In order to have a complete overview of the advantages obtained, it would be interesting to consider the integration of the electronic control unit. A surrogate model developed through the surrogate methodology defined here could be adopted in order to achieve a design of a converter maximised in power density. Taking into account the ECU, a flux-weakening control should be considered, as it could lead (in some cases) to a lightening of the power electronics.

Heat transfer via heat pipes or thermal straps on passive actuators could be analysed, in order to provide an alternative use for heat pipes or thermal straps in case they cannot be interfaced externally to the wing. Another interesting alternative would be to analyse different combinations of TMS such as heat pipes and PCM or thermal strap and PCM. In this case, the end plates of the heat transfer devices could be mounted on PCM modules, e.g. installed close to the wing (in the inner part), on the inspection hatch or on passive actuators.

In order to refine the results, the calculation of the convective heat transfer coefficient around the spreader located on the wing, taking into account a flat surface, could be extended to NACA-type profile.

In order to better take into account the confining environment of the actuator, it would be interesting to develop a model allowing the estimation of the convective resistance of the actuator chamber. A surrogate model could be used for this purpose.

Techniques to implement the PCM on the motor winding could be investigated. One idea could be to fill the empty spaces inside the stator slots with PCM. In this case, a dedicated cap should be installed around the windings in order to ensure the liquid containment. The PCM Slab model used here could be adapted for this purpose.

The preliminary dimensioning conducted here has been carried out taking into account mission profiles representing favourable flight conditions typically encountered. The integration of more severe flight profiles should be considered.

The models and tools developed here could be applied to analyse the thermal manage-

ment of the Spoiler application.

In order to validate the models of the heat transfer devices generated here, it would be interesting to carry out experimental tests. The development of a test bench, on which the different cooling devices will be tested, was one of the main objectives of this thesis. This perspective was in fact already partly implemented, as the details of the test bench were already defined, and the components to be tested were identified and ready to be purchased. Unfortunately, due to the economic crisis following the COVID-19 pandemic, the costs of the experimental test could not be supported.

Bibliography

[1] J. Rosero, J. Ortega, E Aldabas, and L. Romeral, "Moving towards a more electric aircraft," *IEEE Aerospace and Electronic Systems Magazine*, vol. 22, no. 3, pp. 3–9, 2007 (cit. on p. 2).

[2] P. W. Wheeler, J. C. Clare, A. Trentin, and S. Bozhko, "An overview of the more electrical aircraft," *Proceedings of the Institution of Mechanical Engineers, Part G: Journal of Aerospace Engineering*, vol. 227, no. 4, pp. 578–585, 2013 (cit. on p. 2).

[3] I. Chakraborty, D. N. Mavris, M. Emeneth, and A. Schneegans, "A methodology for vehicle and mission level comparison of more electric aircraft subsystem solutions: Application to the flight control actuation system," *Proceedings of the Institution of Mechanical Engineers, Part G: Journal of Aerospace Engineering*, vol. 229, no. 6, pp. 1088–1102, 2015 (cit. on p. 2).

[4] K. Cheng, "Comparative study of ac/dc converters for more electric aircraft," in *IEE conference publication*, IET, 1998, pp. 299–304 (cit. on p. 2).

[5] C. D. Eick, L. T. Gaines, M. J. Laidlaw, D. M. Benson, L. A. Portolese, B. L. Flaherty, and W. T. Pearson, *More electric aircraft power transfer systems and methods*, US Patent 7,552,582, 2009 (cit. on p. 2).

[6] M. Todeschi, "Airbus-emas for flight controls actuation system 2012 status and perspectives," *Recent Advances in Aerospace Actuation Systems and Components*, 2012 (cit. on p. 2).

[7] X. Giraud, M. Budinger, X. Roboam, H. Piquet, M. Sartor, and J. Faucher, "Optimal design of the integrated modular power electronics cabinet," *Aerospace Science and Technology*, vol. 48, pp. 37–52, 2016 (cit. on pp. 2, 30).

[8] J.-C. Maré, *Les actionneurs aéronautiques 2: solutions à puissance et signaux électriques*. ISTE Group, 2017, vol. 2 (cit. on pp. 2, 4, 5, 32).

[9] A. S. Gohardani, G. Doulgeris, and R. Singh, "Challenges of future aircraft propulsion: A review of distributed propulsion technology and its potential application for the all electric commercial aircraft," *Progress in Aerospace Sciences*, vol. 47, no. 5, pp. 369–391, 2011 (cit. on p. 2).

[10] S. Liscouet-Hanke, "A model-based methodology for integrated preliminary sizing and analysis of aircraft power system architectures," Ph.D. dissertation, Institut National des Sciences Appliquées de Toulouse, 2008 (cit. on pp. 3, 12).

[11] W. Murray, L. Feiner, and R. Flores, "Evaluation of all-electric secondary power for transport aircraft," 1992 (cit. on p. 3).

[12] F. Sanchez, "Génération de modèles analytiques pour la conception préliminaire de systèmes multi-physiques: Application à la thermique des actionneurs et des systèmes électriques embarqués," Ph.D. dissertation, Université Paul Sabatier-Toulouse III, 2017 (cit. on pp. 4, 13, 22, 50, 97, 180).

[13] J. Pointon, "Thermal management of electromechanical actuation on an all-electric aircraft," 2007 (cit. on pp. 4, 6, 33, 35, 36, 38).

[14] J. M. Roach, "Flash electrohydrostatic actuation modeling, analysis, and test results," *SAE transactions*, pp. 43–52, 1997 (cit. on p. 5).

[15] A Del Core, *Advances in onboard systems technology*. John Wiley & Son Ltd, 1996, vol. 1 (cit. on p. 5).

[16] D Moorhouse, C Maxwell, and M Bildstein, "Electro hydrostatic actuator for primary flight control of very large aircraft," *Recent Advances in Aerospace Actuation Systems and Components, Toulouse, France*, 2001 (cit. on p. 5).

[17] M. Jean-Charles and F. Jian, "Review on signal-by-wire and power-by-wire actuation for more electric aircraft," *Chinese Journal of Aeronautics*, vol. 30, no. 3, pp. 857–870, 2017 (cit. on p. 5).

[18] N Elliott, S Linforth, and C Moore, "Thermae ii (main landing gear & door eh actuation system)–integration and testing," in *Proceedings of the 7th International Conference on Recent Advances in Aerospace Actuation Systems and Components*, 2016, pp. 112–117 (cit. on p. 5).

[19] J.-C. Maré and M. Budinger, "Comparative analysis of energy losses in servo-hydraulic, electro-hydrostatic and electro-mechanical actuators," 2009 (cit. on p. 6).

[20] A De La Chevasnerie, S Grand, B Legrand, and S Sandler, "Electromechanical actuator/moet project," in *Proceedings of the 4th International Conference on Recent Advances in Aerospace Actuation Systems and Components*, 2010, pp. 83–87 (cit. on p. 6).

[21] J.-C. Derrien, P. Tieys, D. Senegas, and M. Todeschi, "Ema aileron covadis development," SAE Technical Paper, Tech. Rep., 2011 (cit. on p. 6).

[22] S Grand, G Balducci, M Fervel, and M Wenfling, "Actuator control: A successful modular multi-application approach or actuation2015 and beyond," in *Proceedings of the 7th International Conference on Recent Advances in Aerospace Actuation Systems and Components*, 2016, pp. 60–65 (cit. on p. 6).

[23] M. G. Schneider and D. P. Domberg, "Test results of reflux and phase change energy storage electronics cooler," *SAE transactions*, pp. 187–194, 1998 (cit. on p. 6).

[24] N. J. Gernert, D. Sarraf, and M. Steinberg, "Flexible heat pipe cold plates for aircraft thermal control," *SAE transactions*, pp. 2352–2360, 1991 (cit. on pp. 6, 33).

[25] C. P. Lawson and J. M. Pointon, "Thermal management of electromechanical actuation on an all-electric aircraft," in *26th ICAS Congress, Anchorage, Alaska*, 2008, pp. 14–19 (cit. on p. 6).

[26] D. Reay, R. McGlen, and P. Kew, *Heat pipes: theory, design and applications*. Butterworth-Heinemann, 2013 (cit. on pp. 7, 33, 34, 123, 124, 126).

[27] J. R. Martins and A. B. Lambe, "Multidisciplinary design optimization: A survey of architectures," *AIAA journal*, vol. 51, no. 9, pp. 2049–2075, 2013 (cit. on p. 11).

[28] I. Kroo and I. Kroo, "Multidisciplinary optimization applications in preliminary design-status and directions," in *38th Structures, Structural Dynamics, and Materials Conference*, 1997, p. 1408 (cit. on pp. 11, 49).

[29] S. Delbecq, "Knowledge-based multidisciplinary sizing and optimization of embedded mechatronic systems-application to aerospace electro-mechanical actuation systems," Ph.D. dissertation, Toulouse, INSA, 2018 (cit. on pp. 11, 13).

[30] C. Linares, C. P. Lawson, and H. Smith, "Multidisciplinary optimisation framework for minimum rotorcraft fuel and air pollutants at mission level," 2013 (cit. on p. 11).

[31] D. Raymer, *Aircraft design: a conceptual approach*. American Institute of Aeronautics and Astronautics, Inc., 2012 (cit. on p. 12).

[32] G. G. Wang and S. Shan, "Review of metamodeling techniques in support of engineering design optimization," *Journal of Mechanical design*, vol. 129, no. 4, pp. 370–380, 2007 (cit. on pp. 12, 50).

[33] T. W. Simpson, T. M. Mauery, J. J. Korte, and F. Mistree, "Kriging models for global approximation in simulation-based multidisciplinary design optimization," *AIAA journal*, vol. 39, no. 12, pp. 2233–2241, 2001 (cit. on pp. 12, 50).

[34] D. R. Jones, M. Schonlau, and W. J. Welch, "Efficient global optimization of expensive black-box functions," *Journal of Global optimization*, vol. 13, no. 4, pp. 455–492, 1998 (cit. on pp. 12, 50).

[35] S. Liscouët-Hanke, J.-C. Maré, and S Pufe, "Simulation framework for aircraft power system architecting," *Journal of aircraft*, vol. 46, no. 4, pp. 1375–1380, 2009 (cit. on p. 12).

[36] F Hospital, "Conception préliminaire des actionneurs électromagnétiques basée sur les modèles: Lois d'estimations et règles de conception pour la transmission de puissance mécanique.," Ph.D. dissertation, Toulouse, INSA, 2012 (cit. on p. 12).

[37] X. Giraud, "Méthodes et outils pour la conception optimale des réseaux de distribution d'électricité dans les aéronefs," Ph.D. dissertation, Toulouse, INSA, 2014 (cit. on p. 13).

[38] A. Reysset, "Conception préliminaire d'actionneurs électromécaniques-outils d'aide à la spécification et à la génération de procédures de dimensionnement pour l'optimisation," Ph.D. dissertation, Toulouse, INSA, 2015 (cit. on p. 13).

[39] T. Bland and K. Funke, "Advanced cooling for high power electric actuators," SAE Technical Paper, Tech. Rep., 1992 (cit. on pp. 19, 21).

[40] J. C. Akiror, "Rotational core losses in hydro generators," Ph.D. dissertation, Concordia University, 2017 (cit. on p. 19).

[41] E. L. Brancato, "Estimation of lifetime expectancies of motors," *IEEE Electrical Insulation Magazine*, vol. 8, no. 3, pp. 5–13, 1992 (cit. on p. 19).

[42] S. L. Botten, C. R. Whitley, and A. D. King, "Flight control actuation technology for next-generation all-electric aircraft," *Technology Review Journal*, vol. 8, no. 2, pp. 55–68, 2000 (cit. on p. 20).

[43] *Classes of winding insulation material*, `https://www.techbriefs.com/component/content/article/tb/pub/features/technology-leaders/33919` (cit. on p. 21).

[44] C. Buttay, D. Planson, B. Allard, D. Bergogne, P. Bevilacqua, C. Joubert, M. Lazar, C. Martin, H. Morel, D. Tournier, *et al.*, "State of the art of high temperature power electronics," *Materials Science and Engineering: B*, vol. 176, no. 4, pp. 283–288, 2011 (cit. on p. 21).

[45] D. Petersen, R. Rolfes, and R. Zimmermann, "Thermo-mechanical design aspects for primary composite structures of large transport aircraft," *Aerospace science and technology*, vol. 5, no. 2, pp. 135–146, 2001 (cit. on p. 21).

[46] J. Cros and P. Viarouge, "Synthesis of high performance pm motors with concentrated windings," *IEEE transactions on energy conversion*, vol. 17, no. 2, pp. 248–253, 2002 (cit. on pp. 27, 28).

[47] B. Aslan, "Conception de machines polyphasées à aimants et bobinage concentré à pas fractionnaire avec large plage de vitesse," Ph.D. dissertation, Paris, ENSAM, 2013 (cit. on p. 27).

[48] S. Makita, Y. Ito, T. Aoyama, and S. Doki, "The proposal of a new motor which has a high winding factor and a high slot fill factor," in *2014 International Power Electronics Conference (IPEC-Hiroshima 2014-ECCE ASIA)*, IEEE, 2014, pp. 3823–3827 (cit. on p. 27).

[49] K. M. Rahman and S. E. Schulz, "Design of high-efficiency and high-torque-density switched reluctance motor for vehicle propulsion," *IEEE Transactions on Industry Applications*, vol. 38, no. 6, pp. 1500–1507, 2002 (cit. on p. 28).

[50] D. Zarko, D. Ban, and T. A. Lipo, "Design optimization of interior permanent magnet (ipm) motors with maximized torque output in the entire speed range," in *2005 European Conference on Power Electronics and Applications*, IEEE, 2005, 10–pp (cit. on p. 28).

[51] G. R. Slemon and X. Liu, "Modeling and design optimization of permanent magnet motors," *Electric Machines & Power systems*, vol. 20, no. 2, pp. 71–92, 1992 (cit. on p. 28).

[52] Z. Zhu and D Howe, "Halbach permanent magnet machines and applications: A review," *IEE Proceedings-Electric Power Applications*, vol. 148, no. 4, pp. 299–308, 2001 (cit. on p. 28).

[53] C. Mi, G. R. Slemon, and R. Bonert, "Modeling of iron losses of permanent-magnet synchronous motors," *IEEE Transactions on Industry applications*, vol. 39, no. 3, pp. 734–742, 2003 (cit. on p. 29).

[54] C. C. Mi, G. R. Slemon, and R. Bonert, "Minimization of iron losses of permanent magnet synchronous machines," *IEEE Transactions on Energy Conversion*, vol. 20, no. 1, pp. 121–127, 2005 (cit. on p. 29).

[55] H. Wang, G. Li, L. Cao, X. Hong, and R. Wan, "Iron loss reduction method for permanent magnet machine with beveling magnet," in *2010 Asia-Pacific Power and Energy Engineering Conference*, IEEE, 2010, pp. 1–4 (cit. on p. 29).

[56] A Cassat and C Espanet, "Approach to decrease rotor iron losses of high speed or torque bldc motors," in *Conference Record of the 2004 IEEE Industry Applications Conference, 2004. 39th IAS Annual Meeting.*, IEEE, vol. 2, 2004, pp. 1024–1031 (cit. on p. 29).

[57] J.-J. Charrier and A. Kulshreshtha, "Electric actuation for flight and engine control; evolution and current trend," in *45th AIAA Aerospace Sciences Meeting and Exhibit*, 2007, p. 1391 (cit. on pp. 29, 30).

[58] E. C. De Jong, J. Ferreira, and P. Bauer, "Design techniques for thermal management in switch mode converters," *IEEE transactions on industry applications*, vol. 42, no. 6, pp. 1375–1386, 2006 (cit. on p. 30).

[59] J. Montero Yanez, "All electric aircraft flight control actuation (elac)," *Advanced in Onboard System Technology*, 1996 (cit. on p. 30).

[60] S. C. Jensen, G. D. Jenney, and D. Dawson, "Flight test experience with an electromechanical actuator on the f-18 systems research aircraft," in *19th DASC. 19th Digital Avionics Systems Conference. Proceedings (Cat. No. 00CH37126)*, IEEE, vol. 1, 2000, 2E3–1 (cit. on p. 30).

[61] *Amtech international*, `https://www.amtechinternational.com/portfolio/die-cast-motor-housing/` (cit. on p. 31).

[62] A. Bar-Cohen, M. Iyengar, and A. D. Kraus, "Design of optimum plate-fin natural convective heat sinks," *Journal of Electronic Packaging*, vol. 125, no. 2, pp. 208–216, 2003 (cit. on pp. 31, 102).

[63] C. Leung and S. Probert, "Natural-convective heat exchanger with vertical rectangular fins and base: Design criteria," *Proceedings of the Institution of Mechanical Engineers, Part C: Journal of Mechanical Engineering Science*, vol. 201, no. 5, pp. 365–372, 1987 (cit. on p. 31).

[64] D. L. Platus and E. K. Runge, *Thermal straps for spacecraft*, US Patent 9,733,027, 2017 (cit. on p. 32).

[65] *Thermal straps for use in advanced thermal management*, `https://thermal-space.com/thermal-straps/` (cit. on p. 33).

[66] D. L. Vrable and K. L. Yerkes, "A thermal management concept for more electric aircraft power system applications," *SAE transactions*, pp. 181–186, 1998 (cit. on pp. 33, 38).

[67] F. Sarvar, D. C. Whalley, and P. P. Conway, "Thermal interface materials-a review of the state of the art," in *2006 1st electronic systemintegration technology conference*, IEEE, vol. 2, 2006, pp. 1292–1302 (cit. on pp. 34, 35, 138).

[68] G. Qiao, G. Liu, Z. Shi, Y. Wang, S. Ma, and T. C. Lim, "A review of electromechanical actuators for more/all electric aircraft systems," *Proceedings of the Institution of Mechanical Engineers, Part C: Journal of Mechanical Engineering Science*, vol. 232, no. 22, pp. 4128–4151, 2018 (cit. on pp. 38, 160).

[69] A. De Gracia and L. F. Cabeza, "Phase change materials and thermal energy storage for buildings," *Energy and Buildings*, vol. 103, pp. 414–419, 2015 (cit. on p. 38).

[70] *Pcm heat sink design considerations*, `https://www.1-act.com/innovations/thermal-storage/pcm-heat-sink-design-considerations/` (cit. on p. 38).

[71] V Kuvshinov, "Research of aircraft flight dynamics peculiarities due to the using of electric actuators in control system," (cit. on p. 38).

[72] S. Kalra, "Optimal control of electromechanical aerospace actuators for reduction of energy losses," Ph.D. dissertation, 2019 (cit. on p. 38).

[73] Z. Zhou, Y. S. Ong, P. B. Nair, A. J. Keane, and K. Y. Lum, "Combining global and local surrogate models to accelerate evolutionary optimization," *IEEE Transactions on Systems, Man, and Cybernetics, Part C (Applications and Reviews)*, vol. 37, no. 1, pp. 66–76, 2006 (cit. on p. 50).

[74] I. Loshchilov, M. Schoenauer, and M. Sebag, "Self-adaptive surrogate-assisted covariance matrix adaptation evolution strategy," in *Proceedings of the 14th annual conference on Genetic and evolutionary computation*, ACM, 2012, pp. 321–328 (cit. on p. 50).

[75] Y. Tenne and S. Armfield, "A versatile surrogate-assisted memetic algorithm for optimization of computationally expensive functions and its engineering applications," in *Success in evolutionary computation*, Springer, 2008, pp. 43–72 (cit. on p. 50).

[76] N. V. Queipo, R. T. Haftka, W. Shyy, T. Goel, R. Vaidyanathan, and P. K. Tucker, "Surrogate-based analysis and optimization," *Progress in aerospace sciences*, vol. 41, no. 1, pp. 1–28, 2005 (cit. on p. 50).

[77] F. Sanchez, M. Budinger, and I. Hazyuk, "Dimensional analysis and surrogate models for the thermal modeling of multiphysics systems," *Applied Thermal Engineering*, vol. 110, pp. 758–771, 2017 (cit. on pp. 50, 54, 56, 57, 97).

[78] F. De Giorgi, M. Budinger, I. Hazyuk, A. Reysset, and F. Sanchez, "Reusable surrogate models for the preliminary design of aircraft application systems," *AIAA Journal*, pp. 1–13, 2021 (cit. on pp. 50, 57, 113).

[79] F. Sanchez, M. Budinger, and I. Hazyuk, "Dimensional analysis and surrogate models for the thermal modeling of Multiphysics systems," *Applied Thermal Engineering*, vol. 110, pp. 758–771, 2017 (cit. on pp. 53, 54, 99).

[80] E. Buckingham, "On physically similar systems; illustrations of the use of dimensional equations," *Physical review*, vol. 4, no. 4, p. 345, 1914 (cit. on pp. 53, 55).

[81] M. Budinger, J.-C. Passieux, C. Gogu, and A. Fraj, "Scaling-law-based metamodels for the sizing of mechatronic systems," *Mechatronics*, vol. 24, no. 7, pp. 775–787, 2014 (cit. on pp. 53, 91, 94).

[82] I. Hazyuk, M. Budinger, F. Sanchez, and C. Gogu, "Optimal design of computer experiments for surrogate models with dimensionless variables," *Structural and Multidisciplinary Optimization*, vol. 56, no. 3, pp. 663–679, 2017 (cit. on pp. 54, 55).

[83] T. Szirtes, *Applied dimensional analysis and modeling*. Butterworth-Heinemann, 2007 (cit. on p. 55).

[84] D. C. Montgomery, *Applied statistics and probability for engineers 6th edition*. Wiley, 2013 (cit. on p. 56).

[85] Z.-Q. Qu, *Model order reduction techniques with applications in finite element analysis*. Springer Science & Business Media, 2013 (cit. on p. 59).

[86] C. Gogu, R. T. Haftka, S. K. Bapanapalli, and B. V. Sankar, "Dimensionality reduction approach for response surface approximations: Application to thermal design," *AIAA journal*, vol. 47, no. 7, pp. 1700–1708, 2009 (cit. on p. 59).

[87] A. Saltelli, S. Tarantola, and K.-S. Chan, "A quantitative model-independent method for global sensitivity analysis of model output," *Technometrics*, vol. 41, no. 1, pp. 39–56, 1999 (cit. on p. 59).

[88] J. Nossent, P. Elsen, and W. Bauwens, "Sobol'sensitivity analysis of a complex environmental model," *Environmental Modelling & Software*, vol. 26, no. 12, pp. 1515–1525, 2011 (cit. on p. 59).

[89] *Parker hannifin france sas*, `https://ph.parker.com/fr/fr/motors` (cit. on pp. 61, 77).

[90] M. Budinger, F. De Giorgi, and F. Defay, "Surrogate models of PM brushless motor for the preliminary design of a multi-rotor drone," in *AST 2019, Aircraft System Technologies*, Hamburg, Germany, Feb. 2019 (cit. on p. 65).

[91] S. Delbecq, F. Tajan, M. Budinger, J.-C. Maré, and F. Sanchez, "A framework for the conceptual and preliminary design of embedded mechatronic systems," in *6th International Workshop on Aircraft System Technologies (AST 2017)*, 2017 (cit. on p. 74).

[92] *Vexmen robotics*, `https://www.vexmen.com/` (cit. on p. 77).

[93] S. Group *et al.*, "Skf general catalogue 4000/ii f," *SKF Group, Sweden*, 2003 (cit. on pp. 78, 92–96).

[94] J. F. Gieras, *Permanent magnet motor technology: design and applications*. CRC press, 2002 (cit. on pp. 85, 242).

[95] A. Reysset, M. Budinger, and J.-C. Maré, "Computer-aided definition of sizing procedures and optimization problems of mechatronic systems," *Concurrent Engineering*, vol. 23, no. 4, pp. 320–332, 2015 (cit. on pp. 87, 88, 106).

[96] J. Liscouet, "Conception préliminaire des actionneurs électromécaniques: Approche hybride, directe/inverse," Ph.D. dissertation, Toulouse, INSA, 2010 (cit. on p. 89).

[97] G. Pahl and W. Beitz, *Engineering design: a systematic approach*. Springer Science & Business Media, 2013 (cit. on p. 91).

[98] R. Willis, "Lightest-weight gears," *Product engineering*, vol. 5, pp. 64–75, 1963 (cit. on pp. 99–101).

[99] T. L. Bergman, F. P. Incropera, D. P. DeWitt, and A. S. Lavine, *Fundamentals of heat and mass transfer*. John Wiley & Sons, 2011 (cit. on pp. 103, 119, 131, 133).

[100] J. Lloyd and W. Moran, "Natural convection adjacent to horizontal surface of various planforms," 1974 (cit. on p. 103).

[101] M. Budinger, A. Reysset, J.-C. Maré, *et al.*, "Preliminary design of aerospace linear actuator housings," *Aircraft Engineering and Aerospace Technology: An International Journal*, 2015 (cit. on p. 103).

[102] S. Delbecq, M. Budinger, A. Ochotorena, A. Reysset, and F. Defaÿ, "Efficient sizing and optimization of multirotor drones based on scaling laws and similarity models," *Aerospace Science and Technology*, vol. 102, p. 105 873, 2020 (cit. on p. 106).

[103] A. B. Lambe and J. R. Martins, "Extensions to the design structure matrix for the description of multidisciplinary design, analysis, and optimization processes," *Structural and Multidisciplinary Optimization*, vol. 46, no. 2, pp. 273–284, 2012 (cit. on p. 108).

[104] R. Storn and K. Price, "Differential evolution–a simple and efficient heuristic for global optimization over continuous spaces," *Journal of global optimization*, vol. 11, no. 4, pp. 341–359, 1997 (cit. on p. 108).

[105] L. C. Pardini and M. L. Gregori, "Modeling elastic and thermal properties of 2.5d carbon fiber and carbon/sic hybrid matrix composites by homogenization method," *Journal of Aerospace Technology and Management*, vol. 2, pp. 183–194, 2010 (cit. on p. 118).

[106] X Wang, E Bibeau, and G. Naterer, "Experimental correlation of forced convection heat transfer from a naca airfoil," *Experimental Thermal and Fluid Science*, vol. 31, no. 8, pp. 1073–1082, 2007 (cit. on p. 119).

[107] T. A. Ameel, "Average effects of forced convection over a flat plate with an unheated starting length," *International communications in heat and mass transfer*, vol. 24, no. 8, pp. 1113–1120, 1997 (cit. on pp. 119, 120, 186).

[108] *Heat pipes for thermal management*, `https://www.1-act.com/innovations/heat-pipes/` (cit. on p. 121).

[109] *Euro heat pipes sa*, `https://http://www.ehp.be/` (cit. on pp. 127, 128).

[110] R Usinger, P Delouard, and G Miller, "Application of high conductivity carbon fibre materials for flexible thermal straps," in *12th European Conference on Spacecraft Structures, Materials and Environmental Testing*, vol. 691, 2012, p. 7 (cit. on p. 130).

[111] M. O. Kimball and P. J. Shirron, "Ultra-flexible thermal bus for use in the astro-h adiabatic demagnetization refrigerator," in *3rd International Planetary Probe Workshop, June*, 2015 (cit. on p. 130).

[112] S. Kayali, P. Morton, and M. Gross, "International challenges of grace follow-on," in *2017 IEEE Aerospace Conference*, IEEE, 2017, pp. 1–8 (cit. on p. 130).

[113] *Thermal straps*, `https://www.techapps.com/thermal-straps` (cit. on pp. 130–132).

[114] M. Montesano, "High erformance flexible thermal strap," in *39th Aerospace Sciences Meeting and Exhibit*, 2001, p. 218 (cit. on p. 131).

[115] E Urquiza, C Vasquez, J Rodriguez, and B Van Gorp, "Development and testing of an innovative two-arm focal-plane thermal strap (tafts)," *Cryogenics*, vol. 52, no. 4-6, pp. 306–309, 2012 (cit. on p. 131).

[116] J Pappis and S. Blum, "Properties of pyrolytic graphite," *Journal of the American Ceramic Society*, vol. 44, no. 12, pp. 592–597, 1961 (cit. on p. 131).

[117] F. Beer, E. Johnston Jr, J. Dewolf, and D. Mazurek, *Mechanics of materials, sixth edit edition*, 2010 (cit. on p. 131).

[118] R. Dhuley, M Ruschman, J. Link, and J Eyre, "Thermal conductance characterization of a pressed copper rope strap between 0.13 k and 10 k," *Cryogenics*, vol. 86, pp. 17–21, 2017 (cit. on p. 132).

[119] R. Taylor, "The thermal conductivity of pyrolytic graphite," *Philosophical Magazine*, vol. 13, no. 121, pp. 157–166, 1966 (cit. on p. 133).

[120] Y. Muzychka, M. Yovanovich, and J. Culham, "Thermal spreading resistance in compound and orthotropic systems," *Journal of thermophysics and heat transfer*, vol. 18, no. 1, pp. 45–51, 2004 (cit. on p. 136).

[121] G. N. Ellison, "Maximum thermal spreading resistance for rectangular sources and plates with nonunity aspect ratios," *IEEE Transactions on Components and Packaging Technologies*, vol. 26, no. 2, pp. 439–454, 2003 (cit. on p. 136).

[122] Y. Muzychka, J. Culham, and M. Yovanovich, "Thermal spreading resistance of eccentric heat sources on rectangular flux channels," *J. Electron. Packag.*, vol. 125, no. 2, pp. 178–185, 2003 (cit. on p. 136).

[123] S. Lee and K. Moran, "Constriction/spreading resistance model for electronics packaging," 1996 (cit. on p. 136).

[124] R. E. Simons, *Simple formulas for estimating thermal spreading resistance*, `https://www.electronics-cooling.com/2004/05/simple-formulas-for-estimating-thermal-spreading-resistance/` (cit. on p. 137).

[125] F. Hakkak and F. Farhani, "Thermal resistance in satellite bolted joints," in *Proceedings of the International Conference on Mechanical Engineering (ICME 2007)*, 2007, pp. 29–31 (cit. on pp. 138, 139).

[126] S. Vandevelde, A. Daidié, and M. Sartor, "Use of 1d mechanical and thermal models to predetermine the heat transferable by a thermal interface material layer in space applications," *Proceedings of the Institution of Mechanical Engineers, Part C: Journal of Mechanical Engineering Science*, vol. 234, no. 17, pp. 3459–3473, 2020 (cit. on p. 139).

[127] M. Mantelli and M. Yovanovich, "16 thermal contact resistance," *Spacecraft Thermal Control Handbook*, vol. 1, 2002 (cit. on p. 139).

[128] M. M. Yovanovich, "Four decades of research on thermal contact, gap, and joint resistance in microelectronics," *IEEE transactions on components and packaging technologies*, vol. 28, no. 2, pp. 182–206, 2005 (cit. on p. 139).

[129] M. Dempsey, "Dymola for multi-engineering modelling and simulation," in *2006 IEEE Vehicle Power and Propulsion Conference*, 2006, pp. 1–6 (cit. on pp. 150, 163, 176).

[130] J DeSalvo and A Swanson, "Ansys engineering analysis system user's manual," in *Swanson Analysis Systems*, 1985, pp. 1–6 (cit. on p. 150).

[131] C. R. Akli, "Conception systémique d'une locomotive hybride autonome: Application à la locomotive hybride de démonstration et d'investigations en énergétique lhydie développée par la sncf," Ph.D. dissertation, 2008 (cit. on p. 150).

[132] D. N. Nkwetta and F. Haghighat, "Thermal energy storage with phase change material—a state-of-the art review," *Sustainable Cities and Society*, vol. 10, pp. 87–100, 2014 (cit. on pp. 158, 159).

[133] M. G. Schneider and T. J. Bland, "Advanced passive cooling for high power electromechanical actuators," *SAE Transactions*, pp. 317–327, 1993 (cit. on p. 159).

[134] Y. Hong and G. Xin-Shi, "Preparation of polyethylene–paraffin compound as a form-stable solid-liquid phase change material," *Solar Energy Materials and Solar Cells*, vol. 64, no. 1, pp. 37–44, 2000 (cit. on p. 159).

[135] F. Agyenim, N. Hewitt, P. Eames, and M. Smyth, "A review of materials, heat transfer and phase change problem formulation for latent heat thermal energy storage systems (lhtess)," *Renewable and sustainable energy reviews*, vol. 14, no. 2, pp. 615–628, 2010 (cit. on p. 160).

[136] L. F. Cabeza, A. Castell, C. d. Barreneche, A De Gracia, and A. Fernández, "Materials used as pcm in thermal energy storage in buildings: A review," *Renewable and Sustainable Energy Reviews*, vol. 15, no. 3, pp. 1675–1695, 2011 (cit. on p. 160).

[137] M. Kenisarin and K. Mahkamov, "Solar energy storage using phase change materials," *Renewable and sustainable energy reviews*, vol. 11, no. 9, pp. 1913–1965, 2007 (cit. on p. 160).

[138] M. M. Farid, A. M. Khudhair, S. A. K. Razack, and S. Al-Hallaj, "A review on phase change energy storage: Materials and applications," *Energy conversion and management*, vol. 45, no. 9-10, pp. 1597–1615, 2004 (cit. on p. 160).

[139] S. Hasnain, "Review on sustainable thermal energy storage technologies, part i: Heat storage materials and techniques," *Energy conversion and management*, vol. 39, no. 11, pp. 1127–1138, 1998 (cit. on p. 160).

[140] P. Lamberg and K. Siren, "Analytical model for melting in a semi-infinite pcm storage with an internal fin," *Heat and mass transfer*, vol. 39, no. 2, pp. 167–176, 2003 (cit. on p. 160).

[141] P. Huang, A. Verma, D. J. Robles, Q. Wang, P. Mukherjee, and J. Sun, "Probing the cooling effectiveness of phase change materials on lithium-ion battery thermal response under overcharge condition," *Applied thermal engineering*, vol. 132, pp. 521–530, 2018 (cit. on p. 160).

[142] V. Voller and M. Cross, "Accurate solutions of moving boundary problems using the enthalpy method," *International Journal of Heat and Mass Transfer*, vol. 24, no. 3, pp. 545–556, 1981 (cit. on p. 160).

[143] F. Cheung, T. Chawla, and D. Pedersen, "The effects of heat generation and wall interaction on freezing and melting in a finite slab," *International journal of heat and mass transfer*, vol. 27, no. 1, pp. 29–37, 1984 (cit. on p. 160).

[144] C. An and J. Su, "Lumped parameter model for one-dimensional melting in a slab with volumetric heat generation," *Applied thermal engineering*, vol. 60, no. 1-2, pp. 387–396, 2013 (cit. on pp. 160, 162, 163).

[145] J Mennig, T Auerbach, and W Hälg, "Two point hermite approximations for the solution of linear initial value and boundary value problems," *Computer methods in applied mechanics and engineering*, vol. 39, no. 2, pp. 199–224, 1983 (cit. on pp. 160, 162, 163).

[146] J. Delgado-Maciel, G. Cortés-Robles, C. Sánchez-Ramírez, J. García-Alcaraz, and J. M. Méndez-Contreras, "The evaluation of conceptual design through dynamic simulation: A proposal based on triz and system dynamics," *Computers & Industrial Engineering*, vol. 149, p. 106 785, 2020 (cit. on p. 174).

[147] T. Vuletic, A. Duffy, L. Hay, C. McTeague, L. Pidgeon, and M. Grealy, "The challenges in computer supported conceptual engineering design," *Computers in Industry*, vol. 95, pp. 22–37, 2018 (cit. on p. 174).

[148] W. Liu, R. Tan, G. Cao, Z. Zhang, S. Huang, and L. Liu, "A proposed radicality evaluation method for design ideas at conceptual design stage," *Computers & Industrial Engineering*, vol. 132, pp. 141–152, 2019 (cit. on p. 174).

[149] J. Pokojski, K. Oleksiński, and J. Pruszyński, "Knowledge based processes in the context of conceptual design," *Journal of Industrial Information Integration*, vol. 15, pp. 219–238, 2019 (cit. on p. 174).

[150] F. Sanchez and S. Liscouet-Hanke, "Thermal risk prediction methodology for conceptual design of aircraft equipment bays," *Aerospace Science and Technology*, vol. 104, p. 105 946, 2020 (cit. on p. 175).

[151] C. Sciascera, P. Giangrande, C. Brunson, M. Galea, and C. Gerada, "Optimal design of an electro-mechanical actuator for aerospace application," in *IECON 2015-41st Annual Conference of the IEEE Industrial Electronics Society*, IEEE, 2015, pp. 001 903–001 908 (cit. on p. 179).

[152] F Sanchez and S Delbecq, "Surrogate modeling technique for the conceptual and preliminary design of embedded systems and components," in *International Council of Aeronautical Sciences*, 2016 (cit. on p. 180).

[153] M. Cavcar, "The international standard atmosphere (isa)," *Anadolu University, Turkey*, vol. 30, no. 9, pp. 1–6, 2000 (cit. on p. 181).

[154] ESDU, "Data item 68046: Atmospheric data for performance calculations," *IHS ESDU*, 1992 (cit. on p. 181).

[155] I. H. Bell, S. Quoilin, J. Wronski, and V. Lemort, "Coolprop: An open-source reference-quality thermophysical property library," in *ASME ORC 2nd International Seminar on ORC Power Systems*, 2013 (cit. on p. 181).

[156] F. Sanchez, A. M. Huzaifa, and S. Liscouët-Hanke, "Ventilation considerations for an enhanced thermal risk prediction in aircraft conceptual design," *Aerospace Science and Technology*, vol. 108, p. 106 401, 2021 (cit. on p. 184).

[157] *Fmi: Functional mock-up interface*, `https://fmi-standard.org/` (cit. on p. 190).

[158] C. Andersson, "Methods and tools for co-simulation of dynamic systems with the functional mock-up interface," Ph.D. dissertation, Lund University, 2016 (cit. on p. 190).

Appendix A

Finite Element Model of the PM Brushless Motor

Definition of the simulation model

The FEM model of the motor, used to generate the surrogate models, has been developed in FEMM (Finite Element Method Magnetics) software. The model was built using the geometry and materials of the Parvex NX310 (depicted in Fig. A.1) as reference. It consists of an internal permanent magnet servomotor which features 12 slots, 10 permanent magnets (poles) made of samarium-cobalt $S_{m_2}C_{0_{17}}$ and a stator pack of 0.5 mm thick electrical steel laminations ("M 310-50 A"). The FEM model, receiving as inputs the geometric parameters defining the motor dimensions (illustrated in Fig. A.2) and the current density in the slot, provides the electromagnetic torque, the slot cross section area used to estimate the Joule losses and the magnetic flux density which is useful for calculating the iron losses.

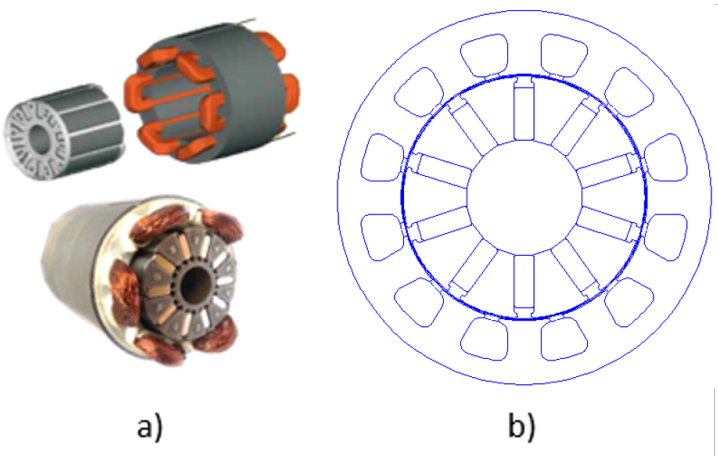

Figure A.1: a) Parvex NX 310 servomotor and b) its representative finite elements model.

The motor losses in fact, cannot be estimated directly from the simulation model but they are derived, as shown in the next sections, from the outputs just mentioned. The choice of the using current density over current intensity as source of excitation is due to the fact that the latter is strictly linked to the structure of the winding, defined by the diameter and number of wires per slot. This leads to take into account two further variables when defining the surrogate models, which is not advantageous, for the many reasons discussed in Chapter 3, in view of realising a model with a reduced number of variable.

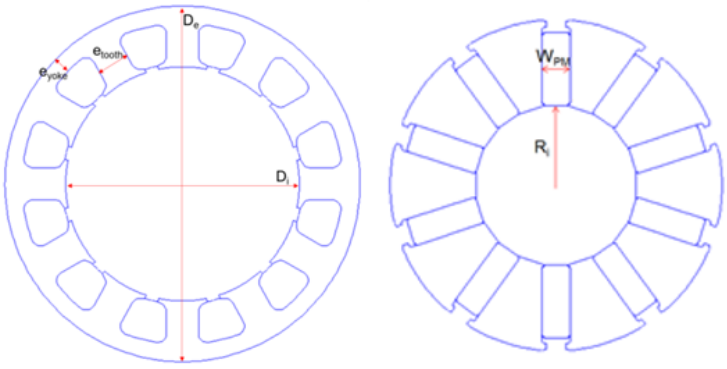

Figure A.2: Stator and Rotor geometrical variables.

Definition of Joule losses

The Joule losses cannot be directly extracted from FEMM because a 2D simulation model has been used. Therefore, it is was not possible to evaluate the effects of the coils head. To assess their contribution on the copper losses, the following considerations have been made.

The Joule losses P_J in the motor are function of the winding volume per slot pair V_{Cu}, current density J, winding factor k_w, copper electrical resistivity ρ_{Cu} and number of slots N_s:

$$P_J = \frac{N_s}{2} k_w \rho_{Cu} J^2 V_{Cu} \tag{A.1}$$

The winding volume per slot pair can be decomposed into the winding volume of the active part of the motor V_{slot} and the winding head V_{head} as follows:

$$V_{Cu} = V_{slot} + V_{head} = \left[S_{slot} L_m + \pi^2 \left(\frac{d_{tor}}{2} \right)^2 R_{tor} \right] \tag{A.2}$$

where S_{slot} is the slot area, L_m the active length of winding, $d_{tor} = 2\sqrt{\frac{S_{slot}}{\pi}}$ the equivalent diameter of the winding head and $R_{tor} = 0.2877 D_e sin\left(\frac{\pi}{12}\right)$ the radius of the winding head from one slot to another.

As can be seen from the above relationship, the winding volume is dependent on the cross-sectional area of the slot S_{slot}. The value of this, is provided by the FEMM according to the considered motor geometry. Since the other variables represent input design parameters, the Joule losses can be therefore estimate with Eq. A.1.

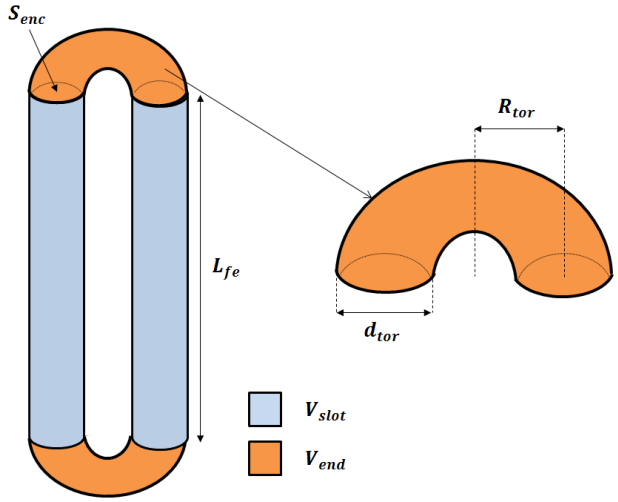

Figure A.3: Geometric description of the copper volume per slot pair.

Definition of iron losses

The iron losses depend on the rotational speed of the motor, so they cannot be evaluated through the static FEMM simulations conducted here. For this reason these are derived through analytical formulas as a function of the flux density, on the yoke and on teeth of the stator, provided by the simulations.

The iron losses P_{Fe} arise from the variation of magnetic flux-density throughout the core. This variation include hysteresis $P_{Fe,h}$ and eddy current $P_{Fe,e}$ losses :

$$P_{Fe} = P_{Fe,h} + P_{Fe,e} \tag{A.3}$$

For both losses, complex differential equations are provided by Gieras [94]. The relationship used here is a simplification of these formulas adapted to the needs of the preliminary design:

$$P_{Fe} = \Delta P_{F_e} \left(\frac{f_{elec}}{50} \right)^{1,5} (m_t B_{mt}^2 + m_y B_{my}^2) \tag{A.4}$$

where $\Delta P_{F_e} = 1.25 W/kg$ are the specific core losses at $1T$ and $50Hz$, $f_{magn} = \frac{N_{PM}/2\omega}{60}$, the electrical frequency, N_{PM} the number of permanent magnets, m_t and m_y the masses of the teeth and yoke, B_{mt} and B_{my} are respectively the magnetic flux density on teeth and on the yoke (Fig. A.4). For a given geometry of the motor, the variables $m_t B_{mt}$ and $m_y B_{my}$ are provided by the FEMM simulation. Depending on the required speed specification, the iron losses can be estimated through the above introduced relationship.

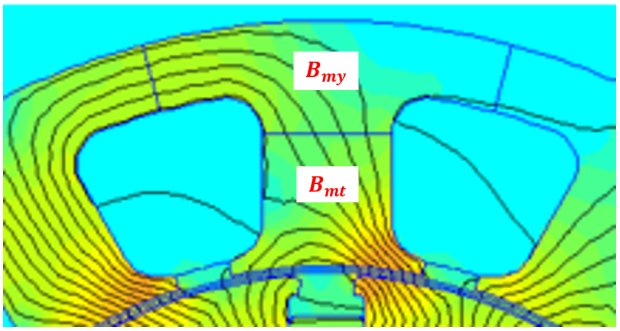

Figure A.4: Magnetic flux density on yoke and teeth.

Appendix B

Mission Profiles used for the Preliminary Designs

Presentation of the mission profiles

The mission profiles analysed here refer to the primary flight control surfaces of an Airbus A320 and are based on a flight duration of 112 minutes. They are represented by the surface deflection order $\vartheta^*(t)$ and the aerodynamic torque $T_{aero}(t)$. As these profiles were provided by COLLINS Aerospace, for reasons of confidentiality these have been normalised with respect to the Aileron profile. Note, that these data are generated by a flight simulator with autopilot. $\vartheta^*(t)$ is therefore the instruction received by the actuator and does not take into account the actuator's own dynamics. The position ϑ, speed $\dot{\vartheta}$ and acceleration $\ddot{\vartheta}$ profiles are deduced from the time response of the actuator, which follows the dynamics of a second-order system:

$$\vartheta^* = \vartheta + \frac{2\zeta}{\omega_0}\dot{\vartheta} + \frac{\ddot{\vartheta}}{\omega_0} \tag{B.1}$$

where ω_0 is the desired bandwidth of $2\,Hz$ and ζ is the damping coefficient equal to 0.7071.

Aileron mission profile

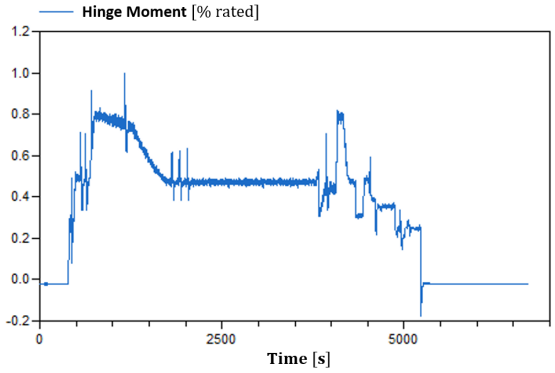

(a) Aerodynamic Torque

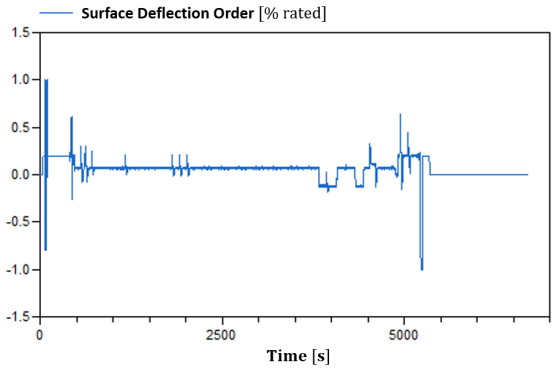

(b) Surface deflection order

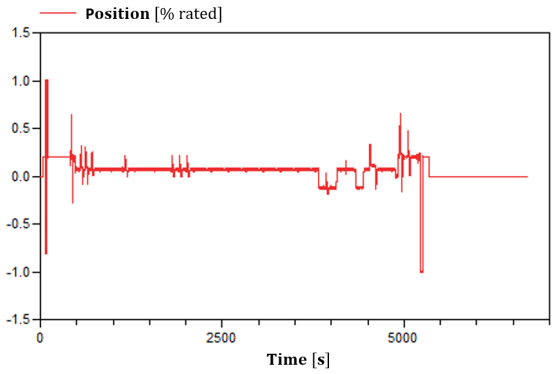

(c) Position

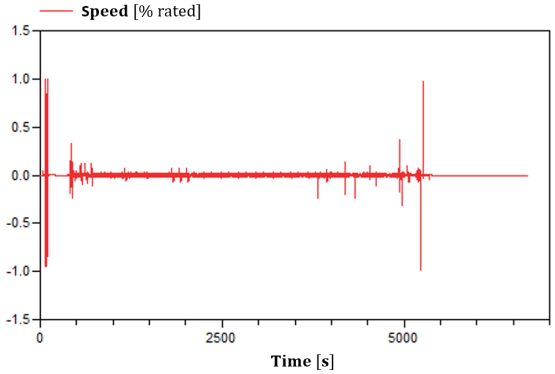

(d) Speed

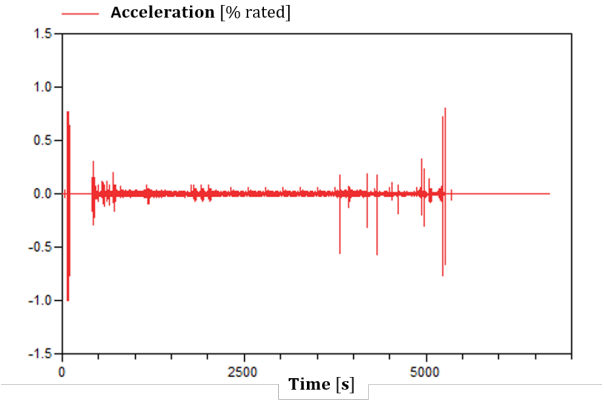

(e) Acceleration

Figure B.1: Mission profiles of an aileron surface of an Airbus A320 (NORMALISED DATA).

Elevator mission profile

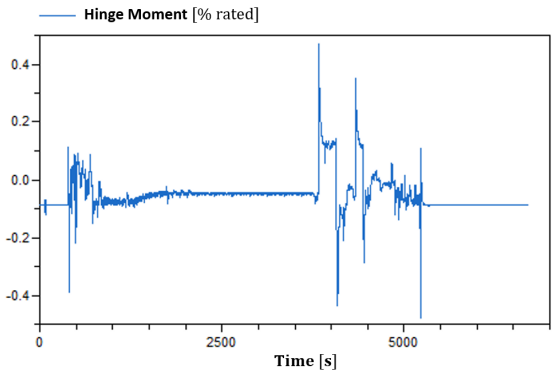

(a) Aerodynamic Torque

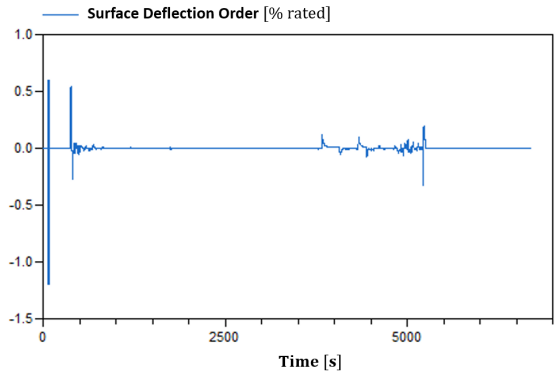

(b) Surface deflection order

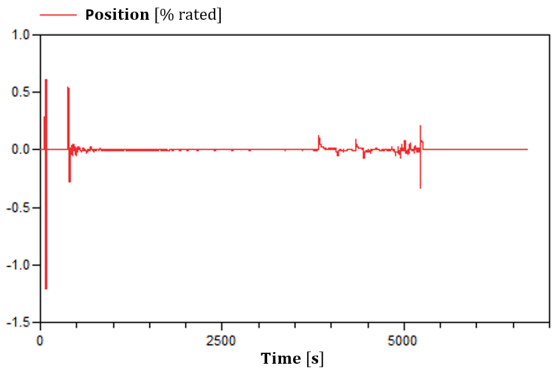

(c) Position

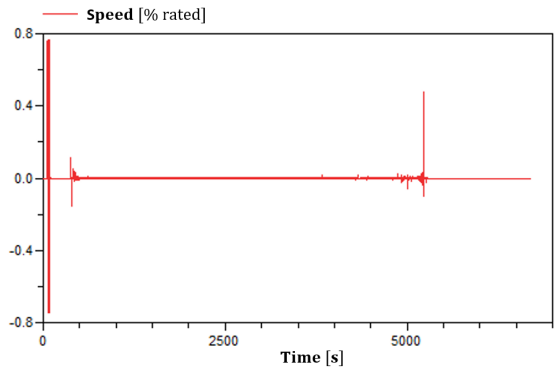

(d) Speed

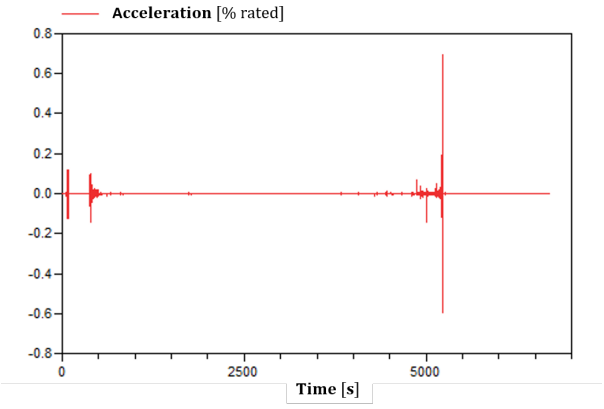

(e) Acceleration

Figure B.2: Mission profiles of an elevator surface of an Airbus A320 (NORMALISED DATA).

Rudder mission profile

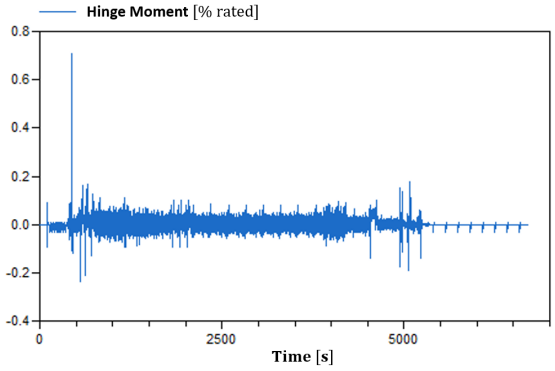

(a) Aerodynamic Torque

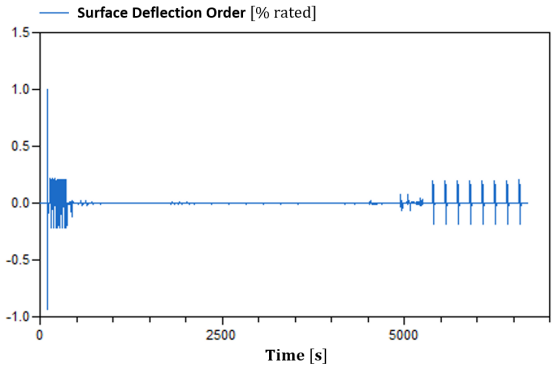

(b) Surface deflection order

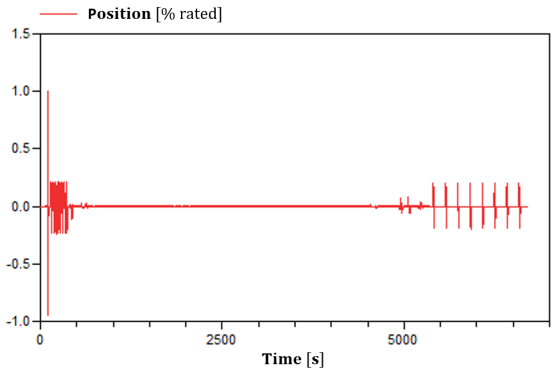

(c) Position

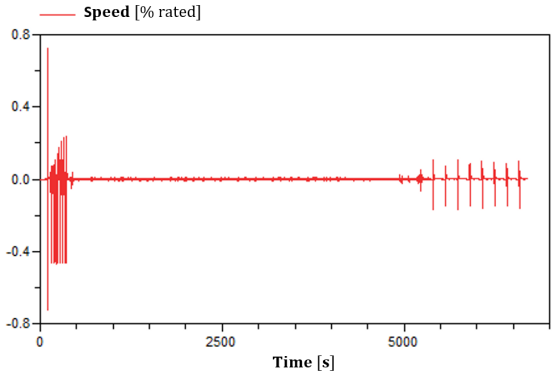

(d) Speed

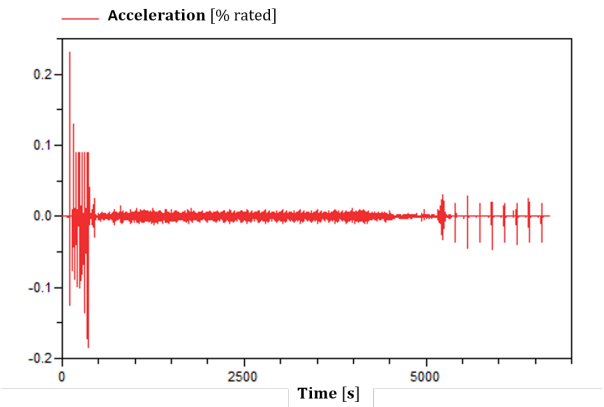

(e) Acceleration

Figure B.3: Mission profiles of an Rudder surface of an Airbus A320 (NORMALISED DATA).

Extracted actuator specifications

Parameter	Value	Definition
$T_{aero_{RMS}}/(T_{aero_{max}})_{Aileron}$	0.43	RMS aerodynamic torque
$T_{aero_{max}}/(T_{aero_{max}})_{Aileron}$	1	Maximum aerodynamic torque
$T_{fat}/(T_{aero_{max}})_{Aileron}$	0.49	Rolling fatigue equivalent torque
$\bar{\omega}/(\omega_{max})_{Aileron}$	0.138	Average speed
$\omega_{max}/(\omega_{max})_{Aileron}$	1	Maximum speed
$\delta/(\delta)_{Aileron}$	1	Magnitude of the oscillatory movement
$n_{osc}/(n_{osc})_{Aileron}$	1	Oscillatory cycles number

Table B.1: Mission profile specifications of Aileron (normalised data).

Parameter	Value	Definition
$T_{aero_{RMS}}/(T_{aero_{max}})_{Aileron}$	0.08	Root mean square aerodynamic torque
$T_{aero_{max}}/(T_{aero_{max}})_{Aileron}$	0.52	Maximum aerodynamic torque
$T_{fat}/(T_{aero_{max}})_{Aileron}$	0.15	Rolling fatigue equivalent torque
$\bar{\omega}/(\omega_{max})_{Aileron}$	0.0058	Average speed
$\omega_{max}/(\omega_{max})_{Aileron}$	0.97	Maximum speed
$\delta/(\delta)_{Aileron}$	6	Magnitude of the oscillatory movement
$n_{osc}/(n_{osc})_{Aileron}$	0.02	Oscillatory cycles number

Table B.2: Mission profile specifications of Elevator (data normalised to aileron specifications).

Parameter	Value	Unit
$T_{aero_{RMS}}/(T_{aero_{max}})_{Aileron}$	0.03	Root mean square aerodynamic torque
$T_{aero_{max}}/(T_{aero_{max}})_{Aileron}$	0.72	Maximum aerodynamic torque
$T_{fat}/(T_{aero_{max}})_{Aileron}$	0.09	Rolling fatigue equivalent torque
$\bar{\omega}/(\omega_{max})_{Aileron}$	0.01	Average speed
$\omega_{max}/(\omega_{max})_{Aileron}$	0.78	Maximum speed
$\delta/(\delta)_{Aileron}$	1.5	Magnitude of the oscillatory movement
$n_{osc}/(n_{osc})_{Aileron}$	0.24	Oscillatory cycles number

Table B.3: Mission profile specifications of Rudder (data normalised to aileron specifications).

Appendix C

Static Preliminary Design Case Studies

Formulation of the optimisation problem

The optimisation problem is formulated as follows:

$$
\begin{aligned}
\text{Minimize} \quad & M_{EMA} \\
\text{with respect to} \quad & D_e, \Pi_1, \Pi_2, k_b, k_{sn}, n_{red}, L_a, S, s_a, k_L, k_H, k_W \\
\text{subject to} \quad & \Theta_{wind} - \Theta_{wind_{lim}} \leq 0 \\
& \omega_{mot_{max}} - \omega_{max} \leq 0 \\
& C_{d_{sn_{req}}} - C_{d_{sn}} \leq 0 \\
& F_{shock} - C_{0_{sn}} \leq 0 \\
& F_{shock} - C_{0_b} \leq 0 \\
& C_{d_{b_{req}}} - C_{d_b} \leq 0 \\
& J_{ref} - J_{ref_{max}} \leq 0 \\
& P_{Fe} + P_J - Q \leq 0 \\
& \sigma - \sigma_{max} \leq 0 \\
& L_{EMA} - L_e \leq 0 \\
& W_{EMA} - W_e \leq 0 \\
& H_{EMA} - H_e \leq 0
\end{aligned}
\tag{C.1}
$$

Design Inputs

Table C.1: Inputs parameters values

	Parameter	Value	Unit	Description
System	L_{arm}	47	$[mm]$	Lever arm
	L_e	200	$[mm]$	Actuator room length
	W_e	250	$[mm]$	Actuator room width
	H_e	120	$[mm]$	Actuator room height
Screw-Nut	$C_{0_{sn_{ref}}}$	108.23	$[kN]$	Reference static load
	$C_{d_{sn_{ref}}}$	63.25	$[kN]$	Reference dynamic load
	$D_{n_{ref}}$	53	$[mm]$	Reference nut diameter
	$d_{s_{ref}}$	25	$[mm]$	Reference screw diameter
	$A_{n_{ref}}$	78	$[mm]$	Reference nut length
	$M_{n_{ref}}$	0.7	$[kg]$	Reference nut mass
	$m_{s_{ref}}$	3.9	$[kg/m]$	Reference screw linear mass
	p_{sn}	5	$[mm]$	Lead
	n_r	10	$[-]$	Rollers number
Bearing	$C_{0_{b_{ref}}}$	92	$[kN]$	Reference static load
	$C_{d_{b_{ref}}}$	86	$[kN]$	Reference dynamic load
	$D_{b_{ref}}$	110	$[mm]$	Reference exterior diameter
	$d_{b_{ref}}$	60	$[mm]$	Reference interior diameter
	$L_{b_{ref}}$	22	$[mm]$	Reference length
	$M_{b_{ref}}$	0.99	$[kg]$	Reference mass
	n_b	14	$[-]$	Balls number
Motor	B_r	1.07	$[T]$	Residual induction
	B_{sat}	2.13	$[T]$	Saturation induction
	N_s	12	$[-]$	Slot numbers
	ρ_{Cu}	$1.68 \cdot 10^{-8}$	$[\Omega m]$	Electrical resistivity of copper ($20°C$)
	$\Delta_{P_{Fe}}$	1.25	$[V]$	Specific core losses
	γ_{Fe}	7.874	$[kg/m^3]$	Density of iron
	e_N	0.3	$[mm]$	Nomex thickness

Continued on next page

	Parameter	Value	Unit	Description
Gear	K	$6.9 \cdot 10^6$	$[N/m^2]$	Surface durability
	A_f	0.3	$[kg/m^3]$	Application factor for weight estimation
Housing	Θ_{hous}	100	$[°C]$	Housing temperature
	Θ_{ext}	20	$[°C]$	Exterior temperature
	Q_m	30	$[-]$	Mechanical quality coefficient
	a	196.2	$[ms/^2]$	Vibratory sinusoidal acceleration
	ρ_a	2700	$[kg/ms^3]$	Aluminium density
	λ_a	284	$[W/mK]$	Aluminium thermal conductivity
	Cp_a	900	$[J/kgK]$	Aluminium specific heat

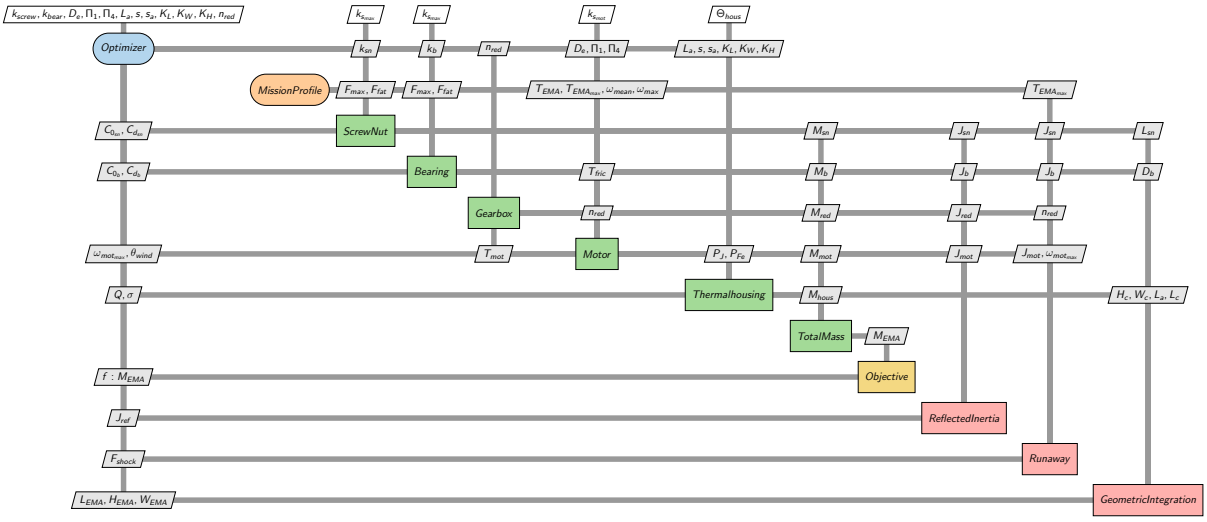

Figure C.1: XDSM of the EMA preliminary design case studies.

Results

Aileron gear drive

Table C.2: Design variables, constraints and objective (Aileron gear drive).

	Parameter	Value	Unit	Description
Design variables	D_e	62.90	$[mm]$	Motor Diameter
	Π_1	0.62	$[-]$	Dimensionless ratio saturation
	Π_2	0.16	$[-]$	Dimensionless ratio yoke to motor diameter
	k_b	3.8	$[-]$	Bearing oversize coefficient
	k_{sn}	2.66	$[-]$	Screw nut oversize coefficient
	n_{red}	4	$[-]$	Reduction ratio
	L_a	25.45	$[mm]$	Fins width
	S	5.62	$[mm]$	Distance between two fins
	s_a	1.58	$[mm]$	Fin thickness
	k_L	2	$[-]$	Housing length oversize coefficient
	k_H	1.09	$[-]$	Housing height oversize coefficient
	k_W	1.09	$[-]$	Housing width oversize coefficient
Constraints	Θ_{wind}	152	$[°C]$	Winding temperature ($\Theta_{wind_{lim}} = 185\,°C$)
	$\omega_{mot_{max}}$	176	$[rad/s]$	Maximum motor speed ($\omega_{max} = 942\,rad/s$)
	$C_{d_{sn}}$	68.34	$[kN]$	Screw dynamic load ($C_{d_{sn_{req}}} = 67.81\,kN$)
	$C_{0_{sn}}$	117.95	$[kN]$	Screw static load ($F_{shock} = 97.65\,kN$)
	C_{d_b}	103.36	$[kN]$	Bearing dynamic load ($C_{d_{b_{req}}} = 67.81\,kN$)
	C_{0_b}	97.766	$[kN]$	Bearing static load ($F_{shock} = 97.65\,kN$)
	J_{ref}	13.26	$[kgm^2]$	Reflected Inertia ($J_{ref_{max}} = 30\,kgm^2$)
	σ	39.74	$[MPa]$	Limit stress of fin ($\sigma_{max} = 40\,MPa$)
	Q	160.27	$[W]$	Heat transfer rate ($P_J + P_{F_e} = 158.63\,W$)
	L_{act}	152.56	$[mm]$	Actuator length ($L_e = 200\,mm$)
	W_{act}	236.11	$[mm]$	Actuator width ($W_e = 250\,mm$)
	H_{act}	116.94	$[mm]$	Actuator height ($W_e = 120\,mm$)
Objective	M_{EMA}	5.6	$[kg]$	EMA Mass

Table C.3: System output values (Aileron gear drive).

	Parameter	Value	Unit	Description
Motor	L_m	76.62	$[mm]$	Motor length
	T_{mot}	4.38	$[Nm]$	Nominal motor torque*
	P_J	158.61	$[W]$	Joule losses (at Θ_{wind})
	P_{F_e}	0.02	$[W]$	Iron losses
	R_{cd}	0.33	$[K/W]$	Motor thermal resistance
	M_{mot}	1.26	$[kg]$	Motor mass
Housing	N_{fin}	22	$[-]$	Fins number
	h_{fin}	7.57	$[W/m^2K]$	Heat transfer fin
	h_{int}	8.77	$[W/m^2K]$	Heat transfer interstice
	h_{top}	10.49	$[W/m^2K]$	Heat transfer top surface
	h_{bottom}	5.25	$[W/m^2K]$	Heat transfer bottom surface
	h_{rad}	7.23	$[W/m^2K]$	Equivalent radiation heat transfer
	M_{hous}	0.82	$[kg]$	Housing mass
Bearing	D_b	116.94	$[mm]$	Exterior diameter
	d_b	63.78	$[mm]$	Interior diameter
	L_b	23.39	$[mm]$	Bearing length
	M_b	1.19	$[kg]$	Bearing mass
Screw-nut	D_n	55.33	$[mm]$	Nut Diameter
	d_s	26.10	$[mm]$	Screw diameter
	A_n	81.43	$[mm]$	Nut length
	l_{sn}	152.56	$[mm]$	Screw length
	M_{sn}	1.44	$[kg]$	Screw nut mass
Gearbox	d_g	107.81	$[mm]$	Gear diameter
	d_p	50.86	$[mm]$	Pinion diameter
	d_i	26.95	$[mm]$	Idler diameter
	M_{red}	0.9	$[kg]$	Gearbox mass
* Motor sized for the RMS actuator load T_{EMA}				

Aileron direct drive

Table C.4: Design variables, constraints and objective (Aileron direct drive).

	Parameter	Value	Unit	Description
Design variables	D_e	113.95	$[mm]$	Motor Diameter
	Π_1	0.77	$[-]$	Dimensionless ratio saturation
	Π_2	0.13	$[-]$	Dimensionless ratio yoke to motor diameter
	k_b	2.95	$[-]$	Bearing oversize coefficient
	k_{sn}	2.66	$[-]$	Screw nut oversize coefficient
	L_a	29.96	$[mm]$	Fins width
	S	6.74	$[mm]$	Distance between two fins
	s_a	2.24	$[mm]$	Fin thickness
	k_L	1.75	$[-]$	Housing length oversize coefficient
	k_H	1.05	$[-]$	Housing height coefficient
	k_W	1.05	$[-]$	Housing height oversize coefficient
Constraints	Θ_{wind}	160	$[°C]$	Winding temperature ($\Theta_{wind_{lim}} = 185\,°C$)
	$\omega_{mot_{max}}$	41.26	$[rad/s]$	Maximum motor speed ($\omega_{max} = 942\,rad/s$)
	$C_{d_{sn}}$	68.42	$[kN]$	Screw dynamic load ($C_{d_{sn_{req}}} = 67.81\,kN$)
	$C_{0_{sn}}$	118.11	$[kN]$	Screw static load ($F_{shock} = 73.57\,kN$)
	C_{d_b}	81.69	$[kN]$	Bearing dynamic load ($C_{d_{b_{req}}} = 64.86\,kN$)
	C_{0_b}	97.766	$[kN]$	Bearing static load ($F_{shock} = 73.57\,kN$)
	J_{ref}	73.8	$[kgm^2]$	Reflected Inertia ($J_{ref_{max}} = 30\,kgm^2$)
	σ	38.87	$[MPa]$	Limit stress of fin ($\sigma_{max} = 40\,MPa$)
	Q	274.8	$[W]$	Heat transfer rate ($P_J + P_{F_e} = 269.38\,W$)
	L_{act}	178.52	$[mm]$	Actuator length ($L_e = 200\,mm$)
	W_{act}	179.26	$[mm]$	Actuator width ($W_e = 250\,mm$)
	H_{act}	119.60	$[mm]$	Actuator height ($W_e = 120\,mm$)
Objective	M_{EMA}	8.61	$[kg]$	EMA Mass

Table C.5: System output values (Aileron direct drive).

	Parameter	Value	Unit	Description
Motor	L_m	95.66	$[mm]$	Motor length
	T_{mot}	16.61	$[Nm]$	Nominal motor torque*
	P_J	269.37	$[W]$	Joule losses (at Θ_{wind})
	P_{F_e}	0.01	$[W]$	Iron losses
	R_{cd}	0.22	$[K/W]$	Motor thermal resistance
	M_{mot}	4.12	$[kg]$	Motor mass
Housing	N_{fin}	20	$[-]$	Fins number
	h_{fin}	6.8	$[W/m^2K]$	Heat transfer fin
	h_{int}	7.64	$[W/m^2K]$	Heat transfer interstice
	h_{top}	9.51	$[W/m^2K]$	Heat transfer top surface
	h_{bottom}	4.76	$[W/m^2K]$	Heat transfer bottom surface
	h_{rad}	7.23	$[W/m^2K]$	Equivalent radiation heat transfer
	M_{hous}	2.26	$[kg]$	Housing mass
Bearing	D_b	102.97	$[mm]$	Exterior diameter
	d_b	56.17	$[mm]$	Interior diameter
	L_b	20.59	$[mm]$	Bearing length
	M_b	0.81	$[kg]$	Bearing mass
Screw-nut	D_n	55.37	$[mm]$	Nut Diameter
	d_s	26.12	$[mm]$	Screw diameter
	A_n	81.48	$[mm]$	Nut length
	l_{sn}	143.40	$[mm]$	Screw length
	M_{sn}	1.42	$[kg]$	Screw nut mass
* Motor sized for the RMS actuator load T_{EMA}				

Elevator gear drive

Table C.6: Design variables, constraints and objective (Elevator gear drive).

	Parameter	Value	Unit	Description
Design variables	D_e	53.29	$[mm]$	Motor Diameter
	Π_1	0.62	$[-]$	Dimensionless ratio saturation
	Π_2	0.18	$[-]$	Dimensionless ratio yoke to motor diameter
	k_b	6.51	$[-]$	Bearing oversize coefficient
	k_{sn}	3.76	$[-]$	Screw nut oversize coefficient
	n_{red}	4	$[-]$	Reduction ratio
	L_a	30.09	$[mm]$	Fins width
	S	5.82	$[mm]$	Distance between two fins
	s_a	2.20	$[mm]$	Fin thickness
	k_L	2	$[-]$	Housing length oversize coefficient
	k_H	1.10	$[-]$	Housing height coefficient
	k_W	1.12	$[-]$	Housing height oversize coefficient
Constraints	Θ_{wind}	153	$[^\circ C]$	Winding temperature ($\Theta_{wind_{lim}} = 185\,^\circ C$)
	$\omega_{mot_{max}}$	163.68	$[rad/s]$	Maximum motor speed ($\omega_{max} = 942\,rad/s$)
	$C_{d_{sn}}$	51.88	$[kN]$	Screw dynamic load ($C_{d_{sn_{req}}} = 10.84\,kN$)
	$C_{0_{sn}}$	86.83	$[kN]$	Screw static load ($F_{shock} = 86.85\,kN$)
	C_{d_b}	92.91	$[kN]$	Bearing dynamic load ($C_{d_{b_{req}}} = 11.68\,kN$)
	C_{0_b}	87.12	$[kN]$	Bearing static load ($F_{shock} = 86.85\,kN$)
	J_{ref}	9.08	$[kgm^2]$	Reflected Inertia ($J_{ref_{max}} = 30\,kgm^2$)
	σ	39.83	$[MPa]$	Limit stress of fin ($\sigma_{max} = 40\,MPa$)
	Q	194.23	$[W]$	Heat transfer rate ($P_J + P_{F_e} = 194.21\,W$)
	L_{act}	131.41	$[mm]$	Actuator length ($L_e = 200\,mm$)
	W_{act}	228.41	$[mm]$	Actuator width ($W_e = 250\,mm$)
	H_{act}	110.39	$[mm]$	Actuator height ($W_e = 120\,mm$)
Objective	M_{EMA}	4.77	$[kg]$	EMA Mass

Table C.7: System output values (Elevator gear drive).

	Parameter	Value	Unit	Description
Motor	L_m	98.33	$[mm]$	Motor length
	T_{mot}	5.04	$[Nm]$	Nominal motor torque*
	P_J	194.2	$[W]$	Joule losses (at Θ_{wind})
	P_{F_e}	0.01	$[W]$	Iron losses
	R_{cd}	0.27	$[K/W]$	Motor thermal resistance
	M_{mot}	1.22	$[kg]$	Motor mass
Housing	N_{fin}	25	$[-]$	Fins number
	h_{fin}	8.23	$[W/m^2K]$	Heat transfer fin
	h_{int}	9.09	$[W/m^2K]$	Heat transfer interstice
	h_{top}	10.61	$[W/m^2K]$	Heat transfer top surface
	h_{bottom}	5.31	$[W/m^2K]$	Heat transfer bottom surface
	h_{rad}	7.23	$[W/m^2K]$	Equivalent radiation heat transfer
	M_{hous}	1.00	$[kg]$	Housing mass
Bearing	D_b	110.39	$[mm]$	Exterior diameter
	d_b	60.21	$[mm]$	Interior diameter
	L_b	22.08	$[mm]$	Bearing length
	M_b	1.00	$[kg]$	Bearing mass
Screw-nut	D_n	47.47	$[mm]$	Nut Diameter
	d_s	22.39	$[mm]$	Screw diameter
	A_n	69.87	$[mm]$	Nut length
	l_{sn}	131.41	$[mm]$	Screw length
	M_{sn}	0.9	$[kg]$	Screw nut mass
Gearbox	d_g	101.66	$[mm]$	Gear diameter
	d_p	25.41	$[mm]$	Pinion diameter
	d_i	47.96	$[mm]$	Idler diameter
	M_{red}	0.65	$[kg]$	Gearbox mass
* Motor sized for the maximum actuator load $T_{EMA_{max}}$				

Elevator direct drive

Table C.8: Design variables, constraints and objective (Elevator direct drive).

	Parameter	Value	Unit	Description
Design variables	D_e	109.62	$[mm]$	Motor Diameter
	Π_1	0.77	$[-]$	Dimensionless ratio saturation
	Π_2	0.13	$[-]$	Dimensionless ratio yoke to motor diameter
	k_b	4.88	$[-]$	Bearing oversize coefficient
	k_{sn}	2.78	$[-]$	Screw nut oversize coefficient
	L_a	26.61	$[mm]$	Fins width
	S	6.55	$[mm]$	Distance between two fins
	s_a	1.75	$[mm]$	Fin thickness
	k_L	1.88	$[-]$	Housing length oversize coefficient
	k_H	1.05	$[-]$	Housing width oversize coefficient
	k_W	1.05	$[-]$	Housing height oversize coefficient
Constraints	Θ_{wind}	164	$[°C]$	Winding temperature ($\Theta_{wind_{lim}} = 185\,°C$)
	$\omega_{mot_{max}}$	38.38	$[rad/s]$	Maximum motor speed ($\omega_{max} = 942\,rad/s$)
	$C_{d_{sn}}$	39.45	$[kN]$	Screw dynamic load ($C_{d_{sn_{req}}} = 10.84\,kN$)
	$C_{0_{sn}}$	64.05	$[kN]$	Screw static load ($F_{shock} = 64.03\,kN$)
	C_{d_b}	71.14	$[kN]$	Bearing dynamic load ($C_{d_{b_{req}}} = 11.68\,kN$)
	C_{0_b}	65.27	$[kN]$	Bearing static load ($F_{shock} = 64.035\,kN$)
	J_{ref}	5.3	$[kgm^2]$	Reflected Inertia ($J_{ref_{max}} = 30\,kgm^2$)
	σ	39.37	$[MPa]$	Limit stress of fin ($\sigma_{max} = 40\,MPa$)
	Q	263.43	$[W]$	Heat transfer rate ($P_J + P_{F_e} = 262.41\,W$)
	L_{act}	200	$[mm]$	Actuator length ($L_e = 200\,mm$)
	W_{act}	168.22	$[mm]$	Actuator width ($W_e = 250\,mm$)
	H_{act}	114.39	$[mm]$	Actuator height ($W_e = 120\,mm$)
Objective	M_{EMA}	6.94	$[kg]$	EMA Mass

Table C.9: System output values (Elevator direct drive).

	Parameter	Value	Unit	Description
Motor	L_m	85.57	$[mm]$	Motor length
	T_{mot}	14.66	$[Nm]$	Nominal motor torque*
	P_J	262.40	$[W]$	Joule losses (at Θ_{wind})
	P_{F_e}	0.01	$[W]$	Iron losses
	R_{cd}	0.23	$[K/W]$	Motor thermal resistance
	M_{mot}	3.62	$[kg]$	Motor mass
Housing	N_{fin}	22	$[-]$	Fins number
	h_{fin}	6.73	$[W/m^2K]$	Heat transfer fin
	h_{int}	7.72	$[W/m^2K]$	Heat transfer interstice
	h_{top}	9.54	$[W/m^2K]$	Heat transfer top surface
	h_{bottom}	4.77	$[W/m^2K]$	Heat transfer bottom surface
	h_{rad}	7.23	$[W/m^2K]$	Equivalent radiation heat transfer
	M_{hous}	2.05	$[kg]$	Housing mass
Bearing	D_b	95.55	$[mm]$	Exterior diameter
	d_b	52.12	$[mm]$	Interior diameter
	L_b	19.11	$[mm]$	Bearing length
	M_b	0.65	$[kg]$	Bearing mass
Screw-nut	D_n	40.77	$[mm]$	Nut Diameter
	d_s	19.23	$[mm]$	Screw diameter
	A_n	60.00	$[mm]$	Nut length
	l_{sn}	131.04	$[mm]$	Screw length
	M_{sn}	0.62	$[kg]$	Screw nut mass
* Motor sized for the maximum actuator load $T_{EMA_{max}}$				

Rudder gear drive

Table C.10: Design variables, constraints and objective (Rudder gear drive).

	Parameter	Value	Unit	Description
Design variables	D_e	59.84	$[mm]$	Motor Diameter
	Π_1	0.62	$[-]$	Dimensionless ratio saturation
	Π_2	0.14	$[-]$	Dimensionless ratio yoke to motor diameter
	k_b	5.81	$[-]$	Bearing oversize coefficient
	k_{sn}	3.38	$[-]$	Screw nut oversize coefficient
	n_{red}	4	$[-]$	Reduction ratio
	L_a	28.83	$[mm]$	Fins width
	S	5.82	$[mm]$	Distance between two fins
	s_a	2.02	$[mm]$	Fin thickness
	k_L	1.98	$[-]$	Housing length oversize coefficient
	k_H	1.25	$[-]$	Housing width oversize coefficient
	k_W	1.08	$[-]$	Housing height oversize coefficient
Constraints	Θ_{wind}	157	$[^\circ C]$	Winding temperature ($\Theta_{wind_{lim}} = 185\,^\circ C$)
	$\omega_{mot_{max}}$	137.18	$[rad/s]$	Maximum motor speed ($\omega_{max} = 942\,rad/s$)
	$C_{d_{sn}}$	63.03	$[kN]$	Screw dynamic load ($C_{d_{sn_{req}}} = 9.76\,kN$)
	$C_{0_{sn}}$	107.81	$[kN]$	Screw static load ($F_{shock} = 107.40\,kN$)
	C_{d_b}	112.75	$[kN]$	Bearing dynamic load ($C_{d_{b_{req}}} = 9.34\,kN$)
	C_{0_b}	107.40	$[kN]$	Bearing static load ($F_{shock} = 107.40\,kN$)
	J_{ref}	15.05	$[kgm^2]$	Reflected Inertia ($J_{ref_{max}} = 30\,kgm^2$)
	σ	38.77	$[MPa]$	Limit stress of fin ($\sigma_{max} = 40\,MPa$)
	Q	194.23	$[W]$	Heat transfer rate ($P_J + P_{F_e} = 223.34\,W$)
	L_{act}	144.87	$[mm]$	Actuator length ($L_e = 200\,mm$)
	W_{act}	246.98	$[mm]$	Actuator width ($W_e = 250\,mm$)
	H_{act}	110.39	$[mm]$	Actuator height ($W_e = 120\,mm$)
Objective	M_{EMA}	5.02	$[kg]$	EMA Mass

Table C.11: System output values (Rudder gear drive).

	Parameter	Value	Unit	Description
Motor	L_m	101.24	$[mm]$	Motor length
	T_{mot}	5.41	$[Nm]$	Nominal motor torque*
	P_J	223.33	$[W]$	Joule losses (at Θ_{wind})
	P_{F_e}	0.01	$[W]$	Iron losses
	R_{cd}	0.25	$[K/W]$	Motor thermal resistance
	M_{mot}	1.46	$[kg]$	Motor mass
Housing	N_{fin}	27	$[-]$	Fins number
	h_{fin}	7.5	$[W/m^2K]$	Heat transfer fin
	h_{int}	8.59	$[W/m^2K]$	Heat transfer interstice
	h_{top}	10.39	$[W/m^2K]$	Heat transfer top surface
	h_{bottom}	5.2	$[W/m^2K]$	Heat transfer bottom surface
	h_{rad}	7.23	$[W/m^2K]$	Equivalent radiation heat transfer
	M_{hous}	1.05	$[kg]$	Housing mass
Bearing	D_b	122.57	$[mm]$	Exterior diameter
	d_b	66.86	$[mm]$	Interior diameter
	L_b	24.51	$[mm]$	Bearing length
	M_b	0.83	$[kg]$	Bearing mass
Screw-nut	D_n	52.90	$[mm]$	Nut Diameter
	d_s	24.95	$[mm]$	Screw diameter
	A_n	77.85	$[mm]$	Nut length
	l_{sn}	144.87	$[mm]$	Screw length
	M_{sn}	0.83	$[kg]$	Screw nut mass
Gearbox	d_g	108.95	$[mm]$	Gear diameter
	d_p	27.41	$[mm]$	Pinion diameter
	d_i	51.40	$[mm]$	Idler diameter
	M_{red}	0.65	$[kg]$	Gearbox mass
* Motor sized for the maximum actuator load $T_{EMA_{max}}$				

Rudder direct drive

Table C.12: Design variables, constraints and objective (Rudder direct drive).

	Parameter	Value	Unit	Description
Design variables	D_e	113.40	$[mm]$	Motor Diameter
	Π_1	0.76	$[-]$	Dimensionless ratio saturation
	Π_2	0.13	$[-]$	Dimensionless ratio yoke to motor diameter
	k_b	3.57	$[-]$	Bearing oversize coefficient
	k_{sn}	2.05	$[-]$	Screw nut oversize coefficient
	L_a	29.89	$[mm]$	Fins width
	S	6.74	$[mm]$	Distance between two fins
	s_a	2.26	$[mm]$	Fin thickness
	k_L	1.66	$[-]$	Housing length oversize coefficient
	k_H	1.05	$[-]$	Housing width oversize coefficient
	k_W	1.04	$[-]$	Housing height oversize coefficient
Constraints	Θ_{wind}	160.78	$[°C]$	Winding temperature ($\Theta_{wind_{lim}} = 185\,°C$)
	$\omega_{mot_{max}}$	32.18	$[rad/s]$	Maximum motor speed ($\omega_{max} = 942\,rad/s$)
	$C_{d_{sn}}$	40.18	$[kN]$	Screw dynamic load ($C_{d_{sn_{req}}} = 9.76\,kN$)
	$C_{0_{sn}}$	65.37	$[kN]$	Screw static load ($F_{shock} = 64.79\,kN$)
	C_{d_b}	71.88	$[kN]$	Bearing dynamic load ($C_{d_{b_{req}}} = 9.34\,kN$)
	C_{0_b}	64.96	$[kN]$	Bearing static load ($F_{shock} = 64.79\,kN$)
	J_{ref}	7.47	$[kgm^2]$	Reflected Inertia ($J_{ref_{max}} = 30\,kgm^2$)
	σ	39.34	$[MPa]$	Limit stress of fin ($\sigma_{max} = 40\,MPa$)
	Q	314.82	$[W]$	Heat transfer rate ($P_J + P_{F_e} = 314.03\,W$)
	L_{act}	200	$[mm]$	Actuator length ($L_e = 200\,mm$)
	W_{act}	178.42	$[mm]$	Actuator width ($W_e = 250\,mm$)
	H_{act}	118.85	$[mm]$	Actuator height ($W_e = 120\,mm$)
Objective	M_{EMA}	8.89	$[kg]$	EMA Mass

Table C.13: System output values (Rudder direct drive).

	Parameter	Value	Unit	Description
Motor	L_m	118.58	$[mm]$	Motor length
	T_{mot}	20.17	$[Nm]$	Nominal motor torque*
	P_J	314.03	$[W]$	Joule losses (at Θ_{wind})
	P_{F_e}	0.01	$[W]$	Iron losses
	R_{cd}	0.18	$[K/W]$	Motor thermal resistance
	M_{mot}	4.93	$[kg]$	Motor mass
Housing	N_{fin}	27	$[-]$	Fins number
	h_{fin}	6.82	$[W/m^2K]$	Heat transfer fin
	h_{int}	7.65	$[W/m^2K]$	Heat transfer interstice
	h_{top}	9.37	$[W/m^2K]$	Heat transfer top surface
	h_{bottom}	4.69	$[W/m^2K]$	Heat transfer bottom surface
	h_{rad}	7.23	$[W/m^2K]$	Equivalent radiation heat transfer
	M_{hous}	2.6	$[kg]$	Housing mass
Bearing	D_b	96.10	$[mm]$	Exterior diameter
	d_b	52.42	$[mm]$	Interior diameter
	L_b	19.22	$[mm]$	Bearing length
	M_b	0.66	$[kg]$	Bearing mass
Screw-nut	D_n	41.19	$[mm]$	Nut Diameter
	d_s	19.43	$[mm]$	Screw diameter
	A_n	60.62	$[mm]$	Nut length
	l_{sn}	161.80	$[mm]$	Screw length
	M_{sn}	0.80	$[kg]$	Screw nut mass
* Motor sized for the maximum actuator load $T_{EMA_{max}}$				

Appendix D

Dynamic Preliminary Design Case Studies

Case Study 1: Finned thermal housing

Formulation of the optimisation problem

$$
\begin{aligned}
\text{Minimize} \quad & M_{EMA} \\
\text{with respect to} \quad & k_{d_{opt}}, D_e, \Pi_2, k_b, k_{sn}, n_{red}, L_a, S, s_a, k_L, k_H, k_W \\
\text{subject to} \quad & \Theta_{wind_{max}} - \Theta_{wind_{lim}} \leq 0 \\
& \Theta_{hous_{max}} - \Theta_{hous_{lim}} \leq 0 \\
& \omega_{mot_{max}} - \omega_{max} \leq 0 \\
& C_{d_{sn_{req}}} - C_{d_{sn}} \leq 0 \\
& F_{shock} - C_{0_{sn}} \leq 0 \\
& F_{shock} - C_{0_b} \leq 0 \\
& C_{d_{b_{req}}} - C_{d_b} \leq 0 \\
& J_{ref} - J_{ref_{max}} \leq 0 \\
& \sigma - \sigma_{max} \leq 0 \\
& L_{EMA} - L_e \leq 0 \\
& W_{EMA} - W_e \leq 0 \\
& H_{EMA} - H_e \leq 0
\end{aligned}
\tag{D.1}
$$

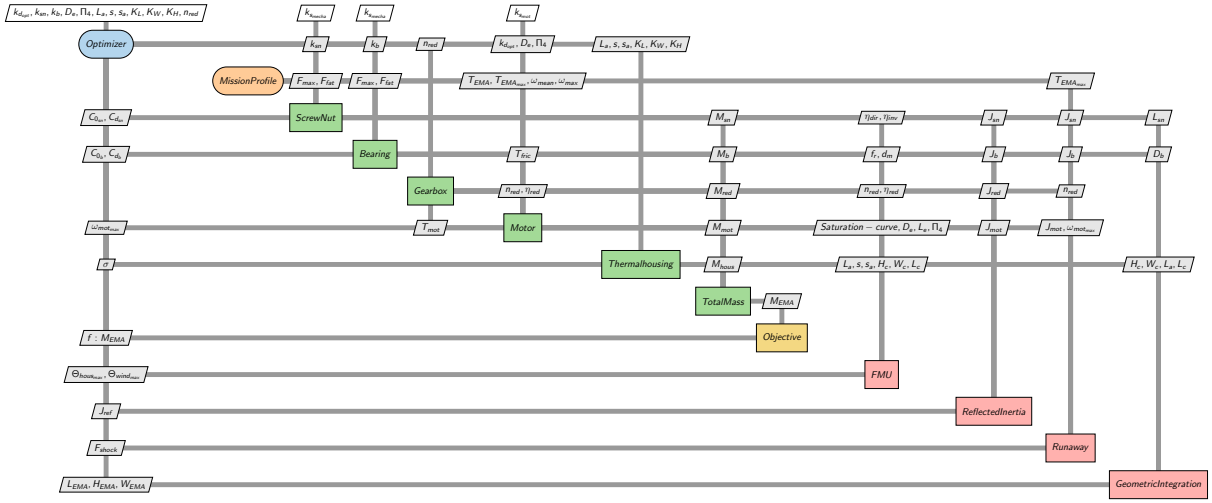

Figure D.1: XDSM of the preliminary designs of case study 1.

Design inputs of TMS

Table D.1: Inputs parameters values (Case study 1).

	Parameter	Value	Unit	Description
Housing	Q_m	30	$[-]$	Mechanical quality coefficient
	a	196.2	$[m/s^2]$	Vibratory sinusoidal acceleration
	ρ_a	2700	$[kg/ms^3]$	Aluminium density
	λ_a	284	$[W/mK]$	Aluminium thermal conductivity
	Cp_a	900	$[J/kgK]$	Aluminium specific heat

Aileron Results

Table D.2: Design variables, constraints and objective (Aileron - Case study 1).

	Parameter	Value	Unit	Description
Design variables	D_e	61.57	$[mm]$	Motor Diameter
	$k_{d_{opt}}$	1.25	$[-]$	Torque oversize coefficient
	Π_2	0.16	$[-]$	Dimensionless ratio yoke to motor diameter
	k_b	4	$[-]$	Bearing oversize coefficient
	k_{sn}	2.65	$[-]$	Screw nut oversize coefficient
	n_{red}	4	$[-]$	Reduction ratio
	L_a	21.73	$[mm]$	Fins width
	S	7.95	$[mm]$	Distance between two fins
	s_a	1.21	$[mm]$	Fin thickness
	k_L	2	$[-]$	Housing length oversize coefficient
	k_H	1.24	$[-]$	Housing height oversize coefficient
	k_W	1.25	$[-]$	Housing width oversize coefficient
Constraints	$\Theta_{wind_{max}}$	150	$[^\circ C]$	Winding temperature ($\Theta_{wind_{lim}} = 185\,^\circ C$)
	$\Theta_{hous_{max}}$	100	$[^\circ C]$	Winding temperature ($\Theta_{hous_{lim}} = 100\,^\circ C$)
	$\omega_{mot_{max}}$	176	$[rad/s]$	Maximum motor speed ($\omega_{max} = 942\,rad/s$)
	$C_{d_{sn}}$	68.02	$[kN]$	Screw dynamic load ($C_{d_{sn_{req}}} = 67.81\,kN$)
	$C_{0_{sn}}$	117.33	$[kN]$	Screw static load ($F_{shock} = 102.87\,kN$)
	C_{d_b}	102.9	$[kN]$	Bearing dynamic load ($C_{d_{b_{req}}} = 64.86\,kN$)
	C_{0_b}	102.9	$[kN]$	Bearing static load ($F_{shock} = 102.87\,kN$)
	J_{ref}	15.42	$[kgm^2]$	Reflected Inertia ($J_{ref_{max}} = 30\,kgm^2$)
	σ	38.39	$[MPa]$	Limit stress of fin ($\sigma_{max} = 40\,MPa$)
	L_{act}	200	$[mm]$	Actuator length ($L_e = 200\,mm$)
	W_{act}	241	$[mm]$	Actuator width ($W_e = 250\,mm$)
	H_{act}	120	$[mm]$	Actuator height ($W_e = 120\,mm$)
Objective	M_{EMA}	6.87	$[kg]$	EMA Mass

Table D.3: System output values (Aileron - Case study 1).

	Parameter	Value	Unit	Description
Motor	L_m	99.76	$[mm]$	Motor length
	T_{mot}	5.44	$[Nm]$	Nominal motor torque
	P_J	Fig. D.4a	$[W]$	Joule losses
	P_{F_e}	Fig. D.4b	$[W]$	Iron losses
	R_{cd}	0.25	$[K/W]$	Motor thermal resistance
	C_{Cu}	71.84	$[J/K]$	Copper thermal capacity
	C_{Fe}	477.88	$[J/K]$	Iron thermal capacity
	M_{mot}	1.26	$[kg]$	Motor mass
Fin Housing	N_{fin}	23	$[-]$	Fins number
	h_{hous}	Fig. D.3	$[W/m^2K]$	Heat transfer coefficients of finned housing
	C_{th}	1506	$[J/k]$	Housing thermal capacity
	M_{fin}	0.12	$[kg]$	Fins mass
	M_{body}	1.55	$[kg]$	Housing body mass
	M_{hous}	1.67	$[kg]$	Housing mass
Bearing	D_b	119.98	$[mm]$	Exterior diameter
	d_b	65.44	$[mm]$	Interior diameter
	L_b	23.99	$[mm]$	Bearing length
	M_b	1.28	$[kg]$	Bearing mass
Screw-nut	D_n	55.18	$[mm]$	Nut Diameter
	d_s	26.03	$[mm]$	Screw diameter
	A_n	81.21	$[mm]$	Nut length
	l_{sn}	152.56	$[mm]$	Screw length
	M_{sn}	1.44	$[kg]$	Screw nut mass
Gearbox	d_g	102.57	$[mm]$	Gear diameter
	d_p	25.64	$[mm]$	Pinion diameter
	d_i	48.39	$[mm]$	Idler diameter
	M_{red}	0.9	$[kg]$	Gearbox mass

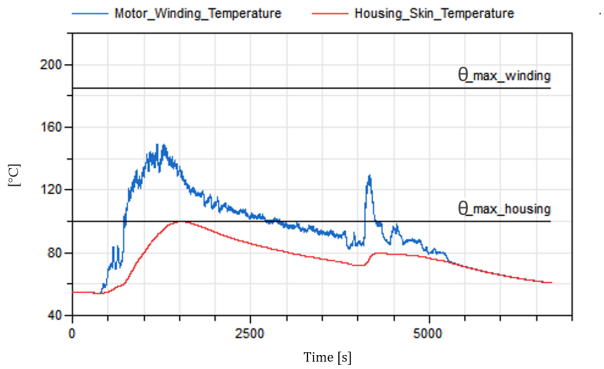

Figure D.2: Thermal profiles (Aileron - Case study 1).

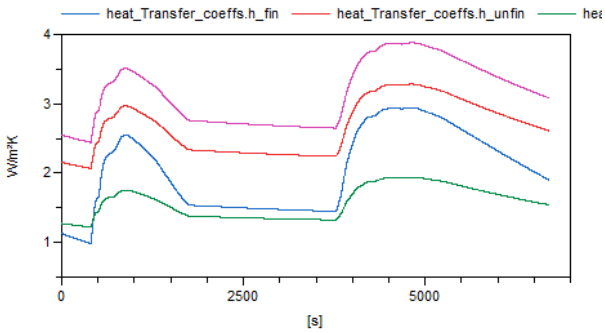

Figure D.3: Heat transfer coefficients of finned thermal housing (Aileron - Case study 1).

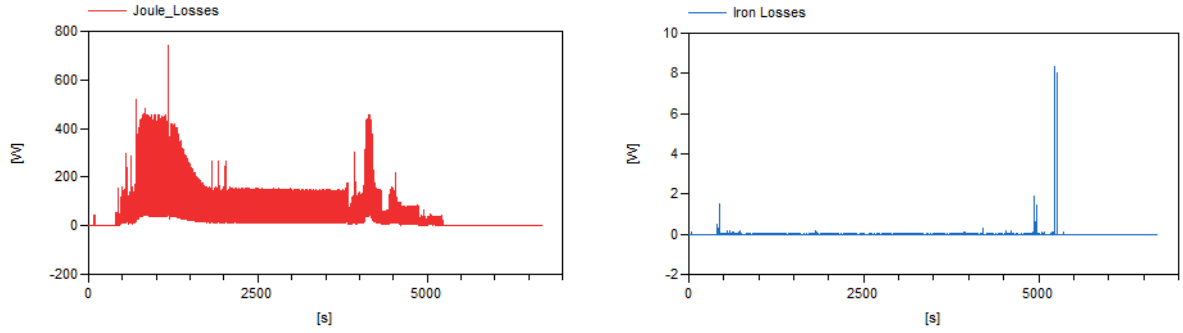

(a) Joule losses (b) Iron losses

Figure D.4: Motor Losses (Aileron - Case study 1).

Elevator Results

Table D.4: Design variables, constraints and objective (Elevator - Case study 2).

	Parameter	Value	Unit	Description
Design variables	D_e	40.25	$[mm]$	Motor Diameter
	$k_{d_{opt}}$	2.68	$[-]$	Torque oversize coefficient
	Π_2	0.13	$[-]$	Dimensionless ratio yoke to motor diameter
	k_b	3.35	$[-]$	Bearing oversize coefficient
	k_{sn}	2.65	$[-]$	Screw nut oversize coefficient
	n_{red}	4	$[-]$	Reduction ratio
	L_a	22.76	$[mm]$	Fins width
	S	11.10	$[mm]$	Distance between two fins
	s_a	1.35	$[mm]$	Fin thickness
	k_L	1	$[-]$	Housing length oversize coefficient
	k_H	1.12	$[-]$	Housing height oversize coefficient
	k_W	1.12	$[-]$	Housing width oversize coefficient
Constraints	$\Theta_{wind_{max}}$	180	$[^\circ C]$	Winding temperature ($\Theta_{wind_{lim}} = 185\,^\circ C$)
	$\Theta_{hous_{max}}$	97.31	$[^\circ C]$	Winding temperature ($\Theta_{hous_{lim}} = 100\,^\circ C$)
	$\omega_{mot_{max}}$	163.68	$[rad/s]$	Maximum motor speed ($\omega_{max} = 942\,rad/s$)
	$C_{d_{sn}}$	28.68	$[kN]$	Screw dynamic load ($C_{d_{sn_{req}}} = 10.84\,kN$)
	$C_{0_{sn}}$	44.87	$[kN]$	Screw static load ($F_{shock} = 44.9\,kN$)
	C_{d_b}	11.27	$[kN]$	Bearing dynamic load ($C_{d_{b_{req}}} = 10.52\,kN$)
	C_{0_b}	50.30	$[kN]$	Bearing static load ($F_{shock} = 44.9\,kN$)
	J_{ref}	2.05	$[kgm^2]$	Reflected Inertia ($J_{ref_{max}} = 30\,kgm^2$)
	σ	40	$[MPa]$	Limit stress of fin ($\sigma_{max} = 40\,MPa$)
	L_{act}	103.21	$[mm]$	Actuator length ($L_e = 200\,mm$)
	W_{act}	172	$[mm]$	Actuator width ($W_e = 250\,mm$)
	H_{act}	79.23	$[mm]$	Actuator height ($W_e = 120\,mm$)
Objective	M_{EMA}	1.74	$[kg]$	EMA Mass

Table D.5: System output values (Elevator - Case study 1).

	Parameter	Value	Unit	Description
Motor	L_m	76.14	$[mm]$	Motor length
	T_{mot}	1.92	$[Nm]$	Nominal motor torque
	P_J	Fig. D.7a	$[W]$	Joule losses
	P_{Fe}	Fig. D.7b	$[W]$	Iron losses
	R_{cd}	0.39	$[K/W]$	Motor thermal resistance
	C_{Cu}	25.19	$[J/K]$	Copper thermal capacity
	C_{Fe}	147.79	$[J/K]$	Iron thermal capacity
	M_{mot}	0.5	$[kg]$	Motor mass
Fin Housing	N_{fin}	7	$[-]$	Fins number
	h_{hous}	Fig. D.6	$[W/m^2K]$	Heat transfer coefficients of finned housing
	C_{th}	181.32	$[J/k]$	Housing thermal capacity
	M_{fin}	0.03	$[kg]$	Fins mass
	M_{body}	0.17	$[kg]$	Housing body mass
	M_{hous}	0.2	$[kg]$	Housing mass
Bearing	D_b	79.23	$[mm]$	Exterior diameter
	d_b	61.22	$[mm]$	Interior diameter
	L_b	15.85	$[mm]$	Bearing length
	M_b	0.37	$[kg]$	Bearing mass
Screw-nut	D_n	34.15	$[mm]$	Nut Diameter
	d_s	16.11	$[mm]$	Screw diameter
	A_n	50.26	$[mm]$	Nut length
	l_{sn}	103.21	$[mm]$	Screw length
	M_{sn}	0.33	$[kg]$	Screw nut mass
Gearbox	d_g	75.22	$[mm]$	Gear diameter
	d_p	35.48	$[mm]$	Pinion diameter
	d_i	18.80	$[mm]$	Idler diameter
	M_{red}	0.33	$[kg]$	Gearbox mass

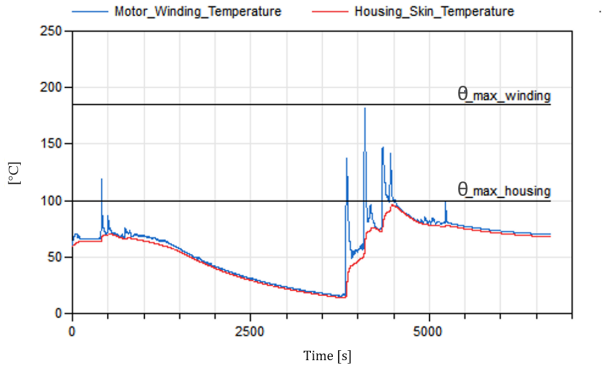

Figure D.5: Thermal profiles (Elevator - Case study 1).

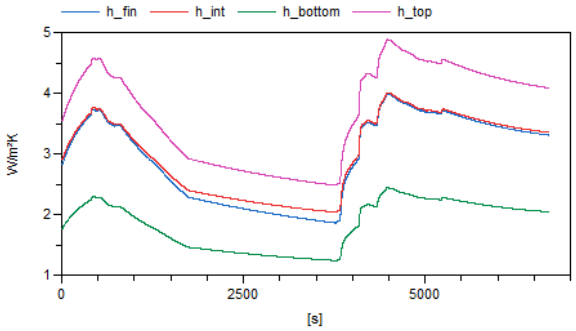

Figure D.6: Heat transfer coefficients of finned thermal housing (Elevator - Case study 1).

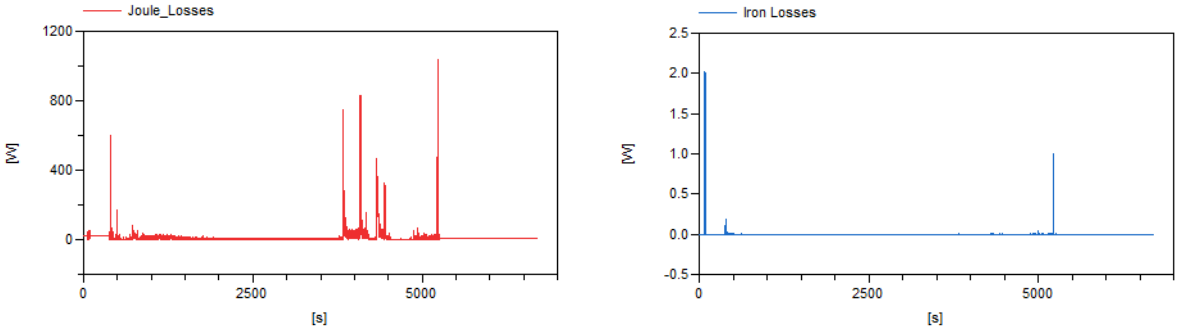

(a) Joule losses (b) Iron losses

Figure D.7: Motor Losses (Elevator - Case study 1).

Rudder Results

Table D.6: Design variables, constraints and objective (Rudder - Case study 1).

	Parameter	Value	Unit	Description
Design variables	D_e	38.77	$[mm]$	Motor Diameter
	$k_{d_{opt}}$	10.2	$[-]$	Torque oversize coefficient
	Π_2	0.11	$[-]$	Dimensionless ratio yoke to motor diameter
	k_b	2.46	$[-]$	Bearing oversize coefficient
	k_{sn}	1.42	$[-]$	Screw nut oversize coefficient
	n_{red}	4	$[-]$	Reduction ratio
	L_a	5	$[mm]$	Fins width
	S	12.5	$[mm]$	Distance between two fins
	s_a	1	$[mm]$	Fin thickness
	k_L	1	$[-]$	Housing length oversize coefficient
	k_H	1.12	$[-]$	Housing height oversize coefficient
	k_W	1.12	$[-]$	Housing width oversize coefficient
Constraints	$\Theta_{wind_{max}}$	180	$[^\circ C]$	Winding temperature ($\Theta_{wind_{lim}} = 185\,^\circ C$)
	$\Theta_{hous_{max}}$	73	$[^\circ C]$	Winding temperature ($\Theta_{hous_{lim}} = 100\,^\circ C$)
	$\omega_{mot_{max}}$	137.18	$[rad/s]$	Maximum motor speed ($\omega_{max} = 942\,rad/s$)
	$C_{d_{sn}}$	28.92	$[kN]$	Screw dynamic load ($C_{d_{sn_{req}}} = 9.76\,kN$)
	$C_{0_{sn}}$	45.37	$[kN]$	Screw static load ($F_{shock} = 45.34\,kN$)
	C_{d_b}	51.03	$[kN]$	Bearing dynamic load ($C_{d_{b_{req}}} = 9.34\,kN$)
	C_{0_b}	50.30	$[kN]$	Bearing static load ($F_{shock} = 45.34\,kN$)
	J_{ref}	2.30	$[kgm^2]$	Reflected Inertia ($J_{ref_{max}} = 30\,kgm^2$)
	σ	2.3	$[MPa]$	Limit stress of fin ($\sigma_{max} = 40\,MPa$)
	L_{act}	106.43	$[mm]$	Actuator length ($L_e = 200\,mm$)
	W_{act}	133.85	$[mm]$	Actuator width ($W_e = 250\,mm$)
	H_{act}	79.85	$[mm]$	Actuator height ($W_e = 120\,mm$)
Objective	M_{EMA}	1.98	$[kg]$	EMA Mass

Table D.7: System output values (Elevator - Case study 1).

	Parameter	Value	Unit	Description
Motor	L_m	102.02	$[mm]$	Motor length
	T_{mot}	2.43	$[Nm]$	Nominal motor torque
	P_J	Fig. D.10a	$[W]$	Joule losses
	P_{Fe}	Fig. D.10b	$[W]$	Iron losses
	R_{cd}	0.29	$[K/W]$	Motor thermal resistance
	C_{Cu}	31.99	$[J/K]$	Copper thermal capacity
	C_{Fe}	180.68	$[J/K]$	Iron thermal capacity
	M_{mot}	0.62	$[kg]$	Motor mass
Fin Housing	N_{fin}	8	$[-]$	Fins number
	h_{hous}	Fig. D.9	$[W/m^2K]$	Heat transfer coefficients of finned housing
	C_{th}	197.37	$[J/k]$	Housing thermal capacity
	M_{fin}	0.005	$[kg]$	Fins mass
	M_{body}	0.21	$[kg]$	Housing body mass
	M_{hous}	0.21	$[kg]$	Housing mass
Bearing	D_b	79.85	$[mm]$	Exterior diameter
	d_b	43.55	$[mm]$	Interior diameter
	L_b	15.97	$[mm]$	Bearing length
	M_b	0.38	$[kg]$	Bearing mass
Screw-nut	D_n	34.31	$[mm]$	Nut Diameter
	d_s	16.19	$[mm]$	Screw diameter
	A_n	50.50	$[mm]$	Nut length
	l_{sn}	106.43	$[mm]$	Screw length
	M_{sn}	0.36	$[kg]$	Screw nut mass
Gearbox	d_g	58.45	$[mm]$	Gear diameter
	d_p	14.61	$[mm]$	Pinion diameter
	d_i	27.57	$[mm]$	Idler diameter
	M_{red}	0.4	$[kg]$	Gearbox mass

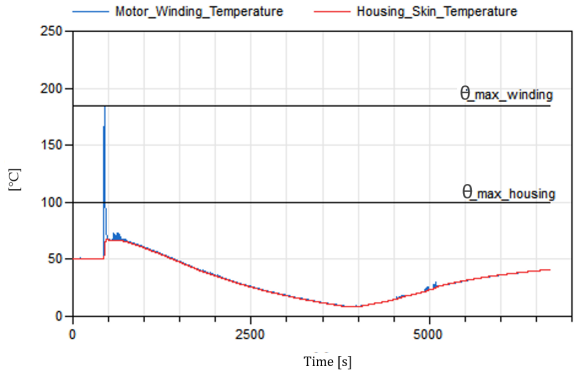

Figure D.8: Thermal profiles (Rudder - Case study 1).

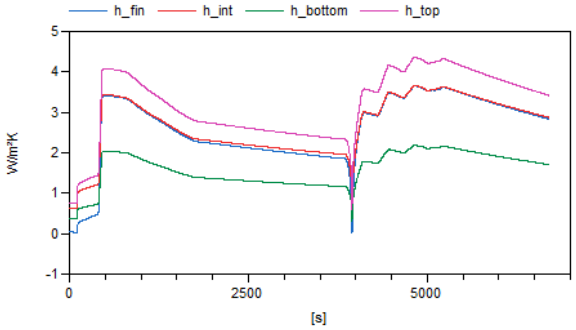

Figure D.9: Heat transfer coefficients of finned thermal housing (Rudder - Case study 1).

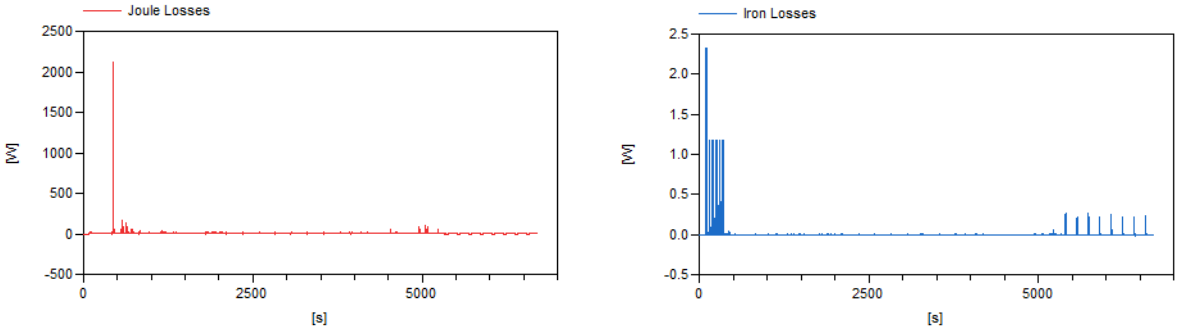

(a) Joule losses (b) Iron losses

Figure D.10: Motor Losses (Rudder - Case study 1).

Case Study 2: Heat pipes

Formulation of the optimisation problem

$$
\begin{aligned}
\text{Minimize} \quad & M_{EMA} \\
\text{with respect to} \quad & k_{d_{opt}}, D_e, \Pi_2, k_b, k_{sn}, n_{red}, n_{HP}, l_c, d_{HP}, w_s, l_s, k_{bt_e}, k_{bt_c}, \Pi_{4_{T_e}}, \Pi_{4_{T_c}} \\
\text{subject to} \quad & \Theta_{wind_{max}} - \Theta_{wind_{lim}} \leq 0 \\
& \Theta_{hous_{max}} - \Theta_{hous_{lim}} \leq 0 \\
& \omega_{mot_{max}} - \omega_{max} \leq 0 \\
& C_{d_{sn_{req}}} - C_{d_{sn}} \leq 0 \\
& F_{shock} - C_{0_{sn}} \leq 0 \\
& F_{shock} - C_{0_b} \leq 0 \\
& C_{d_{b_{req}}} - C_{d_b} \leq 0 \\
& J_{ref} - J_{ref_{max}} \leq 0 \\
& d_{HP} - d_{HP_{req}} \leq 0 \\
& \Phi_c - \Phi_{e_{max}} \leq 0 \\
& \Phi_e - \Phi_{c_{max}} \leq 0 \\
& L_{EMA} - L_e \leq 0 \\
& W_{EMA} - W_e \leq 0 \\
& H_{EMA} - H_e \leq 0
\end{aligned}
\tag{D.2}
$$

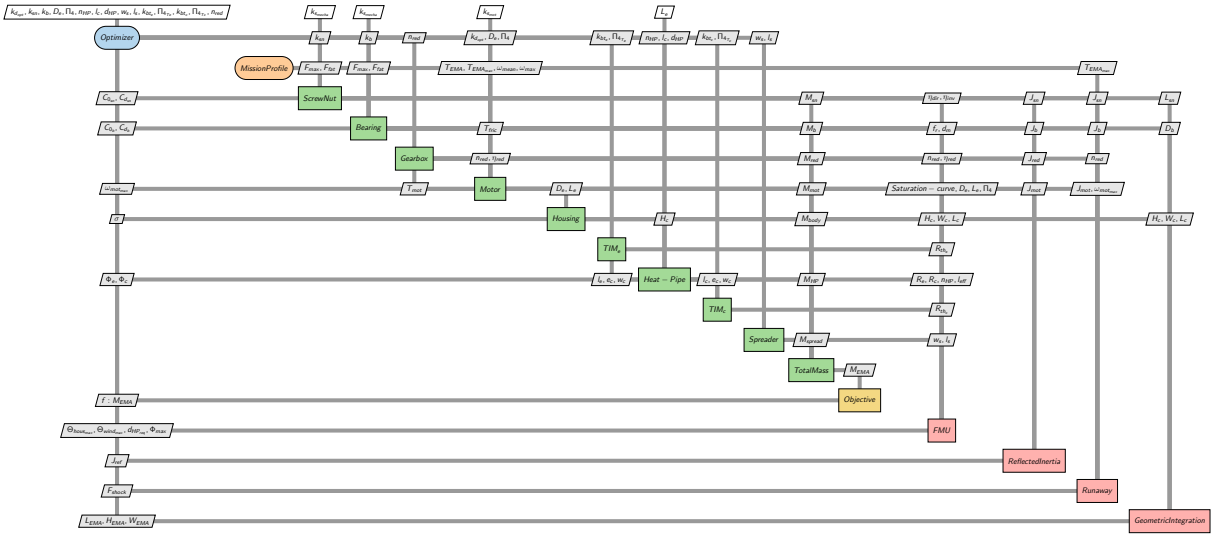

Figure D.11: XDSM of the preliminary designs of case study 2.

Design inputs of TMS

Table D.8: Inputs parameters values (Case study 2).

	Parameter	Value	Unit	Description
Heat Pipe	w_c	30	$[mm]$	Condenser/Evaporator plate length
	e_c	1.5	$[mm]$	Condenser/Evaporator plate thickness
	Λ_e	7000	$[W/m^2K]$	Evaporator conductance
	Λ_c	5000	$[W/m^2K]$	Condenser conductance
Spread	t	2	$[mm]$	Spreader thickness
	λ_a	238	$[W/mK]$	Aluminium conductivity
TIM	e_{TIM}	0.38	$[mm]$	TIM thickness
	r_{TIM}	$1.48 \cdot 10^{-4}$	$[Km^2/W]$	Surface thermal resistivity

Aileron Results

Table D.9: Design variables, constraints and objective (Aileron - Case study 2).

	Parameter	Value	Unit	Description
Design variables	D_e	51.66	$[mm]$	Motor Diameter
	$k_{d_{opt}}$	1.15	$[-]$	Torque oversize coefficient
	Π_2	0.13	$[-]$	Dimensionless ratio yoke to motor diameter
	k_b	3.24	$[-]$	Bearing oversize coefficient
	k_{sn}	2.64	$[-]$	Screw nut oversize coefficient
	n_{red}	4	$[-]$	Reduction ratio
	n_{HP}	2	$[-]$	Heat pipes number
	d_{HP}	10.49	$[mm]$	Heat pipe diameter
	l_c	151.49	$[mm]$	Condenser length
	w_s	212	$[mm]$	Spreader width
	l_s	182.66	$[mm]$	Spreader length
	k_{bt_e}	2	$[-]$	Bolts number (evaporator side)
	k_{bt_c}	3	$[-]$	Bolts number (evaporator side)
	$\Pi_{4_{T_e}}$	0.26	$[-]$	Dimensionless ratio bolt position (evaporator side)
	$\Pi_{4_{T_c}}$	0.31	$[-]$	Dimensionless ratio bolt position (condenser side)
Constraints	$\Theta_{wind_{max}}$	185	$[°C]$	Winding temperature ($\Theta_{wind_{lim}} = 185\,°C$)
	$\Theta_{hous_{max}}$	98.73	$[°C]$	Winding temperature ($\Theta_{hous_{lim}} = 100\,°C$)
	$\omega_{mot_{max}}$	176	$[rad/s]$	Maximum motor speed ($\omega_{max} = 942\,rad/s$)
	$C_{d_{sn}}$	67.83	$[kN]$	Screw dynamic load ($C_{d_{sn_{req}}} = 67.81\,kN$)
	$C_{0_{sn}}$	116.96	$[kN]$	Screw static load ($F_{shock} = 83.34\,kN$)
	C_{d_b}	89.29	$[kN]$	Bearing dynamic load ($C_{d_{b_{req}}} = 64.86\,kN$)
	C_{0_b}	83.46	$[kN]$	Bearing static load ($F_{shock} = 83.34\,kN$)
	J_{ref}	9.41	$[kgm^2]$	Reflected Inertia ($J_{ref_{max}} = 30\,kgm^2$)
	d_{HP}	10.49	$[mm]$	Minimum required diameter ($d_{HP_{req}} = 10.37\,mm$)
	Φ_e	6.06	$[W/cm^2]$	Maximum evaporator heat flux ($\Phi_{e_{max}} = 7\,W/cm^2$)
	Φ_c	5	$[W/cm^2]$	Maximum evaporator heat flux ($\Phi_{c_{max}} = 5\,W/cm^2$)
	L_{act}	147.58	$[mm]$	Actuator length ($L_e = 200\,mm$)
	W_{act}	164.71	$[mm]$	Actuator width ($W_e = 250\,mm$)
	H_{act}	108.05	$[mm]$	Actuator height ($W_e = 120\,mm$)
Objective	M_{EMA}	5.42	$[kg]$	EMA Mass

Table D.10: System output values (Aileron - Case study 2).

	Parameter	Value	Unit	Description
Motor	L_m	124.39	$[mm]$	Motor length
	T_{mot}	5	$[Nm]$	Nominal motor torque
	P_J	Fig. D.13a	$[W]$	Joule losses
	P_{F_e}	Fig. D.13b	$[W]$	Iron losses
	R_{cd}	0.22	$[K/W]$	Motor thermal resistance
	C_{Cu}	66.92	$[J/K]$	Copper thermal capacity
	C_{Fe}	398	$[J/K]$	Iron thermal capacity
	M_{mot}	1.35	$[kg]$	Motor mass
Heat pipe Unit	l_e	124.39	$[mm]$	Evaporator length
	l_a	96.67	$[mm]$	Adiabatic length
	R_e	0.05	$[K/W]$	Evaporator resistance
	R_c	0.06	$[K/W]$	Condenser resistance
	M_{HP}	0.1	$[kg]$	HP mass
Spreader	R_{spread}	Fig. D.14c	$[K/W]$	Spreader resistance
	h_{eff}	Fig. D.14b	$[W/m^2K]$	Convective heat transfer coefficient
	M_{spread}	0.31	$[kg]$	Spreader mass
TIM	R_{th_c}	0.032	$[K/W]$	Contact resistance condenser side
	R_{th_e}	0.039	$[K/W]$	Contact resistance evaporator side
Housing	L_c	124.39	$[mm]$	Housing length
	W_c	56.66	$[mm]$	Housing width
	H_c	56.66	$[mm]$	Housing height
	M_{body}	0.35	$[kg]$	Housing Mass
	C_{th}	206.84	$[J/K]$	Housing thermal capacity
Bearing	D_b	108.05	$[mm]$	Exterior diameter
	d_b	58.94	$[mm]$	Interior diameter
	L_b	21.61	$[mm]$	Bearing length
	M_b	0.94	$[kg]$	Bearing mass
Screw-nut	D_n	55.10	$[mm]$	Nut Diameter
	d_s	25.99	$[mm]$	Screw diameter
	A_n	81.09	$[mm]$	Nut length
	l_{sn}	147.58	$[mm]$	Screw length
	M_{sn}	1.43	$[kg]$	Screw nut mass

continued on next page

– continued from previous page

	Parameter	Value	Unit	Description
Gearbox	d_g	72.94	$[mm]$	Gear diameter
	d_p	18.23	$[mm]$	Pinion diameter
	d_i	72.94	$[mm]$	Idler diameter
	M_{red}	0.83	$[kg]$	Gearbox mass

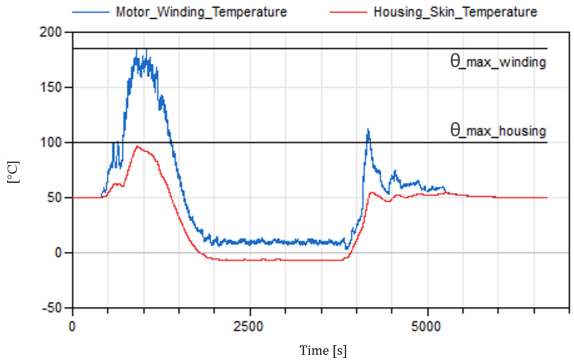

Figure D.12: Thermal profiles (Aileron - Case study 2).

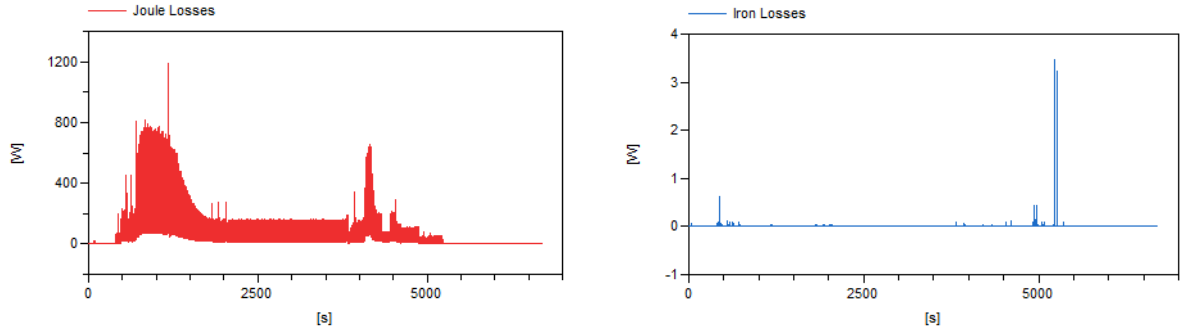

(a) Joule losses (b) Iron losses

Figure D.13: Motor Losses (Aileron - Case study 2).

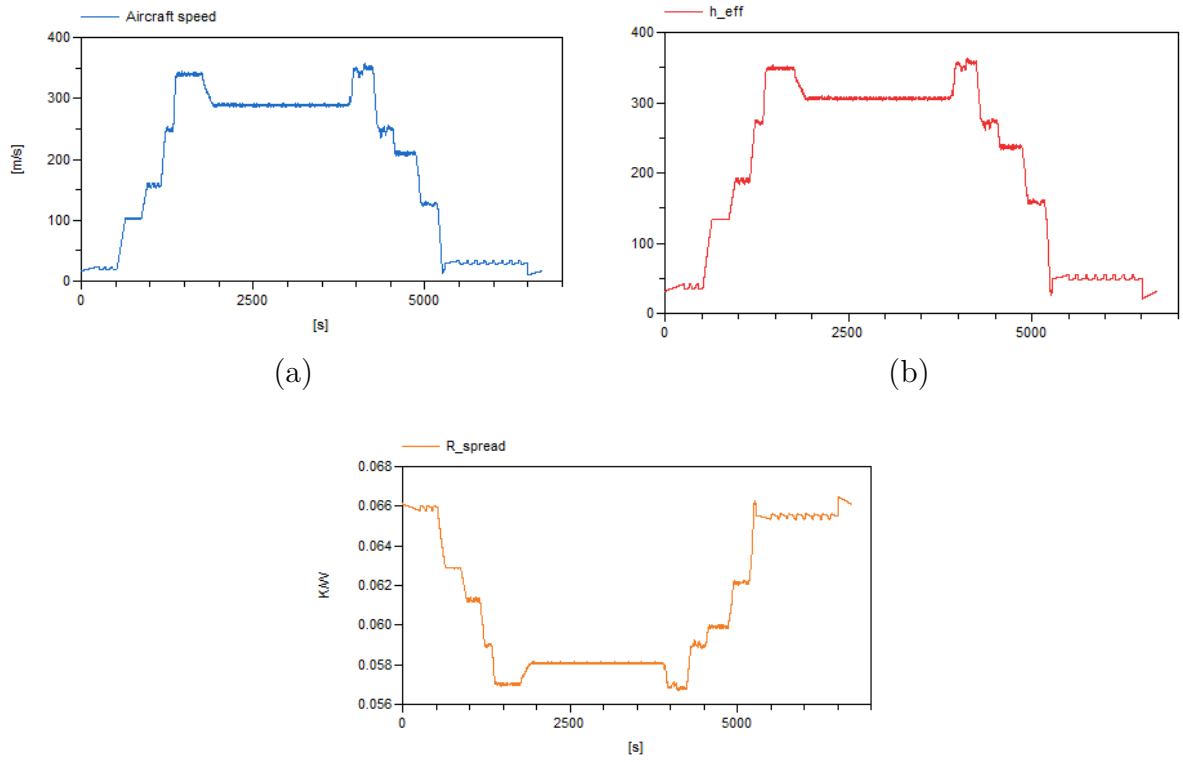

Figure D.14: Aircraft speed profile (TAS) (a), convective heat transfer coefficient on wing (b) and spreader resistance (per TMS unit) (c) (Aileron - Case study 2).

Elevator Results

Table D.11: Design variables, constraints and objective (Elevator - Case study 2).

	Parameter	Value	Unit	Description
Design variables	D_e	36.46	$[mm]$	Motor Diameter
	$k_{d_{opt}}$	3	$[-]$	Torque oversize coefficient
	Π_2	0.13	$[-]$	Dimensionless ratio yoke to motor diameter
	k_b	3.14	$[-]$	Bearing oversize coefficient
	k_{sn}	1.82	$[-]$	Screw nut oversize coefficient
	n_{red}	4	$[-]$	Reduction ratio
	n_{HP}	1	$[-]$	Heat pipes number
	d_{HP}	10.04	$[mm]$	Heat pipe diameter
	l_c	42.41	$[mm]$	Condenser length
	w_s	48.21	$[mm]$	Spreader width
	l_s	50.75	$[mm]$	Spreader length
	k_{bt_e}	2	$[-]$	Bolts number (evaporator side)
	k_{bt_c}	1	$[-]$	Bolts number (evaporator side)
	$\Pi_{4_{T_e}}$	0.34	$[-]$	Dimensionless ratio bolt position (evaporator side)
	$\Pi_{4_{T_c}}$	0.37	$[-]$	Dimensionless ratio bolt position (condenser side)
Constraints	$\Theta_{wind_{max}}$	185	$[°C]$	Winding temperature ($\Theta_{wind_{lim}} = 185\,°C$)
	$\Theta_{hous_{max}}$	92.67	$[°C]$	Winding temperature ($\Theta_{hous_{lim}} = 100\,°C$)
	$\omega_{mot_{max}}$	163.68	$[rad/s]$	Maximum motor speed ($\omega_{max} = 942\,rad/s$)
	$C_{d_{sn}}$	26.93	$[kN]$	Screw dynamic load ($C_{d_{sn_{req}}} = 10.84\,kN$)
	$C_{0_{sn}}$	41.91	$[kN]$	Screw static load ($F_{shock} = 41.88\,kN$)
	C_{d_b}	47.33	$[kN]$	Bearing dynamic load ($C_{d_{b_{req}}} = 11.27\,kN$)
	C_{0_b}	41.88	$[kN]$	Bearing static load ($F_{shock} = 41.88\,kN$)
	J_{ref}	1.68	$[kgm^2]$	Reflected Inertia ($J_{ref_{max}} = 30\,kgm^2$)
	d_{HP}	10.04	$[mm]$	Minimum required diameter ($d_{HP_{req}} = 10.03\,mm$)
	Φ_e	1.41	$[W/cm^2]$	Maximum evaporator heat flux ($\Phi_{e_{max}} = 7\,W/cm^2$)
	Φ_c	3.04	$[W/cm^2]$	Maximum evaporator heat flux ($\Phi_{c_{max}} = 5\,W/cm^2$)
	L_{act}	100.98	$[mm]$	Actuator length ($L_e = 200\,mm$)
	W_{act}	118.13	$[mm]$	Actuator width ($W_e = 250\,mm$)
	H_{act}	76.67	$[mm]$	Actuator height ($W_e = 120\,mm$)
Objective	M_{EMA}	1.69	$[kg]$	EMA Mass

Table D.12: System output values (Elevator - Case study 2).

	Parameter	Value	Unit	Description
Motor	L_m	90.57	$[mm]$	Motor length
	T_{mot}	1.81	$[Nm]$	Nominal motor torque
	P_J	Fig. D.16a	$[W]$	Joule losses
	P_{F_e}	Fig. D.16b	$[W]$	Iron losses
	R_{cd}	0.34	$[K/W]$	Motor thermal resistance
	C_{Cu}	24.39	$[J/K]$	Copper thermal capacity
	C_{Fe}	143.8	$[J/K]$	Iron thermal capacity
	M_{mot}	0.49	$[kg]$	Motor mass
Heat pipe Unit	l_e	90.57	$[mm]$	Evaporator length
	l_a	104.27	$[mm]$	Adiabatic length
	R_e	0.07	$[K/W]$	Evaporator resistance
	R_c	0.21	$[K/W]$	Condenser resistance
	M_{HP}	0.6	$[kg]$	HP mass
Spreader	R_{spread}	Fig. D.17c	$[K/W]$	Spreader resistance
	h_{eff}	Fig. D.17b	$[W/m^2K]$	Convective heat transfer coefficient
	M_{spread}	0.02	$[kg]$	Spreader mass
TIM	R_{th_c}	0.11	$[K/W]$	Contact resistance condenser side
	R_{th_e}	0.054	$[K/W]$	Contact resistance evaporator side
Housing	L_c	90.57	$[mm]$	Housing length
	W_c	41.46	$[mm]$	Housing width
	H_c	41.46	$[mm]$	Housing height
	M_{body}	0.16	$[kg]$	Housing Mass
	C_{th}	148.51	$[J/K]$	Housing thermal capacity
Bearing	D_b	76.67	$[mm]$	Exterior diameter
	d_b	41.82	$[mm]$	Interior diameter
	L_b	15.33	$[mm]$	Bearing length
	M_b	0.36	$[kg]$	Bearing mass
Screw-nut	D_n	32.98	$[mm]$	Nut Diameter
	d_s	15.56	$[mm]$	Screw diameter
	A_n	48.54	$[mm]$	Nut length
	l_{sn}	100.98	$[mm]$	Screw length
	M_{sn}	0.34	$[kg]$	Screw nut mass

continued on next page

– continued from previous page

	Parameter	Value	Unit	Description
Gearbox	d_g	53.34	$[mm]$	Gear diameter
	d_p	13.34	$[mm]$	Pinion diameter
	d_i	25.16	$[mm]$	Idler diameter
	M_{red}	0.33	$[kg]$	Gearbox mass

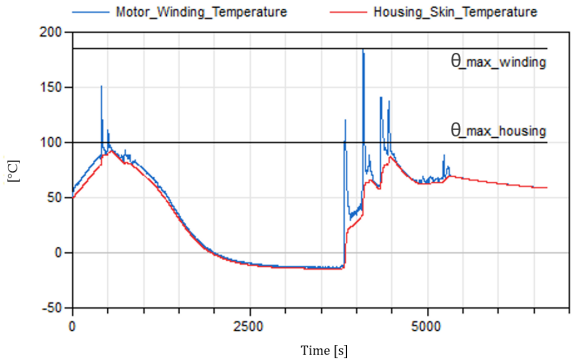

Figure D.15: Thermal profiles (Elevator - Case study 2).

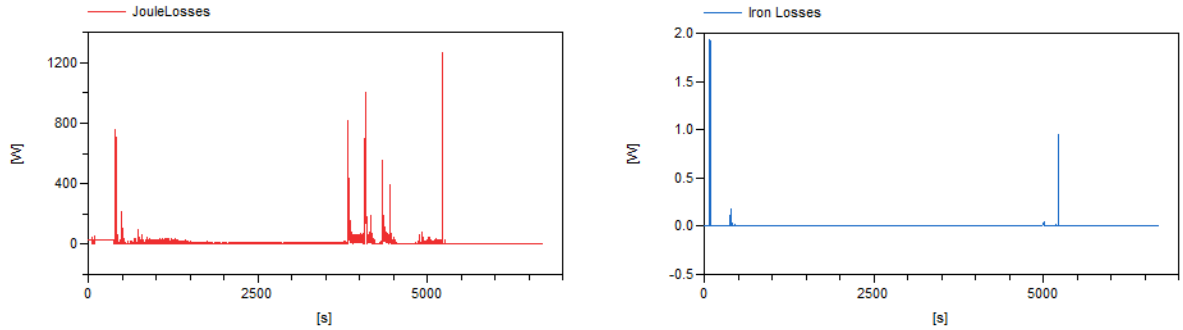

(a) Joule losses (b) Iron losses

Figure D.16: Motor Losses (Elevator - Case study 2).

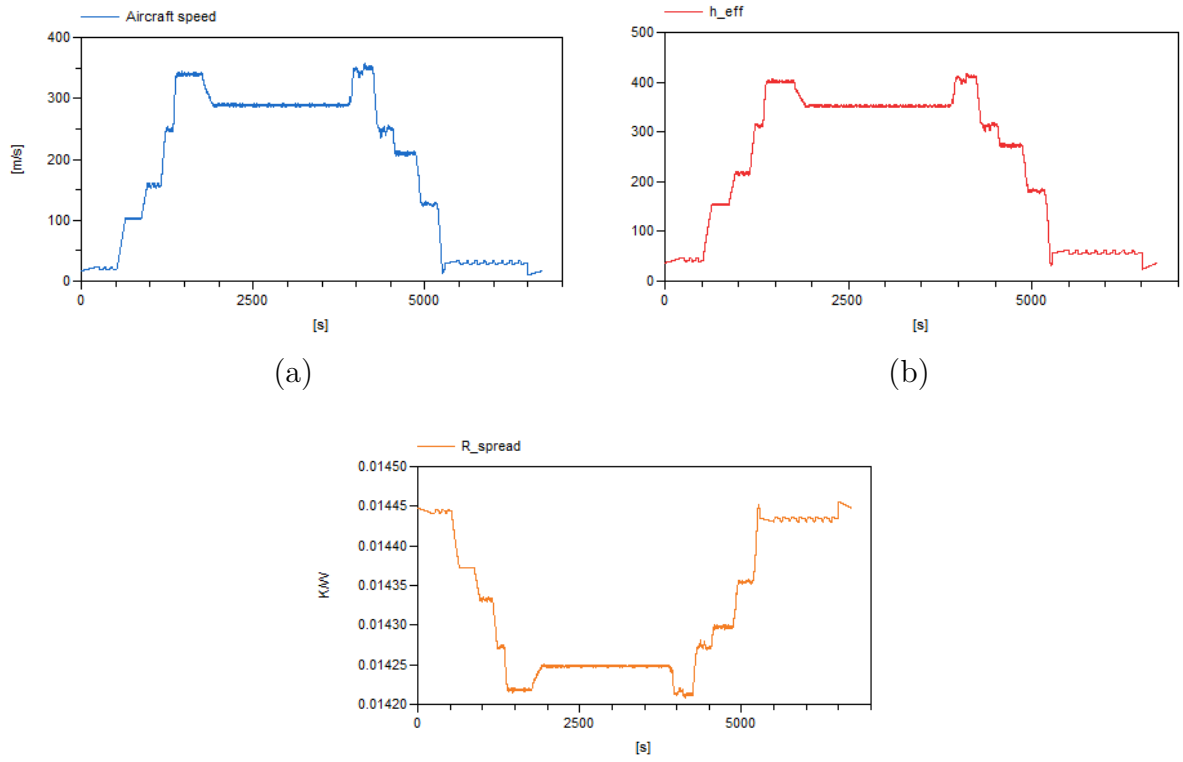

(a) (b)

(c)

Figure D.17: Aircraft speed profile (TAS) (a), convective heat transfer coefficient on wing (b) and spreader resistance (per TMS unit) (c) (Elevator - Case study 2).

Case Study 3: Thermal straps

Formulation of the optimisation problem

$$
\begin{aligned}
\text{Minimize} \quad & M_{EMA} \\
\text{with respect to} \quad & k_{d_{opt}}, D_e, \Pi_2, k_b, k_{sn}, n_{red}, n_{TS}, W_b, w_s, l_s, k_{bt}, \Pi_{4_T} \\
\text{subject to} \quad & \Theta_{wind_{max}} - \Theta_{wind_{lim}} \leq 0 \\
& \Theta_{hous_{max}} - \Theta_{hous_{lim}} \leq 0 \\
& \omega_{mot_{max}} - \omega_{max} \leq 0 \\
& C_{d_{sn_{req}}} - C_{d_{sn}} \leq 0 \\
& F_{shock} - C_{0_{sn}} \leq 0 \\
& F_{shock} - C_{0_b} \leq 0 \\
& C_{d_{b_{req}}} - C_{d_b} \leq 0 \\
& J_{ref} - J_{ref_{max}} \leq 0 \\
& W_b - W_c \leq 0 \\
& L_{EMA} - L_e \leq 0 \\
& W_{EMA} - W_e \leq 0 \\
& H_{EMA} - H_e \leq 0
\end{aligned}
\tag{D.3}
$$

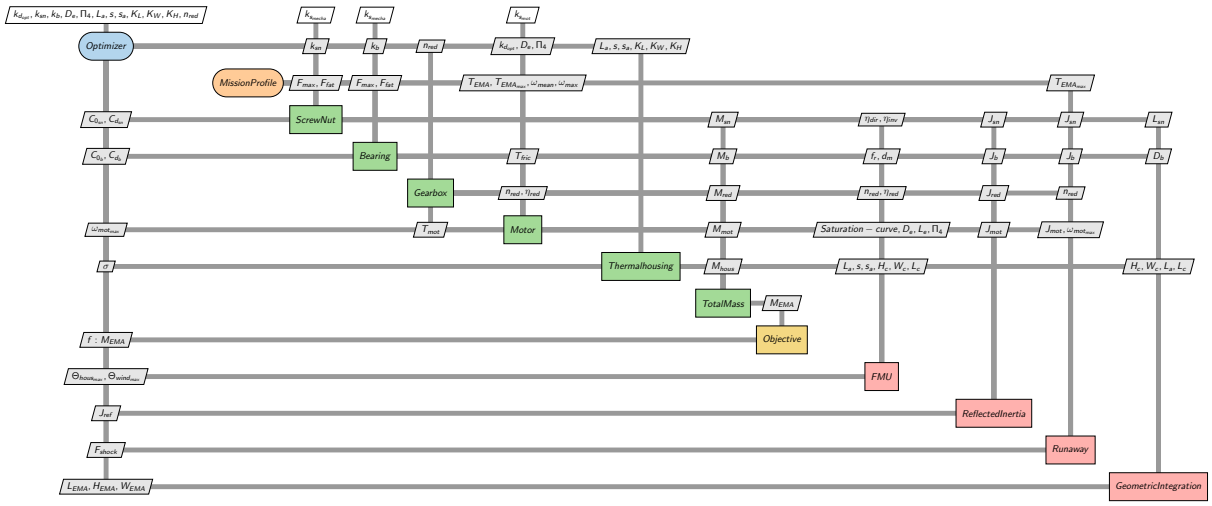

Figure D.18: XDSM of the preliminary designs of case study 3.

Design inputs of thermal strap

Table D.13: Inputs parameters values (Case study 3).

	Parameter	Value	Unit	Description
Thermal straps	$L_{b_{ref}}$	101.6	$[mm]$	Reference strap length
	$W_{b_{ref}}$	50.8	$[mm]$	Reference braid width
	$t_{b_{ref}}$	4.6	$[mm]$	Reference braid thickness
	$w_{p_{ref}}$	15	$[mm]$	Reference plate width
	$e_{p_{ref}}$	6.35	$[mm]$	Reference plate thickness
	$R_{plates_{ref}}$	0.242	$[K/W]$	Reference plates resistance
	$R_{braid_{ref}}$	0.272	$[K/W]$	Reference braid resistance
	$M_{plates_{ref}}$	19.6	$[g]$	Reference plates mass
	$M_{braid_{ref}}$	51.4	$[g]$	Reference braid mass
Spread	t	2	$[mm]$	Spreader thickness
	λ_a	238	$[W/mK]$	Aluminium conductivity
TIM	e_{TIM}	0.38	$[mm]$	TIM thickness
	r_{TIM}	$1.48 \cdot 10^{-4}$	$[Km^2/W]$	Surface thermal resistivity

Aileron Results

Table D.14: Design variables, constraints and objective (Aileron - Case study 3).

	Parameter	Value	Unit	Description
Design variables	D_e	58.11	$[mm]$	Motor Diameter
	$k_{d_{opt}}$	1.15	$[-]$	Torque oversize coefficient
	Π_2	0.13	$[-]$	Dimensionless ratio yoke to motor diameter
	k_b	3.55	$[-]$	Bearing oversize coefficient
	k_{sn}	2.64	$[-]$	Screw nut oversize coefficient
	n_{red}	4	$[-]$	Reduction ratio
	n_{TS}	6	$[-]$	Thermal strap number
	W_b	35.88	$[mm]$	Braid width
	w_s	228.98	$[mm]$	Spreader width
	l_s	142.28	$[mm]$	Spreader length
	k_{bt}	2	$[-]$	Bolts number (per plate)
	Π_{4_T}	0.15	$[-]$	Dimensionless ratio bolt position (per plate)
Constraints	$\Theta_{wind_{max}}$	185	$[°C]$	Winding temperature ($\Theta_{wind_{lim}} = 185\,°C$)
	$\Theta_{hous_{max}}$	98.10	$[°C]$	Winding temperature ($\Theta_{hous_{lim}} = 100\,°C$)
	$\omega_{mot_{max}}$	176	$[rad/s]$	Maximum motor speed ($\omega_{max} = 942\,rad/s$)
	$C_{d_{sn}}$	67.83	$[kN]$	Screw dynamic load ($C_{d_{sn_{req}}} = 67.81\,kN$)
	$C_{0_{sn}}$	116.96	$[kN]$	Screw static load ($F_{shock} = 91.02\,kN$)
	C_{d_b}	96.96	$[kN]$	Bearing dynamic load ($C_{d_{b_{req}}} = 64.86\,kN$)
	C_{0_b}	91.23	$[kN]$	Bearing static load ($F_{shock} = 91.02\,kN$)
	J_{ref}	11.75	$[kgm^2]$	Reflected Inertia ($J_{ref_{max}} = 30\,kgm^2$)
	W_b	35.88	$[mm]$	Braid width ($W_c = 63.11\,mm$)
	L_{act}	148.55	$[mm]$	Actuator length ($L_e = 200\,mm$)
	W_{act}	176.08	$[mm]$	Actuator width ($W_e = 250\,mm$)
	H_{act}	112.97	$[mm]$	Actuator height ($W_e = 120\,mm$)
Objective	M_{EMA}	5.6	$[kg]$	EMA Mass

Table D.15: System output values (Aileron - Case study 3)

	Parameter	Value	Unit	Description
Motor	L_m	97.63	$[mm]$	Motor length
	T_{mot}	5.02	$[Nm]$	Nominal motor torque
	P_J	Fig. D.20a	$[W]$	Joule losses
	P_{Fe}	Fig. D.20b	$[W]$	Iron losses
	R_{cd}	0.26	$[K/W]$	Motor thermal resistance
	C_{Cu}	67.34	$[J/K]$	Copper thermal capacity
	C_{Fe}	396.56	$[J/K]$	Iron thermal capacity
	M_{mot}	1.34	$[kg]$	Motor mass
TS Unit	L_b	93.44	$[mm]$	Braid length
	R_{plates}	0.34	$[mm]$	Plates resistance
	R_{braid}	Fig. D.22	$[K/W]$	Braid resistance
	M_{TS}	0.05	$[kg]$	Ts mass
Spreader	R_{spread}	Fig. D.21c	$[K/W]$	Spreader resistance
	h_{eff}	Fig. D.21b	$[W/m^2K]$	Convective heat transfer coefficient
	M_{spread}	0.27	$[kg]$	Spreader mass
TIM	R_{th_c}	0.137	$[K/W]$	Contact resistance on terminal plates
Housing	L_c	97.63	$[mm]$	Housing length
	W_c	63.11	$[mm]$	Housing width
	H_c	63.11	$[mm]$	Housing height
	M_{body}	0.35	$[kg]$	Housing Mass
	C_{th}	206.84	$[J/K]$	Housing thermal capacity
Bearing	D_b	112.97	$[mm]$	Exterior diameter
	d_b	61.62	$[mm]$	Interior diameter
	L_b	22.59	$[mm]$	Bearing length
	M_b	1.07	$[kg]$	Bearing mass
Screw-nut	D_n	55.18	$[mm]$	Nut Diameter
	d_s	25.99	$[mm]$	Screw diameter
	A_n	81.09	$[mm]$	Nut length
	l_{sn}	147.58	$[mm]$	Screw length
	M_{sn}	1.43	$[kg]$	Screw nut mass

continued on next page

– continued from previous page				
	Parameter	Value	Unit	Description
Gearbox	d_g	72.94	$[mm]$	Gear diameter
	d_p	18.23	$[mm]$	Pinion diameter
	d_i	72.94	$[mm]$	Idler diameter
	M_{red}	0.83	$[kg]$	Gearbox mass

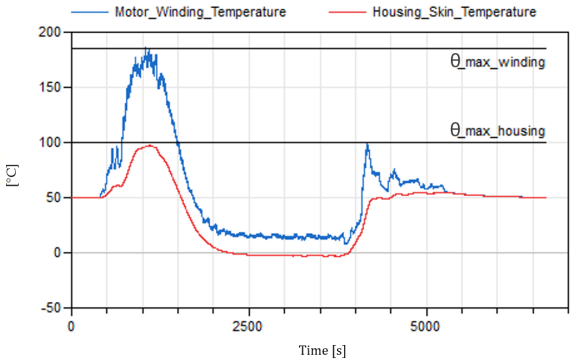

Figure D.19: Thermal profiles (Aileron - Case study 3).

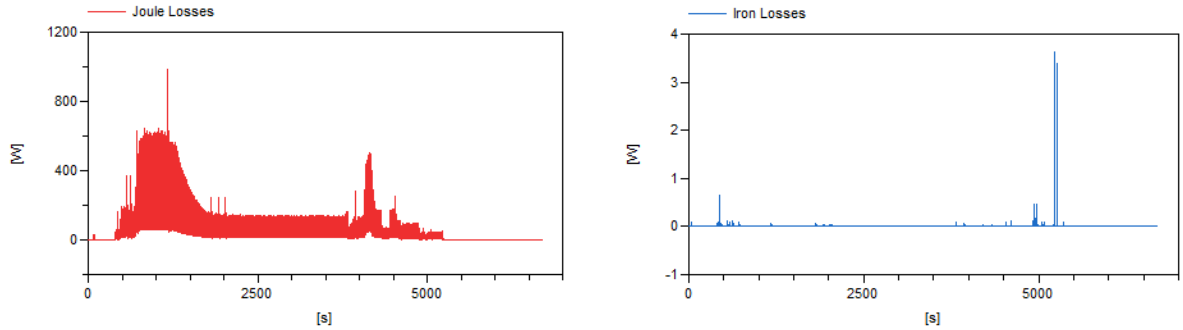

(a) Joule losses (b) Iron losses

Figure D.20: Motor Losses (Aileron - Case study 3).

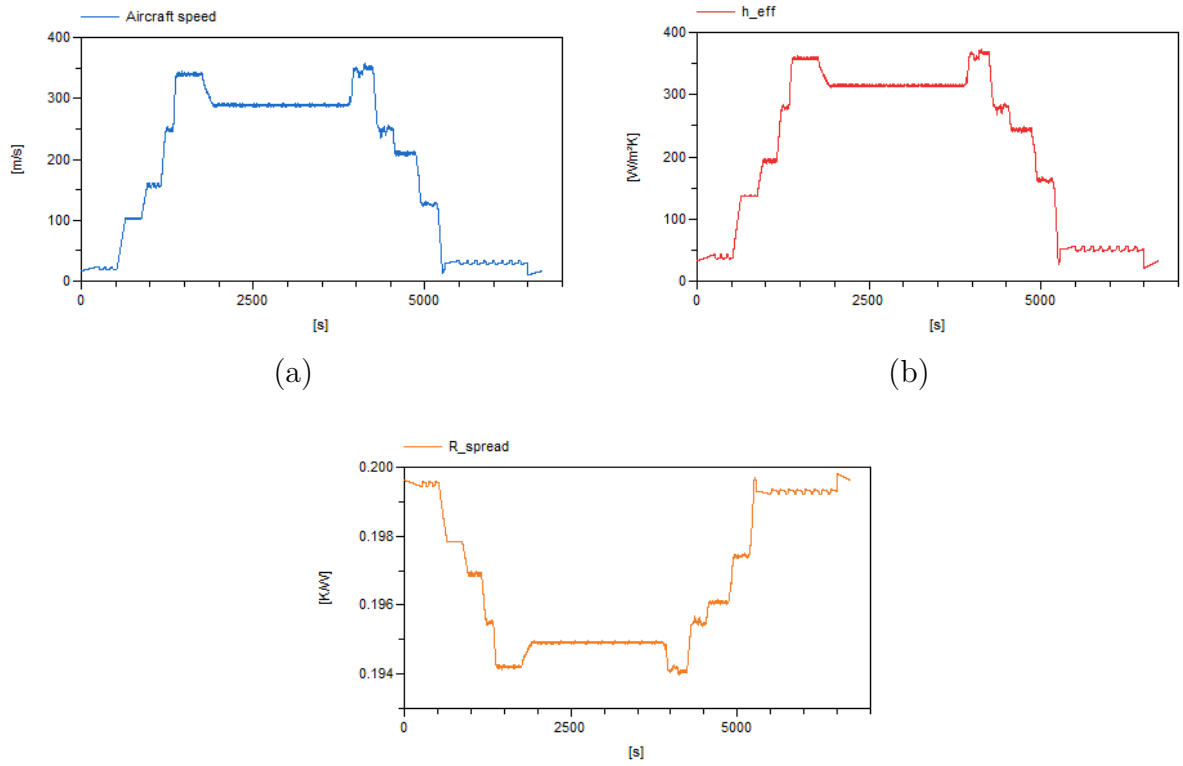

Figure D.21: Aircraft speed profile (TAS) (a), convective heat transfer coefficient on wing (b) and spreader resistance (per TMS unit) (c) (Aileron - Case study 3).

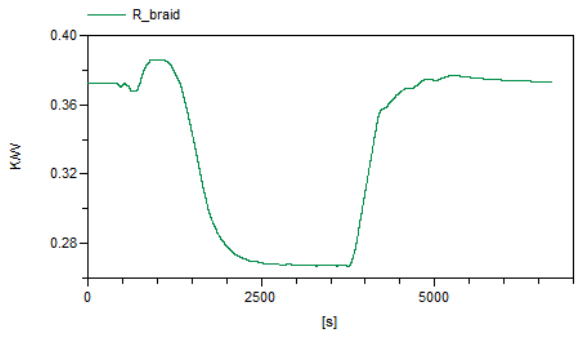

Figure D.22: Braid resistance (Aileron - Case study 3).

Elevator Results

Table D.16: Design variables, constraints and objective (Elevator - Case study 3).

	Parameter	Value	Unit	Description
Design variables	D_e	42.41	$[mm]$	Motor Diameter
	$k_{d_{opt}}$	3	$[-]$	Torque oversize coefficient
	Π_2	0.14	$[-]$	Dimensionless ratio yoke to motor diameter
	k_b	2.5	$[-]$	Bearing oversize coefficient
	k_{sn}	1.49	$[-]$	Screw nut oversize coefficient
	n_{red}	4	$[-]$	Reduction ratio
	n_{TS}	2	$[-]$	Thermal strap number
	W_b	30.73	$[mm]$	Braid width
	w_s	63.65	$[mm]$	Spreader width
	l_s	51.6	$[mm]$	Spreader length
	k_{bt}	2	$[-]$	Bolts number (per plate)
	Π_{4_T}	0.15	$[-]$	Dimensionless ratio bolt position (per plate)
Constraints	$\Theta_{wind_{max}}$	185	$[°C]$	Winding temperature ($\Theta_{wind_{lim}} = 185\,°C$)
	$\Theta_{hous_{max}}$	86.18	$[°C]$	Winding temperature ($\Theta_{hous_{lim}} = 100\,°C$)
	$\omega_{mot_{max}}$	163.68	$[rad/s]$	Maximum motor speed ($\omega_{max} = 942\,rad/s$)
	$C_{d_{sn}}$	22.47	$[kN]$	Screw dynamic load ($C_{d_{sn_{req}}} = 10.84\,kN$)
	$C_{0_{sn}}$	40.73	$[kN]$	Screw static load ($F_{shock} = 40.73\,kN$)
	C_{d_b}	26.24	$[kN]$	Bearing dynamic load ($C_{d_{b_{req}}} = 11.27\,kN$)
	C_{0_b}	40.86	$[kN]$	Bearing static load ($F_{shock} = 40.73\,kN$)
	J_{ref}	1.63	$[kgm^2]$	Reflected Inertia ($J_{ref_{max}} = 30\,kgm^2$)
	W_b	30.73	$[mm]$	Braid width ($W_c = 47.41\,mm$)
	L_{act}	94.68	$[mm]$	Actuator length ($L_e = 200\,mm$)
	W_{act}	115.83	$[mm]$	Actuator width ($W_e = 250\,mm$)
	H_{act}	68.42	$[mm]$	Actuator height ($W_e = 120\,mm$)
Objective	M_{EMA}	1.75	$[kg]$	EMA Mass

Table D.17: System output values (Elevator - Case study 3).

	Parameter	Value	Unit	Description
Motor	L_m	59.9	$[mm]$	Motor length
	T_{mot}	1.81	$[Nm]$	Nominal motor torque
	P_J	Fig. D.24a	$[W]$	Joule losses
	P_{Fe}	Fig. D.24b	$[W]$	Iron losses
	R_{cd}	0.48	$[K/W]$	Motor thermal resistance
	C_{Cu}	21.88	$[J/K]$	Copper thermal capacity
	C_{Fe}	131.06	$[J/K]$	Iron thermal capacity
	M_{mot}	0.49	$[kg]$	Motor mass
TS Unit	L_b	101.29	$[mm]$	Braid length
	R_{plates}	0.4	$[mm]$	Plates resistance
	R_{braid}	Fig. D.26	$[K/W]$	Braid resistance
	M_{TS}	0.04	$[kg]$	Ts mass
Spreader	R_{spread}	Fig. D.25c	$[K/W]$	Spreader resistance
	h_{eff}	Fig. D.25b	$[W/m^2K]$	Convective heat transfer coefficient
	M_{spread}	0.026	$[kg]$	Spreader mass
TIM	R_{th_c}	0.16	$[K/W]$	Contact resistance on terminal plates
Housing	L_c	59.9	$[mm]$	Housing length
	W_c	47.41	$[mm]$	Housing width
	H_c	47.41	$[mm]$	Housing height
	M_{body}	0.15	$[kg]$	Housing Mass
	C_{th}	135	$[J/K]$	Housing thermal capacity
Bearing	D_b	75.60	$[mm]$	Exterior diameter
	d_b	41.24	$[mm]$	Interior diameter
	L_b	15.12	$[mm]$	Bearing length
	M_b	0.36	$[kg]$	Bearing mass
Screw-nut	D_n	32.74	$[mm]$	Nut Diameter
	d_s	15.33	$[mm]$	Screw diameter
	A_n	48.47	$[mm]$	Nut length
	l_{sn}	100.74	$[mm]$	Screw length
	M_{sn}	0.34	$[kg]$	Screw nut mass

continued on next page

– continued from previous page				
	Parameter	Value	Unit	Description
Gearbox	d_g	52.88	$[mm]$	Gear diameter
	d_p	13.22	$[mm]$	Pinion diameter
	d_i	24.94	$[mm]$	Idler diameter
	M_{red}	0.31	$[kg]$	Gearbox mass

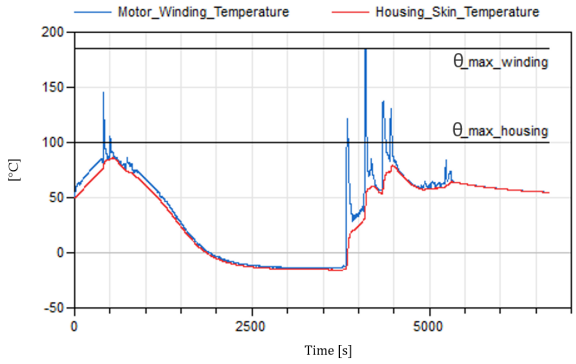

Figure D.23: Thermal profiles (Elevator - Case study 3).

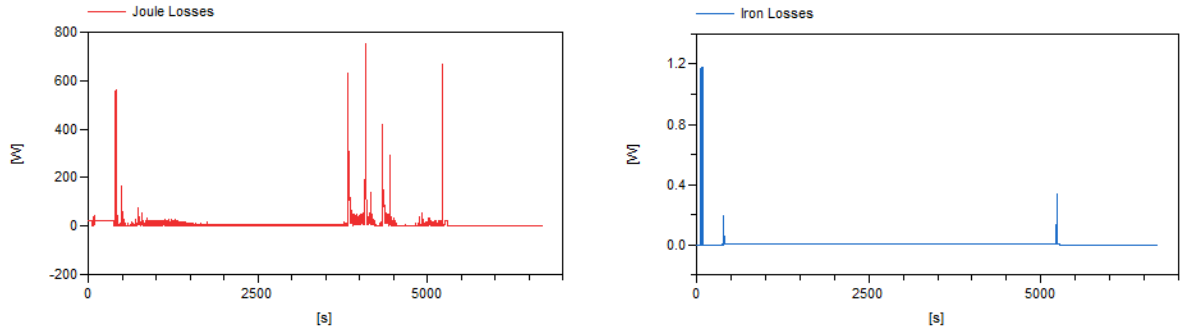

(a) Joule losses (b) Iron losses

Figure D.24: Motor Losses (Elevator - Case study 3).

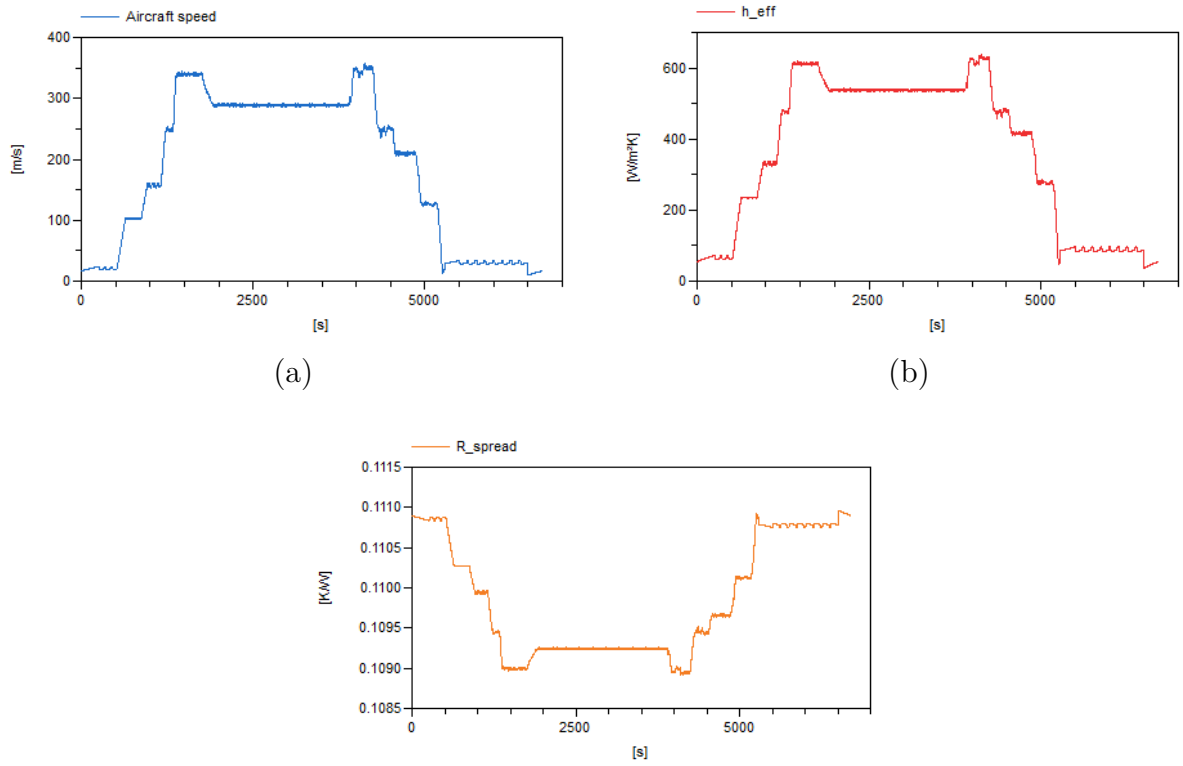

Figure D.25: Aircraft speed profile (TAS) (a), convective heat transfer coefficient on wing (b) and spreader resistance (per TMS unit) (c) (Elevator - Case study 3).

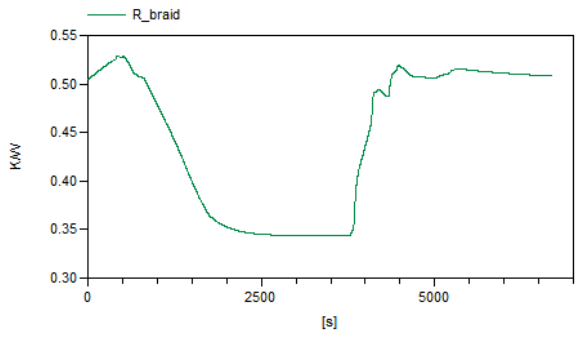

Figure D.26: Braid resistance (Elevator - Case study 3).

Case Study 4: PCM

Formulation of the optimisation problem

$$
\begin{aligned}
\text{Minimize} \quad & M_{EMA} \\
\text{with respect to} \quad & k_{d_{opt}}, D_e, \Pi_2, k_b, k_{sn}, n_{red}, L_a, S, s_a, k_L, k_H, k_W, H_{fin}, L \\
\text{subject to} \quad & \Theta_{wind_{max}} - \Theta_{wind_{lim}} \leq 0 \\
& \Theta_{hous_{max}} - \Theta_{hous_{lim}} \leq 0 \\
& \omega_{mot_{max}} - \omega_{max} \leq 0 \\
& C_{d_{sn_{req}}} - C_{d_{sn}} \leq 0 \\
& F_{shock} - C_{0_{sn}} \leq 0 \\
& F_{shock} - C_{0_b} \leq 0 \\
& C_{d_{b_{req}}} - C_{d_b} \leq 0 \\
& J_{ref} - J_{ref_{max}} \leq 0 \\
& \sigma - \sigma_{max} \leq 0 \\
& L_{EMA} - L_e \leq 0 \\
& W_{EMA} - W_e \leq 0 \\
& H_{EMA} - H_e \leq 0
\end{aligned}
\tag{D.4}
$$

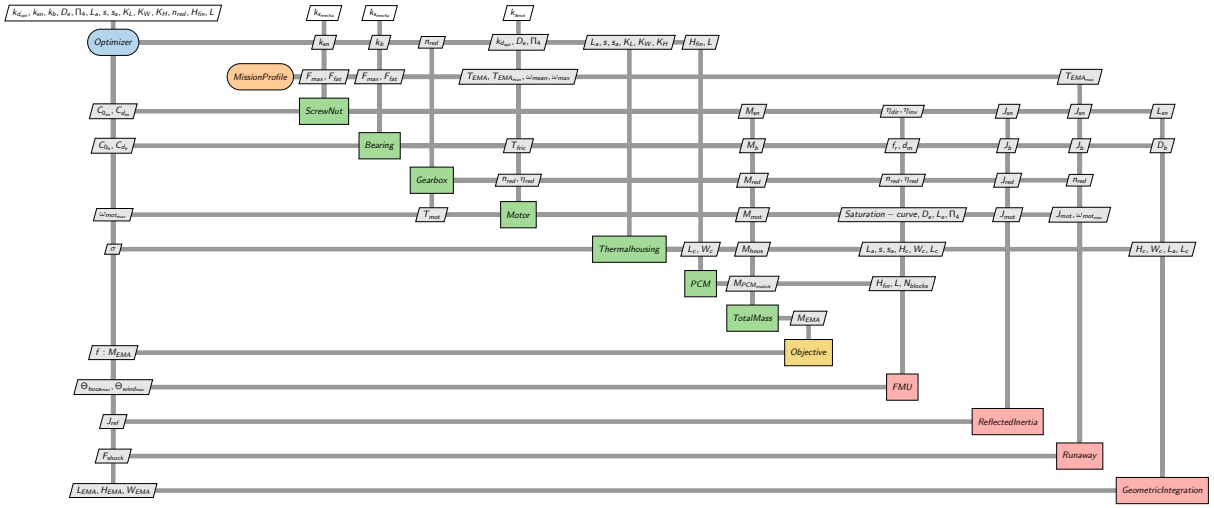

Figure D.27: XDSM of the preliminary design of case study 4.

Design inputs of TMS

Table D.18: Inputs parameters values (Case study 4).

	Parameter	Value	Unit	Description
Housing	Q_m	30	$[-]$	Mechanical quality coefficient
	a	196.2	$[ms^2]$	Vibratory sinusoidal acceleration
	ρ_a	2700	$[kg/ms^3]$	Aluminium density
	λ_a	284	$[W/mK]$	Aluminium thermal conductivity
	Cp_a	900	$[J/kgK]$	Aluminium specific heat
PCM module	s_{a_p}	1.5	$[mm]$	Fin thickness
	e_p	2.5	$[mm]$	Plate base thickness
	T_m	90	$[°C]$	Melting temperature
	ρ_{PCM}	1250	$[kg/m^3]$	PCM density
	Cp_{PCM}	4300	$[J/kgK]$	PCM specific heat
	λ_{PCM}	0.7	$[W/m]$	PCM thermal conductivity
	H	270	$[kJ/kg]$	Heat of fusion

Aileron Results

Table D.19: Design variables, constraints and objective (Aileron - Case study 4).

	Parameter	Value	Unit	Description
Design variables	D_e	61.39	$[mm]$	Motor Diameter
	$k_{d_{opt}}$	1.2	$[-]$	Torque oversize coefficient
	Π_2	0.14	$[-]$	Dimensionless ratio yoke to motor diameter
	k_b	3.72	$[-]$	Bearing oversize coefficient
	k_{sn}	2.64	$[-]$	Screw nut oversize coefficient
	n_{red}	4	$[-]$	Reduction ratio
	L_a	21.45	$[mm]$	Fins width
	S	7.92	$[mm]$	Distance between two fins
	s_a	1.01	$[mm]$	Fin thickness
	k_L	1.57	$[-]$	Housing length oversize coefficient
	k_H	1.09	$[-]$	Housing height oversize coefficient
	k_W	1.09	$[-]$	Housing width oversize coefficient
Constraints	$\Theta_{wind_{max}}$	185	$[^\circ C]$	Winding temperature ($\Theta_{wind_{lim}} = 185\,^\circ C$)
	$\Theta_{hous_{max}}$	100	$[^\circ C]$	Winding temperature ($\Theta_{hous_{lim}} = 100\,^\circ C$)
	$\omega_{mot_{max}}$	176	$[rad/s]$	Maximum motor speed ($\omega_{max} = 942\,rad/s$)
	$C_{d_{sn}}$	67.92	$[kN]$	Screw dynamic load ($C_{d_{sn_{req}}} = 67.81\,kN$)
	$C_{0_{sn}}$	117.15	$[kN]$	Screw static load ($F_{shock} = 95.78\,kN$)
	C_{d_b}	101.45	$[kN]$	Bearing dynamic load ($C_{d_{b_{req}}} = 64.86\,kN$)
	C_{0_b}	95.8	$[kN]$	Bearing static load ($F_{shock} = 95.78\,kN$)
	J_{ref}	13.07	$[kgm^2]$	Reflected Inertia ($J_{ref_{max}} = 30\,kgm^2$)
	σ	39.98	$[MPa]$	Limit stress of fin ($\sigma_{max} = 40\,MPa$)
	L_{act}	149.18	$[mm]$	Actuator length ($L_e = 200\,mm$)
	W_{act}	225.66	$[mm]$	Actuator width ($W_e = 250\,mm$)
	H_{act}	115.76	$[mm]$	Actuator height ($W_e = 120\,mm$)
Objective	M_{EMA}	5.82	$[kg]$	EMA Mass

Table D.20: System output values (Aileron - Case study 4).

	Parameter	Value	Unit	Description
Motor	L_m	86.54	$[mm]$	Motor length
	T_{mot}	5.23	$[Nm]$	Nominal motor torque
	P_J	Fig. D.30a	$[W]$	Joule losses
	P_{F_e}	Fig. D.30b	$[W]$	Iron losses
	R_{cd}	0.29	$[K/W]$	Motor thermal resistance
	C_{Cu}	67.21	$[J/K]$	Copper thermal capacity
	C_{Fe}	392.85	$[J/K]$	Iron thermal capacity
	M_{mot}	1.35	$[kg]$	Motor mass
Fin Housing	N_{fin}	16	$[-]$	Fins number
	h_{hous}	Fig. D.29	$[W/m^2K]$	Heat transfer coefficients of finned housing
	C_{th}	543.56	$[J/k]$	Housing thermal capacity
	M_{fin}	0.06	$[kg]$	Fins mass
	M_{body}	0.56	$[kg]$	Housing body mass
	M_{hous}	0.61	$[kg]$	Housing mass
PCM Module Unit	H_{fin}	15.11	$[-]$	Fins number
	L	1.34	$[kg]$	Half thickness PCM slab
	$N_{fin_{PCM}}$	10	$[-]$	Fin number
	M_{plate}	0.14	$[kg]$	Aluminium container mass
	M_{PCM}	0.06	$[kg]$	PCM mass
	$M_{PCM_{Module}}$	0.2	$[kg]$	PCM module mass
Bearing	D_b	115.76	$[mm]$	Exterior diameter
	d_b	63.14	$[mm]$	Interior diameter
	L_b	23.15	$[mm]$	Bearing length
	M_b	1.15	$[kg]$	Bearing mass
Screw-nut	D_n	55.14	$[mm]$	Nut Diameter
	d_s	26.01	$[mm]$	Screw diameter
	A_n	81.15	$[mm]$	Nut length
	l_{sn}	149.18	$[mm]$	Screw length
	M_{sn}	1.44	$[kg]$	Screw nut mass
Gearbox	d_g	82.97	$[mm]$	Gear diameter
	d_p	20.74	$[mm]$	Pinion diameter
	d_i	39.14	$[mm]$	Idler diameter
	M_{red}	0.87	$[kg]$	Gearbox mass

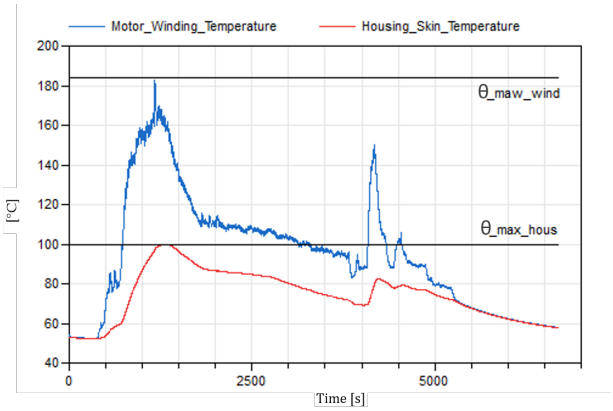

Figure D.28: Thermal profiles (Aileron - Case study 4).

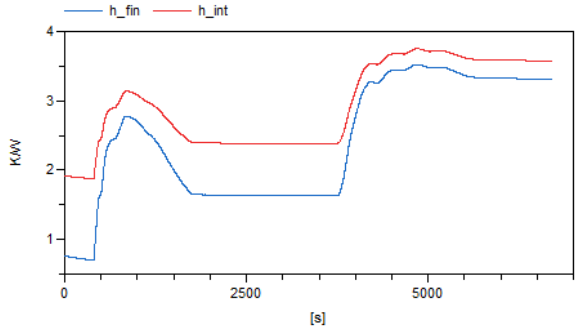

Figure D.29: Heat transfer coefficients of finned thermal housing (Aileron - Case study 4).

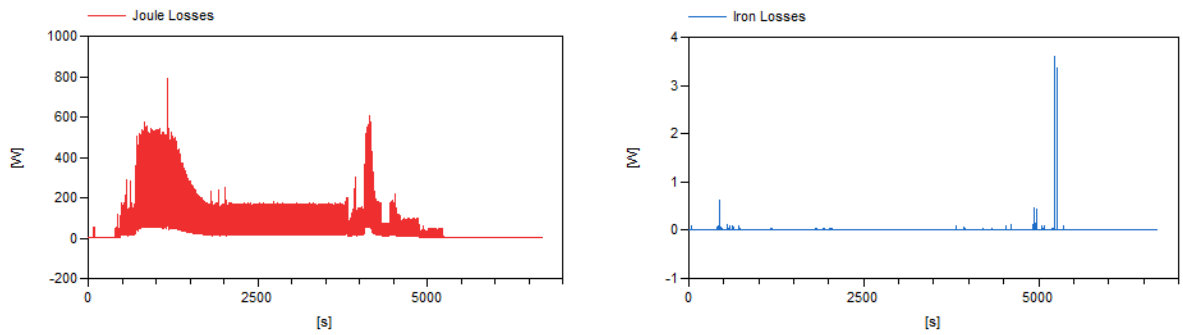

(a) Joule losses (b) Iron losses

Figure D.30: Motor Losses (Aileron - Case study 4).